UNIVERSITY COLLEGE LONDON

Faculty of Mathematics and Physical Sciences

Department of Physics & Astronomy

MOLECULE AND DUST EMISSION AT THE BEGINNINGS AND ENDS OF STELLAR EVOLUTION

Thesis submitted for the Degree of Doctor of Philosophy of the University of London

by

Felix D. Priestley

Supervisors:

Prof. Mike Barlow

Prof. Serena Viti

Examiners:

Dr. Jeremy Yates

Prof. David Flower

January 3, 2019

I, Felix Priestley, confirm that the work presented in this thesis is my own. Where information has been derived from other sources, I confirm that this has been indicated in the thesis.

Abstract

A combination of photoionization and photodissociation region codes is used to model planetary nebulae and the Crab Nebula supernova remnant, to explain the observed molecular emission. The inclusion of ionizing ultraviolet flux is necessary to reproduce the observed H_2 emission and the trend in OH^+ detections with central star temperature in PNe. The highest observed H_2 line strengths may require an additional heating mechanism, such as shocks. The observed ArH^+ and OH^+ line strengths in the Crab Nebula, and the lack of [C I] emission, are explained by high values of the cosmic ray ionization rate, appropriate for the environment. Models with extinctions similar to observed dusty globules can also reproduce the H_2 and fine structure line emission from the Crab.

The thermal dust emission from grains heated by the synchrotron radiation field and by particle collisions is calculated under conditions appropriate for the Cassiopeia A supernova remnant. The observed spectral energy distribution requires $\sim 0.6\,M_\odot$ of silicate dust, primarily in the unshocked ejecta. Other dust species cannot comprise a significant fraction of the total dust mass. Gas-to-dust ratios for each gas component show that the condensation efficiency in the ejecta is high, and dust located in clumps is protected from destruction by the reverse shock.

Gravitational collapses of prestellar cores are approximated analytically, and used to model the evolution of the molecular abundances with time and radius. It is shown that the mode of collapse has observable consequences for many important molecules - CO profiles observed in cores appear to differ significantly from those predicted by collapse via ambipolar diffusion. The potential of this method to decrease the required computing time is shown by creating a grid of models with varying input parameters, and the effects of these changes discussed.

Impact

A new method for studying the chemistry of star formation has been developed, making observational tests of various proposed theoretical models more feasible. The reduced computational expense compared to previous work allows a full exploration of parameter space, which can be combined with the large datasets now available to constrain the allowed regions. Molecular ions have been shown to be useful probes of physical conditions within ionized nebulae, being particularly sensitive to the rate of ionization processes. That the gas responsible for the molecular emission in the Crab Nebula is likely strongly affected by cosmic rays should be taken into account by future work on this object. A new code for calculating dust emission has been written, and designed to be flexible enough to be of use in modelling any astrophysical environment where dust is present.

The public are interested in space, particularly parts related to the formation of stars, planets and potentially life, and also parts which explode. This thesis contains results relevant to both areas, and communicating these results could inspire further interest in astrophysics, and science in general. Given the reliance of the economy and society in general on technology, encouraging both public support for science and potential interest in pursuing scientific careers is an important objective.

Acknowledgements

I'd mostly like to thank Mike and Serena, for putting up with my occasionally questionable work ethic for the last three years, and my parents, for putting up with a lot more for a lot longer. Additional thanks to everyone who kept me company in the pub and on excessively long tea breaks - I won't bother listing them all, but special mentions for Luisa, who listened to an enormous amount of complaining, Will, who bought plenty of rounds and provided the best career advice ('pull your finger out and get some bloody work done') and Giuliana, who kept us all well supplied with crisps and had to sit next to me for a year. Finally, I'm eternally grateful to the staff in the Devonshire Arms, Sheephaven Bay, Square Tavern, the Court, the Black Heart, Huntley's, the Bree Louise (RIP) and the Housman Room - I couldn't have done it without them.

...for lasers or some similar phenomenon could only be reflected by dust,
and there is not so much dust in space.

Eternity - Greg Bear

Contents

Table of Contents **9**

List of Figures **13**

List of Tables **23**

1 Introduction **27**

1.1 The interstellar medium 27

1.2 Dust properties in the ISM 29

1.3 Gravitational collapse 30

1.4 Astrochemistry 33

1.4.1 Gas-phase chemistry 33

1.4.2 Surface chemistry 34

1.4.3 X-ray chemistry 35

1.5 Interaction of radiation and matter 35

1.5.1 Photoionized regions 36

1.5.2 PDRs 37

1.5.3 Molecular regions 39

1.6 Emission processes 39

1.6.1 Line emission 39

1.6.2 Rotational lines 40

1.6.3 Vibrational lines 41

1.6.4 Atomic forbidden and fine-structure lines 41

1.6.5 Dust continuum emission 42

1.7 The evolution of low- and high-mass stars 44

1.8 This thesis 47

2 Description of the codes used **49**

2.1 UCLCHEM 49

2.2 UCL_PDR 52

2.3 MOCASSIN 55

3 Molecular emission from planetary nebulae **61**

3.1 Introduction 61

3.2 Method 63

3.3 Results 68

3.4 Discussion 77

3.4.1 Location of the molecular emission 77

3.4.2 Treatment of EUV flux 79

3.4.3 Effect of input parameters 81

3.4.4 Shock heating and fluorescent emission 82

3.4.5 Non-detections of OH^+ 84

3.4.6 ArH^+ and HeH^+ emission 85

3.4.7 Systematic uncertainties 85

3.5 Conclusions 86

4 ArH^+ emission from the Crab Nebula **89**

4.1 Introduction 89

4.2 Method 90

4.3 Results 92

4.3.1 Cloud properties 93

4.3.2 Herschel SPIRE FTS observations 94

4.3.3 Other observations 99

4.4 Discussion 102

4.5 Conclusions 106

5 Description of DINAMO **107**

5.1 Radiative heating 108

5.2 Radiative cooling 109

5.3 Collisional heating 110

5.4 Solution algorithm 111

6 Dust emission from Cassiopeia A **113**

6.1 Introduction 113

6.2 Physical properties of the Cas A SNR 115

6.3 Method 116

6.4 Results 119

6.5 Discussion 126

6.5.1 Comparison with previous results 126

6.5.2 The mid-infrared spectrum 128

6.5.3 Gas-to-dust mass ratios 129

6.6 Conclusions 131

7 Conclusions **133**

A Prestellar cores **137**

A.1 Introduction 137

A.2 Methodology 139

A.2.1 Parametrization of numerical simulations 139

A.2.2 Chemical modelling 144

A.3 Results 147

A.3.1 Molecular abundances across the different modes of collapse 147

A.3.2 Cosmic ray ionization rate 148

A.3.3 Metallicity 149

A.3.4 Desorption efficiencies 149

A.4 Star formation efficiencies 152

A.5 Discussion & Conclusions 153

B Approximations for the collapse of prestellar cores **157**

B.1 Density approximations 157

B.1.1 BES1 157

B.1.2 BES4 158

B.1.3 MS 158

B.1.4 AD 158

B.2 Velocity profiles 159

B.2.1 MS 159
B.2.2 AD 160

Bibliography **161**

List of Figures

1.1 Normalised interstellar extinction curves from various sources, taken from Fitzpatrick (1999). 30

1.2 ISOCAM IR spectrum of NGC 7023, showing PAH features, from Cesarsky et al. (1996). The solid line is the spectrum from the region of peak 16 μm emission, while the dotted line is from a region with lower 16 μm intensity. . 31

1.3 Density profile of a BE sphere with $n_0 = 2 \times 10^4\,\mathrm{cm}^{-3}$, $T = 10\,\mathrm{K}$ and $\mu = 2m_\mathrm{H}$. The critical radius, beyond which the cloud is unstable, is marked with a dashed line. 32

1.4 Abundances versus visual extinction of H (blue solid line), H_2 (blue dashed line), O (red solid line), C (black solid line), C^+ (black dashed line) and CO (black dotted line), for a PDR with $n_\mathrm{H} = 10^3\,\mathrm{cm}^{-3}$ and a radiation field of 5 Draines. 38

1.5 Energy levels and transitions of neutral oxygen. The energy levels are not to scale, to allow the fine structure splitting to be visible. Wavelengths are in vacuo values. 42

1.6 Emitted dust SED from the BARE-GR-S Zubko et al. (2004) model, heated by the Mathis et al. (1983) ISM radiation field. 44

1.7 Evolutionary track of a $5\,\mathrm{M}_\odot$ star on a Hertzsprung-Russell diagram, from Iben (1967). 47

2.1 Gas density (thick black solid line) and abundances of CO (thin black solid line), NH_3 (blue solid line), HCN (red solid line), HCO^+ (black dashed line) and N_2H^+ (blue dashed line) versus time, for a cloud with an initial density of $100\,cm^{-3}$ and gas temperature 10 K collapsing under free-fall conditions, as calculated by UCLCHEM. 51

2.2 Heating rate versus visual extinction of the dust PE effect (solid black line), H_2 formation (solid blue line), H_2 photodissociation (dashed blue line), cosmic ray heating (solid red line) and exothermic chemical reactions (solid green line), for the UCL_PDR model described in Section 1.5.2. . . . 54

2.3 Cooling rate versus visual extinction from the emission lines of C^+ (dashed black line), C (solid black line), O (solid blue line) and CO (dotted black line), for the UCL_PDR model described in Section 1.5.2. 55

2.4 MOCASSIN model for hydrogen (solid black line) and electron (dotted black line) densities and electron temperature (solid red line) versus radius for a nebula with $n_H = 100\,cm^{-3}$, and stellar parameters $T_* = 40\,000$ K and $L_* = 8.11 \times 10^5\,L_\odot$, for a blackbody spectrum. The density scale is on the left-hand side, the temperature scale is on the right. 56

2.5 MOCCASSIN ion fractions relative to the total elemental abundance of H^+ (dashed blue line), H^0 (solid blue line), He^{++} (dotted red line), He^+ (dashed red line) and He^0 (solid red line) versus radius for a nebula with $n_H = 100\,cm^{-3}$, and stellar parameters $T_* = 40\,000$ K and $L_* = 8.11 \times 10^5\,L_\odot$. 57

2.6 MOCASSIN ion fractions, relative to the total carbon abundance, for C^{3+} (dotted black line), C^{2+} (dashed black line) and C^+ (solid black line) versus radius for a nebula with $n_H = 100\,cm^{-3}$, and stellar parameters $T_* = 40\,000$ K and $L_* = 8.11 \times 10^5\,L_\odot$. 58

3.1 Composite Hubble Space Telescope image of NGC 7293, the Helix Nebula. The image dimensions are 28.7×28.7 arcmin. Image credit: NASA, ESA and C. R. O'Dell. 63

3.2 Schematic diagram of the modelling strategy. Left: a central source illuminates a surrounding shell of dense gas, with diffuse material occupying the interior of the shell. Right: the radiation field emerging from the shell is treated as a unidirectional field incident on a slab of gas, with a thickness much smaller than the radius of the shell. 64
3.3 Flowchart of the modelling strategy. 65
3.4 OH^+ 971 GHz surface brightness versus T_*, for models with $n_H = 10^5\,cm^{-3}$, $\log g = 7.0$ and $L_* = 100\,L_\odot$ (solid line) and $1000\,L_\odot$ (dashed line). The dotted horizontal lines show the range of observed values from Etxaluze et al. (2014) and Aleman et al. (2014). 70
3.5 H_2 2.12 μm surface brightness versus T_*, for models with $n_H = 10^5\,cm^{-3}$, $\log g = 7.0$ and $L_* = 100\,L_\odot$ (solid line) and $1000\,L_\odot$ (dashed line). The dotted horizontal lines show the range of observed values from Hora et al. (1999). 70
3.6 CO $J = 4-3$ surface brightness versus T_*, for models with $n_H = 10^5\,cm^{-3}$, $\log g = 7.0$ and $L_* = 100\,L_\odot$ (solid line) and $1000\,L_\odot$ (dashed line). The dotted horizontal lines show the range of observed values from Etxaluze et al. (2014) and Ueta et al. (2014). 71
3.7 ArH^+ 617 GHz surface brightness versus T_*, for models with $n_H = 10^5\,cm^{-3}$, $\log g = 7.0$ and $L_* = 100\,L_\odot$ (solid line) and $1000\,L_\odot$ (dashed line). The dotted horizontal line shows the surface brightness of the weakest SPIRE OH^+ detection from Aleman et al. (2014). 71
3.8 OH^+ 971 GHz surface brightness versus T_*, for models with $n_H = 10^6\,cm^{-3}$, $\log g = 7.0$ and $L_* = 100\,L_\odot$ (solid line) and $1000\,L_\odot$ (dashed line). The dotted horizontal lines show the range of observed values from Etxaluze et al. (2014) and Aleman et al. (2014). 72
3.9 CO $J = 4-3$ surface brightness versus T_*, for models with $n_H = 10^6\,cm^{-3}$, $\log g = 7.0$ and $L_* = 100\,L_\odot$ (solid line) and $1000\,L_\odot$ (dashed line). The dotted horizontal lines show the range of observed values from Etxaluze et al. (2014) and Ueta et al. (2014). 73
3.10 Model central star spectra for model atmospheres with $T_* = 120\,kK$ and $\log g = 6.0$ (solid line), 7.0 (dashed line) and 8.0 (dotted line), obtained from the TheoSSA database (Rauch 2003). 73

3.11 OH^+ 971 GHz surface brightness versus T_*, for models with $n_H = 10^5\,cm^{-3}$, $\log g = 6.0$ and $L_* = 100\,L_\odot$ (solid line) and $1000\,L_\odot$ (dashed line). The dotted horizontal lines show the range of observed values from Etxaluze et al. (2014) and Aleman et al. (2014). 74

3.12 OH^+ 971 GHz surface brightness versus T_*, for models with $n_H = 10^5\,cm^{-3}$, $\log g = 7.0$ and $L_* = 100\,L_\odot$ (solid line) and $1000\,L_\odot$ (dashed line) including the EUV flux. The dotted horizontal lines show the range of observed values from Etxaluze et al. (2014) and Aleman et al. (2014). 75

3.13 H_2 2.12 μm surface brightness versus T_*, for models with $n_H = 10^5\,cm^{-3}$, $\log g = 7.0$ and $L_* = 100\,L_\odot$ (solid line) and $1000\,L_\odot$ (dashed line) including the EUV flux. The dotted horizontal lines show the range of observed values from Hora et al. (1999). 76

3.14 ArH^+ 617 GHz surface brightness versus T_*, for models with $n_H = 10^5\,cm^{-3}$, $\log g = 7.0$ and $L_* = 100\,L_\odot$ (solid line) and $1000\,L_\odot$ (dashed line) including the EUV flux. The dotted horizontal line shows the surface brightness of the weakest SPIRE OH^+ detection from Aleman et al. (2014). 76

3.15 OH^+ column density versus T_*, for models with $n_H = 10^5\,cm^{-3}$, $\log g = 7.0$ and $L_* = 100\,L_\odot$ (solid line) and $1000\,L_\odot$ (dashed line) including the EUV flux. The dotted horizontal lines show the range of values calculated from observations by Aleman et al. (2014). 77

3.16 Abundances of H (thin solid line), H_2 (dashed line) and e^- (dotted line) and gas temperature (thick solid line) versus distance into the knot for the 120 kK $100\,L_\odot$ $\log g = 7.0$ EUV model. The left y-axis shows the abundance relative to hydrogen nuclei, and the right the gas temperature. 78

3.17 Line emissivities of H_2 2.12 μm (solid line), CO $J = 4 - 3$ (dashed line), OH^+ 971 GHz (dotted line) and ArH^+ 617 GHz (dot-dashed line) versus distance into the knot for the 120 kK $100\,L_\odot$ $\log g = 7.0$ EUV model. 79

3.18 Formation timescales versus distance into the knot for HeH^+ (solid line), OH^+ (dashed line) and ArH^+ (dotted line), for the 150 kK $1000\,L_\odot$ $\log g = 7.0$ EUV model. 86

4.1 Composite image of the Crab Nebula, from combined Hubble Space Telescope optical emission line (blue-white) and Herschel Space Observatory 70 μm (red) images. The image dimensions are 5.65×5.65 arcmin. Taken from Owen and Barlow (2015). 91

4.2 Abundances of H (solid black line), H_2 (dashed black line), e^- (dotted black line), ArH^+ (solid blue line) and OH^+ (dashed blue line), and gas temeperature (solid red line) for the $n_H = 2 \times 10^4\,cm^{-3}$, $\zeta = \zeta_0$ model. The abundance scale is on the left axis, the temperature scale on the right. . . . 94

4.3 Abundances of H (solid black line), H_2 (dashed black line), e^- (dotted black line), ArH^+ (solid blue line) and OH^+ (dashed blue line), and gas temeperature (solid red line) for the $n_H = 2 \times 10^4\,cm^{-3}$, $\zeta = 10^7\zeta_0$ model. The abundance scale is on the left axis, the temperature scale on the right. 95

4.4 ArH^+ 617 GHz surface brightness versus ζ, for models with $n_H = 2 \times 10^3$ (blue), 2×10^4 (green) and $2 \times 10^5\,cm^{-3}$ (red). The dotted horizontal lines show the observed range of values from Barlow et al. (2013). 96

4.5 OH^+ 971 GHz surface brightness versus ζ, for models with $n_H = 2 \times 10^3$ (blue), 2×10^4 (green) and $2 \times 10^5\,cm^{-3}$ (red). The dotted horizontal lines show the observed range of values from Barlow et al. (2013). 96

4.6 [C I] 809 GHz surface brightness versus ζ, for models with $n_H = 2 \times 10^3$ (blue), 2×10^4 (green) and $2 \times 10^5\,cm^{-3}$ (red). The dotted horizontal lines show the observed upper limit from Barlow et al. (2013). 97

4.7 ArH^+ 617 GHz surface brightness versus ζ, for models with $n_H = 2 \times 10^3$ (blue), 2×10^4 (green) and $2 \times 10^5\,cm^{-3}$ (red). The dotted horizontal lines show the observed range of values from Barlow et al. (2013). The visual extinction of the cloud is 0.1 mag. 98

4.8 OH^+ 971 GHz surface brightness versus ζ, for models with $n_H = 2 \times 10^3$ (blue), 2×10^4 (green) and $2 \times 10^5\,cm^{-3}$ (red). The dotted horizontal lines show the observed range of values from Barlow et al. (2013). The visual extinction of the cloud is 0.1 mag. 98

4.9 [C I] 809 GHz surface brightness versus ζ, for models with $n_H = 2 \times 10^3$ (blue), 2×10^4 (green) and $2 \times 10^5\,cm^{-3}$ (red). The dotted horizontal lines show the observed upper limit from Barlow et al. (2013). The visual extinction of the cloud is 0.1 mag. 99

4.10 ArH^+ 617 GHz surface brightness versus ζ, for models with $n_H = 2 \times 10^3$ (blue), 2×10^4 (green) and $2 \times 10^5\,cm^{-3}$ (red). The dotted horizontal lines show the observed range of values from Barlow et al. (2013). The visual extinction of the cloud is 0.05 mag, and the argon abundance is 5×10^{-5}. . 100

4.11 [C I] 809 GHz surface brightness versus ζ, for models with $n_H = 2 \times 10^3$ (blue), 2×10^4 (green) and $2 \times 10^5\,cm^{-3}$ (red). The dotted horizontal lines show the observed upper limit from Barlow et al. (2013). The visual extinction of the cloud is 0.05 mag, and the argon abundance is 5×10^{-5}. . 100

5.1 Dust emission for the Mathis et al. (1983) ISM radiation field benchmark case from Camps et al. (2015), as calculated by DINAMO (solid black line) and DustEM (dashed red line). 108

6.1 Herschel PACS far-infrared image of the Galactic supernova remnant Cassiopeia A. Blue shows supernova dust emission at a wavelength of 70 microns and red shows interstellar dust emission at a wavelength of 160 microns. The image dimensions are 22×22 arcmin. Image credit: Oliver Krause (MPIA). 115

6.2 X-ray image of Cas A, with Si Hα emission in red, Fe K in blue and continuum in green, from Hwang et al. (2004). The image dimensions are 5×5 arcmin. 117

6.3 Best-fit total dust SED (black solid line) to the $G = 0.6G_0$ SNR dust fluxes from De Looze et al. (2017) (black crosses) for $MgSiO_3$ grains with an MRN size distribution, and the model fluxes (red crosses). The SEDs from each dust component as defined in Table 6.1 are shown as dashed lines (preshock: blue, clump: red, diffuse: green, blastwave: purple). 121

6.4 Best-fit total dust SED (black solid line) to the $G = 0.6G_0$ SNR dust fluxes from De Looze et al. (2017) (black crosses) for $Mg_{0.7}SiO_{2.7}$ grains with an MRN size distribution, and the model fluxes (red crosses). The SEDs from each dust component as defined in Table 6.1 are shown as dashed lines (preshock: blue, clump: red, diffuse: green, blastwave: purple). 122

6.5 Best-fit total dust SED (black solid line) to the $G = 0.6G_0$ SNR dust fluxes from De Looze et al. (2017) (black crosses) for $Mg_{0.4}Fe_{0.6}SiO_3$ grains with an MRN size distribution, and the model fluxes (red crosses). The SEDs from each dust component as defined in Table 6.1 are shown as dashed lines (preshock: blue, clump: red, diffuse: green, blastwave: purple). 123

6.6 Best-fit total dust SED (black solid line) to the $G = 0.6G_0$ SNR dust fluxes from De Looze et al. (2017) (black crosses) for ACAR grains with an MRN size distribution, and the model fluxes (red crosses). The SEDs from each dust component as defined in Table 6.1 are shown as dashed lines (preshock: blue, clump: red, diffuse: green, blastwave: purple). 124

6.7 Best-fit total dust SED (black solid line) to the $G = 0.6G_0$ SNR dust fluxes from De Looze et al. (2017) (black crosses) for $MgSiO_3$ grains with an MRN size distribution, and the model fluxes (red crosses), using only the three ejecta components. The SEDs from each dust component as defined in Table 6.1 are shown as dashed lines (preshock: blue, clump: red, diffuse: green). 125

6.8 Best-fit total dust SED (black solid line) to the $G = 0.6G_0$ SNR dust fluxes from De Looze et al. (2017) (black crosses) for $MgSiO_3$ grains with an MRN size distribution, and the model fluxes (red crosses) with the radiation field strength increased by a factor of 10. The SEDs from each dust component as defined in Table 6.1 are shown as dashed lines (preshock: blue, clump: red, diffuse: green, blastwave: purple). 126

6.9 Best-fit total dust SED (black solid line) to the $G = 0.6G_0$ SNR dust fluxes from De Looze et al. (2017) (black crosses) for $MgSiO_3$ grains, and the model fluxes (red crosses) with the radiation field strength increased by a factor of 10. The preshock component MRN-like grain radius distribution is between 0.1 and 1.0 μm. The SEDs from each dust component as defined in Table 6.1 are shown as dashed lines (preshock: blue, clump: red, diffuse: green, blastwave: purple). 127

A.1 Density profiles taken from Aikawa et al. (2005) (solid lines), with the approximate profiles calculated using Eq. A.1 (dashed lines). The labels indicate the time since collapse in 10^6 yr. 141

A.2 Central density n_0 against t for the approximations to the Aikawa et al. (2005) data (solid), with the approximate fit to the time evolution (dashed). 141
A.3 As Figure A.1, but with the parameters for Eq. A.1 calculated as a function of time. 142
A.4 As Figure A.3, for the BES4 collapse 142
A.5 As Figure A.3, for the MS collapse 143
A.6 As Figure A.3, for the AD collapse 143
A.7 Parcel density versus time for the BES1 collapse, for different initial parcel radii. 144
A.8 Flowchart showing the interaction between the density approximations and the chemical solver in UCLCHEM. r is the initial particle radius, n is the gas density, t is the current timestep, $t-1$ and $t+1$ the preceding and following timesteps and $Y(t)$ the molecular abundances at time t. 145
A.9 Density profiles of the BES1 (solid black), BES4 (dashed black), MS (blue) and AD (red) approximations, at a central number density of $n_0 = 2 \times 10^5\,\mathrm{cm}^{-3}$. 149
A.10 Abundances of CO, NH_3, HCO^+ and HCN at a central density $n_0 = 2 \times 10^5\,\mathrm{cm}^{-3}$ for model A, using the BES1 (solid black), BES4 (dashed black), MS (blue) and AD (red) density approximations. 150
A.11 Abundance of CO versus radius at a central density $n_0 = 2 \times 10^5\,\mathrm{cm}^{-3}$ for models A (solid line), B1 (dashed line) and B2 (dotted line), using the BES1 (left) and AD (right) density approximations. 150
A.12 Abundance of HCO^+ versus radius at a central density $n_0 = 2 \times 10^5\,\mathrm{cm}^{-3}$ for models A (solid line), B1 (dashed line) and B2 (dotted line), using the BES1 (left) and AD (right) density approximations. 151
A.13 Abundance of CO (left) and HCN (right) versus radius at a central density $n_0 = 2 \times 10^5\,\mathrm{cm}^{-3}$ for models A (solid line), C1 (dashed line) and C2 (dotted line), using the BES1 density approximation. 151
A.14 Abundance of CO versus radius at a central density $n_0 = 2 \times 10^5\,\mathrm{cm}^{-3}$ for models A (solid line), D1 (dashed line) and D2 (dotted line), using the MS (left) and AD (right) density approximations. 152

A.15 N_2H^+ abundance at a central density $n_0 = 2 \times 10^5\,\mathrm{cm}^{-3}$ for model A, using the BES1 (solid black), BES4 (dashed black), MS (blue) and AD (red) density approximations. 156

This page was intentionally left blank

List of Tables

3.1 Gas-phase elemental abundances, relative to hydrogen, adopted for the PN modelling. 67

3.2 Central star luminosities L_* and effective temperatures T_*, and output UV and X-ray fluxes from our MOCASSIN modelling of PNe with $\log g = 7.0$. The X-ray component includes all transmitted flux between 0.1 Å and 200 Å. 67

3.3 Central star luminosities L_* and effective temperatures T_*, and output UV and X-ray fluxes from our MOCASSIN modelling of PNe with $\log g = 6.0$ and 8.0. The X-ray component includes all transmitted flux between 0.1 Å and 200 Å. 67

3.4 Central star luminosities L_* and effective temperatures T_*, and output UV and X-ray fluxes from our MOCASSIN modelling of PNe, for model atmospheres with $\log g = 7.0$ including the EUV flux. The X-ray component now includes all flux up to 750 Å. 68

3.5 Observed line surface brightnesses for NGC 7293 and NGC 6781, and models with $L_* = 100\,\mathrm{L}_\odot$ and $T_* = 120\,\mathrm{kK}$. Details of models are described in the text. Surface brightnesses are in $\mathrm{erg\,cm^{-2}\,s^{-1}\,sr^{-1}}$. Observed values are from Aleman et al. (2011) (H_2) and Etxaluze et al. (2014) (CO, OH^+, ArH^+) for NGC 7293, and Otsuka et al. (2017) (H_2, CO) and Aleman et al. (2014) (OH^+, ArH^+, HeH^+) for NGC 6871. 83

4.1 Gas phase elemental abundances, relative to hydrogen, used in PDR modelling, taken from model IV of Owen and Barlow (2015). 92

4.2 Model name, cloud size, density and cosmic ray ionization rate for UCL_PDR models. 93

4.3 Observed and predicted line surface brightnesses for models with Ar/H = 5×10^{-5} and $A_V = 0.1$ (D3Z6), 0.03 (D4Z7) and 0.01 (D5Z8). Surface brightnesses are in erg cm^{-2} s^{-1} sr^{-1}. References are (1) Barlow et al. (2013) (2) Rudy et al. (1994) (3) Gomez et al. (2012) (4) Richardson et al. (2013) (5) Loh et al. (2011). 102

4.4 Observed (Gomez et al. 2012) and predicted surface brightness ratios for models with Ar/H = 5×10^{-5} and $A_V = 0.1$ (D3Z6), 0.03 (D4Z7) and 0.01 (D5Z8). 102

4.5 Observed (Loh et al. 2012) and predicted H_2 line surface brightnesses, relative to the 2.12 μm 1 − 0 S(1) line, for models with Ar/H = 5×10^{-5} and $A_V = 0.1$ (D3Z6), 0.03 (D4Z7) and 0.01 (D5Z8). 103

4.6 Density, temperature, physical size and H_2 and electron abundances for models D3Z6, D4Z7 and D5Z8, with Ar/H = 5×10^{-5} and $A_V = 0.1$ (D3Z6), 0.03 (D4Z7) and 0.01 (D5Z8). 103

4.7 Observed and predicted line surface brightnesses for models with Ar/H = 5×10^{-5} and $A_V = 1$ (D4Z7) and 0.5 (D5Z8), and beam size of the observations relative to the maximum size of H_2 knots in Loh et al. (2011) (30 arcsec^2). Surface brightnesses are in erg cm^{-2} s^{-1} sr^{-1}. References are (1) Barlow et al. (2013) (2) Gomez et al. (2012) (3) Loh et al. (2011). . . . 105

6.1 Adopted gas masses, ion and electron number densities and temperatures, and dominant ionic species for the four gas components. References are (1) Smith et al. (2009) (2) Raymond et al. (2018) (3) Arias et al. (2018) (4) Docenko and Sunyaev (2010) (5) M. J. Barlow (private communication) (6) Willingale et al. (2003). 118

6.2 Dust species and their adopted densities ρ_g, sublimation temperatures T_{sub} and references for the optical constants. References are (1) Dorschner et al. (1995) (2) Jäger et al. (2003) (3) Laor and Draine (1993) (4) Zubko et al. (1996) (5) Uspenskii et al. (2006). 119

6.3 Cas A SNR dust fluxes and uncertainties from De Looze et al. (2017), for an ISM radiation field strength $G = 0.6G_0$. 120

6.4 Best-fit model dust masses for each component, total dust masses and reduced χ^2 values for different grain species. 122

6.5 Best-fit model gas-to-dust mass ratios for each component for different grain species. 122

A.1 Model input parameters 147

A.2 Elemental abundances 147

A.3 Collapse duration and ambipolar diffusion timescales at increasing density for BES1, BES4 and MS models with varying ζ and Z. 153

This page was intentionally left blank

Chapter 1

Introduction

1.1 The interstellar medium

The interstellar medium (ISM) is the matter in galaxies which exists outside of stellar systems. Despite this separation, the ISM is strongly coupled to the stars within it - stars form from denser regions of the ISM, with the local environment determining properties such as the initial mass and the chemical composition. The ISM in turn is affected by the radiation and stellar winds generated by stars, and is enriched with the products of nuclear fusion when stars return material at the end of their lives. Understanding the beginning and end points of stellar evolution is vital to understand their relationship with the rest of the Galaxy.

Stars are formed within molecular clouds, cold ($\sim 10\,\mathrm{K}$), dense ($> 10^4\,\mathrm{cm}^{-3}$) regions of space where hydrogen is almost entirely in the form of H_2 (Bergin and Tafalla 2007), in localised overdense regions known as prestellar cores, with sizes of the order of 0.1 pc. While the location of star formation is widely accepted, the process by which gas collapses to form a star is much less clear. The core's self gravity must overcome the thermal pressure of the gas, in addition to possible support from magnetic fields and turbulence. The relative importance of each component is uncertain, with potential consequences for the accretion rate and subsequent evolution of the protostar (McKee and Ostriker 2007).

Low and intermediate-mass stars ($\lesssim 8\,\mathrm{M}_\odot$) develop degenerate cores and end their lives as planetary nebulae (PNe), as the outer layers are expelled and the remaining

central object contracts and cools to form a white dwarf. Higher mass stars ($\gtrsim 8\,M_\odot$) never develop degenerate cores and explode as core-collapse supernovae (CCSNe), ejecting stellar material at high velocities ($2000 - 10\,000\,km\,s^{-1}$) and forming shock waves that propagate through the ISM. As the initial explosion fades, the ejecta can remain visible as a supernova remnant (SNR), which continues to evolve and interact with its environment. In both cases, the matter returned to the ISM has been processed by nuclear fusion, resulting in enriched abundances of some heavy elements, and studying these objects is one of the few available probes of processes in the interior of stars. CCSNe have also been proposed to be an important source of dust in the ISM, particularly at high redshifts (Dwek 1998; Morgan and Edmunds 2003; Maiolino et al. 2004; Gall et al. 2011), which has been reinforced by the detection of large quantities of dust ($0.1 - 1.0\,M_\odot$) in a number of nearby young SNRs (e.g. Barlow et al. 2010; Matsuura et al. 2011; Gomez et al. 2012).

The ISM can be studied by the absorption, at ultraviolet (UV) and optical wavelengths, of background starlight by the intervening gas and dust. However, a more direct probe is observations of the emission originating from the ISM and from younger evolved objects themselves. For prestellar cores, the low gas temperatures ($\sim 10\,K$) mean that this is mostly through rotational line emission from molecules with a non-zero dipole moment, for which the excitation energies of the upper levels are low enough to be significantly populated, and thermal emission from dust grains heated by collisions with the gas. PNe and supernova remnants (SNRs) are hot enough that UV, optical and infrared (IR) emission lines from atomic and ionic species are observed, which can be used to diagnose the temperature, density and elemental composition of the gas (e.g. Wesson and Liu 2004). However, both types of object also often show molecular emission lines - H_2 emission is frequently observed in PNe (Hora et al. 1999), while the remnant of SN 1987A has been found to contain a variety of molecules (Matsuura et al. 2017) - along with thermal dust emission, potentially tracing very different regions to the atomic lines produced in the warmer gas.

Modelling the emission from these objects is a complicated problem involving a number of different physical processes, some of which must be neglected in order to keep the problem tractable. In all cases the material is in a non-equilibrium state, either infalling in the case of prestellar cores or being ejected in the case of PNe and SNRs, while time-dependent effects can also be important for the chemical evolution of the gas. For PNe and, in some cases, SNRs, the presence of a radiation source in the nebula means that radiative

transfer must be included to correctly describe the structure and thermal balance. The following sections provide a brief overview of the physical processes relevant to the work presented in this thesis.

1.2 Dust properties in the ISM

Observations of the colours of stars of the same spectral type show that the extinction of light is wavelength-dependent (e.g. Fitzpatrick 1999), which is attributed to dust grains (Trumpler 1930). Figure 1.1 shows the normalized extinction versus wavenumber for three proposed Galactic extinction curves. The key features of the extinction curve are an increase in extinction with decreasing wavelength from the IR to the UV, and a number of features superimposed on the underlying continuum at particular wavelengths, most notably the 'bump' at 2175 Å. Its properties depend on the sizes, shapes and composition of the dust grains responsible for the extinction, allowing these to be investigated.

For wavelengths small compared to the grain size a ($\lambda << 2\pi a$), the interaction between the grain and radiation is in the geometrical optics limit and is independent of wavelength. The continuing rise in extinction into the UV therefore requires the presence of small ($a \lesssim 0.01\,\mu$m) dust grains, in a large enough quantity to contribute significantly to the extinction at all wavelengths. Mathis et al. (1977) found that a power law grain size distribution,

$$\frac{dn}{da} \propto a^{-3.5}, \tag{1.1}$$

was capable of reproducing the observed extinction curve, with $a_{\rm min} \sim 0.005\,\mu$m and $a_{\rm max} \sim 0.1\,\mu$m (known as the MRN distribution). Graphite grains were found to be necessary to reproduce the 2175 Å feature, while some other material was also required, although various silicates, iron grains, silicon carbide and iron oxide were all found to be acceptable for this additional component. The presence of features at 9.7 and 18 μm in the extinction curve, which can be attributed to Si-O stretching and bending modes, suggest silicates must be present in the ISM. Another feature at 3.4 μm is attributed to aliphatic C-H bond stretching, which can be used to determine the column density of carbon locked up in this form along a sightline (Günay et al. 2018). Additional IR emission features in regions where dust has been heated, and broad absorption features in the optical which cannot be attributed to atomic or ionic species, have been explained by the presence of

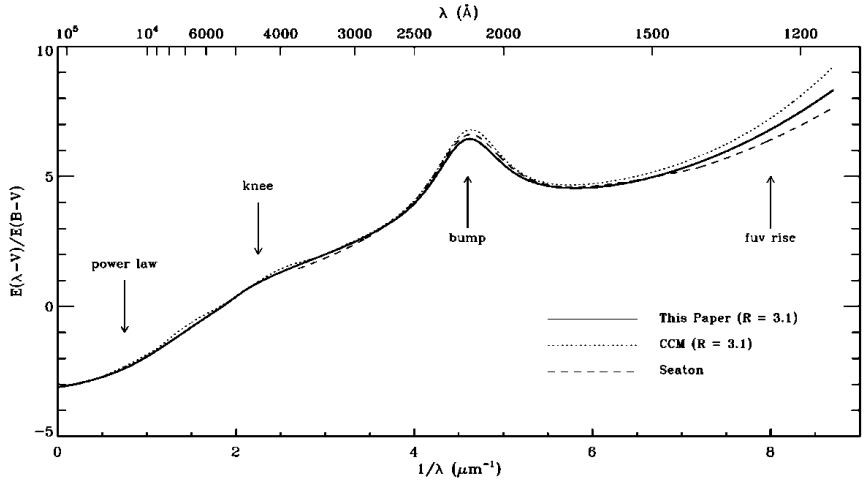

Figure 1.1: Normalised interstellar extinction curves from various sources, taken from Fitzpatrick (1999).

polycyclic aromatic hydrocarbons (PAHs), large planar carbon molecules with hydrogen atoms attached at the edges (Weingartner and Draine 2001a; Jones et al. 2013). Figure 1.2 shows the IR spectrum of NGC 7023, a reflection nebula, showing characteristic PAH emission features.

1.3 Gravitational collapse

In the absence of any opposing forces, a spherical cloud of gas of constant density will collapse under its own self-gravity in one free-fall time, $t_{\rm ff} = \sqrt{\frac{3\pi}{32G\rho}}$, where G is the gravitational constant and ρ is the gas density. In reality, a number of forces may act to oppose gravitational collapse, the most obvious being thermal pressure, $P = nk_bT$, where k_b is the Boltzmann constant and T is the gas temperature. For an isothermal spherically symmetric cloud of gas in hydrostatic equilibrium, the equation

$$\frac{dP}{dr} = k_bT\frac{dn}{dr} = -\frac{GM(r)}{r^2}\rho(r) \tag{1.2}$$

holds at all points in the cloud, where $M(r)$ is the mass contained within a radius r and $\rho(r)$ is the mass density, which can be solved numerically to give the density profile $n(r)$. The solutions are known as Bonnor-Ebert (BE) spheres (Bonnor 1956; Ebert 1957), and are unstable to collapse beyond a critical radius or, equivalently, above a critical mass. Figure 1.3 shows the density profile of a BE sphere with central density $n_0 = 2\times10^4\,{\rm cm}^{-3}$, $T = 10\,{\rm K}$ and a mean molecular weight $\mu = 2m_{\rm H}$ where $m_{\rm H}$ is the proton mass. Prestellar

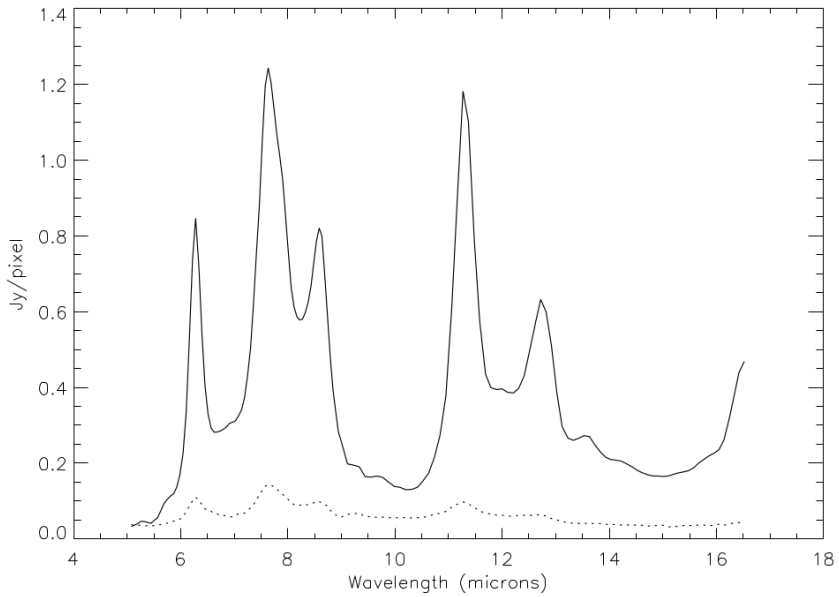

Figure 1.2: ISOCAM IR spectrum of NGC 7023, showing PAH features, from Cesarsky et al. (1996). The solid line is the spectrum from the region of peak 16 μm emission, while the dotted line is from a region with lower 16 μm intensity.

cores have been observed to have similar flattened power-law density structures to BE spheres (Tafalla et al. 2002; Kandori et al. 2005), while simulations of unstable BE spheres (Foster and Chevalier 1993; Ogino et al. 1999) show that these profiles persist during gravitational collapse.

Molecular clouds, like the rest of the ISM, are permeated by magnetic fields (Goodman et al. 1990; Crutcher 1999). Molecular clouds and prestellar cores are almost entirely made up of neutral gas, with typical ionization fractions of $\sim 10^{-8}$ (Hartquist and Williams 1989), and so most of the matter does not directly experience magnetic forces. However, collisions between ions and neutral molecules can transmit the magnetic forces experienced by the charged species to the rest of the gas, resulting in an effective magnetic pressure. As with thermal pressure, magnetic support can prevent a cloud from collapsing under self-gravity up to a critical mass (Tomisaka et al. 1988), beyond which dynamical collapse is inevitable, although further impeded compared to the non-magnetised case. Simulations of the collapse of magnetised clouds (e.g. Tomisaka 1995; Nakamura et al. 1995) find that material collapses rapidly along the magnetic field lines, forming a thin disk, the density profile along which at least superficially resembles a BE sphere, with a flattened central region steepening into approximately a power-law at large radii.

The coupling between the magnetic field and the (mostly neutral) gas is not perfect,

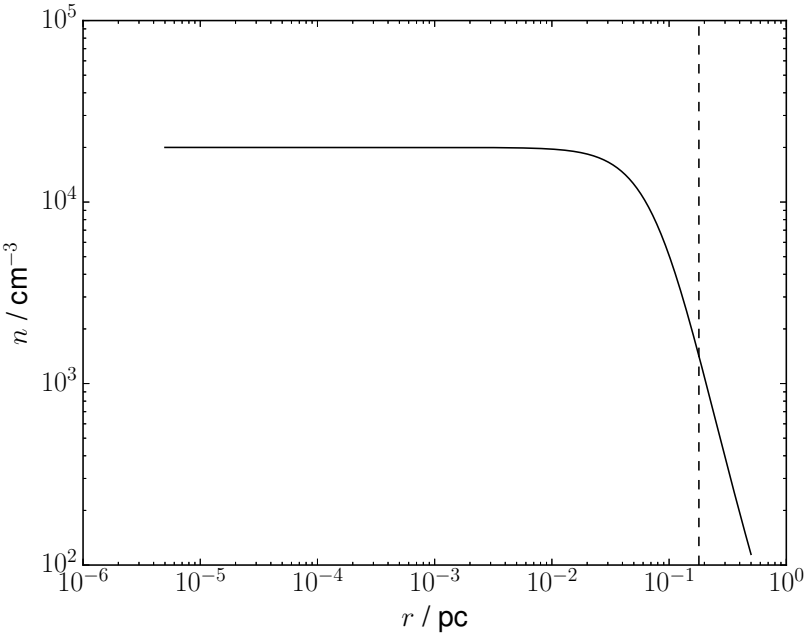

Figure 1.3: Density profile of a BE sphere with $n_0 = 2 \times 10^4\,\mathrm{cm}^{-3}$, $T = 10\,\mathrm{K}$ and $\mu = 2m_\mathrm{H}$. The critical radius, beyond which the cloud is unstable, is marked with a dashed line.

and over time material will drift across the field lines, a process known as ambipolar diffusion (Mestel and Spitzer 1956). This reduces the magnetic flux in the cloud on the ambipolar diffusion timescale (Hartquist and Williams 1989),

$$t_\mathrm{amb} = 4 \times 10^5 \left(\frac{x_i}{10^{-8}}\right)\ \mathrm{yr} \tag{1.3}$$

where x_i is the ionization fraction, and can allow a cloud below the critical mass to become supercritical and collapse. Ambipolar diffusion proceeds faster in regions with low x_i, which in prestellar cores occurs in regions of higher density (Mouschovias 1979). The result is that the denser central regions lose magnetic support and collapse dynamically, while the outer envelope remains magnetically supported (Fiedler and Mouschovias 1993). The dependence on the fractional ionization means that the dynamical evolution of the cloud is affected at least in part by the chemical conditions in the gas-phase material, and a full description of the collapse of a prestellar core must account for both.

1.4 Astrochemistry

1.4.1 Gas-phase chemistry

At the gas densities relevant for the ISM, most significant chemical processes are two-body reactions, for example the dissociative recombination of the H_2^+ molecular ion with a free electron,

$$H_2^+ + e^- \rightarrow H + H. \tag{1.4}$$

The rate of change of the number density of each species involved in the reaction is proportional to the product of the densities of the two reactants, for example

$$\frac{d}{dt} n(H_2^+) = -k(T) n(H_2^+) n_e \tag{1.5}$$

where $k(T)$ is the temperature-dependent rate coefficient. For a two-body reaction the rate coefficient can be assumed to be given by

$$k(T) = \alpha \left(\frac{T}{300} \right)^{\beta} \exp\left(-\frac{\gamma}{T} \right) \text{ cm}^3\,\text{s}^{-1} \tag{1.6}$$

where α, β and γ are determined from fits to either experimental or theoretical data (McElroy et al. 2013). At temperatures typical of prestellar cores ($\sim 10\,\text{K}$), the majority of reactions with significant rates are between ionic and neutral species, due to their generally being exothermic and having small/no activation energies (Herbst and Klemperer 1973).

As well as chemical reactions, other important processes are cosmic ray ionization

$$X + \text{c.r.} \rightarrow X^+ + e^- \tag{1.7}$$

and cosmic-ray induced photoreactions, where photons produced by the ejected electron following a cosmic ray event interact with other atomic or molecular species. The rates for these processes are given by

$$k = \alpha\zeta\,\text{s}^{-1} \tag{1.8}$$

for cosmic-ray ionizations, and

$$k = \alpha\zeta \left(\frac{T}{300}\right)^{\beta} \frac{\gamma_{\mathrm{c.r.}}}{1-\omega}\,\mathrm{s}^{-1} \tag{1.9}$$

for cosmic-ray induced photoreactions, where ζ is the cosmic ray ionization rate (in units of $\zeta_0 = 1.3 \times 10^{-17}\,\mathrm{s}^{-1}$, the standard ISM value for H_2), $\gamma_{\mathrm{c.r.}}$ is the number of photoreactions per primary ionization and ω is the dust grain albedo at optical/UV wavelengths, which must be accounted for as dust grains may also absorb photons at these wavelengths. Molecules may also interact with photons from interstellar sources, for which

$$k = \alpha \exp\left(-\gamma_{\mathrm{UV}} A_{\mathrm{V}}\right)\,\mathrm{s}^{-1} \tag{1.10}$$

where α is the rate in the unshielded radiation field, A_{V} is the visual extinction, and γ_{UV} is a factor to account for the increased extinction efficiency at the ultraviolet wavelengths relevant for photoreactions. These processes are important for producing ionic species, allowing further chemical reactions to proceed rapidly.

1.4.2 Surface chemistry

As well as the gas-phase reactions listed above, molecules may become adsorbed onto the surface of dust grains, and undergo further reactions there. The most important of these is the formation of molecular hydrogen, H_2. The gas-phase reaction between two H atoms is too slow to convert atomic gas into molecular form over reasonable timescales (Gould and Salpeter 1963), and the formation rate of molecular hydrogen on grain surfaces (Hollenbach and Salpeter 1971) has been empirically constrained to be

$$\frac{d}{dt} n(\mathrm{H_2}) = R n(\mathrm{H}) n_{\mathrm{H}} \tag{1.11}$$

with $R \approx 3 \times 10^{-17}\,\mathrm{cm}^3\,\mathrm{s}^{-1}$ (Jura 1974; Gry et al. 2002) and $n_{\mathrm{H}} = n(\mathrm{H}) + 2n(\mathrm{H_2})$ the total number density of hydrogen nuclei. The presence of other species can lead to a series of surface reactions between molecules (e.g. Hasegawa et al. 1992) building up more complex species, which can then be desorbed by various processes back into the gas phase (Roberts et al. 2007).

1.4.3 X-ray chemistry

Astrochemical calculations often assume the only radiation field present is the background UV interstellar field, over the range $912 - 2400\,\text{Å}$ (Habing 1968; Draine 1978), possibly scaled by some factor or attenuated by dust extinction. Photons below 912 Å can ionize neutral hydrogen atoms, and are assumed to be absorbed well before interacting with any molecular gas. However, the photon absorption cross-section drops with increasing photon energy (Verner and Yakovlev 1995), meaning that X-rays are capable of penetrating much further into neutral gas than longer-wavelength UV photons (Maloney et al. 1996; Meijerink and Spaans 2005). Similarly to cosmic rays, X-rays provide an additional source of ionization both through the initial absorption of a photon, with a rate

$$k = \int \sigma(E) \frac{F(E)}{E} dE\,\text{s}^{-1} \tag{1.12}$$

where E is the energy of the photon, $\sigma(E)$ is the ionization cross-section for the relevant species and $F(E)$ is the X-ray flux, and through secondary ionizations caused by the energetic electrons ejected in the initial event.

Lower energy X-rays are absorbed more strongly than high energy ones, so the X-ray spectral energy distribution (SED) varies with depth into a cloud. As the impinging SED determines the effect of the X-rays on the gas, it is important to properly take into account the transport of radiation through the system.

1.5 Interaction of radiation and matter

The transfer of radiation through a medium in 1D (neglecting scattering processes) is governed by

$$\frac{dI_\nu}{ds} = -\kappa_\nu I_\nu + j_\nu \tag{1.13}$$

where I_ν is the intensity at frequency ν, ds is an increment of distance along the path s, and κ_ν and j_ν are the coefficients of absorption and emission per unit volume. If scattering is also included, an additional contribution to the intensity may come from photons being rescattered into the path of the beam from outside. This equation has the general solution

$$I_\nu(\tau_\nu) = I_\nu(0)\exp(-\tau_\nu) + \int_0^{\tau_\nu} \exp(\tau_\nu - \tau') S_\nu(\tau') d\tau' \tag{1.14}$$

where $d\tau_\nu = \kappa_\nu ds$ and $S_\nu = j_\nu/\kappa_\nu$. Solving this equation requires knowledge of κ_ν and j_ν at every point along the path, which are functions of the density, temperature and composition of the material - all of these properties can be affected by interactions with the radiation field, with different processes becoming important at different wavelengths. A cloud irradiated by a source of ionizing radiation can roughly be divided into three zones, located from nearest to furthest from the source - an ionized region, a photodissociation region (PDR) and a molecular region.

1.5.1 Photoionized regions

Hydrogen atoms in the ground state are ionized by photons with wavelengths less than 912 Å, while free electrons and protons can recombine, emitting a photon which carries away the excess energy. Recombination to the ground state involves the emission of a photon with wavelength < 912 Å, which can immediately ionize another hydrogen atom. Neglecting these direct recombinations to the ground state, the effective recombination rate (known as case B) at low temperature ($T < 2500\,\mathrm{K}$) is approximately

$$\alpha_\mathrm{B}(T) \approx 3.5 \times 10^{-12} \left(\frac{T}{300\,\mathrm{K}}\right)^{-0.7} \mathrm{cm^3\,s^{-1}} \tag{1.15}$$

(Prasad and Huntress 1980). At higher temperatures this equation overestimates the rates, which have been tabulated by Osterbrock and Ferland (2006) (Table 2.7). In equilibrium, the rate of recombinations within the ionized volume around a source must equal the rate of emission, Q_0, of ionizing photons per second by the ionization source,

$$Q_0 = \frac{4\pi}{3} R^3 \alpha_\mathrm{B}(T) n_\mathrm{e} n_\mathrm{H} \tag{1.16}$$

for a sphere of constant density. This equation can be rearranged to find the radius of the ionized volume, known as the Strömgren radius (Strömgren 1939). In reality the transition from ionized to neutral gas is not instantaneous, and the absorption of photons by other elements and dust grains must be taken into account.

The electrons ejected by photoionization lose their excess kinetic energy by interactions with the gas, which is generally the dominant heating mechanism for ionized regions, and for neutral gas strongly irradiated by X-rays. The fraction of electron energy which goes into heating the gas is not unity - energy can also be lost to secondary ionizations, or by

collisional excitation of atoms and molecules. The heating rate due to photoionizations is given by

$$\Gamma = \eta n_{\rm H} \int \sigma(E) F(E) dE \,{\rm erg\,cm^{-3}\,s^{-1}} \tag{1.17}$$

where $F(E)$ is the X-ray flux, which provides the heating energy, $\sigma(E)$ is the total absorption cross-section per hydrogen nucleus and η is the heating efficiency (Meijerink and Spaans 2005). η accounts for the fact that some of the energy of the photoelectrons may be lost to ionizing or exciting additional atoms and molecules, rather than deposited as thermal energy in the gas. As the ionization fraction increases, η tends towards unity (Dalgarno et al. 1999), as the probability of interacting with a free electron and thermalising rises compared to the probability of exciting a bound electron.

1.5.2 PDRs

Beyond the ionized region, the flux at wavelengths below 912 Å is effectively reduced to zero (with the possible exception of X-rays), so hydrogen is predominantly neutral. UV photons in the range $912 - 2400$ Å are still present, and elements with ionization potentials below 13.6 eV (most significantly, carbon) can be photoionized, while molecules which form are subjected to photodissociation. The composition of the gas changes from almost entirely atomic to almost entirely molecular with increasing depth, as the UV field is absorbed by atoms, molecules and dust grains. The main heating mechanism is photoelectric emission of electrons from dust grains (Watson 1972; Tielens and Hollenbach 1985), the rate of which depends on not only the radiation field but also dust properties including the grain size, charge and composition. Calculations using plausible assumptions about the grain properties (Tielens and Hollenbach 1985; Bakes and Tielens 1994; Weingartner and Draine 2001b) have found that small ($a < 100$ Å) grains dominate the heating rate, as they absorb UV radiation more strongly and are less positively charged, making it easier for electrons to escape. For an MRN size distribution, small grains account for the majority of the total grain surface area.

The transition from atomic to molecular gas is due to the absorption of UV photons, reducing the photodissociation rate further into the cloud. Figure 1.4 shows the chemical structure of a PDR with $n_{\rm H} = 10^3\,{\rm cm^{-3}}$, with an incident radiation field 5 times the Draine (1978) field (1.7 times the Habing (1968) field). Whereas the photoionization of atoms

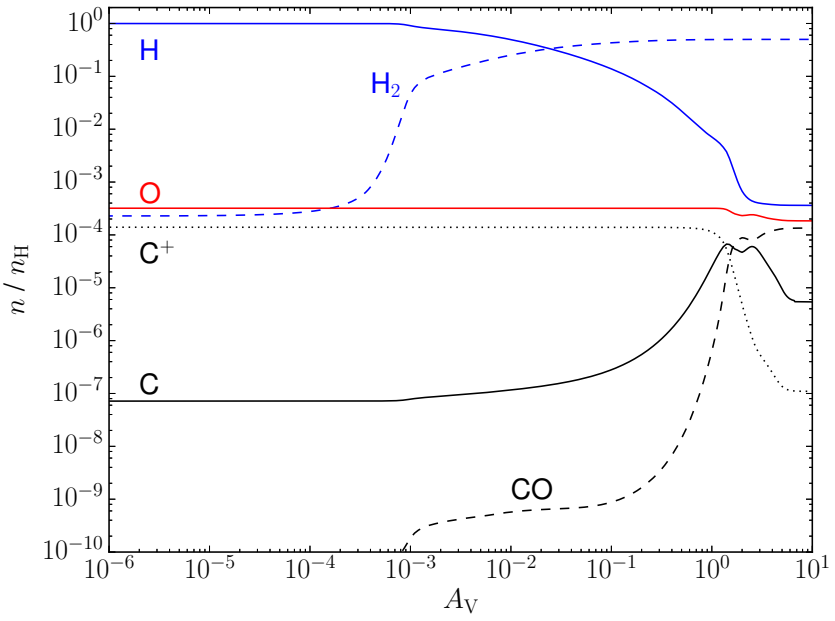

Figure 1.4: Abundances versus visual extinction of H (blue solid line), H_2 (blue dashed line), O (red solid line), C (black solid line), C^+ (black dashed line) and CO (black dotted line), for a PDR with $n_H = 10^3\,cm^{-3}$ and a radiation field of 5 Draines.

involves the continuous absorption of photons beyond the threshold energy, molecules may also be photodissociated by line absorption - the molecule decays to an unstable configuration from the excited state, and is destroyed. This is the main mechanism of destruction by UV photons for H_2 and CO, the two most common molecules in the ISM (Stecher and Williams 1967; van Dishoeck and Black 1988). As the line absorption can be much stronger than the dust continuum absorption, molecules in the interior are shielded from dissociation by those closer to the cloud surface, and the abundances can rise more rapidly than would be expected if this self-shielding was neglected. In order to calculate the reduction in the photodissociation rate, in principle the level populations of the molecule at each point need to be calculated to solve the radiative transfer through the cloud, although Abgrall et al. (1992) found that a relatively simple approximation (Federman et al. 1979) for the H_2 line absorption agrees well with a more rigorous treatment - the transition from atomic to molecular gas occurs at a slightly lower A_V, but the region where this occurs is too thin for the difference to have any significant observational consequences.

1.5.3 Molecular regions

Beyond some level of visual extinction ($\sim 5-10$ mag; Hollenbach et al. 1991), the UV flux in a cloud is reduced to the level where photon interactions are no longer dominant, either for the heating rate or for chemical reactions. Although hydrogen and carbon are mostly in molecular form at lower extinctions, beyond this point the lack of photodissociation can enable more complex molecules to appear. The main heating mechanism is the energy deposited by cosmic ray ionization (Goldsmith and Langer 1978; Hollenbach et al. 1991). Unlike radiation, cosmic rays are not significantly attenuated when passing through a cloud, so that the heating rate is essentially independent of the position in the cloud, and the gas temperatures in molecular regions are fairly uniform at $\sim 10\,\mathrm{K}$ (Dickman 1975; Martin and Barrett 1978). Due to the low temperatures, only low-lying energy levels can be significantly populated, so the emission from molecular clouds is largely made up of molecular rotational lines and thermal continuum emission from dust grains.

1.6 Emission processes

1.6.1 Line emission

Much of the information extracted from observations of astrophysical objects comes from the analysis of spectral lines. Atoms have discrete energy levels which their electrons may occupy, while molecules additionally have rotational and vibrational states with different characteristic energy scales. An atom/molecule may transition from one state to another by emitting or absorbing a photon with an energy corresponding to the difference between states, giving rise to emission and absorption lines in the observed spectrum. Transitions between states can also be caused by particle collisions, or by stimulated emission triggered by photons of the correct wavelength. The assumption of local thermodynamic equilibrium (LTE) can be used to simplify the problem, where the occupancy of each state is assumed to be the Boltzmann equilibrium value at the local temperature. However, this is often a poor assumption in the ISM, where the local radiation field is rarely a blackbody and densities are too low for collisions to equilibrate the energy levels, and the level populations must be calculated from the transition rates.

The rate of change of the number of atoms in an energy level i is given by

$$\frac{dn_i}{dt} = \sum_{j \neq i} n_j k_{ji} - \sum_{l \neq i} n_i k_{il} \tag{1.18}$$

where k_{ij} is the transition rate from level i to j,

$$k_{ij} = A_{ij} + B_{ij} J_\nu + C_{ij} n_\mathrm{e} \tag{1.19}$$

where A_{ij} is the Einstein coefficient for spontaneous emission, B_{ij} is the coefficient for absorption (for $i < j$) or stimulated emission (for $i > j$), C_{ij} is the collisional rate coefficient, J_ν is the mean intensity at the frequency corresponding to the energy difference between the two levels, and n_e is the electron density. Although electrons are usually the most important collisional partner due to their lower mass and correspondingly higher thermal velocities, in mostly neutral regions hydrogen atoms or molecules can become more significant. In equilibrium, $\frac{dn_i}{dt} = 0$, and the system of equations can be solved (with the additional condition that $\sum_i n_i = n_\mathrm{tot}$ where n_tot is the total number of atoms of that type). The emissivity of the spectral line corresponding to a transition from upper level u to lower level l is then

$$j_{ul} = n_u (A_{ul} + B_{ul} J_\nu) h\nu \tag{1.20}$$

where h is the Planck constant.

1.6.2 Rotational lines

Under the rigid rotor approximation (Tennyson 2011), a diatomic molecule has rotational energy levels

$$E(J) = B_J J(J+1) \tag{1.21}$$

where J is the rotational quantum number and B_J is the rotational constant for the molecule in quesiton. For dipole-allowed transitions from J to $J-1$, this means

$$\Delta E = E(J) - E(J-1) = 2B_J J \tag{1.22}$$

and the rotational lines are separated by constant frequency intervals of $2B_J/h$. At higher J, the rigid rotor approximation begins to break down, and the spacing between lines will no longer be constant. In order to have dipole transitions, a molecule must have a permanent electric dipole. H_2, due to its symmetry, does not, and so only has much weaker quadrupole ($J \rightarrow J-2$) rotational transitions. Non-linear molecules have more complex rotational spectra, with multiple axes of rotation, while the effects of nuclear spin can also complicate the process.

1.6.3 Vibrational lines

As well as rotating, the nuclei of a molecule can vibrate along the bond axis. If the potential is approximated by a simple harmonic oscillator, the vibrational energy levels are

$$E(v) = h\nu(v + \frac{1}{2}) \tag{1.23}$$

where v is the vibrational quantum number and ν is the vibrational frequency. The frequency of transitions between vibrational levels v and $v-1$ is ν, regardless of the value of v, as long as the harmonic oscillator approximation holds. However, molecules also change rotational states at the same time as the vibrational transition, as $\Delta J = 0$ is dipole (and quadrupole) forbidden, giving a transition energy of $h\nu \pm 2B_J n$ where n is a non-zero integer. The spectrum is therefore a series of emission lines evenly spaced to either side of the vibrational frequency, with the relative strengths determined by the rotational level populations. Vibrational energy levels are generally much higher than rotational ones, and so vibrational emission is only seen in relatively hot gas - the first H_2 vibrational energy level corresponds to a temperature of $\sim 6000\,\mathrm{K}$ (Dabrowski 1984), although heavier molecules have lower vibrational energies.

1.6.4 Atomic forbidden and fine-structure lines

Hydrogen - and ions of heavier elements with only one electron - has a relatively simple level structure, with the energy of level n given by the Rydberg formula,

$$E(n) = -\frac{13.6}{n^2}\,\mathrm{eV}. \tag{1.24}$$

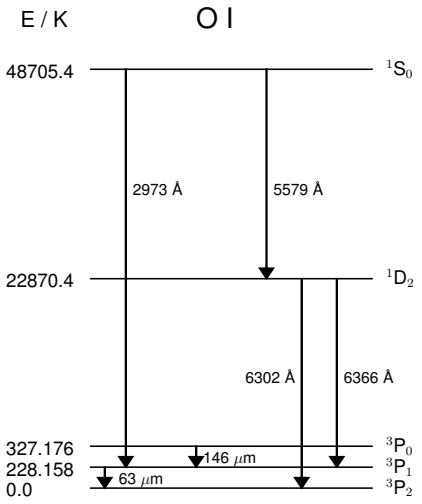

Figure 1.5: Energy levels and transitions of neutral oxygen. The energy levels are not to scale, to allow the fine structure splitting to be visible. Wavelengths are in vacuo values.

The gap between the first and second levels is 10.2 eV, corresponding to a temperature of $\sim 10^5$ K, meaning that hydrogen is not an efficient coolant at the temperatures typical of ionized gas in the ISM ($\sim 10^4$ K). Instead, cooling is dominated by UV, optical and IR forbidden line emission from heavier atoms and their ions, particularly carbon and oxygen, which have energy levels low enough to be significantly populated by collisions with thermal electrons at these temperatures. Figure 1.5 shows the energy level structure and important cooling transitions of neutral oxygen. Radiative transitions between these levels are dipole-forbidden, having significantly lower A-coefficients than allowed transitions. At ISM densities, the rates of collisional deexcitation are low enough that an atom collisionally excited to the higher state is still likely to decay radiatively. In addition, the interaction between the electron orbital and spin angular momentum can lead, for some atoms or ions, to the splitting of the ground state into multiple energy levels, separated by only a few 100 K (see Figure 1.5). This allows for the efficient cooling of lower temperature gas, giving rise to emission lines in the IR region.

1.6.5 Dust continuum emission

Although in principle dust grains, like atoms and molecules, also have discrete energy levels (Draine and Li 2001), due to the large number of atoms in even the smallest dust particles,

they can generally be treated classically. The large number of closely spaced energy levels means that dust emission is a continuum rather than line emission, determined by the optical properties and temperature of the grain. The energy emitted by a spherical dust grain is given by

$$L_{\rm em}(T) = 4\pi^2 a^2 \int Q_{{\rm em},\nu}(a) B_\nu(T) d\nu \tag{1.25}$$

while the energy absorbed from an isotropic local radiation field is

$$L_{\rm abs}(T) = 4\pi^2 a^2 \int Q_{{\rm abs},\nu}(a) J_\nu d\nu \tag{1.26}$$

where a is the grain radius, T is the grain temperature and $Q_{{\rm abs},\nu}$ and $Q_{{\rm em},\nu}$ are the absorption and emission efficiencies, which depend on the grain composition and radius (generally $Q_{{\rm abs},\nu} = Q_{{\rm em},\nu}$). In equilibrium,

$$\int Q_{{\rm abs},\nu}(a) J_\nu d\nu = \int Q_{{\rm em},\nu}(a) B_\nu(T) d\nu \tag{1.27}$$

so given some knowledge of the radiation field and dust optical properties, the dust temperature and therefore emission can be determined. Dust emission is most significant at IR wavelengths and longer, due to the typical grain sizes and properties in the ISM. Figure 1.6 shows the emitted dust SED from the BARE-GR-S model of Zubko et al. (2004), heated by the ISM radiation field given by Mathis et al. (1983).

The previous equations assume dust is heated only by the radiation field, whereas in some regions of the ISM heating by particle collisions may also become important (Dwek et al. 1996; Bocchio et al. 2013). At high enough densities this can become a significant cooling process for the gas, and couples the temperatures of the dust grains and gas (Burke and Hollenbach 1983; Goldsmith 2001), although in these situations radiative heating is usually still dominant for the dust. The heating rate of a dust grain by electron collisions is

$$H = \pi a^2 n_{\rm e} \int_0^\infty f(E) v(E) E \zeta(E) dE \tag{1.28}$$

where $f(E)$ is the energy distribution of the electrons (generally assumed to be a Boltzmann distribution), $v(E)$ is the velocity of an electron with energy E and $\zeta(E)$ is the

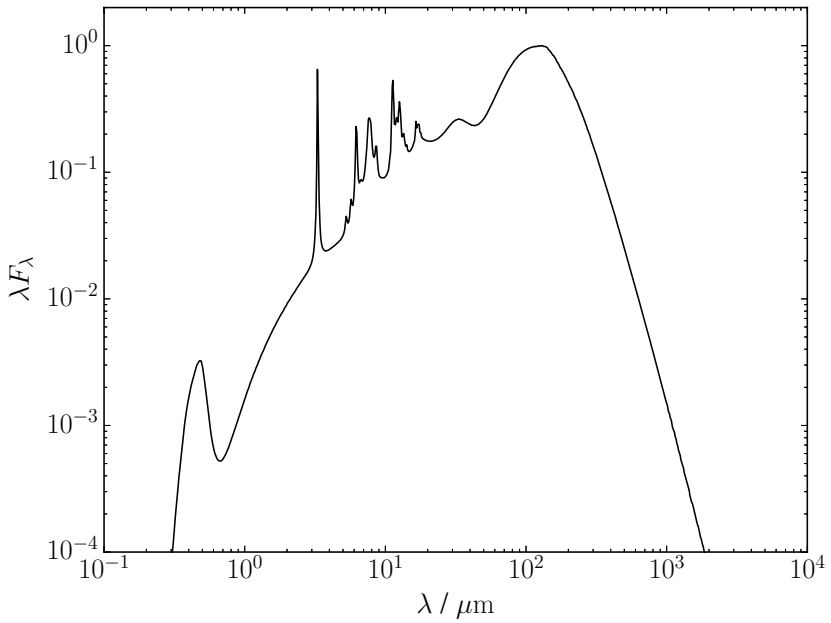

Figure 1.6: Emitted dust SED from the BARE-GR-S Zubko et al. (2004) model, heated by the Mathis et al. (1983) ISM radiation field.

fraction of energy transferred to the dust grain (Dwek 1986).

For very small dust grains absorbing a high-energy photon (or undergoing an energetic particle impact), the temperature will increase sharply due to the low grain enthalpy. If these events are infrequent (occuring at a rate lower than the cooling rate), the dust grain will not be able to reach equilibrium, but will instead fluctuate, reaching much higher temperatures briefly before cooling below the theoretical equilibrium temperature (Draine and Anderson 1985; Dwek 1986). The presence of high-temperature dust grains leads to an excess in the emitted SED at near-IR wavelengths, which can often be significantly higher than the prediction assuming equilibrium temperatures.

1.7 The evolution of low- and high-mass stars

All stars spend the majority of their lifetimes on the main sequence of the Hertzsprung-Russell (HR) diagram, where energy is produced by the fusion of hydrogen into helium in the core, either directly or through the CNO cycle. Higher mass stars have shorter main-sequence lifetimes, as stellar luminosity increases with mass as $L \propto M^{3-4}$ (Iben 1967), so the rate of consumption of hydrogen rises faster than the amount of hydrogen available as fuel. When the hydrogen in the core is exhausted, stars begin post-main sequence

evolution. Stars with $M \lesssim 2\,\mathrm{M}_\odot$ ('low-mass') develop a degerate helium core, where the main support against gravitational collapse is electron degeneracy pressure, immediately following the main sequence (Iben and Renzini 1983); stars with $2\,\mathrm{M}_\odot \lesssim M \lesssim 8\,\mathrm{M}_\odot$ ('intermediate-mass') begin helium fusion without going through a degenerate phase, but later develop a degenerate carbon-oxygen core when the core helium is exhausted. The evolution of a star with an initial mass of $5\,\mathrm{M}_\odot$ on an HR diagram is shown in Figure 1.7. Stars with $M \gtrsim 8\,\mathrm{M}_\odot$ ('high-mass') have non-degenerate cores throughout their lifetimes, which causes their post-main sequence evolution to differ considerably from those with lower masses.

Hydrogen fusion continues in a shell around the core after ending in the core itself. For low-mass stars, the core cannot be supported by thermal pressure, and contracts until it becomes degenerate. Intermediate-mass stars have non-degenerate helium cores throughout the hydrogen shell-burning phase, while for high-mass stars connditions in the core allow helium fusion to begin immediately following the main sequence. Low- and intermediate-mass stars go through a red giant phase, where the envelope expands leading to lower temperatures and higher luminosities. Helium produced in the hydrogen-burning shell falls onto the core until the temperature is high enough to ignite helium fusion via the triple-alpha process. For low-mass stars, the degenerate core allows a 'helium flash' of extremely rapid energy generation Mestel (1952) to occur, until degeneracy is lifted, after which core helium burning continues normally, surrounded by the hydrogen-burning shell.

As with main-sequence hydrogen burning, helium fusion in the core eventually ceases when all the helium is converted into heavier elements, mainly carbon and oxygen. For low- and intermediate-mass stars, further fusion reactions cannot be ignited, and the core becomes degenerate, surrounded by a shell of helium (Herwig 2005). Fusion in the helium shell causes the star to expand and undergo another giant phase, known as the asymptotic giant branch (AGB). The helium shell eventually runs out of fuel and ceases fusion, at which point energy generation switches to fusion in a hydrogen shell outside this. The helium shell mass increases as 'ashes' from the hydrogen shell fall onto it, until the triple-alpha process can be ignited in another helium flash. The high energy generation causes the shell to expand, quenching fusion in the hydrogen shell above it and eventually in the helium shell itself, after which the star returns to hydrogen-shell burning, allowing the process, known as thermal pulsing, to repeat (e.g. Gingold and Faulkner 1974).

At various stages during a star's lifetime, fusion-processed material can be brought to

the surface layers of the star if convection in the envelope reaches down into regions that previously underwent fusion, known as dredge-up. This first occurs during the red giant phase, when core hydrogen is exhausted, while the second dredge-up occurs at the corresponding stage of AGB evolution, when helium fusion in the core ceases (Becker and Iben 1979). For stars undergoing thermal pulsing, a third dredge-up can occur in which material from the expanding helium-fusing shell is pushed into the convective envelope (Iben and Renzini 1983), which can result in a significant increase in surface carbon abundances. Multiple 'third dredge-ups' can occur, following each thermal pulse in the star. For the highest-mass AGB stars, the convective envelope may extend into the hydrogen-burning shell, resulting in an increased supply of fuel, and therefore higher fusion rates and temperatures (Iben 1976). The high temperatures convert carbon dredged up from the lower layers into nitrogen, which prevents the formation of carbon-rich envelopes (Boothroyd et al. 1993).

AGB stars lose mass through stellar winds throughout their lifetimes (Iben and Renzini 1983). Towards the end of their evolution, this mass loss rate increases dramatically into a superwind (van Winckel 2003), which expels the remaining envelope material, causing the effective temperature to increase while the star remains at roughly constant luminosity (Vassiliadis and Wood 1994). The ionized ejected material forms a planetary nebula around the central star, which moves onto a white dwarf cooling track and decreases in both luminosity and temperature as the surrounding nebula expands and fades.

High-mass stars do not develop degenerate carbon-oxygen cores when helium is exhausted - instead, further fusion reactions, beginning with carbon fusion and progressing through neon, oxygen and silicon, are ignited in the central regions (Woosley et al. 2002), leading to a layered structure with an outer hydrogen envelope and progressively more processed elements occuring towards a central core of the products of silicon fusion (mostly iron-group elements). At this point further fusion reactions are endothermic, and so cannot support the core against gravity. If the core exceeds the Chandrasekhar mass ($\sim 1.4\,\mathrm{M}_{\odot}$), electron degeneracy pressure can no longer prevent further collapse, and the core collapses to either a neutron star or black hole. The infalling outer layers 'bounce' outwards, by a mechanism thought to involve energy deposition by neutrinos (Bethe 1990), resulting in a supernova explosion. The material ejected by the supernova drives a blast wave into the surrounding ISM - the impact with the ISM simultaneously propagates a 'reverse' shock into the ejecta, which reheats the by-now cooled ejecta material (Reynolds 2008), forming

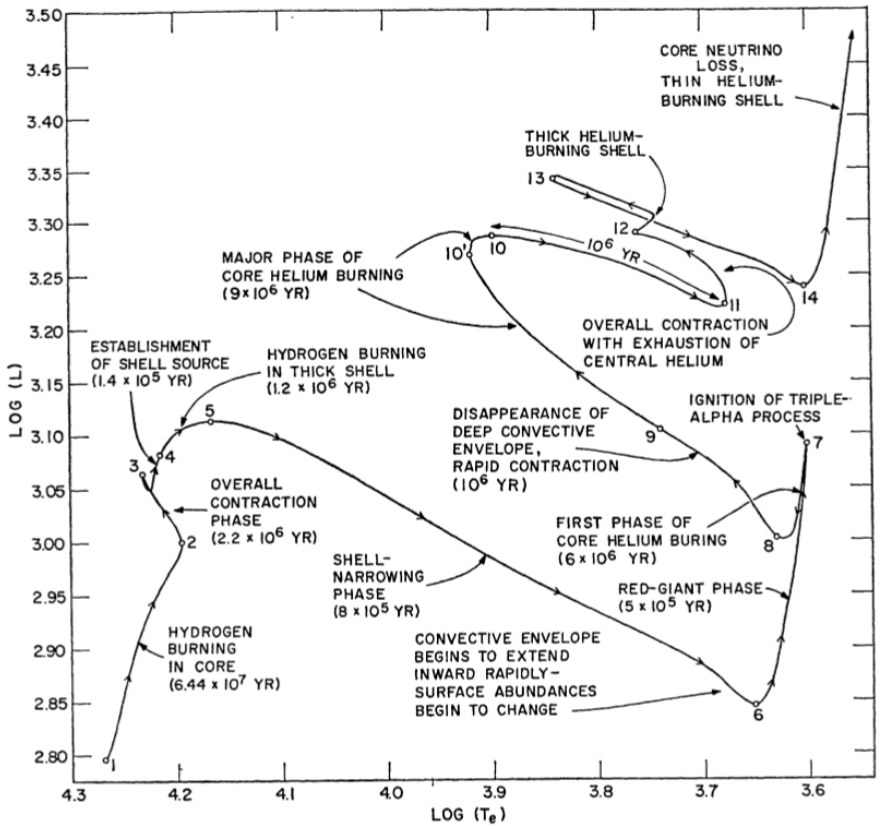

Figure 1.7: Evolutionary track of a $5\,M_\odot$ star on a Hertzsprung-Russell diagram, from Iben (1967).

a supernova remnant.

1.8 This thesis

This thesis is concerned with the numerical modelling of gas and dust emission from stellar remnants, and its use in deducing the properties of these objects by comparison with observation. In Chapter 2, three numerical codes used in the thesis are described. In Chapter 3, a combined photoionization-photodissociation region model is applied to cometary knots in planetary nebulae with a range of central star properties, to determine the resulting molecular emission. Comparison with molecular line observations suggests that the inclusion of ionizing UV radiation, usually neglected in PDR studies, is necessary to correctly reproduce the observed fluxes, leading to a high-temperature surface layer responsible for the H_2 and OH^+ emission. In Chapter 4, this modelling technique is applied to the Crab Nebula, a nearby supernova remnant in which the molecular ions ArH^+ and OH^+ have been detected. These are used to investigate the ionization rate caused by the

central pulsar wind nebula and the density of the dense gas in the SNR. In Chapter 5, a new code, DINAMO , developed during the course of this thesis, is described. DINAMO calculates the emission from a population of dust grain heated by particle collisions and the local radiation field. In Chapter 6 the code is applied to the Cassiopeia A supernova remnant. Fitting the observed infrared spectral energy distribution with multiple dust components, corresponding to different regions of the ejecta, is used to determine the dust mass in each region. Chapter 7 summarises the previous chapters and suggests topics for further investigation. Appendix A focuses on the formation of stars, rather than their remnants, and presents analytical approximations to the gravitational collapse of prestellar cores by various mechanisms. These are incorporated in a time-dependent chemical model to investigate possible molecular tracers of different collapse modes.

Chapter 2

Description of the codes used

The work in this thesis has involved the use of three publicly available codes written at UCL: UCLCHEM, a time-dependent gas-grain chemical code; UCL_PDR, a one-dimensional photodissociation region (PDR) code with the inclusion of additional physics such as X-rays; and MOCASSIN, a three-dimensional Monte Carlo photoionization code. The following chapter summarises the important features of each code, and presents examples of their use.

2.1 UCLCHEM

UCLCHEM (Viti et al. 2004; Holdship et al. 2017) is a time-dependent gas-grain chemical code, which solves a system of coupled ordinary differential equations (ODEs) to determine the time evolution of the molecular abundances (relative to the number density of hydrogen nuclei, n_{H}) in a parcel of gas. The molecular species included and the reaction network are both user-defined - the abundance of each species is goverened by one ODE, given by the sum of the rates of all reactions involving that species (positive for formation reactions, negative for destruction). Grain surface chemistry is incorporated by treating molecules in grain mantles as separate species, with additional reactions for freeze-out and desorption controlling the abundance of molecules in each phase. The system of ODEs is then evolved forward in time until a user-specified final time or final density is reached.

The physical parameters controlling the reaction rates, and therefore the molecular abundances, are the gas density, temperature, radiation field strength (measured relative

to the Habing (1968) field), cosmic ray ionization rate and the visual extinction. The rates of gas-phase reactions are calculated as explained in Section 1.4, with the rate coefficients provided in the reaction network (e.g. the UMIST database; McElroy et al. 2013). The contribution of a gas-phase reaction between species A and B to the ODE for species C is of the form

$$\frac{d}{dt}Y(\mathrm{C}) = k_{\mathrm{AB}}(T)Y(\mathrm{A})Y(\mathrm{B})n_{\mathrm{H}} \tag{2.1}$$

where $Y(\mathrm{X})$ is the fractional abundance of species X with respect to hydrogen nuclei, $k_{\mathrm{AB}}(T)$ is the rate coefficient for the reaction at temperature T and n_{H} is the number density of hydrogen nuclei. For reactions with cosmic rays, UV photons and cosmic ray secondary ionizations, the ODE contribution is

$$\frac{d}{dt}Y(\mathrm{C}) = kY(\mathrm{A})n_{\mathrm{H}} \tag{2.2}$$

where k is the relevant rate coefficient.

The H_2 formation rate on grain surfaces is given by

$$\frac{d}{dt}Y(\mathrm{H_2}) = 10^{-17}\sqrt{T}Y(\mathrm{H})n_{\mathrm{H}} \tag{2.3}$$

(de Jong 1977), as it is assumed that the formation of H_2 releases enough energy to eject the molecule back into the gas-phase. At a gas temperature of 10 K, suitable for molecular clouds, this gives a rate coefficient of $3.16 \times 10^{-17}\,\mathrm{cm^3\,s^{-1}}$, consistent with that of Jura (1974). Other grain surface reactions involve the conversion of gas-phase species to mantle species, or reactions between mantle species. Molecules freeze out onto grain surfaces with the rate

$$\frac{d}{dt}Y(X) = -4.57 \times 10^4 SCn_g a_g^2 \sqrt{\frac{T}{\mu m_{\mathrm{H}}}}Y(X)n_{\mathrm{H}} \tag{2.4}$$

(Rawlings et al. 1992) where n_g is the number density of dust grains per hydrogen atom, a_g is the grain radius, μ is the molecular mass in atomic units, S is the sticking coefficient (between 0 and 1) and C is a factor to account for the effect of grain charge - for neutral species $C = 1$ and for singly charged positive ions $C = 1 + \frac{16.71\times10^{-4}}{a_g T}$ (Umebayashi and Nakano 1980). UCL_CHEM allows molecules to freeze out via multiple pathways, allowing

grain surface reactions to be incorporated as the instantaneous hydrogenation of some proportion of the original molecule. Additionally, grain surface reactions can be included directly as reactions between mantle species, including the effects of diffusion across the grain surface as treated by Quénard et al. (2018).

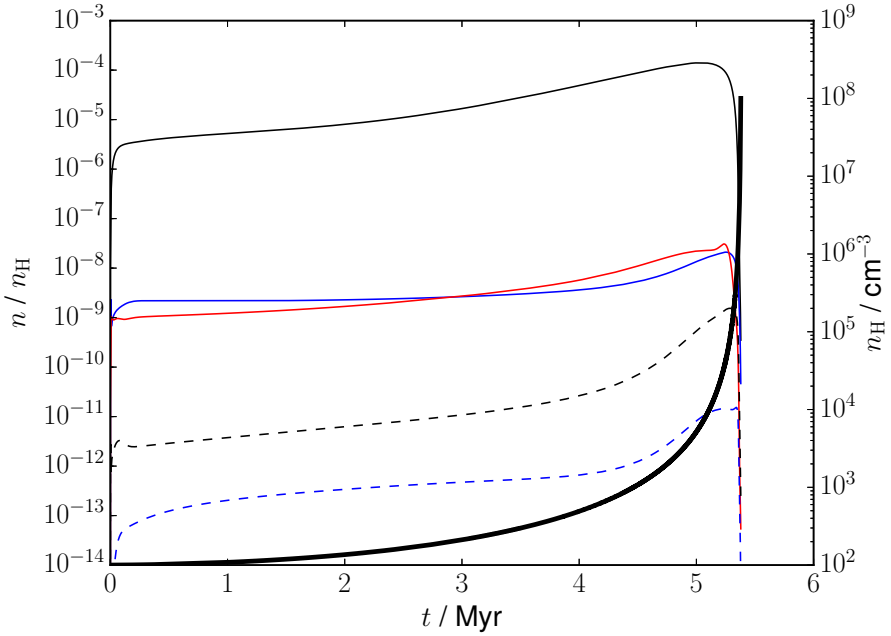

Figure 2.1: Gas density (thick black solid line) and abundances of CO (thin black solid line), NH_3 (blue solid line), HCN (red solid line), HCO^+ (black dashed line) and N_2H^+ (blue dashed line) versus time, for a cloud with an initial density of $100\,\mathrm{cm}^{-3}$ and gas temperature 10 K collapsing under free-fall conditions, as calculated by UCLCHEM.

Mantle species are desorbed back into the gas phase as the dust temperature rises, through various mechanisms discussed in Collings et al. (2004) and Viti et al. (2004). In the case of prestellar cores, where there is no internal energy source and the dust temperature remains constant, these processes can be neglected. Desorption back into the gas phase instead occurs through non-thermal processes. The formation of H_2 on grain surfaces releases heat, which desorbs mantle species with the rate

$$\frac{d}{dt}Y(X) = \epsilon R_{\mathrm{H_2}} Y_m(X) n_{\mathrm{H}} \tag{2.5}$$

where $R_{\mathrm{H_2}}$ is the H_2 formation rate, $Y_m(X)$ is the fraction of the mantle composed of species X and ϵ is desorption efficiency, the number of molecules desorbed per H_2 molecule

formed. Cosmic rays also heat grains, both directly, which desorbs molecules with the rate

$$\frac{d}{dt}Y(X) = \phi F_{\rm cr}\pi a_g^2 n_g Y_m(X) \tag{2.6}$$

where $F_{\rm cr}$ is the flux of cosmic rays and ϕ is the efficiency, and through the cosmic-ray generated UV flux (Prasad and Tarafdar 1983), with the rate

$$\frac{d}{dt}Y(X) = \epsilon_{\rm UV} F_{\rm p}\pi a_g^2 n_g Y_m(X) \tag{2.7}$$

where $F_{\rm p}$ is the photon flux and $\epsilon_{\rm UV}$ is the efficiency. The values of these parameters are given by Roberts et al. (2007). Grain surface reactions can also desorb molecules back into the gas phase, which is included in the reaction network.

Figure 2.1 shows the evolution with time of the abundances of several observationally important molecules, along with the density, of a cloud of initial density $n_{\rm H} = 100\,{\rm cm}^{-3}$ and a constant temperature of 10 K, collapsing under free-fall using the treatment of Rawlings et al. (1992) from initially atomic conditions. The molecular abundances initially increase as the cloud collapses, as the higher density increases the rates of the formation reactions, but as the density rises beyond $\sim 10^5\,{\rm cm}^{-3}$ freeze-out onto dust grains becomes more efficient than the desorption processes, and the gas-phase abundances decrease sharply.

2.2 UCL_PDR

UCL_PDR (Bell et al. 2005, 2006; Bayet et al. 2011; Priestley et al. 2017) is a 1D PDR code, treating the model cloud as a slab of gas with radiation incident on one or both sides. The density profile of the cloud and the radiation field are both user-specified - the code requires as inputs the density and radius of an arbitrary number of depth points, and the UV field in Draines (Draine 1978) and X-ray flux in erg cm^{-2} s^{-1} at the cloud surfaces. Starting from an initial temperature guess (based on a fit to a grid of models), the code first determines the equilibrium abundances of species in the chemical network (also provided by the user) at each depth point, then calculates the heating and cooling rates and updates the gas temperature if necessary. The code iterates this process until all points have converged in temperature.

UCL_PDR treats gas-phase reactions, including those caused by X-rays, as described

in Section 1.4, with the exception of H_2 formation on grain surfaces, which is treated using the more detailed rate given by Cazaux and Tielens (2002) and Cazaux and Tielens (2004). Reductions in the photodissociation rates of H_2 and CO, and the photoionization of C, due to self-shielding are incorporated using the treatments of Federman et al. (1979), van Dishoeck and Black (1988) and Kamp and Bertoldi (2000) respectively. The radiative transfer of UV photons and X-rays are handled separately. The UV field is given by

$$G(x) = G_0 \exp(-F_{\rm UV} A_{\rm V}(x)) \tag{2.8}$$

where $G(x)$ is the UV field at a distance x into the cloud, G_0 is the unattenuated value, $A_{\rm V}(x)$ is the visual extinction at distance x and $F_{\rm UV}$ is a factor relating visual extinction to the extinction at UV wavelengths. $A_{\rm V}$ is calculated using a fixed ratio between the column density of hydrogen nuclei, $N_{\rm H}$, and the extinction. As the absorption of X-ray photons is strongly dependent on their wavelength, the attenuation of the X-ray flux is calculated for each energy bin as

$$F_E(x) = F_E(0) \exp(-\sigma(E) N_{\rm H}(x)) \tag{2.9}$$

where $F_E(x)$ is the flux at energy E at a distance x into the cloud, and $\sigma(E)$ is the absorption cross-section per hydrogen atom calculated from the elemental abundances of the gas using the fits from Verner and Yakovlev (1995). The initial X-ray SED can be specified by the user.

Radiative cooling of the gas can be included for any species for which the required data (energy levels, Einstein coefficients, collisional excitation/deexcitation rates) are available - for many important species, these can be found in the LAMDA database (Schöier et al. 2010). The local radiation field is calculated using the large velocity gradient (LVG) approximation as described in de Jong et al. (1975), with an additional contribution from dust grain thermal emission. The level populations for each species are then calculated as described in Section 1.6, and the cooling rate for each species is given by the sum of the emissivities of all transitions.

Gas heating occurs through many different mechanisms, the importance of each varying depending on the temperature, ionization state, molecular abundances and local radiation field. Photoelectric (PE) heating from dust grains is treated according to Bakes and Tielens (1994), with the modifications of Wolfire et al. (2003) included to account for the

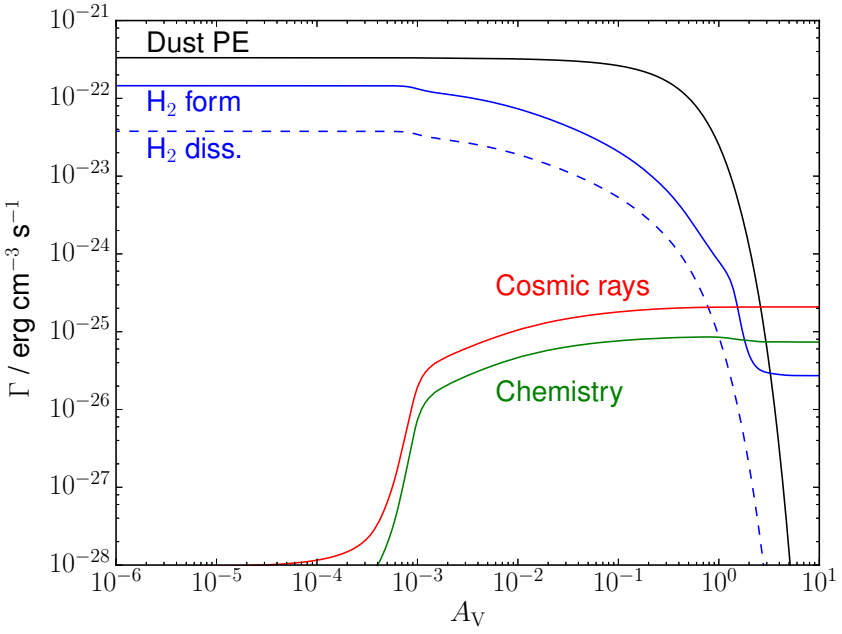

Figure 2.2: Heating rate versus visual extinction of the dust PE effect (solid black line), H_2 formation (solid blue line), H_2 photodissociation (dashed blue line), cosmic ray heating (solid red line) and exothermic chemical reactions (solid green line), for the UCL_PDR model described in Section 1.5.2.

increased polycyclic aromatic hydrocarbon (PAH) abundance inferred from observations. Heating by H_2 formation is assumed to contribute 1.5 eV of energy per molecule formed, while H_2 molecules vibrationally excited by FUV photons are assumed to release 2.2 eV of energy per molecule, following the treatment of Hollenbach and McKee (1979), and photodissociation of H_2 releases 0.4 eV per reaction on average (Stephens and Dalgarno 1973). Photoionization of carbon is assumed to release 1.0 eV, and cosmic ray ionization of H_2 20 eV following Goldsmith (2001). Heating from turbulent dissipation (Rodríguez-Fernández et al. 2001), which may become important in the inner regions of galaxies, is included by assuming a typical length scale of 5.0 pc and the user-defined turbulent velocity used to calculate linewidths for the treatment of self-shielding. Heating by exothermic chemical reactions assumes that the excess energy is entirely transferred to the thermal energy of the gas (Clavel et al. 1978). Gas-grain collisional heating is treated following Burke and Hollenbach (1983) - if the gas temperature is higher than that of the dust grains, which is frequently the case in PDRs, this becomes a cooling mechanism, and the contribution to the net heating rate is negative. Heating by the electrons produced by X-ray ionization uses the energy deposition rate of Meijerink and Spaans (2005), and the

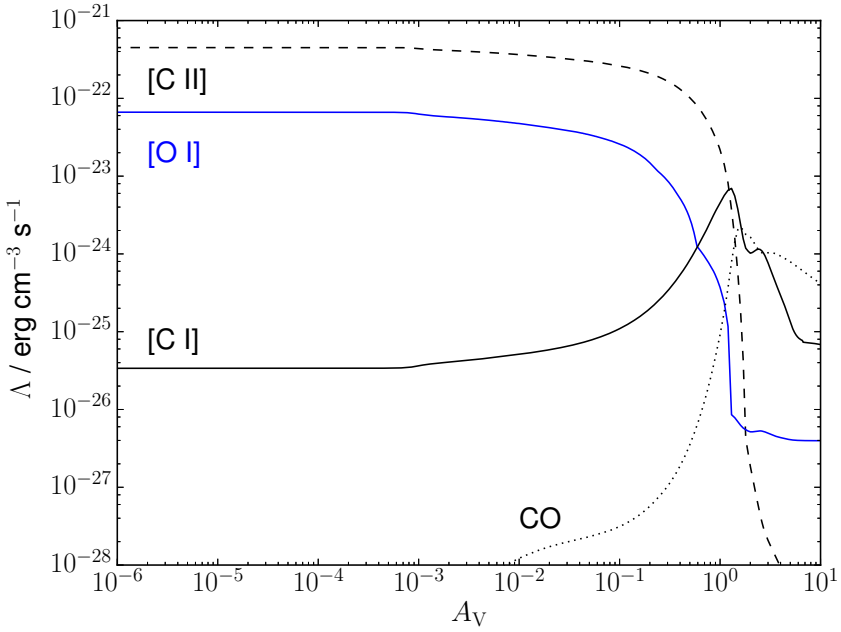

Figure 2.3: Cooling rate versus visual extinction from the emission lines of C^+ (dashed black line), C (solid black line), O (solid blue line) and CO (dotted black line), for the UCL_PDR model described in Section 1.5.2.

heating efficiencies from Dalgarno et al. (1999).

Figures 2.2 and 2.3 show the heating and cooling rates of significant processes versus visual extinction, respectively, for the PDR model described in Section 1.5.2 ($n_{\rm H} = 10^3\,{\rm cm}^{-3}$, incident FUV field 5 Draine). In the atomic region, the heating rate is dominated by the dust PE effect, with significant contributions from H_2 formation and photodissociation, while the cooling is from [C II] and [O I] forbidden lines. At higher visual extinctions, the UV field is lower and so the heating from dust PE and photodissociation is correspondingly reduced. The amount of ionized carbon also falls, so that [C I] cooling becomes more important than [C II]. Lower gas temperatures reduce the effectiveness of [O I] cooling and H_2 formation heating. In the molecular regions, heating is dominated by cosmic ray ionization, which is unaffected by the extinction, and exothermic chemical reactions, while cooling is mostly due to CO rotational emission lines.

2.3 MOCASSIN

MOCASSIN (Ercolano et al. 2003, 2005, 2008) is a 3D Monte Carlo photoionization code, including both gas and dust. The object to be modelled is defined as a distribution of

matter on a 3D Cartesian grid of arbitrary dimensions - the gas density, dust-to-gas ratio, elemental abundances and dust properties can all be varied from cell to cell. The radiation source, which may be either a point source or a diffuse field emitted from the grid, is defined by its luminosity and SED. Photon packets from the source are propagated through the grid until all have escaped, giving the mean intensity of the radiation field at each point. This is used to update the ionization and temperature balance of the gas and dust, which correspondingly alters the opacity of the material. The code then repeats the radiative transfer, and iterates between the two stages until convergence is reached, defined by the rate of change of either the hydrogen ionization fraction or, for dust-only models, the dust temperatures.

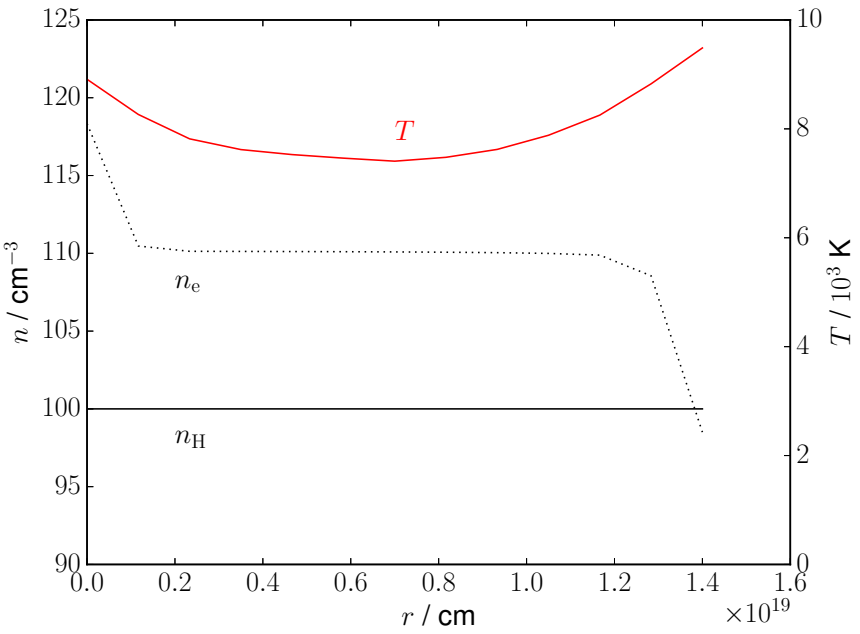

Figure 2.4: MOCASSIN model for hydrogen (solid black line) and electron (dotted black line) densities and electron temperature (solid red line) versus radius for a nebula with $n_{\rm H} = 100\,{\rm cm}^{-3}$, and stellar parameters $T_* = 40\,000\,{\rm K}$ and $L_* = 8.11 \times 10^5\,{\rm L}_\odot$, for a blackbody spectrum. The density scale is on the left-hand side, the temperature scale is on the right.

MOCASSIN divides the source luminosity into packets of constant energy, ϵ_0, with the initial frequency ν determined by sampling the SED of the source. The unit vector of the propagation direction is assumed to be randomly distributed, and the optical depth traversed by the packet is

$$\tau_\nu = -\log x \tag{2.10}$$

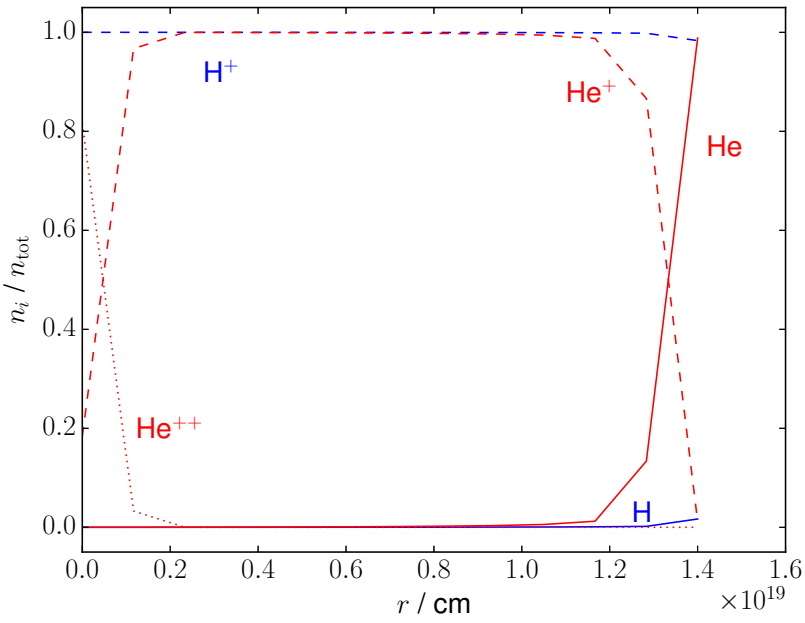

Figure 2.5: MOCCASSIN ion fractions relative to the total elemental abundance of H^+ (dashed blue line), H^0 (solid blue line), He^{++} (dotted red line), He^+ (dashed red line) and He^0 (solid red line) versus radius for a nebula with $n_{\rm H} = 100\,{\rm cm}^{-3}$, and stellar parameters $T_* = 40\,000\,{\rm K}$ and $L_* = 8.11 \times 10^5\,{\rm L}_\odot$.

where x is a random number between 0 and 1 (Lucy 1999). This optical depth corresponds to a physical distance l travelled under the conditions of the cell the particle is located in,

$$\tau_\nu = \rho \kappa_\nu l \tag{2.11}$$

where ρ is the density and κ_ν the frequency-dependent opacity of the cell. If travelling a distance l in the direction of propagation would carry the packet out of the cell, it is moved to the edge of the cell and the process is repeated. Otherwise, the packet interacts at the location given by l and the propagation direction, and is either scattered or absorbed with a probability given by the ratio of the scattering opacity to the total opacity. Scattered packets have a new direction of travel and a new optical depth calculated, and the process is repeated until the packet escapes the grid. For absorbed packets, a new frequency is also calculated, based on the emissivity in the grid cell where absorption takes place. The packet energy is the same, meaning that energy is conserved at the expense of changing the number of photons per packet. The assumption that all packets escape is justified as in steady-state, the energy input from the source must equal the total energy emerging from the modelled region. Using constant-energy packets, those with initial frequencies

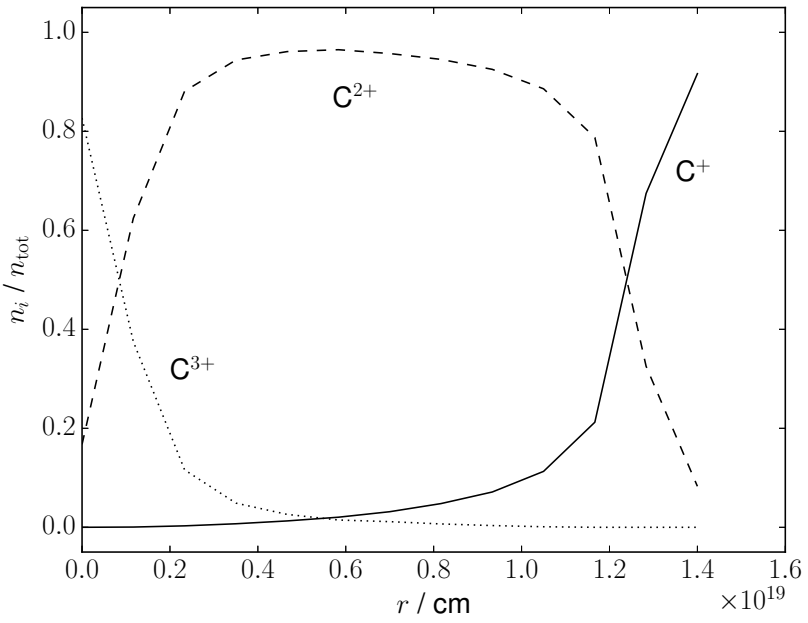

Figure 2.6: MOCASSIN ion fractions, relative to the total carbon abundance, for C^{3+} (dotted black line), C^{2+} (dashed black line) and C^{+} (solid black line) versus radius for a nebula with $n_{\rm H} = 100\,{\rm cm}^{-3}$, and stellar parameters $T_* = 40\,000\,{\rm K}$ and $L_* = 8.11 \times 10^5\,{\rm L}_\odot$.

with high optical depths to the edges (e.g. UV frequencies) are rapidly absorbed, and only escape when reemitted at optically thin frequencies (e.g. the infrared). Thus the initial ionizing fluz from the source is converted into lower frequency optical and IR cooling radiation in the output SED.

The mean radiation field, J_ν, is estimated from the paths of the energy packets following Lucy (1999), which relies on the fact that the radiation energy density $u_\nu = \frac{4\pi}{c} J_\nu$. Each energy packet contributes to the energy density of a cell depending on the length of time spent in it, or equivalently the length of its path from emission to escape which crosses the cell. The energy density between frequencies ν and $\nu + d\nu$ in a cell can therefore be estimated by

$$u_\nu d\nu = \frac{4\pi}{c} J_\nu d\nu = \frac{\epsilon_0}{\Delta t} \frac{1}{V} \sum \frac{l}{c} \tag{2.12}$$

where V is the cell volume, $\frac{\epsilon_0}{\Delta t} = \frac{L_*}{N}$ where ϵ_0 is the energy of one packet, Δt is the time interval of the simulation, L_* is the total luminosity and N is the number of energy packets, l is the length of a section of path crossing the cell and the sum is over all sections of path crossing the cell from energy packets with frequency between ν and $\nu + d\nu$.

The local radiation field is used to determine the temperature and ionization balance in each grid cell, which in turn determines the opacity and emissivity. Dust absorption efficiencies, $Q_{\rm abs}(\nu, a)$, are calculated using Mie theory for each grain species and size present. Contributions from free-free, bound-free and line processes are included for both the emissivity and opacity. Resonance lines, which may undergo multiple resonant scatterings before escaping the grid and therefore have longer path lengths, are more likely to be absorbed by dust grains, and can have significant effects on the dust energy balance. These are treated using the approximate escape probability method of Cohen et al. (1984) and Harrington et al. (1988). As well as radiative processes, the thermal balance of the gas includes the effects of photoelectric heating and collisional cooling from dust grains, following Baldwin et al. (1991).

Figure 2.4 shows the hydrogen and electron density and the electron temperature versus radius, for a spherically symmetric nebula with $n_{\rm H} = 100\,{\rm cm}^{-3}$, central star temperature $T_* = 40\,000\,{\rm K}$ and luminosity $L_* = 8.11 \times 10^5\,{\rm L}_\odot$, appropriate for an H II region surrounding an O-type star. The spectrum of the central star is assumed to be a blackbody. The ionization structures of hydrogen and helium are shown in Figure 2.5. The electron density is initially ~ 1.2 times larger than the hydrogen density, as a significant fraction of the helium (~ 0.1 times as abundant as hydrogen) is doubly ionized, but as photons capable of ionizing He^+ are absorbed this becomes the dominant ionization state, and $n_{\rm e}$ falls to $\sim 1.1 n_{\rm H}$. A similar transition between He^+ and He^0 occurs further towards the edge of the nebula, while hydrogen-ionizing photons also begin to be fully absorbed. The gas temperature falls initially before rising again at large radii, due to lower energy photons being absorbed more rapidly, so that at the edge of the nebula the average ejected electron energy is higher, and the heating rate subsequently larger. Figure 2.6 shows the ionization structure versus radius of carbon. Neutral carbon can be ionized by photons with energies $< 13.6\,{\rm eV}$, so is never present in significant quantities in ionized nebulae.

This page was intentionally left blank

Chapter 3

Molecular emission from planetary nebulae

The work in this chapter is based on the paper Priestley and Barlow (2018) with M. J. Barlow.

3.1 Introduction

Planetary nebulae (PNe) are the end-stage of the life cycle of low- and intermediate-mass stars, consisting of the gas ejected during previous phases of stellar evolution, surrounding a hot central star. Following the discovery of CO and H_2 emission from PNe (Mufson et al. 1975; Treffers et al. 1976), surveys have established that both molecules are commonly present in PNe (e.g. Huggins et al. 1996; Hora et al. 1999), with the molecular gas component in some cases forming a significant fraction of the total nebular mass. Other molecules, such as HCN, HCO^+ and CS, have also been detected in PNe (Edwards et al. 2014; Schmidt and Ziurys 2016), allowing investigation of the otherwise undetectable neutral regions.

In order to survive the ultraviolet (UV) radiation from the central star, molecules must be shielded within regions with significant optical depths (Tielens and Hollenbach 1993; Natta and Hollenbach 1998), such as the cometary knots commonly observed in PNe (O'Dell and Handron 1996; O'Dell et al. 2002). Matsuura et al. (2009) found that

the H_2 emission from NGC 7293, pictured in Figure 3.1, is highly localised within these knots, although in NGC 6781 the molecular emission more resembles a ring surrounding the central star (Bachiller et al. 1993; Hiriart 2005). Aleman et al. (2011) were able to reproduce the observed H_2 surface brightnesses of cometary knots in NGC 7293 with a combined photoionization/photodissociation region (PDR) code, finding that the low-density/diffuse gas surrounding the knots contributes very little to the overall H_2 emission. A detailed model of NGC 6781, assuming a dense, shock-heated PDR surrounding the inner ionized region, was produced by Otsuka et al. (2017) to fit a wide range of observational data from the UV to radio, including H_2 and CO molecular emission.

The molecular ion OH^+, originally observed in emission around ultraluminous galaxies (van der Werf et al. 2010), in the ISM (Wyrowski et al. 2010), the Orion bar (van der Tak et al. 2013) and, along with ArH^+, in the Crab Nebula (Barlow et al. 2013), was detected in five PNe by Etxaluze et al. (2014) and Aleman et al. (2014). Aleman et al. (2014) noted that all five PNe had central star temperatures greater than 100 kK, and suggested that soft X-rays may be responsible for producing this emission, as in the case of ultraluminous galaxies (van der Werf et al. 2010). X-rays were also found to be needed to reproduce the observed abundances of CN and HCO^+ (Kimura et al. 2012) in PNe. In their model of NGC 6781, Otsuka et al. (2017) predicted a significantly larger quantity of OH^+ than deduced from observations, despite good agreement with other molecular abundances.

In this chapter, we model the molecular emission from cometary knots in PNe using a combination of photoionization and PDR codes. Previous efforts (Aleman and Gruenwald 2004; Aleman et al. 2011; Kimura et al. 2012; Otsuka et al. 2017) have treated both problems simultaneously, ensuring that the PDRs are modelled self-consistently by solving the full radiative transfer problem throughout the knot. We use the approach adopted in Priestley et al. (2017) for modelling of the Crab Nebula, assuming that the photoionized region can be modelled separately from the PDR, providing an incident radiation field which determines the properties of the neutral gas. This allows us to use more detailed PDR models, including more molecular species and calculating the emission self-consistently, and to investigate a larger range of parameter space, due to the lower computational cost. Rather than attempt to reproduce the properties of one specific object, we vary the input parameters of our models and compare the resulting molecular emission predictions to the values typically observed in PNe.

Figure 3.1: Composite Hubble Space Telescope image of NGC 7293, the Helix Nebula. The image dimensions are 28.7 × 28.7 arcmin. Image credit: NASA, ESA and C. R. O'Dell.

3.2 Method

To determine the incident radiation field on the knots, we model the photoionized region of the PNe using MOCASSIN (Ercolano et al. 2003, 2005, 2008), a Monte Carlo photoionization code. We assume a 1D spherically symmetric geometry, with an inner region of diffuse gas of density n_d extending up to a radius r_k at which the knot is located, beyond which the gas density is increased to n_k. We increase the width of this dense region until the ionizing extreme UV (EUV) flux (taken to be $200 - 912$ Å) has been fully absorbed, marking the transition from a photoionized region to a PDR. We then integrate the emerging spectral energy distribution (SED) from 912 to 2400 Å to determine the far UV (FUV) field (in Draine units, ~ 1.7 times the Habing field; Habing 1968; Draine 1978) and from 0.1 to 200 Å to determine the X-ray flux incident on the PDR. We then model the PDR as a 1D slab with constant density n_k and a thickness of Δr_k using UCL_PDR (Bell et al. 2005, 2006; Bayet et al. 2011; Priestley et al. 2017), a PDR code that is also capable of treating

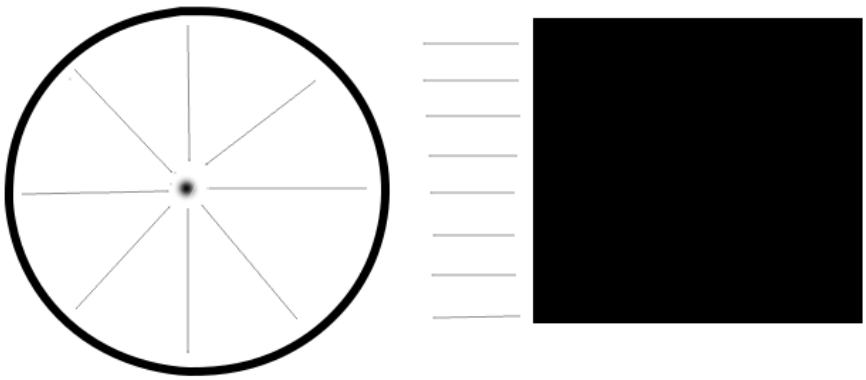

Figure 3.2: Schematic diagram of the modelling strategy. Left: a central source illuminates a surrounding shell of dense gas, with diffuse material occupying the interior of the shell. Right: the radiation field emerging from the shell is treated as a unidirectional field incident on a slab of gas, with a thickness much smaller than the radius of the shell.

X-rays. We assume Δr_k is small enough compared to r_k that we can ignore the effect of geometrical dilution on the radiation field inside the PDR. A schematic diagram of of our modelling strategy is shown in Figure 3.2, while a flowchart of the computational process is shown in Figure 3.3. We take $n_d = 100\,\mathrm{cm}^{-3}$, at the lower end of the typical density range of $10^2 - 10^4\,\mathrm{cm}^{-3}$ for diffuse gas in PNe (Osterbrock and Ferland 2006), and $n_k = 10^5\,\mathrm{cm}^{-3}$, appropriate for the cometary knots in NGC 7293 (Meaburn et al. 1998; Matsuura et al. 2007). We use $r_k = 0.2\,\mathrm{pc}$ and $\Delta r_k = 0.003\,\mathrm{pc}$, again consistent with values for the cometary knots in NGC 7293 (Matsuura et al. 2009).

The gas-phase elemental abundances used are listed in Table 3.1. We used values typical of PNe (Kingsburgh and Barlow 1994; Pottasch et al. 2005), with the exception of Mg, Si and Fe, where we assumed solar abundances (Lodders 2010) depleted by the maximum ISM values from Jenkins (2009). We assumed a dust-to-gas mass ratio of 0.005, typical of values found for PNe (Aleman et al. 2011; Ueta et al. 2014; Otsuka et al. 2017). We used a dust composition of half amorphous carbon, half silicate grains and a power law grain size distribution with an exponent of -3.5, and minimum/maximum grain radii of $0.005/0.25\,\mu\mathrm{m}$, appropriate for the ISM (Mathis et al. 1977). The choice of grain composition has been found to have only a small effect on H_2 abundances and emission - while the dust-to-gas mass ratio and dust grain size can cause significant variations

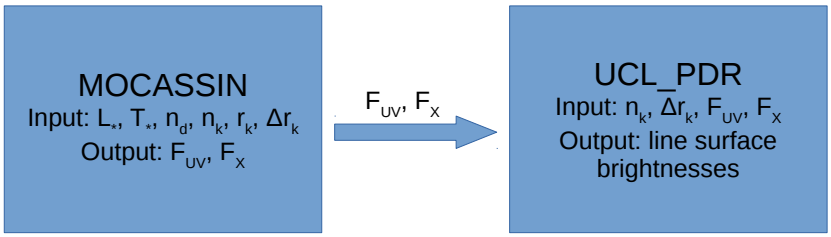

Figure 3.3: Flowchart of the modelling strategy.

(Aleman and Gruenwald 2004, 2011; Aleman et al. 2011), we do not investigate varying the dust properties in our models.

We investigate central star luminosities of $L_* = 100$ and $1000\,L_\odot$, and temperatures of $T_* = 50$, 80, 100, 120 and 150 kK, covering much of the parameter space relevant to old PNe (Vassiliadis and Wood 1994; Miller Bertolami 2016). We used model stellar spectra from the TheoSSA database (Rauch 2003), using $\log g = 6.0$, 7.0 and 8.0 as typical values for PNe without stellar winds or outflows (Guerrero and De Marco 2013), and take $\log g = 7.0$ as our standard value. We found that the transmitted X-ray SED output from our MOCASSIN models could be well fitted by a four-component power law. The transmitted UV and X-ray fluxes for each combination of L_*, T_* and $\log g$ are listed in Tables 3.2 and 3.3.

ArH^+ was incorporated into an existing XDR chemical network using the reaction network from Schilke et al. (2014), with their photodissociation rate replaced by the one calculated by Roueff et al. (2014) for the Crab Nebula, and the electron dissociative recombination rate with that calculated by Abdoulanziz et al. (2018). The photoionization cross-section for argon was taken from Verner and Yakovlev (1995), while the rate of ionization by secondary electrons was calculated from Lennon et al. (1988) following Meijerink and Spaans (2005). The recombination rates of Ar^{++} with electrons and neutral hydro-

gen were taken from Shull and van Steenberg (1982) and Kingdon and Ferland (1996) respectively. We included HeH^+ using the reactions and rate coefficients from Roberge and Dalgarno (1982), with the exception of the $He^+ + H$ reaction, for which we used the rate coefficient from Zygelman and Dalgarno (1990), and the $HeH^+ + e^-$ reaction, where we used the experimentally determined rate from Yousif and Mitchell (1989). We also neglected photodissociation of HeH^+, as our input SED from MOCASSIN has negligible flux in the wavelength range beyond the Lyman limit relevant for the cross-section given by Roberge and Dalgarno (1982).

Electron impact excitation rates for the rotational levels of ArH^+ and HeH^+ were taken from Hamilton et al. (2016), and energy levels and Einstein A-coefficients from the Cologne Database for Molecular Spectroscopy (CDMS) (Müller et al. 2001, 2005), in order to calculate the emissivity of ArH^+ and HeH^+ rotational transitions. We included the collisional excitation of OH^+ by H using the rate coefficients calculated by Lique et al. (2016), which may become important in lower ionization regions, in addition to collisional excitation by electrons (van der Tak et al. 2013). We assume a typical ISM value for the cosmic ray ionization rate ($1.3 \times 10^{-17}\,s^{-1}$) and an A_V/N_H conversion factor of 3.0×10^{-22} mag cm^2, reduced from ISM values by a factor of two to account for our lower dust-to-gas mass ratio. Values of the cosmic ray ionization rate derived from observations can be higher than our adopted value by over an order of magnitude (e.g. Neufeld and Wolfire 2017), which may become important if the ionization rate exceeds that from the X-ray flux.

We also investigate the likely effects of the EUV ($200 - 912$ Å) flux, suggested to be responsible for powering H_2 emission in NGC 7293 by O'Dell et al. (2007), by running MOCASSIN models consisting of only diffuse gas up to r_k, without the denser shell absorbing the ionizing radiation. The transmitted fluxes are listed in Table 3.4. The 'X-ray' fluxes, now defined as over the wavelength range $0.1 - 750$ Å, are significantly increased for all models, and are much less affected by T_*, as the expanded range includes the SED peak for all central star temperatures. The UV fields are slightly reduced from the previous values, as the diffuse UV emission from the dense ionized gas (calculated in MOCASSIN but not UCL_PDR) is no longer included. UCL_PDR treats X-rays following the methods described in Meijerink and Spaans (2005) - the extent to which this approach is valid for EUV photons, and the likely impact on our results, is discussed in Section 3.4.2.

Table 3.1: Gas-phase elemental abundances, relative to hydrogen, adopted for the PN modelling.

Element	Abundance	Element	Abundance
H	1.00	Mg	1.5×10^{-6}
He	0.10	Si	1.5×10^{-6}
C	2.5×10^{-4}	S	1.5×10^{-5}
N	1.0×10^{-4}	Cl	1.8×10^{-7}
O	5.0×10^{-4}	Ar	2.0×10^{-6}
Ne	1.0×10^{-4}	Fe	1.5×10^{-7}

Table 3.2: Central star luminosities L_* and effective temperatures T_*, and output UV and X-ray fluxes from our MOCASSIN modelling of PNe with $\log g = 7.0$. The X-ray component includes all transmitted flux between 0.1 Å and 200 Å.

$L_*/L_\odot$	T_*/kK	$F_{\rm UV}$/Draines	$F_{\rm X}$/ erg cm^{-2} s^{-1}
10^2	50	233	0.00
10^2	80	91.5	3.24×10^{-7}
10^2	100	69.8	2.18×10^{-5}
10^2	120	59.2	6.56×10^{-4}
10^2	150	48.1	4.55×10^{-2}
10^3	50	2230	0.00
10^3	80	817	1.05×10^{-6}
10^3	100	606	2.39×10^{-4}
10^3	120	501	7.38×10^{-3}
10^3	150	366	0.570

Table 3.3: Central star luminosities L_* and effective temperatures T_*, and output UV and X-ray fluxes from our MOCASSIN modelling of PNe with $\log g = 6.0$ and 8.0. The X-ray component includes all transmitted flux between 0.1 Å and 200 Å.

		$\log g = 6.0$		$\log g = 8.0$	
$L_*/L_\odot$	T_*/kK	$F_{\rm UV}$/Draines	$F_{\rm X}$/ erg cm^{-2} s^{-1}	$F_{\rm UV}$/Draines	$F_{\rm X}$/ erg cm^{-2} s^{-1}
10^2	50	226	0.00	238	0.00
10^2	80	92.9	3.67×10^{-7}	90.6	3.73×10^{-7}
10^2	100	71.5	7.31×10^{-5}	68.7	4.96×10^{-6}
10^2	120	60.0	2.32×10^{-3}	58.8	4.04×10^{-4}
10^2	150	47.2	6.16×10^{-2}	48.7	3.52×10^{-2}
10^3	50	2160	0.00	2280	0.00
10^3	80	829	1.01×10^{-6}	815	2.13×10^{-6}
10^3	100	622	8.61×10^{-4}	596	5.75×10^{-5}
10^3	120	499	4.19×10^{-2}	497	4.43×10^{-3}
10^3	150	351	0.713	377	0.459

Table 3.4: Central star luminosities L_* and effective temperatures T_*, and output UV and X-ray fluxes from our MOCASSIN modelling of PNe, for model atmospheres with $\log g = 7.0$ including the EUV flux. The X-ray component now includes all flux up to 750 Å.

L_* / $L_\odot$	T_* / kK	$F_{\rm UV}$ / Draines	$F_{\rm X}$ / erg cm^{-2} s^{-1}
10^2	50	233	0.183
10^2	80	85.1	0.550
10^2	100	62.7	0.605
10^2	120	51.7	0.613
10^2	150	41.7	0.580
10^3	50	2110	6.54
10^3	80	609	11.8
10^3	100	387	12.6
10^3	120	284	12.4
10^3	150	175	13.4

3.3 Results

Figure 3.4 shows the predicted OH^+ 971 GHz line surface brightness versus T_*, for models with $\log g = 7.0$. The emission strength increases rapidly for central star temperatures above 100 kK, while also increasing with L_*, as increasing X-ray fluxes enhance the ionized fraction in the gas and thus the OH^+ abundance (van der Werf et al. 2010). The observed range of surface brightnesses (Aleman et al. 2014; Etxaluze et al. 2014) can be explained by models with central star temperatures close to 150 kK, although these models have OH^+ column densities in excess of the values calculated by Aleman et al. (2014). For $T_* \leq 120$ kK the surface brightnesses are well below those observed, despite several PNe with OH^+ detections having central star temperatures in this region. The line ratios between the three lowest frequency OH^+ rotational transitions, at 909, 971 and 1033 GHz, are essentially constant across all models, with relative strengths of 0.2 : 1 : 0.6 respectively. This is in qualitative agreement with the ratios for all the PNe with detected OH^+ emission, from Aleman et al. (2014) and Etxaluze et al. (2014), with the exception of NGC 6781.

Figure 3.5 shows the predicted H_2 2.12 μm line surface brightness versus T_* for two values of the central star luminosity. The range of values observed in PNe from Hora et al. (1999) is also shown. The predicted emission strength is barely affected by L_*, and is roughly constant below 120 kK, as the H_2 line requires significant population of the $v = 1$ vibrational state, and the PDR gas temperature is far higher for the 150 kK models than for those with lower T_*. For $T_* = 150$ kK, the predicted H_2 surface brightnesses are consistent with the smallest values detected by Hora et al. (1999), but the highest surface

brightnesses in this line are not reproduced by these models.

Figure 3.6 shows the predicted CO $J = 4 - 3$ line surface brightness versus T_*. In this case the emission is strongly affected by the value of L_*, as the increased UV field for the $1000\,L_\odot$ models readily dissociates CO molecules. Surface brightness increases with T_* for the same L_* as less of the central star flux is emitted at FUV wavelengths. The $100\,L_\odot$, 150 kK model has a predicted surface brightness comparable with the lowest values measured by Etxaluze et al. (2014) and Ueta et al. (2014), but again, no model reproduces the higher observed values. Increasing the elemental abundance of carbon is unlikely to resolve this discrepancy, as our oxygen abundance is only a factor of two higher, limiting the amount of CO which can be formed. Elemental oxygen abundances in PNe are rarely significantly higher than our value of 5×10^{-4} (Kingsburgh and Barlow 1994).

Figure 3.7 shows the predicted ArH^+ $J = 1 - 0$ 617 GHz line surface brightness versus T_*. ArH^+ has not been detected in any PN to date, despite the $J = 1 - 0$ and $2 - 1$ transitions falling within the Herschel SPIRE frequency range. The dashed line in Figure 3.7 corresponds to the surface brightness of the weakest OH^+ SPIRE line detection from Aleman et al. (2014). If this is taken as a lower limit, only the 150 kK, $1000\,L_\odot$ model predicts detectable ArH^+ emission in this line, although the 150 kK, $100\,L_\odot$ model is only a factor of a few below the limit. The $J = 2 - 1$ transition at 1234 GHz is generally brighter in all models by a factor of a few, but considering the lower signal-to-noise at higher frequencies, we still find only the 150 kK, $1000\,L_\odot$ model produces a surface brightness above the weakest OH^+ (1033 GHz) line detection. A similar situation is found for the HeH^+ 149 μm line, using the OH^+ 152 μm PACS detections as a lower limit for detectability - all models except for 150 kK, $1000\,L_\odot$ are below the detection threshold.

Increasing the gas density to $n_H = 10^6\,cm^{-3}$, while reducing Δr_k to 3×10^{-4} pc to ensure the same column density, the OH^+ and H_2 line surface brightnesses are increased for all models, with the effect greater for $L_* = 1000\,L_\odot$. Figure 3.8 shows the OH^+ 971 GHz line surface brightness versus T_*, for these increased density models. Even for $1000\,L_\odot$, the increase in surface brightness is not great enough to bring models with $T_* < 150$ kK within the range of observed values. The CO $J = 4 - 3$ emission, shown in Figure 3.9, is much more strongly affected, with all the $100\,L_\odot$ models now exceeding the observational upper limits, while for $L_* = 1000\,L_\odot$ the predicted surface brightnesses are comparable to observation, with the exception of the 50 kK model, for which it is still too low. ArH^+ and HeH^+ surface brightnesses both decrease, although the 150 kK, $1000\,L_\odot$ model still

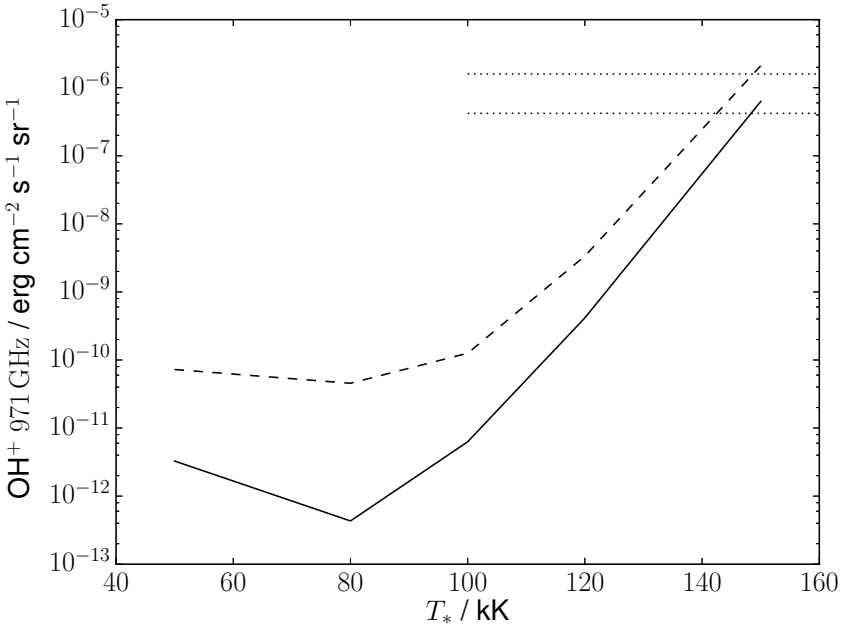

Figure 3.4: OH^+ 971 GHz surface brightness versus T_*, for models with $n_\mathrm{H} = 10^5\,\mathrm{cm}^{-3}$, $\log g = 7.0$ and $L_* = 100\,\mathrm{L}_\odot$ (solid line) and $1000\,\mathrm{L}_\odot$ (dashed line). The dotted horizontal lines show the range of observed values from Etxaluze et al. (2014) and Aleman et al. (2014).

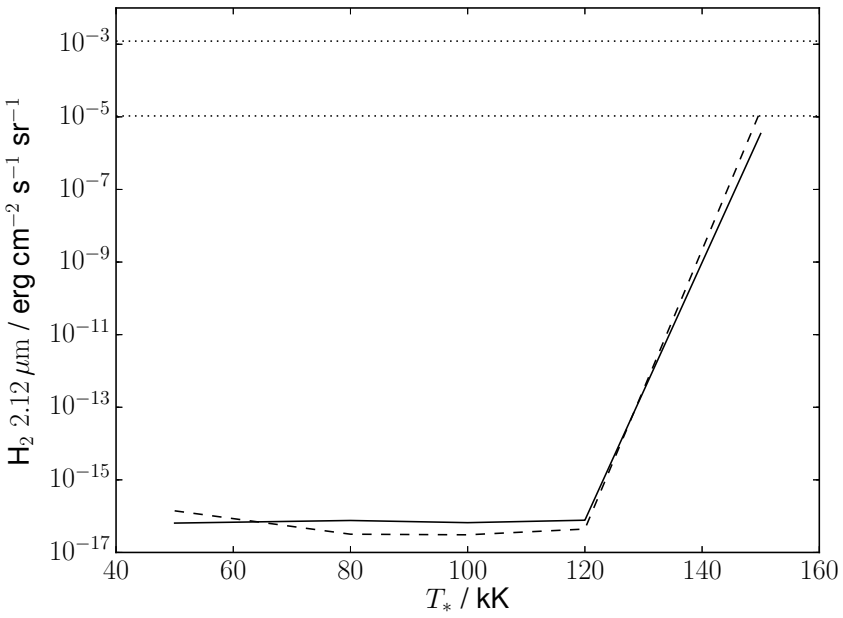

Figure 3.5: H_2 2.12 μm surface brightness versus T_*, for models with $n_\mathrm{H} = 10^5\,\mathrm{cm}^{-3}$, $\log g = 7.0$ and $L_* = 100\,\mathrm{L}_\odot$ (solid line) and $1000\,\mathrm{L}_\odot$ (dashed line). The dotted horizontal lines show the range of observed values from Hora et al. (1999).

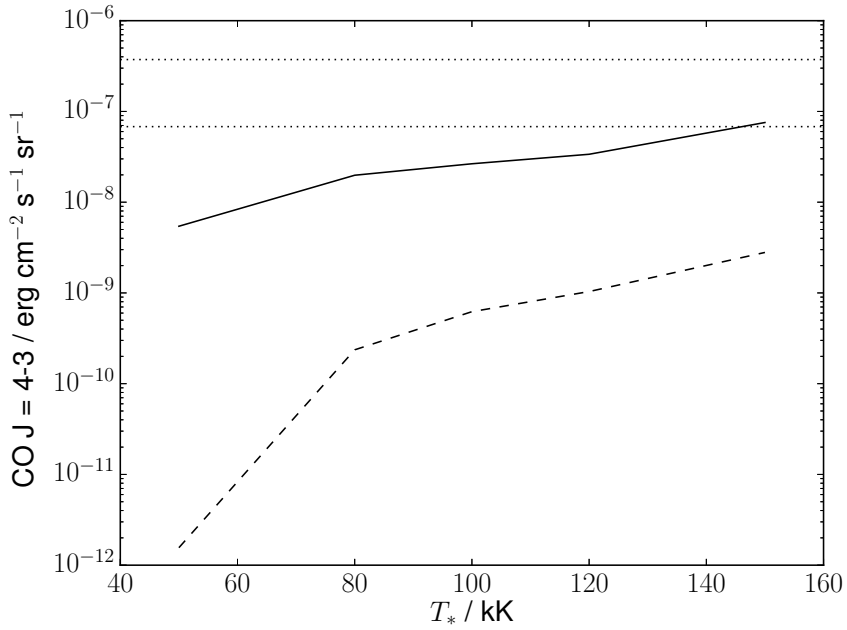

Figure 3.6: CO $J = 4 - 3$ surface brightness versus T_*, for models with $n_{\rm H} = 10^5\,{\rm cm}^{-3}$, $\log g = 7.0$ and $L_* = 100\,{\rm L}_\odot$ (solid line) and $1000\,{\rm L}_\odot$ (dashed line). The dotted horizontal lines show the range of observed values from Etxaluze et al. (2014) and Ueta et al. (2014).

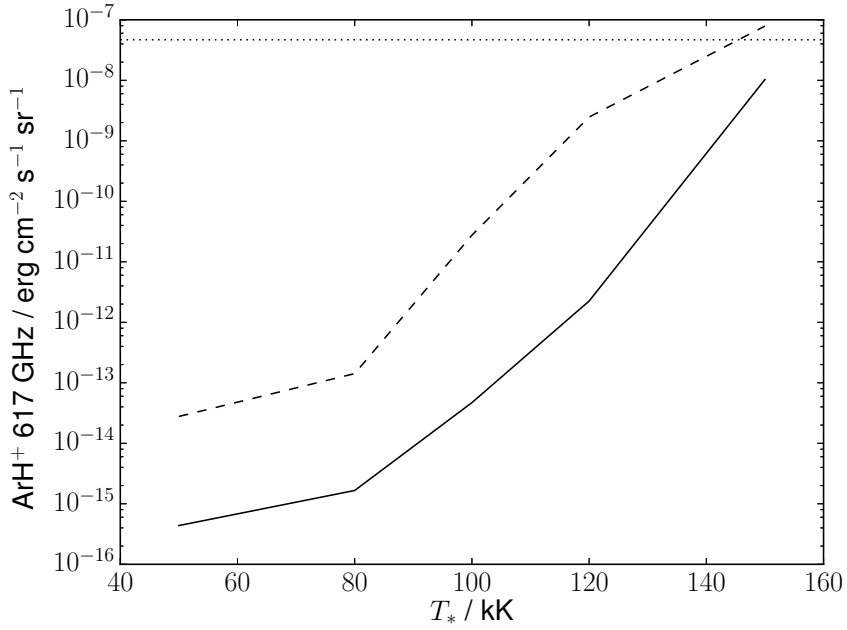

Figure 3.7: ArH$^+$ 617 GHz surface brightness versus T_*, for models with $n_{\rm H} = 10^5\,{\rm cm}^{-3}$, $\log g = 7.0$ and $L_* = 100\,{\rm L}_\odot$ (solid line) and $1000\,{\rm L}_\odot$ (dashed line). The dotted horizontal line shows the surface brightness of the weakest SPIRE OH$^+$ detection from Aleman et al. (2014).

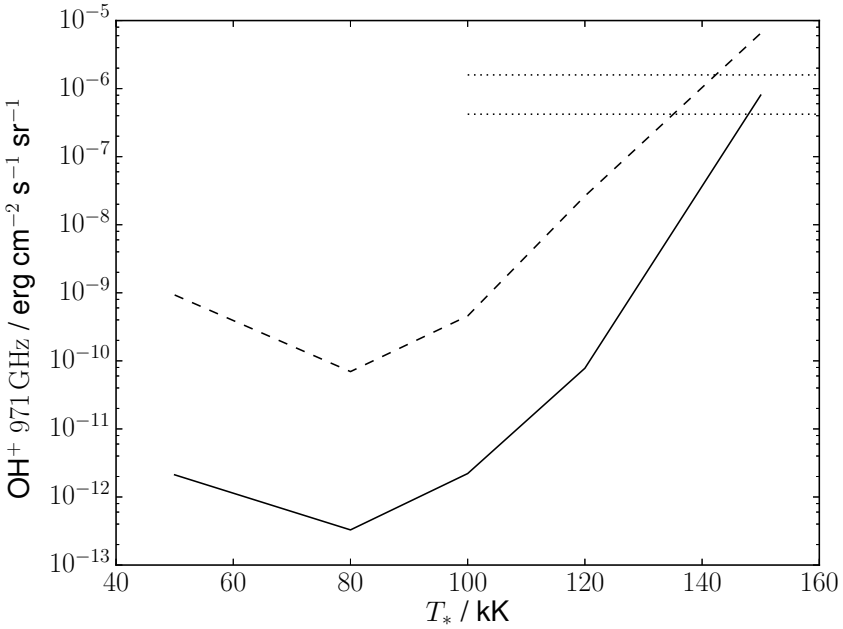

Figure 3.8: OH^+ 971 GHz surface brightness versus T_*, for models with $n_H = 10^6\,cm^{-3}$, $\log g = 7.0$ and $L_* = 100\,L_\odot$ (solid line) and $1000\,L_\odot$ (dashed line). The dotted horizontal lines show the range of observed values from Etxaluze et al. (2014) and Aleman et al. (2014).

predicts detectable levels for both molecules.

Figure 3.10 shows the input stellar spectra for model atmospheres with $T_* = 120\,kK$ and $\log g$ ranging from 6.0 to 8.0, demonstrating the large variation at X-ray wavelengths between the models (note that the total flux up to 200 Å is highest for $\log g = 6.0$, despite F_λ being much lower at the shortest wavelengths). The results from our photoionization modelling, listed in Tables 3.2 and 3.3, show that the incident X-ray flux is generally higher for $\log g = 6.0$ and lower for $\log g = 8.0$, while the UV field is not significantly affected.

Figure 3.11 shows the OH^+ 971 GHz line surface brightness versus T_*, for models with $\log g = 6.0$. The increased X-ray flux results in stronger OH^+ emission, particularly for $T_* = 120\,kK$, for which the $1000\,L_\odot$ model gives a surface brightness within a factor of a few of observations. This model also predicts H_2 surface brightnesses consistent with observed values, compared to the $\log g = 7.0$ case, where the emission is far weaker. The CO $J = 4 - 3$ surface brightnesses are largely unchanged from the $\log g = 7.0$ case, while the ArH^+ and HeH^+ lines are only slightly weaker than the detection limits taken from Aleman et al. (2014). Increasing $\log g$ to 8.0 reduces model surface brightnesses by at most a factor of a few compared to $\log g = 7.0$.

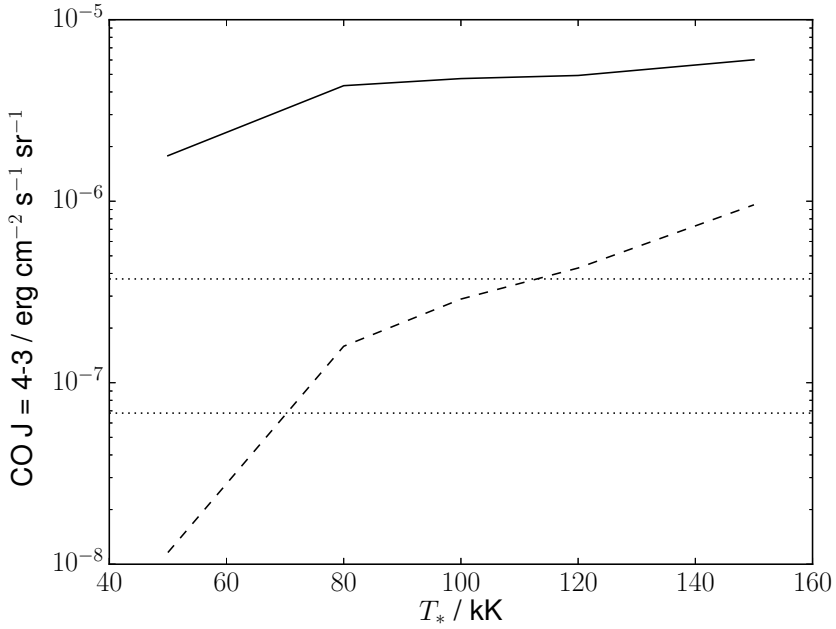

Figure 3.9: CO $J = 4 - 3$ surface brightness versus T_*, for models with $n_{\rm H} = 10^6\,{\rm cm}^{-3}$, $\log g = 7.0$ and $L_* = 100\,{\rm L}_\odot$ (solid line) and $1000\,{\rm L}_\odot$ (dashed line). The dotted horizontal lines show the range of observed values from Etxaluze et al. (2014) and Ueta et al. (2014).

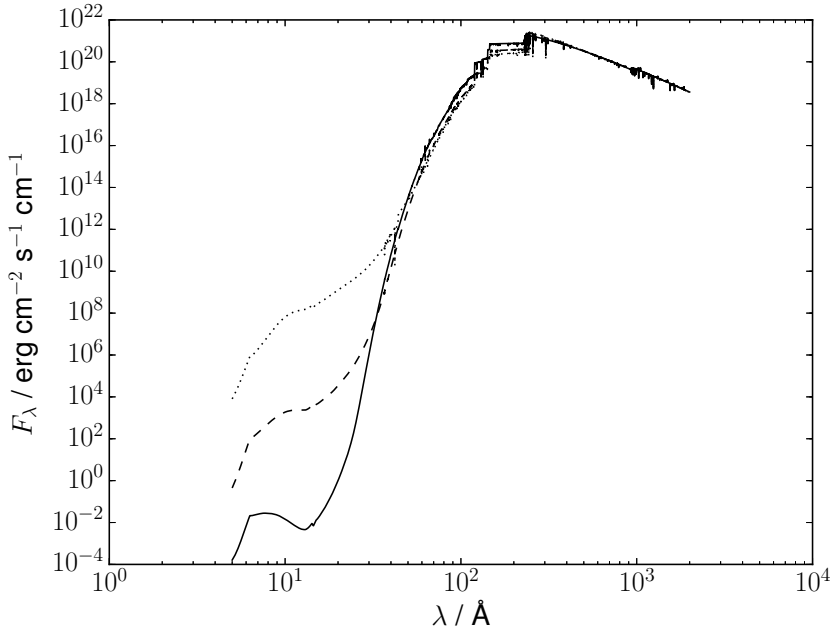

Figure 3.10: Model central star spectra for model atmospheres with $T_* = 120\,{\rm kK}$ and $\log g = 6.0$ (solid line), 7.0 (dashed line) and 8.0 (dotted line), obtained from the TheoSSA database (Rauch 2003).

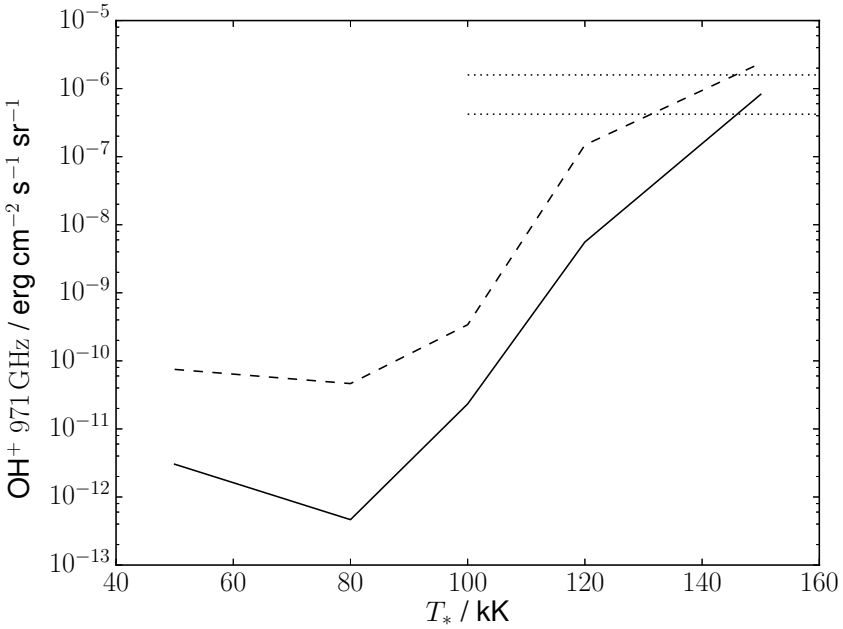

Figure 3.11: OH^+ 971 GHz surface brightness versus T_*, for models with $n_H = 10^5\,cm^{-3}$, $\log g = 6.0$ and $L_* = 100\,L_\odot$ (solid line) and $1000\,L_\odot$ (dashed line). The dotted horizontal lines show the range of observed values from Etxaluze et al. (2014) and Aleman et al. (2014).

Figures 3.12 and 3.13 show respectively the predicted OH^+ 971 GHz and H_2 2.12 μm line surface brightnesses versus T_*, for models including the EUV flux. Models with $T_* < 150\,kK$ have much higher surface brightnesses in both lines than the corresponding models without the additional flux, as the EUV flux heats the gas at the edge of the knot to much higher temperatures, as well as increasing the ionization fraction. The H_2 2.12 μm surface brightnesses are increased to within a factor of a few of observed values for $T_* \geq 80\,kK$. As with H_2, for $T_* < 150\,kK$ there is a significant increase in the OH^+ surface brightnesses. Models with $T_* > 80\,kK$ all predict surface brightnesses similar to or higher than observations, while for $T_* = 50\,kK$ the predicted values are below the lowest observed. Aleman et al. (2014) only detected OH^+ emission from PNe with $T_* \geq 100\,kK$ - while our models in this temperature range are consistent with the observed surface brightness, we also predict similar values for $T_* = 80\,kK$, whereas observations by Aleman et al. (2014) of three high-luminosity PNe with $80\,kK \leq T_* < 100\,kK$ did not detect any OH^+ lines. The reasons for this are discussed in Section 3.4.5. The CO $J = 4 - 3$ surface brightnesses are essentially unchanged from the previous values. Figure 3.14 shows the ArH^+ 617 GHz surface brightnesses versus T_* for the models including the EUV flux. The

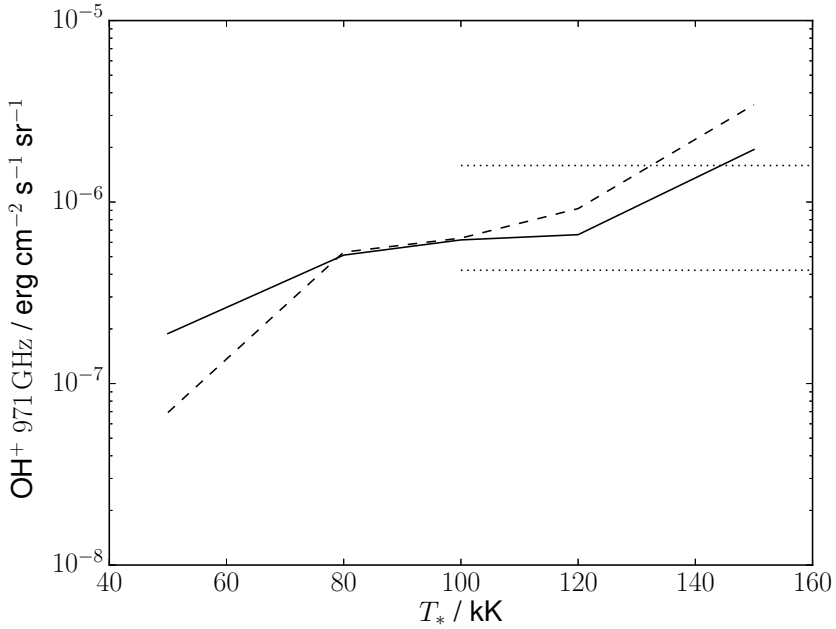

Figure 3.12: OH$^+$ 971 GHz surface brightness versus T_*, for models with $n_{\rm H} = 10^5\,{\rm cm}^{-3}$, $\log g = 7.0$ and $L_* = 100\,{\rm L}_\odot$ (solid line) and $1000\,{\rm L}_\odot$ (dashed line) including the EUV flux. The dotted horizontal lines show the range of observed values from Etxaluze et al. (2014) and Aleman et al. (2014).

$T_* = 150\,{\rm kK}$ models both predict surface brightnesses above the detection threshold, while for lower T_* the predicted values are much higher than the original case, although still consistent with the non-detection of this line in PNe. For HeH$^+$, the predicted $149\,\mu{\rm m}$ surface brightnesses are above the detection threshold for all models.

Figure 3.15 shows the OH$^+$ column density versus T_* for models including the EUV flux. The column density is calculated by integrating through a single knot - multiple knots along the line of sight would result in higher values. The range of values in PNe calculated by Aleman et al. (2014) from observations, assuming local thermodynamic equilibrium (LTE), are also shown. All models which reproduce the observed OH$^+$ line surface brightnesses have column densities significantly larger than those found by Aleman et al. (2014). Otsuka et al. (2017) found an OH$^+$ column density of $10^{13}\,{\rm cm}^{-2}$ in their model of NGC 6781, also significantly higher than the value for this PN derived from observations. As we calculate the line emission directly, without assuming LTE, and since models without the EUV flux, which have lower OH$^+$ column densities, predict surface brightnesses below that observed, the higher values from our models are likely to be more accurate.

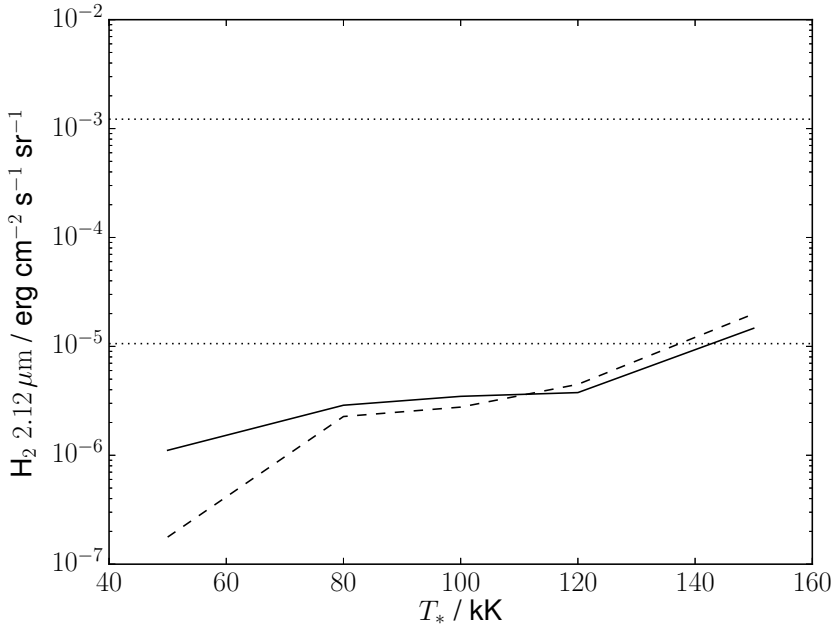

Figure 3.13: H_2 2.12 μm surface brightness versus T_*, for models with $n_{\rm H} = 10^5\,{\rm cm}^{-3}$, $\log g = 7.0$ and $L_* = 100\,{\rm L}_\odot$ (solid line) and $1000\,{\rm L}_\odot$ (dashed line) including the EUV flux. The dotted horizontal lines show the range of observed values from Hora et al. (1999).

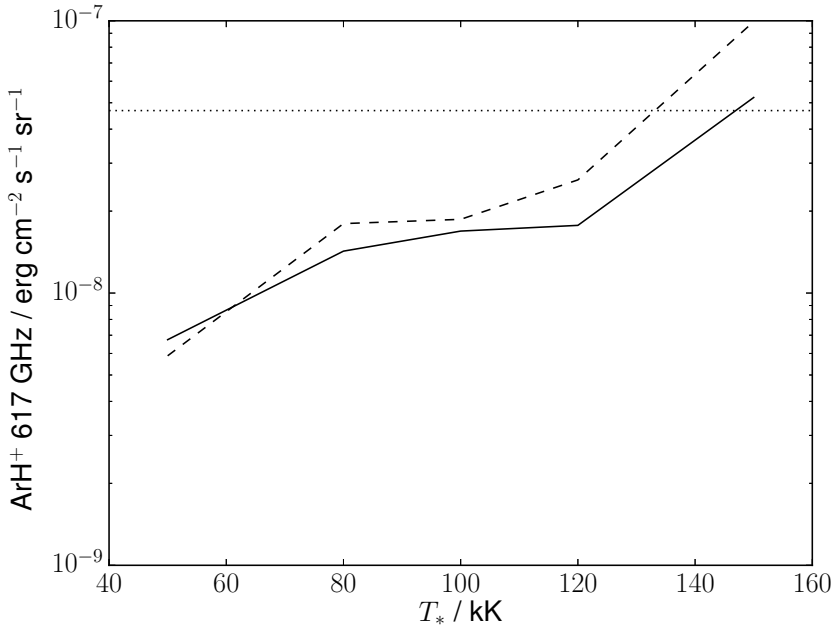

Figure 3.14: ArH^+ 617 GHz surface brightness versus T_*, for models with $n_{\rm H} = 10^5\,{\rm cm}^{-3}$, $\log g = 7.0$ and $L_* = 100\,{\rm L}_\odot$ (solid line) and $1000\,{\rm L}_\odot$ (dashed line) including the EUV flux. The dotted horizontal line shows the surface brightness of the weakest SPIRE OH^+ detection from Aleman et al. (2014).

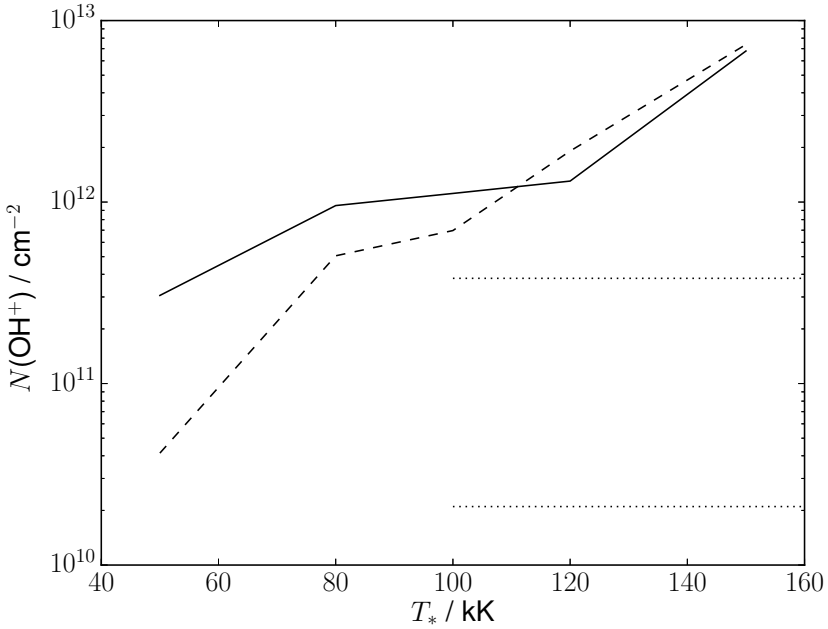

Figure 3.15: OH^+ column density versus T_*, for models with $n_H = 10^5\,cm^{-3}$, $\log g = 7.0$ and $L_* = 100\,L_\odot$ (solid line) and $1000\,L_\odot$ (dashed line) including the EUV flux. The dotted horizontal lines show the range of values calculated from observations by Aleman et al. (2014).

3.4 Discussion

3.4.1 Location of the molecular emission

Figure 3.16 shows the abundances of H, H_2 and e^-, and the gas temperature, versus distance into the knot for the 120 kK $100\,L_\odot$ UCL_PDR model including the EUV flux. At the edge of the knot the gas temperature and ionization fraction are high ($\sim 10^4$ K and ~ 0.2 respectively). The ionization fraction decreases smoothly with distance as the EUV flux is rapidly attenuated, while the gas temperature drops much more sharply at a distance of $\sim 2 \times 10^{14}$ cm. Aleman et al. (2011), who used similar values for the gas and central star properties, found similar temperatures and ionization fractions for their K1 model (with a step-function density profile), although the decrease in temperature is less sharp than in our models. The H_2 abundance rises slowly from an initial level of 10^{-4} before rapidly increasing at $\sim 2 \times 10^{14}$ cm, with the PDR region where hydrogen is mostly atomic taking up a relatively small part of the knot. Aleman et al. (2011) stopped their models once the gas temperature reached 100 K - in this region, our models are in good agreement, although our H_2 abundances in the 100 K region are slightly lower.

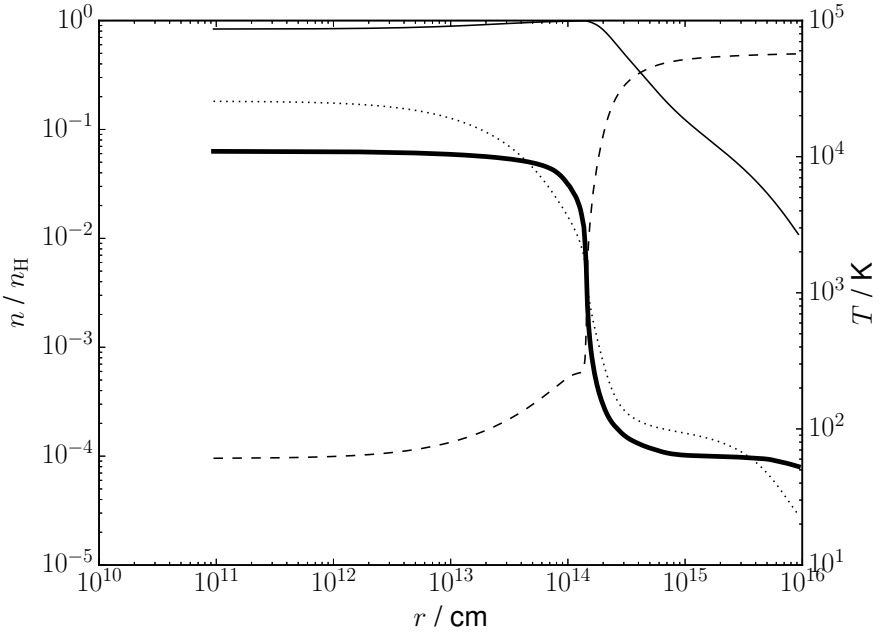

Figure 3.16: Abundances of H (thin solid line), H_2 (dashed line) and e^- (dotted line) and gas temperature (thick solid line) versus distance into the knot for the 120 kK 100 $L_\odot$ $\log g = 7.0$ EUV model. The left y-axis shows the abundance relative to hydrogen nuclei, and the right the gas temperature.

Figure 3.17 shows the emissivities of the H_2 2.12 μm, CO $J = 4-3$, OH^+ 971 GHz and ArH^+ 617 GHz lines versus distance. The 2.12 μm emission is concentrated in the ionized and PDR regions, despite the H_2 abundance not rising above 10^{-3}, and the emissivity is negligible in the molecular region of the knot as the much lower gas temperatures are unable to significantly populate the upper vibrational levels. Aleman et al. (2011) found similar peak emissivities for this line, although in our models the emissivity drops off much more sharply into the cloud, as with the temperature. The OH^+ and ArH^+ emissivities are also highest at the edge of the knot, but decrease more gradually than for H_2, with the emission extending into the molecular region. The CO $J = 4-3$ emissivity, unlike the other lines, is highest in the molecular region, with the contribution from the ionized/atomic parts of the knot negligible. Increasing L_* produces higher temperatures and ionization fractions, and a smaller molecular region, while the size of the molecular region increases with T_* as the FUV flux decreases, due to a larger proportion of the flux being emitted at shorter wavelengths.

Our models assume that the molecular emission arises from dense knots of gas, such as is observed in NGC 7293. Alternative geometries are clearly possible, such as the

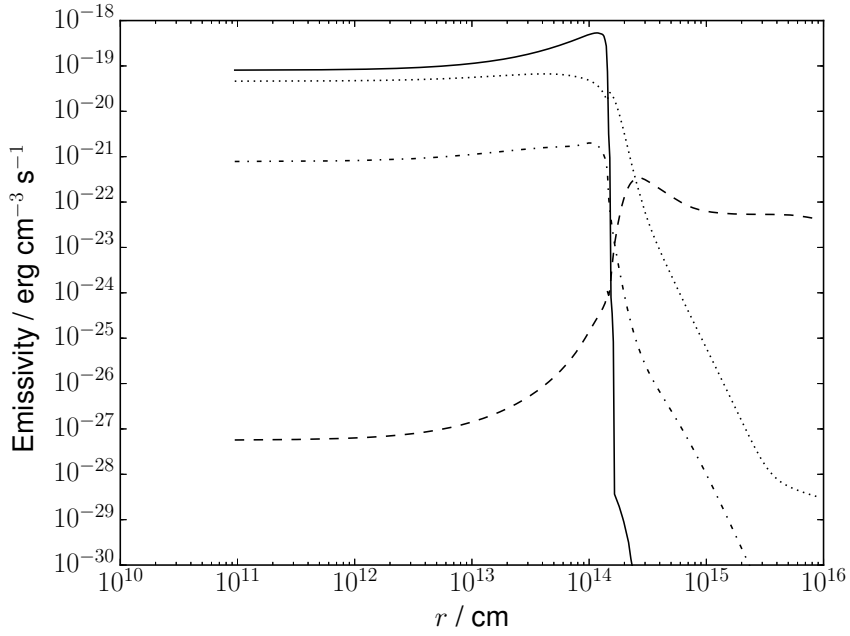

Figure 3.17: Line emissivities of H_2 2.12 μm (solid line), CO $J = 4-3$ (dashed line), OH^+ 971 GHz (dotted line) and ArH^+ 617 GHz (dot-dashed line) versus distance into the knot for the 120 kK 100 $L_\odot$ $\log g = 7.0$ EUV model.

ring-like structure seen in NGC 6781, or a simple spherical shell surrounding the central star. However, given the simplicity of our PDR models, different geometries are unlikely to significantly alter our results. As UCL_PDR treats the gas as a 1D slab, the assumed geometry enters the modelling only as the slab thickness and the incident radiation field. The radiation field depends much more strongly on the distance from the central star then on the configuration of the dense gas, while changing the slab thickness would not greatly alter the H_2 and OH^+ surface brightnesses as long as the high-T ionized region at the edge is entirely included, as beyond this point the emissivities drop off sharply.

3.4.2 Treatment of EUV flux

Our EUV models include, as part of the X-ray flux in UCL_PDR, the ionizing photon flux from $0.1-750$ Å as X-rays in UCL_PDR. The $750-912$ Å flux is absorbed in the ionized region treated by MOCASSIN. UCL_PDR uses the methods described by Meijerink and Spaans (2005) to treat X-rays, which are not necessarily applicable to lower-energy EUV photons. The code calculates the wavelength-dependent cross-section for photoionization using the fits from Verner and Yakovlev (1995), and uses this to calculate the ionization and heating rates at each point in the knot. As the fits are not limited to X-ray wavelengths, the contri-

bution to the ionization and gas heating by the EUV radiation will be correctly included. However, the chemical network only includes singly- and doubly-ionized elements, and of these, only cooling by C^+, Si^+ and Fe^+ is accounted for. The cooling rate is therefore likely to be underestimated, and the model gas temperatures likely too high.

Molecular photodissociation rates are based on the UMIST database (McElroy et al. 2013) rates, scaled by the ratio of the energy density between 912 and 2400 Å to that of the Draine field (Draine 1978), and so does not include the effects of EUV photons. Significantly for our results, OH^+ (Saxon and Liu 1986), ArH^+ (Roueff et al. 2014) and HeH^+ (Roberge and Dalgarno 1982) all have photodissociation cross-sections which peak at EUV wavelengths. The EUV flux is also not included in the treatments of dust heating and gas heating by the dust photoelectric (PE) effect, which may be important in the deeper regions of our models where the dust PE effect is the dominant heating mechanism.

EUV photons are attenuated rapidly in the knots - in both MOCASSIN and UCL_PDR the flux at these wavelengths is reduced to zero within $\sim 10^{-4}$ pc, so the effects are only significant in the outer regions of the knot (corresponding to the transition zones in Aleman and Gruenwald (2011)). As the CO emission originates from the PDR regions deeper into the knots, we do not expect those values to be sensitive to the EUV treatment - the differences between models with and without EUV are minimal. For the other molecules, the effects of including EUV are much more significant as the majority of the emission originates in the transition zones. In these parts of the knots, the heating rate is dominated by the X-ray/EUV flux, so the PE effect can be neglected. The main coolant in our models in these regions is atomic hydrogen - assuming that this would be the case even if cooling from all atomic/ionic species were included, we can be reasonably confident in the calculated temperatures in these regions.

The main issue with our treatment of the EUV flux is therefore the neglect of photodissociation by EUV photons, which will only have a significant impact if it is the main destruction mechanism for a particular molecule. Aleman and Gruenwald (2004) and Aleman et al. (2011) found charge exchange to be more significant in the destruction of H_2 in the transition zones of PNe, and as photodissociation by FUV photons, longwards of 912 Å, is accounted for, our H_2 abundances are unlikely to be strongly affected. For OH^+, ArH^+ and HeH^+, the increased photodissociation cross-sections in the EUV region (compared to the FUV) means that the photodissociation rates used are lower than the true values, and therefore the molecular abundances and the line emission will be over-

estimated. The extent will depend on the rates of other destruction mechanisms - in the transition zones, dissociative recombination with electrons is likely to be the most important destruction mechanism for the molecular ions, and if this is significantly higher than the photodissociation rates the effect on the abundances will be minimal.

3.4.3 Effect of input parameters

We have not investigated changing the values of a number of input parameters, including the dust-to-gas ratio, cosmic ray ionization rate and the distance of the knot from the ionizing source, r_k, from their 'standard' values, all of which may affect the resulting molecular emission. Aleman et al. (2011) found that increasing the dust-to-gas mass ratio by an order of magnitude resulted in a $\sim$ 20 per cent increase in H_2 2.12 μm surface brightness in their models of cometary knots in NGC 7293. As this increase is most likely due to the increased H_2 formation rate on dust grains (Aleman and Gruenwald 2011), other molecules are unlikely to be as strongly affected, and it is not enough to remove the need for the EUV flux. Similarly, we find increasing the cosmic ray ionization rate by a factor of 100 has little effect except for a moderate increase in the OH^+ surface brightness for the lowest T_* models - with the inclusion of the EUV flux, the effects are negligible in all models.

Aleman et al. (2011) also found that the knot size, r_k, has an impact on the H_2 emission, which presumably applies to other molecules as well. The results shown in Aleman et al. (2011) suggest that the H_2 surface brightness (for a given set of knot parameters) does not vary enormously with distance, unless the knot is beyond the ionization front, at which point it decreases rapidly. Our value of $r_k = 0.2$ pc is within the nebular ionization front radius for all central star parameters investigated. Reducing r_k to 0.1 pc for the 100 $L_\odot$ 120 kK model, we find the H_2, OH^+, ArH^+ and HeH^+ surface brightnesses all increase by a factor of ~ 2, while the CO surface brightness decreases by a similar factor. Aleman et al. (2011) also found that in some cases the H_2 surface brightness decreases with r_k below a certain radius, presumably due to the increased UV flux dissociating the molecules. This behaviour might also be expected for OH^+, ArH^+ and HeH^+, although as discussed in Section 3.4.2, this is not treated in our models due to the non-inclusion of EUV photodissociation for these molecules.

3.4.4 Shock heating and fluorescent emission

With the inclusion of EUV photons, our models predict H_2 surface brightnesses for $T_* \geq 80\,\mathrm{kK}$ within a factor of a few of the lowest values observed in PNe (Hora et al. 1999). However, H_2 2.12 μm emission is observed in PNe with a much wider range of central star temperatures, down to 48 kK for NGC 40 (Hora et al. 1999; Ueta et al. 2014), and many PNe have surface brightnesses far higher than the values we obtain. This suggests that an additional source of H_2 emission is present in actual PNe which is missing from our models.

We assume that the PN knots are in thermal equilibrium, with the heating from the incident radiation field balanced by cooling from line emission and gas-grain interactions. H_2 emission can, however, be produced in the shocked region produced by the interaction of nebular material with the AGB wind from earlier evolutionary stages (Natta and Hollenbach 1998), in which case the gas may be heated to higher temperatures. Otsuka et al. (2017) proposed that the H_2 emission from NGC 6781 - one of the PNe with an OH^+ detection - is in fact due to shock heating, which they modelled by setting a minimum gas temperature. Table 3.5 lists observed molecular line surface brightnesses for NGC 6781 and NGC 7293, a PN with similar central star properties to those used by Otsuka et al. (2017) (100 $L_\odot$, 120 kK; Henry et al. 1999) but with H_2 emission which does not appear to be caused by shocks (O'Dell et al. 2007), along with predicted values from three PDR models with these central star parameters - our initial model (without any incident EUV radiation), the same model including the EUV flux and a model with both EUV flux and a minimum temperature $T_{\mathrm{min}} = 1500\,\mathrm{K}$ (Otsuka et al. 2017 used $T_{\mathrm{min}} = 1420\,\mathrm{K}$ for NGC 6781).

The initial model fails to reproduce the observed surface brightness of any line for both PNe, although the values for ArH^+ and HeH^+ are consistent with the non-detection of these lines. The EUV model is at worst within a factor of a few of observed surface brightnesses in NGC 7293 for H_2, CO and OH^+, but predicts much lower H_2 and CO surface brightnesses than observed in NGC 6781. Aleman et al. (2011) also modelled the H_2 emission from the cometary knots in NGC 7293, and found surface brightnesses in good agreement with observed values, without incorporating shock heating, assuming the knot is seen edge on and integrating the peak emissivity over knot depths of order $\sim 0.001\,\mathrm{pc}$. If we adopt this approach, rather than integrating the emissivity through the knot, we find

Table 3.5: Observed line surface brightnesses for NGC 7293 and NGC 6781, and models with $L_* = 100\,\mathrm{L}_\odot$ and $T_* = 120\,\mathrm{kK}$. Details of models are described in the text. Surface brightnesses are in $\mathrm{erg\,cm^{-2}\,s^{-1}\,sr^{-1}}$. Observed values are from Aleman et al. (2011) (H_2) and Etxaluze et al. (2014) (CO, OH^+, ArH^+) for NGC 7293, and Otsuka et al. (2017) (H_2, CO) and Aleman et al. (2014) (OH^+, ArH^+, HeH^+) for NGC 6871.

Model	H_2 2.12 μm	CO $J = 4-3$	OH^+ 971 GHz	ArH^+ 617 GHz	HeH^+ 149 μm
NGC 7293	$0.9 - 3.7 \times 10^{-5}$	$0.7 - 2.0 \times 10^{-7}$	$4.1 - 9.3 \times 10^{-7}$	$\lesssim 4 \times 10^{-8}$	-
NGC 6781	2.7×10^{-4}	3.7×10^{-7}	$4.3 - 4.7 \times 10^{-7}$	$\lesssim 5 \times 10^{-8}$	$\lesssim 9 \times 10^{-7}$
Initial	7.7×10^{-17}	3.4×10^{-8}	4.2×10^{-10}	2.5×10^{-12}	9.5×10^{-12}
EUV	3.8×10^{-6}	4.2×10^{-8}	6.6×10^{-7}	1.8×10^{-8}	2.1×10^{-6}
T_{min}	9.0×10^{-4}	2.3×10^{-5}	1.1×10^{-6}	1.8×10^{-8}	2.1×10^{-6}

a 2.12 μm surface brightness of $1.3 \times 10^{-5}\,\mathrm{erg\,cm^{-2}\,s^{-1}\,sr^{-1}}$, within the range of observed values. The T_{min} model predicts H_2 and OH^+ surface brightnesses somewhat higher than observed in NGC 6871, while the CO $J = 4-3$ line is ~ 100 times stronger than observed. The H_2 surface brightness is significantly higher than for NGC 7293 and for all of our other models, and is of the same order as the highest values observed in PNe (Hora et al. 1999), suggesting that the emission from these object may originate from shocked gas. Akras et al. (2017) found higher H_2 surface brightnesses (up to $10^{-3}\,\mathrm{erg\,cm^{-2}\,s^{-1}\,sr^{-1}}$) in K $4-47$, which they suggest shows evidence of shock interactions. The ArH^+ and HeH^+ surface brightnesses are unchanged by the imposition of a minimum temperature. The ArH^+ 617 GHz surface brightness is below the detection threshold for both models, while the HeH^+ 149 μm surface brightness is higher.

An alternative excitation mechanism for H_2 line emission is fluorescence following the absorption of UV photons (Sternberg and Dalgarno 1989), a mechanism which is not treated by UCL_PDR as this requires a more detailed treatment of the wavelength-dependent radiative transfer than is currently included. O'Dell et al. (2007) found that in the case of NGC 7293, fluorescence caused by non-ionizing UV photons (in the range $912-1100$ Å) is an implausible mechanism for producing the observed H_2 emission, as too great a proportion of the flux must be reprocessed. For $\log g = 7.0$, the $T_* = 50\,\mathrm{kK}$ model atmosphere emits the highest proportion of its flux in this range, about 0.14, while for higher T_* this decreases to $\lesssim 0.03$. The unattenuated flux at 0.2 pc from a $100\,\mathrm{L}_\odot$ central star is $0.08\,\mathrm{erg\,cm^{-2}\,s^{-1}}$, so the maximum possible energy available to power fluorescence for $T_* = 50\,\mathrm{kK}$ is $0.01\,\mathrm{erg\,cm^{-2}\,s^{-1}}$. A 2.12 μm line surface brightness of $10^{-5}\,\mathrm{erg\,cm^{-2}\,s^{-1}\,sr^{-1}}$ (the lowest observed values from Hora et al. (1999)) would require $\sim 10^{-4}\,\mathrm{erg\,cm^{-2}\,s^{-1}}$ if the emission is powered by fluorescence, corresponding to

only 1% of the available flux, suggesting that H_2 emission from PN with $T_* \lesssim 100\,\mathrm{kK}$ could plausibly originate from this mechanism. For higher T_*, the lower flux in the range producing fluorescence means that the criticisms of O'Dell et al. (2007) still stand, and the highest H_2 surface brightnesses observed in PNe seem incapable of being produced by this mechanism.

3.4.5 Non-detections of OH^+

In the sample of Aleman et al. (2014), all the PNe with OH^+ detections have central star temperature $T_* \gtrsim 100\,\mathrm{kK}$. However, two PNe listed as having central star temperatures in this range, NGC 7027 and Mz 3, are not detected in OH^+. Aleman et al. (2014) suggested that the high (2.3) C/O ratio in NGC 7027 may explain the non-detection of OH^+, as the available oxygen is locked up in CO molecules. Increasing the carbon abundance and reducing the oxygen abundance to 6×10^{-4} and 2×10^{-4} respectively, our $100\,\mathrm{L}_\odot$, 120 kK model predicts an OH^+ surface brightness of $2.4 \times 10^{-7}\,\mathrm{erg\,cm^{-2}\,s^{-1}\,sr^{-1}}$, only slightly reduced from the original value of $6.6 \times 10^{-7}\,\mathrm{erg\,cm^{-2}\,s^{-1}\,sr^{-1}}$. This reflects the lower oxygen abundance rather than any locking-up of the oxygen, as the OH^+ emission originates in the ionized/PDR region where the CO abundance is low. The lack of observed OH^+ emission in NGC 7027 is therefore unlikely to be due to the C/O ratio, and may instead be due to the smaller nebular radius (0.03 pc compared to ~ 0.1 pc for PNe with OH^+ detections), and its very high central star luminosity ($10^4\,\mathrm{L}_\odot$; Middlemass 1990) which would imply a much higher flux of UV photons in the knot and therefore a higher photodissociation rate for OH^+. This could also account for the non-detection of ArH^+ and HeH^+ in this PN, which was in apparent conflict with the predictions of our models. Mz 3 was listed by Aleman et al. (2014) as having $T_* = 107\,\mathrm{kK}$, citing Phillips (2003). However, a number of other authors have estimated a much lower central star temperature of $32 - 36\,\mathrm{kK}$ (Cohen et al. 1978; Zhang and Liu 2002; Smith 2003), for which our models predict no detectable OH^+ emission.

Our models with $T_* = 80\,\mathrm{kK}$ predict OH^+ surface brightnesses similar to those with $T_* = 100\,\mathrm{kK}$. However, of the three PNe listed by Aleman et al. (2014) as having T_* in the range of $80 - 90\,\mathrm{kK}$, none have OH^+ detections. All three PNe (NGC 3242, NGC 7009 and NGC 7026) are highly luminous ($L_* \sim 2000 - 5000\,\mathrm{L}_\odot$; Frew 2008), and have ionized radii of ~ 0.1 pc, smaller than assumed in our low luminosity models, so the increase in the UV flux, and therefore the photodissociation rates, will be very substantial, accounting

for their lack of detectable molecular line emission.

3.4.6 ArH^+ and HeH^+ emission

Our EUV models all predict HeH^+ surface brightnesses at or above detection thresholds, and our models with $T_* = 150\,\mathrm{kK}$ also predict detectable levels of ArH^+ emission, despite neither molecule having yet been detected in PNe. HeH^+ has previously been predicted to form in detectable quantities in PNe (e.g. Cecchi-Pestellini and Dalgarno 1993), while ArH^+ is known to be present in mainly atomic regions with low H_2 abundances and a suitable ionization source (Schilke et al. 2014; Priestley et al. 2017), conditions which certainly apply to the surface regions of knots in PNe.

In models for the clumps in the Crab Nebula (Priestley et al. 2017), it was found that the predicted equilibrium level of HeH^+ emission was large enough to have been detected in Herschel PACS spectra. However, the formation timescale for HeH^+ was found to be significantly larger than the age of the Crab, suggesting that the assumption of chemical equilibrium can lead to an overestimate for the molecule's abundance. The formation timescacle for ArH^+, by contrast, is short enough that the assumption of equilibrium is justified. Figure 3.18 shows the formation timescales for HeH^+, OH^+ and ArH^+ versus distance into a knot at a distance of 0.2 pc, for the 150 kK, $1000\,L_\odot$ EUV model. The abundances of all three molecules drop off beyond $\sim 10^{15}\,\mathrm{cm}$, which combined with the lower temperature means that there is no significant emission beyond this point. The formation timescales in this region for ArH^+ and OH^+ are similar, of order a few to ten years, whereas for HeH^+ the timescale is much larger ($\tau_{\mathrm{form}} \sim 300 - 1000\,\mathrm{yr}$). Given typical ages of these old PNe (> 1000 yr; Ueta et al. (2014)), this is unlikely to be long enough to significantly reduce the abundance of these species. A possible explanation is the EUV field - as discussed in Section 3.4.2, photodissociation by EUV photons is not treated by our models. The inclusion of the EUV flux would therefore be expected to reduce the abundances of both molecules, potentially reducing the emission to below the detection threshold.

3.4.7 Systematic uncertainties

As stated above, neglecting EUV photodissociation is a potentially important omission, particularly as it could counteract the increased OH^+ emission produced by these models due to the higher temperatures and ionization fractions. As the SED of the impinging

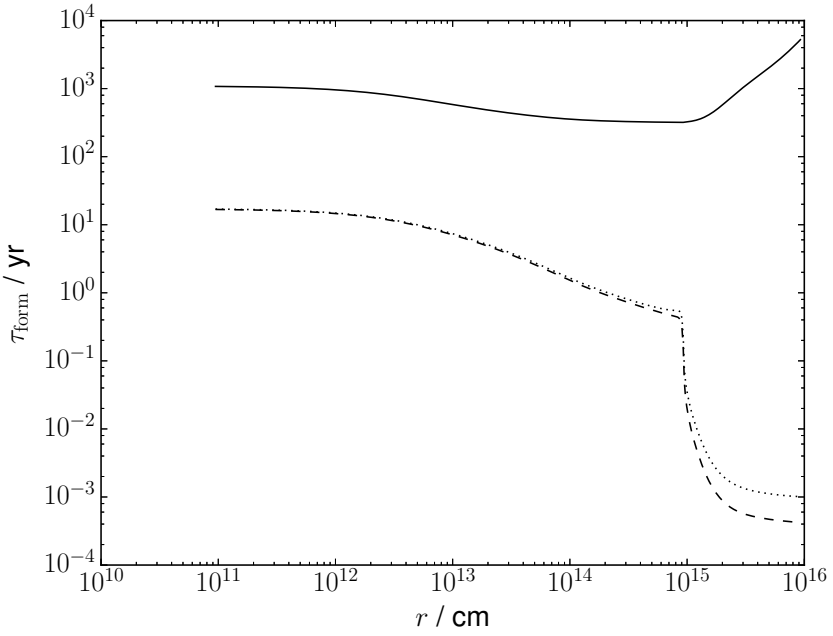

Figure 3.18: Formation timescales versus distance into the knot for HeH^+ (solid line), OH^+ (dashed line) and ArH^+ (dotted line), for the 150 kK 1000 $L_\odot$ $\log g = 7.0$ EUV model.

radiation field, and the photodissociation cross-sections for OH^+, ArH^+ and HeH^+, are known, the rates could in principle be calculated in UCL_PDR, which would require 'X-ray' interactions with molecules to be added to the code. EUV photons could also be important for the photodissociation rate of H_2, although this would be more complicated to incorporate as H_2 is primarily destroyed by line absorption and as such depends on the level populations. Regardless of these effects, however, our main conclusion - that the observed surface brightnesses can only be explained by a dense, high temperature layer at the surfaces of knots - is unlikely to be affected, as in purely radiatively heated gas there seems to be no other way to generate the required emissivities.

3.5 Conclusions

We have performed combined photoionization and PDR modelling of PN cometary knots, for a range of central star parameters and gas densities. Our initial PDR models fail to reproduce the observed H_2 and OH^+ surface brightnesses for PNe with $T_* < 150$ kK. Only by including the ionizing UV flux from the central star do the models predict surface brightnesses for $T_* \geq 100$ kK consistent with the values observed in PNe. Predicted OH^+ column densities are $\gtrsim 10^{12}$ cm^{-2}, significantly larger than those derived from observa-

tions assuming LTE, but in agreement with previous modelling work (Otsuka et al. 2017). Predicted H_2 surface brightnesses are somewhat lower than observed values, and our models do not explain the highest emission strengths observed in PNe, or the detection of H_2 emission in PNe with cooler ($T_* < 80\,\mathrm{kK}$) central stars. The presence of shocks may be capable of producing the higher H_2 surface brightnesses observed, while fluorescence due to excitation by UV photons could be a viable source of H_2 emission for nebulae with central star temperatures below 50 kK. Our models predict HeH^+ (and, for $T_* = 150\,\mathrm{kK}$, ArH^+) line surface brightnesses potentially above detection thresholds, despite neither molecule having been detected in PNe. As photodissociation by EUV photons is not treated for either molecule, the true surface brightnesses may be significantly lower than our predicted values if this is an important destruction mechanism.

This page was intentionally left blank

Chapter 4

ArH^+ emission from the Crab Nebula

The work in this chapter is based on Priestley et al. (2017), with M. J. Barlow and S. Viti. The models have been updated following the publication of a calculated reaction rate for the dissociative recombination of ArH^+ (Abdoulanziz et al. 2018). The photoionization modelling has also been changed to the method presented in Chapter 3, and additional coolants (Si^+ and Fe^+) added to the PDR models.

4.1 Introduction

Argonium (ArH^+), the first noble gas molecule discovered in space, was detected by Barlow et al. (2013) in emission in the J=1-0 and J=2-1 transitions in the Crab Nebula, along with an OH^+ transition at 971 GHz. The Crab Nebula is a young supernova remnant (SNR), consisting of a central pulsar wind nebula (PWN) and a surrounding network of filaments ionised by the PWN synchrotron emission (Hester 2008). Molecular hydrogen (H_2) (Graham et al. 1990; Loh et al. 2010, 2011, 2012) emission had previously been detected in the Crab Nebula, with modelling by Richardson et al. (2013) suggesting it originates from a trace molecular component in mostly atomic gas, shielded from ionising radiation at the centre of the filaments. Barlow et al. (2013) noted that ArH^+ is principally formed by the reaction $Ar^+ + H_2 \rightarrow ArH^+ + H$ (Roach and Kuntz 1970), while the main

destruction mechanism is $ArH^+ + H_2 \rightarrow Ar + H_3^+$ (Schilke et al. 2014).

Since its discovery in the Crab Nebula, ArH^+ has been found to be a fairly common molecule in the interstellar medium (ISM). Schilke et al. (2014) reported ArH^+ J=1-0 absorption at a range of velocities along several galactic sightlines, while Müller et al. (2015) detected ArH^+ absorption from a foreground galaxy in the spectrum of a lensed blazar. Schilke et al. (2014) found the interstellar ArH^+ abundance to be uncorrelated with the abundances of the molecular gas tracers HF and H_2O^+, while chemical modelling of ArH^+ in the ISM by Schilke et al. (2014) and Neufeld and Wolfire (2016) showed that it traces gas where the hydrogen is almost entirely atomic. ArH^+ was predicted to peak in abundance at the edges of interstellar clouds, where the ultraviolet (UV) radiation field is strongest.

Since their discovery in the ISM, hydride ions including ArH^+ and OH^+ have been used to investigate the molecular hydrogen fraction (Neufeld et al. 2010; Neufeld and Wolfire 2016) and the cosmic ray ionization rate (Neufeld and Wolfire 2017), as their abundances are highly sensitive to both quantities. The detection of these two molecules in the Crab Nebula allows a similar analysis of these properties to be undertaken: Barlow et al. (2013) additionally used the ArH^+ lines to constrain the isotopic ratios of argon in the Crab, with implications for nucleosynthesis models. The Crab Nebula, shown in Figure 4.1 in a combined optical-infrared image, is a substantially different environment to the interstellar clouds considered by Schilke et al. (2014). The PWN is a strong source of synchrotron radiation, including X-rays, which behave very differently to the UV radiation in the interstellar case. Additionally, the filaments must be permeated by the high energy charged particles which produce the synchrotron radiation, equivalent to but much more intense than the cosmic rays included in ISM astrochemical modelling. Both can provide an additional source of Ar^+, potentially allowing more ArH^+ to be formed, while the strong radiation field and generally harsh environment would tend to destroy molecules. This chapter presents models of the chemistry of ArH^+ under the conditions present in the Crab Nebula, with the goal of reproducing the observed emission.

4.2 Method

As in Chapter 3, we determine the incident radiation field on a clump of material in the Crab Nebula using MOCASSIN (Ercolano et al. 2003, 2005, 2008) modelling of the ionized

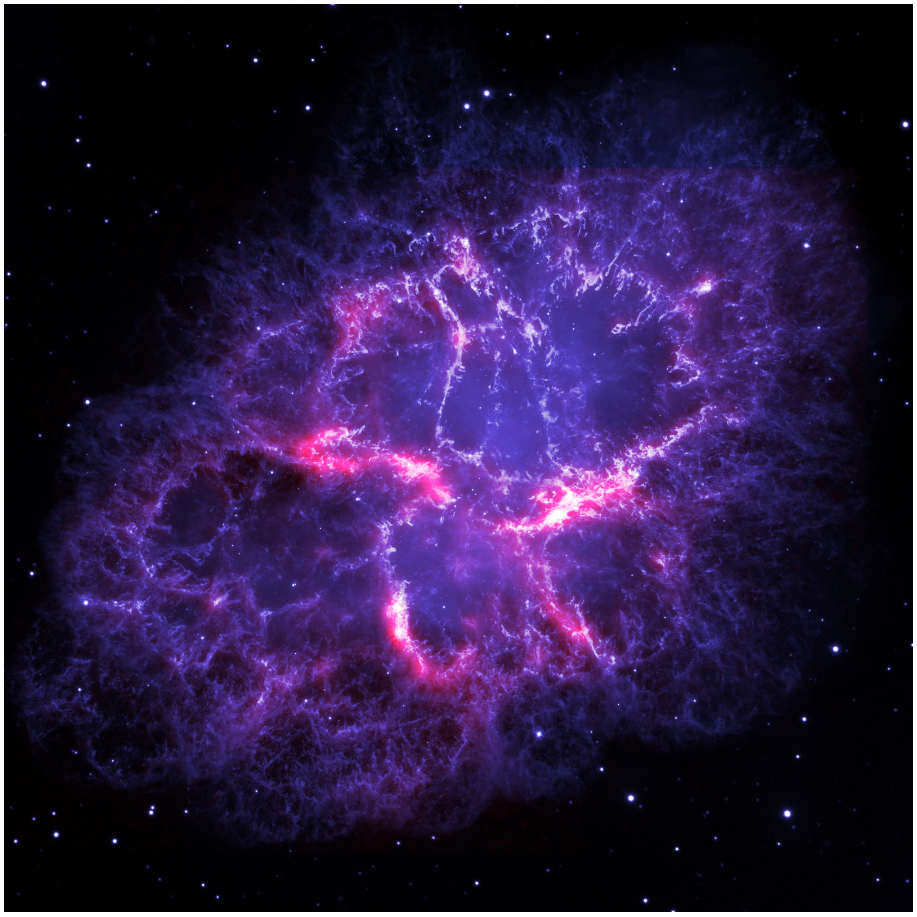

Figure 4.1: Composite image of the Crab Nebula, from combined Hubble Space Telescope optical emission line (blue-white) and Herschel Space Observatory 70 μm (red) images. The image dimensions are 5.65 × 5.65 arcmin. Taken from Owen and Barlow (2015).

gas. We take the gas elemental abundances and dust properties from Owen and Barlow (2015), using their model VI with amorphous carbon grains. The adopted elemental abundances are listed in Table 4.1 - for the three clumped models of Owen and Barlow (2015), which those authors considered most realistic, the elemental abundances do not vary significantly, although for their model IV the argon abundance is a factor of 5 larger than the value of 1×10^{-5} we adopt here. We also include silicon and iron at solar abundance, due to their potential importance as coolants (Richardson et al. 2013). Our photoionization model is a sphere of gas and dust with a radius of 2.5 pc, gas number density $n_{\rm H} = 10\,{\rm cm}^{-3}$ and a dust-to-gas mass ratio of 0.036. We treat the PWN as a point source with a total luminosity of $1.3 \times 10^{38}\,{\rm erg\,s}^{-1}$ (Owen and Barlow 2015), with the input SED from Hester (2008). From the transmitted SED, we find an incident FUV field of 57.5 Draine (Draine 1978) and an ionizing radiation (< 912 Å) flux of $0.531\,{\rm erg\,cm}^{-2}\,{\rm s}^{-1}$. The SED below 912 Å is fitted with a three-component power law.

Table 4.1: Gas phase elemental abundances, relative to hydrogen, used in PDR modelling, taken from model IV of Owen and Barlow (2015).

Element	Abundance	Element	Abundance
H	1.00	Ne	4.9×10^{-3}
He	1.85	Si	3.0×10^{-5}
C	1.02×10^{-2}	S	4.5×10^{-5}
N	2.5×10^{-4}	Ar	1.0×10^{-5}
O	6.2×10^{-3}	Fe	3.0×10^{-5}

We model the clump using UCL_PDR as a one-dimensional slab with the radiation fields from MOCASSIN incident on one side. We run models with number densities of 2×10^3, 2×10^4 and $2 \times 10^5\,\mathrm{cm}^{-3}$, with thicknesses of 0.2, 0.02 and 0.002 pc so that the column density is the same for all models. Owen and Barlow (2015) required clump densities of $1900\,\mathrm{cm}^{-3}$ to fit observed line and SED fluxes, while Loh et al. (2012) determined a lower limit of $2 \times 10^4\,\mathrm{cm}^{-3}$ in the H_2-emitting regions. We modify UCL_PDR in order to account for the Crab Nebula's higher dust-to-gas mass ratio (0.036) compared to the ISM, which affects H_2 formation on grain surfaces and dust photoelectric heating rates, and use an A_V/N_H ratio of $2.26 \times 10^{-21}\,\mathrm{mag\,cm}^2$, increased from typical ISM values by the same factor, giving a total clump extinction of 2.8 mag. We used the cosmic ray heating rate from CLOUDY (Ferland et al. 1998), more appropriate for significantly ionized gas than the default rate from Goldsmith (2001), which only accounts for ionization of H_2 molecules, and the X-ray heating effiencies for pure helium (the most abundant element in the Crab Nebula) from Dalgarno et al. (1999). We use the chemical network described in Chapter 3, including ArH^+ and HeH^+.

The PWN at the centre of the Crab Nebula produces a flux of relativistic particles, which may have significant effects on the properties of the gas. This can be modelled as an increase in the cosmic ray ionization rate ζ, which has been proposed to account for the observed H_2 line emission strength by Graham et al. (1990) and Richardson et al. (2013). We repeat our models with values of ζ between 10^4 and $10^8\zeta_0$, where $\zeta_0 = 1.3 \times 10^{-17}\,\mathrm{s}^{-1}$ is the standard ISM value for the cosmic ray ionization rate, the minimum and maximum values suggested by Richardson et al. (2013).

4.3 Results

We ran models with varying densities and cosmic ray ionization rates, as listed in Table 4.2. The resulting gas properties and emission line fluxes are discussed in the following

Table 4.2: Model name, cloud size, density and cosmic ray ionization rate for UCL_PDR models.

Name	d/ pc	n_{H}/ cm^{-3}	ζ/ζ_0
D3Z0	0.2	2×10^3	1
D3Z4	0.2	2×10^3	10^4
D3Z5	0.2	2×10^3	10^5
D3Z6	0.2	2×10^3	10^6
D3Z7	0.2	2×10^3	10^7
D3Z8	0.2	2×10^3	10^8
D4Z0	0.02	2×10^4	1
D4Z4	0.02	2×10^4	10^4
D4Z5	0.02	2×10^4	10^5
D4Z6	0.02	2×10^4	10^6
D4Z7	0.02	2×10^4	10^7
D4Z8	0.02	2×10^4	10^8
D5Z0	0.002	2×10^5	1
D5Z4	0.002	2×10^5	10^4
D5Z5	0.002	2×10^5	10^5
D5Z6	0.002	2×10^5	10^6
D5Z7	0.002	2×10^5	10^7
D5Z8	0.002	2×10^5	10^8

section.

4.3.1 Cloud properties

Figure 4.2 shows the gas temperature and abundances of H, H_2, e^-, ArH^+ and OH^+ for D4Z0. The ArH^+ abundance shows the same behaviour as the ISM model of Schilke et al. (2014), decreasing as the molecular hydrogen fraction rises as ArH^+ is readily destroyed by the reaction $ArH^+ + H_2 \rightarrow Ar + H_3^+$. The ArH^+ abundance is an order of magnitude larger than in the ISM, however, due to the added production of Ar^+ ions by the X-ray flux. OH^+, the other molecular ion detected in the Crab Nebula, follows a different trend - it is more readily destroyed by UV photons than ArH^+, so the abundance initially increases with depth as the photodissociation rate decreases, before falling once reactions with H_2 become the dominant destruction mechanism.

Figure 4.3 shows the same information for model D4Z7. At this level, cosmic ray effects dominate both the gas heating and much of the chemistry, and as our model does not attenuate the flux the cloud properties do not change significantly with depth. The H_2 abundance decreases to 10^{-4}, while the OH^+ and ArH^+ abundances are higher, along with the ionization fraction of the gas. Under these conditions the dominant destruction

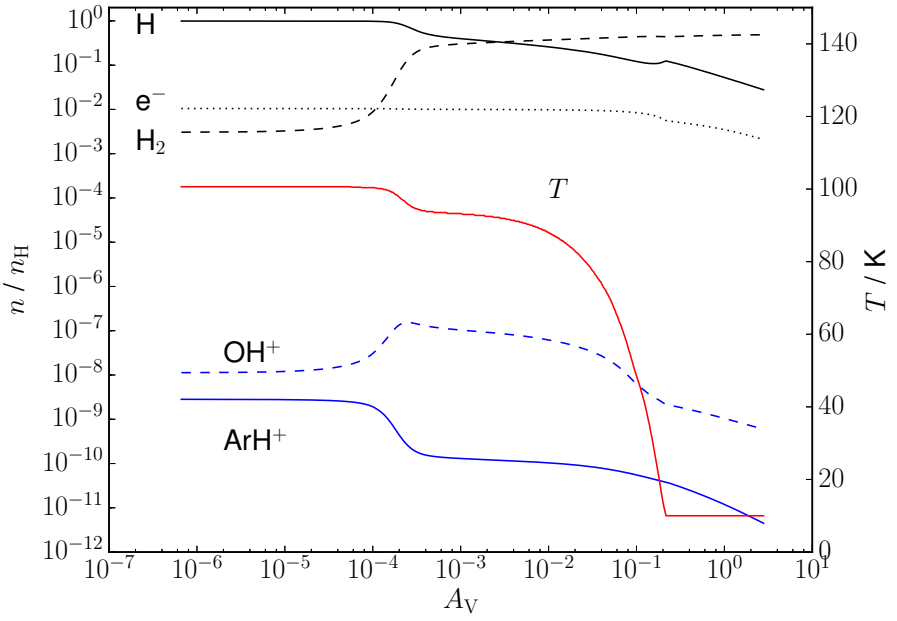

Figure 4.2: Abundances of H (solid black line), H_2 (dashed black line), e^- (dotted black line), ArH^+ (solid blue line) and OH^+ (dashed blue line), and gas temeperature (solid red line) for the $n_H = 2 \times 10^4\,cm^{-3}$, $\zeta = \zeta_0$ model. The abundance scale is on the left axis, the temperature scale on the right.

mechanism for both molecular ions is dissociative recombination with electrons.

The same trends occur in lower and higher density models - increasing cosmic ray ionization rates lead to higher temperatures, lower H_2 and higher OH^+/ArH^+ abundances and higher ionization fractions. Increasing density has the opposite effect, resulting in lower temperatures and less ionized, more molecular gas for the same ζ. Gas temperatures range from 120 K, falling to the temperature limit of 10 K at high A_V, for D5Z0, to $> 10^4$ K for D3Z8. The corresponding ionization fractions are $\sim 10^{-3}$ and 1.2, while H_2 abundances at the cloud edge are between $10^{-6} - 10^{-2}$.

4.3.2 Herschel SPIRE FTS observations

Figure 4.4 shows the ArH^+ $J = 1-0$ 617 GHz line surface brightness versus ζ. The surface brightness initially increases with ζ due to higher gas temperatures and the increased production of Ar^+ by cosmic ray ionization, before falling as the higher electron density increases the rate of dissociative recombination. Cosmic ray ionization rates of $10^6\zeta_0$ or higher are required to reach surface brightnesses consistent with than those found by Barlow et al. (2013). The $J = 2 - 1$ 1234 GHz line shows similar behaviour to the

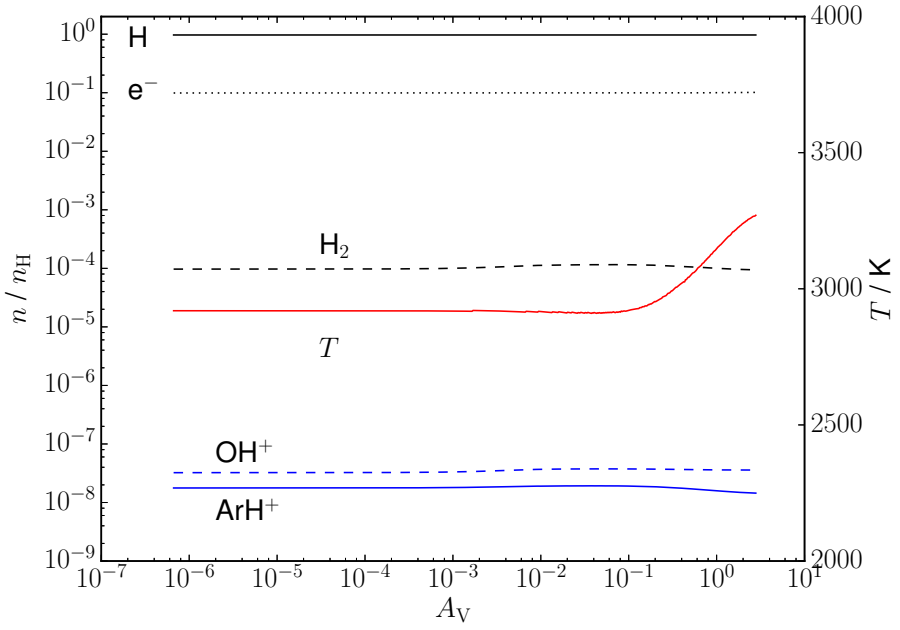

Figure 4.3: Abundances of H (solid black line), H_2 (dashed black line), e^- (dotted black line), ArH^+ (solid blue line) and OH^+ (dashed blue line), and gas temeperature (solid red line) for the $n_H = 2 \times 10^4\,cm^{-3}$, $\zeta = 10^7\zeta_0$ model. The abundance scale is on the left axis, the temperature scale on the right.

$J = 1 - 0$ line, with a cosmic ray ionization rate $\geq 10^6\zeta_0$ required to produce sufficient ArH^+ emission to match the observations.

Figure 4.5 shows the OH^+ 971 GHz line surface brightness versus ζ. The cosmic ray ionization rates required to reproduce the ArH^+ observations lead to OH^+ emission significantly in excess of the values observed. For $n_H = 2 \times 10^3\,cm^{-3}$, the predicted surface brightness is higher than the maximum observed value for all values of ζ. Models with $\zeta \geq 10^6\zeta_0$ also predict significant ($> 10^7\,erg\,cm^{-2}\,s^{-1}\,sr^{-1}$) surface brightnesses for the OH^+ transitions at 909 and 1033 GHz, neither of which was detected by Barlow et al. (2013). Two undetected [C I] transitions which fall in the Herschel SPIRE FTS frequency range, at 492 and 809 GHz, are also predicted to have large surface brightnesses. Figure 4.6 shows the [C I] 809 GHz surface brightness versus ζ - the predicted surface brightness is above the adopted detection threshold of $10^{-7}\,erg\,cm^{-2}\,s^{-1}\,sr^{-1}$ for all models, and is far higher for $\zeta < 10^6\zeta_0$. The SPIRE FTS frequency range also covers CO rotational transitions from $J = 4-3$ to $J = 13-12$, but for $\zeta \geq 10^6\zeta_0$ these have surface brightnesses below $10^{-8}\,erg\,cm^{-2}\,s^{-1}\,sr^{-1}$ in our models, well below the detection threshold.

In order to reduce the line surface brightnesses to within observational limits, we

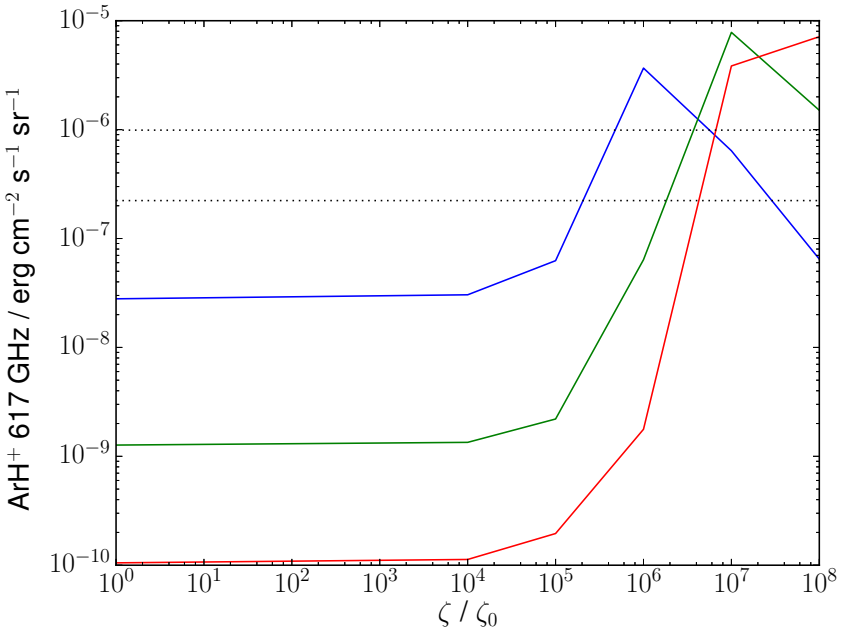

Figure 4.4: ArH$^+$ 617 GHz surface brightness versus ζ, for models with $n_{\rm H} = 2 \times 10^3$ (blue), 2×10^4 (green) and $2 \times 10^5\,{\rm cm}^{-3}$ (red). The dotted horizontal lines show the observed range of values from Barlow et al. (2013).

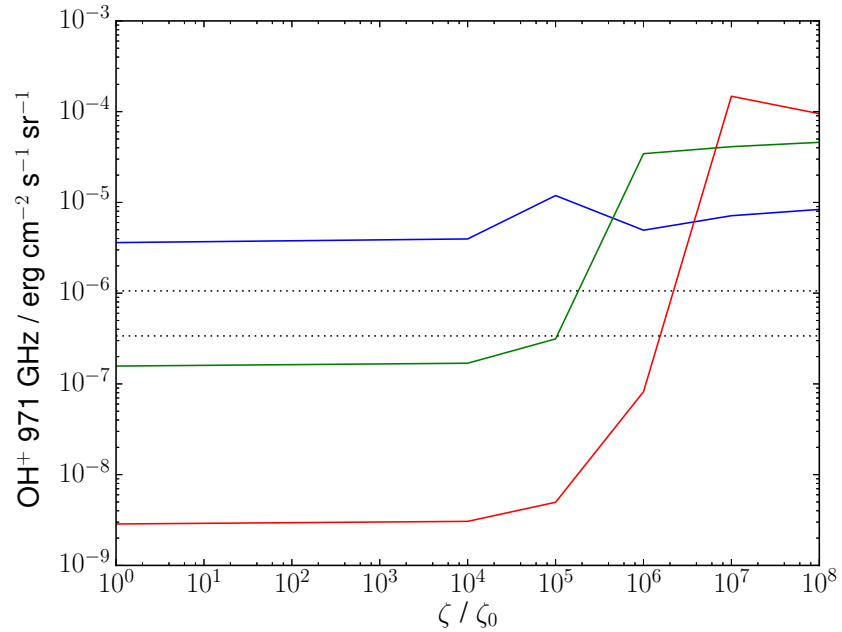

Figure 4.5: OH$^+$ 971 GHz surface brightness versus ζ, for models with $n_{\rm H} = 2 \times 10^3$ (blue), 2×10^4 (green) and $2 \times 10^5\,{\rm cm}^{-3}$ (red). The dotted horizontal lines show the observed range of values from Barlow et al. (2013).

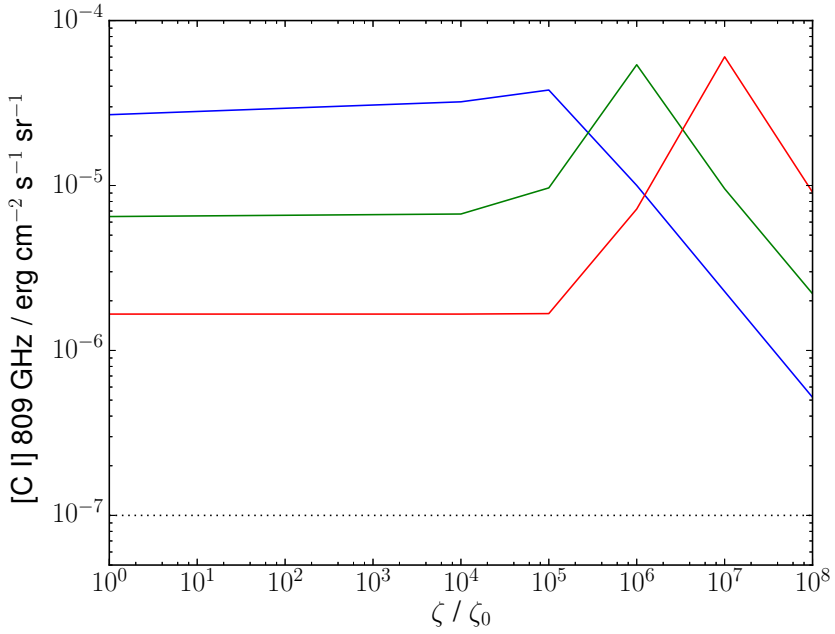

Figure 4.6: [C I] 809 GHz surface brightness versus ζ, for models with $n_{\rm H} = 2 \times 10^3$ (blue), 2×10^4 (green) and $2 \times 10^5\,{\rm cm}^{-3}$ (red). The dotted horizontal lines show the observed upper limit from Barlow et al. (2013).

consider smaller cloud sizes. Figures 4.7, 4.8 and 4.9 show the ArH^+ 617 GHz, OH^+ 971 GHz and [C I] 809 GHz surface brightnesses respectively versus ζ, for clouds with visual extinctions of 0.1 mag, respectively. Three models (D3Z6, D4Z7, D5Z8) produce ArH^+ emission consistent with the observations, although somewhat towards the low end of the range. The OH^+ 971 GHz surface brightnesses are also consistent with observations for these models, although for D5Z8 it is a factor of a few above the highest observed value. While somewhat reduced, the predicted [C I] emission is still above the detection threshold for all three models. This differs from the situation found by Priestley et al. (2017), where the dissociative recombination rate was fixed to $10^{-11}\,{\rm cm}^3\,{\rm s}^{-1}$ in order to reproduce observations - using the calculated rate from Abdoulanziz et al. (2018), which rises to $> 10^{-10}\,{\rm cm}^3\,{\rm s}^{-1}$ at $\sim 10^3\,{\rm K}$, increasing values of ζ (and therefore temperature and electron density) result in lower ArH^+ abundances than previously found, and lower emissivities.

Our adopted value for the Ar/H ratio, 1×10^{-5}, comes from model IV of Owen and Barlow (2015). However, those authors found that different assumptions about the geometry of the nebula can lead to an increased abundance of 5×10^{-5} (model VI), which would correspondingly increase the strength of the ArH^+ lines. Figure 4.10 shows the

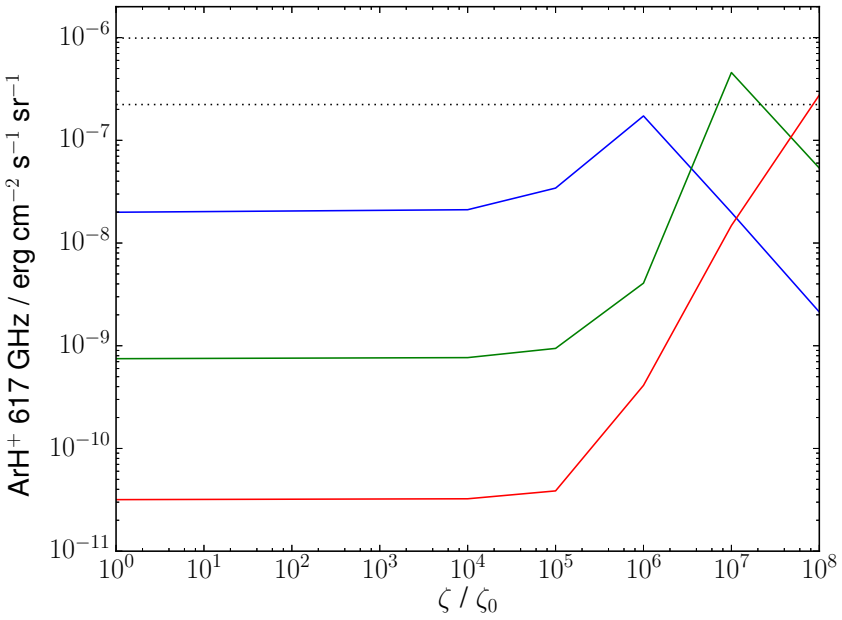

Figure 4.7: ArH$^+$ 617 GHz surface brightness versus ζ, for models with $n_{\rm H} = 2 \times 10^3$ (blue), 2×10^4 (green) and $2 \times 10^5\,{\rm cm}^{-3}$ (red). The dotted horizontal lines show the observed range of values from Barlow et al. (2013). The visual extinction of the cloud is 0.1 mag.

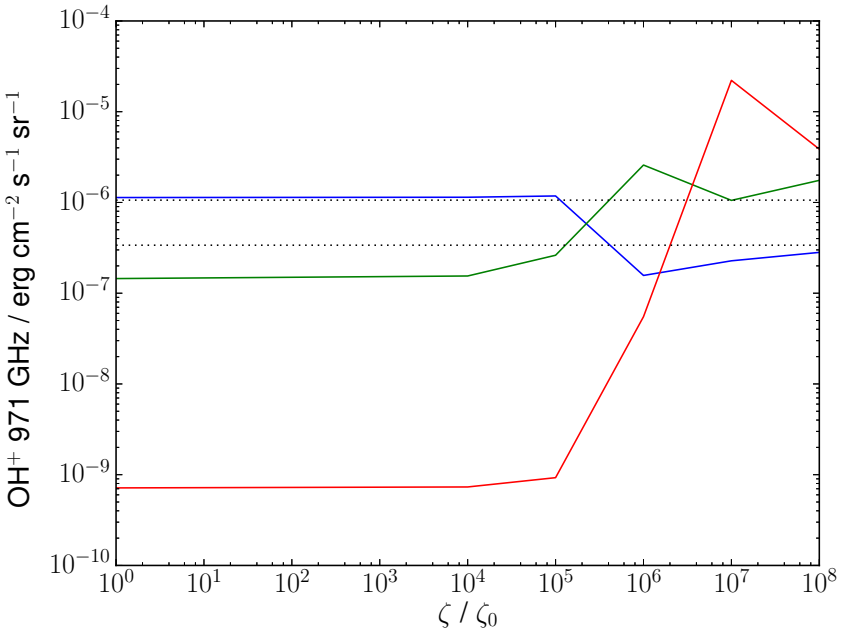

Figure 4.8: OH$^+$ 971 GHz surface brightness versus ζ, for models with $n_{\rm H} = 2 \times 10^3$ (blue), 2×10^4 (green) and $2 \times 10^5\,{\rm cm}^{-3}$ (red). The dotted horizontal lines show the observed range of values from Barlow et al. (2013). The visual extinction of the cloud is 0.1 mag.

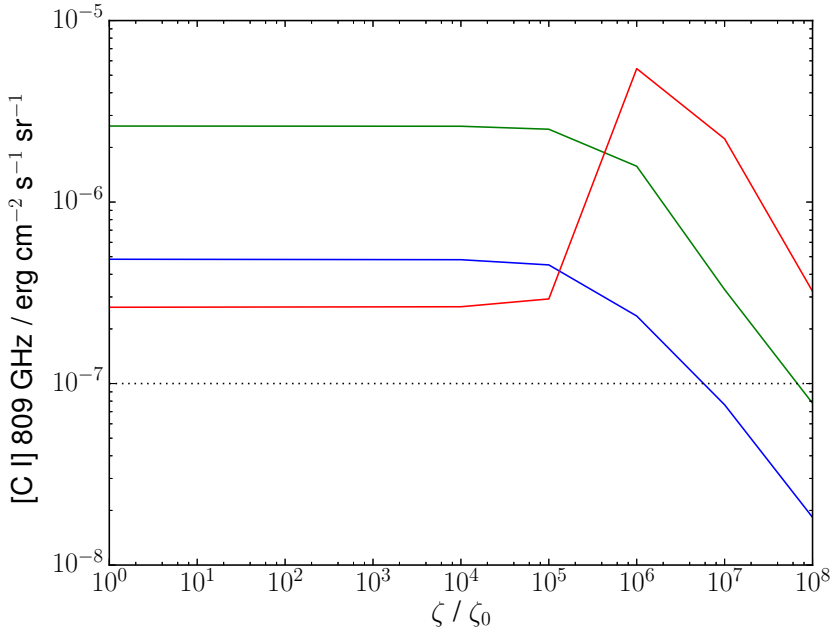

Figure 4.9: [C I] 809 GHz surface brightness versus ζ, for models with $n_{\rm H} = 2\times10^3$ (blue), 2×10^4 (green) and $2 \times 10^5\,{\rm cm}^{-3}$ (red). The dotted horizontal lines show the observed upper limit from Barlow et al. (2013). The visual extinction of the cloud is 0.1 mag.

ArH^+ 617 GHz surface brightness versus ζ for models with ${\rm Ar/H} = 5 \times 10^{-5}$ and a cloud thickness of 0.05 mag. The observed surface brightnesses can be reproduced with a cloud thickness half the previous size, leading to a reduction in the other emission lines. Figure 4.11 shows the [C I] 809 GHz surface brightnesses - models D3Z6, D4Z7 and D5Z8 all predict [C I] emission at or below the detection threshold, and weaker than the ArH^+ line. OH^+ surface brightnesses are also in line with observed values or limits for these models, while CO emission from the rotational transitions in the SPIRE FTS spectral region is $< 10^{-8}\,{\rm erg\,cm^{-2}\,s^{-1}\,sr^{-1}}$.

4.3.3 Other observations

Table 4.3 lists the observed surface brightnesses of various emission lines detected in the Crab Nebula, and the predicted values from models D3Z6, D4Z7 and D5Z8, with cloud thicknesses of 0.1, 0.03 and 0.01 mag respectively. The cloud thicknesses are chosen to reproduce the SPIRE FTS observations as well as possible. The ArH^+ $J = 1 - 0$ line strength is well reproduced by all three models, and models D4Z7 and D5Z8 also have the correct strength for the $J = 2-1$ transition, while D3Z6 predicts a lower surface brightness than $1 - 0$, in conflict with the data. All models predict similar levels of OH^+ emission

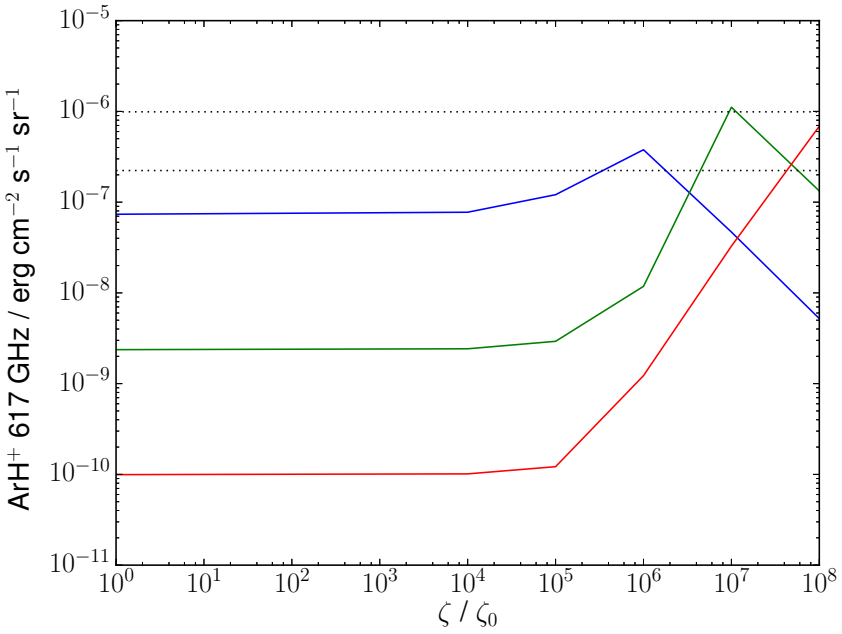

Figure 4.10: ArH$^+$ 617 GHz surface brightness versus ζ, for models with $n_{\rm H} = 2 \times 10^3$ (blue), 2×10^4 (green) and $2 \times 10^5\,{\rm cm}^{-3}$ (red). The dotted horizontal lines show the observed range of values from Barlow et al. (2013). The visual extinction of the cloud is 0.05 mag, and the argon abundance is 5×10^{-5}.

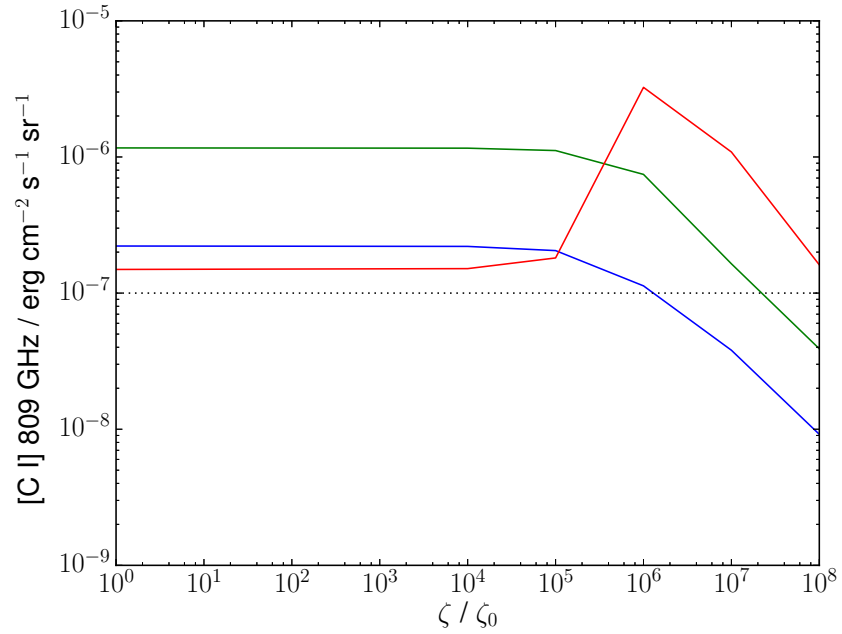

Figure 4.11: [C I] 809 GHz surface brightness versus ζ, for models with $n_{\rm H} = 2 \times 10^3$ (blue), 2×10^4 (green) and $2 \times 10^5\,{\rm cm}^{-3}$ (red). The dotted horizontal lines show the observed upper limit from Barlow et al. (2013). The visual extinction of the cloud is 0.05 mag, and the argon abundance is 5×10^{-5}.

for the three lines of interest, which are consistent with the observations - although the 1033 GHz line has predicted surface brightnesses above our assumed detection threshold of $10^{-7}\,\mathrm{erg\,cm^{-2}\,s^{-1}\,sr^{-1}}$, from inspection of the spectrum in this region from Barlow et al. (2013) it is clear that the predicted emission strength would not produce a clear detection above the continuum noise. The [C I] transitions at 492 and 809 GHz, and the ten CO rotational lines covered by SPIRE FTS, are also predicted to be undetectable.

Gomez et al. (2012) presented Herschel PACS IFU and ISO LWS spectra of the Crab Nebula, including [O I] (63 and 146 μm) and [C II] (158 μm) emission lines. This spectral range also includes two HeH^+ rotational transitions at 149 and 75 μm, which are not detected. The predicted surface brightnesses for all three models are higher than those observed, with only the D5Z8 value for [C II] 158 μm being consistent. Predicted HeH^+ surface brightnesses are consistent with non-detection. Table 4.4 lists the surface brightness ratios from the individual spectra in Gomez et al. (2012) and for our models. The ratio of the two [O I] lines is in good agreement with models D4Z7 and D5Z8, but these models predict a [O I] 146 μm/[C II] 158 μm ratio around twice that observed. The D3Z6 model reproduces the latter ratio well but is somewhat lower for the former. All models predict HeH^+ line strengths well below the nearby [O I] lines, except for the 149 μm transition in model D5Z8, which is still significantly weaker than the 146 μm line.

Forbidden lines from oxygen and carbon have also been observed in the optical and near-infrared in the Crab Nebula. Our models show a uniform trend of increasing surface brightness with density for both the [C I] $9825 + 9850$ Å and [O I] 6300 and 6363 Å transitions. When compared with the observed values (from Rudy et al. (1994) and Richardson et al. (2013) respectively), model D4Z7 correctly reproduces the [C I] emission, and D5Z8 the [O I] lines, but none of our models simultaneously predicts both. D3Z6 has surface brightnesses an order of magnitude lower than observed for both carbon and oxygen lines.

H_2 emission in the Crab Nebula Loh et al. (2010, 2011, 2012) is localised into compact knots, associated with low-ionization gas, with typical surface brightnesses of order $10^{-5}\,\mathrm{erg\,cm^{-2}\,s^{-1}\,sr^{-1}}$ for the 2.12 μm line Loh et al. (2011). Our models predict surface brightnesses $\sim 100\times$ lower than this - the required cloud thickness to produce the observed levels of H_2 emission result in conflicts with the SPIRE FTS data of a similar magnitude. Table 4.5 shows the H_2 rovibrational line ratios relative to the 2.12 μm line from Loh et al. (2012) and our predicted values. The $1-0$ ratios are in reasonable agreement with observations for all models, whereas only the D5Z8 model predicts $2-1$ transition ratios

Table 4.3: Observed and predicted line surface brightnesses for models with Ar/H = 5×10^{-5} and $A_V = 0.1$ (D3Z6), 0.03 (D4Z7) and 0.01 (D5Z8). Surface brightnesses are in erg cm^{-2} s^{-1} sr^{-1}. References are (1) Barlow et al. (2013) (2) Rudy et al. (1994) (3) Gomez et al. (2012) (4) Richardson et al. (2013) (5) Loh et al. (2011).

Line	Obs.	D3Z6	D4Z7	D5Z8	Ref.
ArH^+ 617 GHz	$2.2 - 9.7(-7)$	$8.1(-7)$	$6.7(-7)$	$1.4(-7)$	(1)
ArH^+ 1234 GHz	$1.0 - 3.4(-6)$	$7.3(-7)$	$1.3(-6)$	$1.5(-6)$	(1)
OH^+ 971 GHz	$3.4 - 10.6(-7)$	$1.6(-7)$	$3.2(-7)$	$3.9(-7)$	(1)
OH^+ 1033 GHz	$\lesssim 10^{-7}$	$1.0(-7)$	$2.0(-7)$	$2.6(-7)$	(1)
OH^+ 909 GHz	$\lesssim 10^{-7}$	$3.0(-8)$	$5.9(-8)$	$6.8(-8)$	(1)
[C I] 492 GHz	$\lesssim 10^{-7}$	$2.7(-8)$	$1.1(-8)$	$3.5(-9)$	(1)
[C I] 809 GHz	$\lesssim 10^{-7}$	$2.4(-7)$	$9.9(-8)$	$3.2(-8)$	(1)
CO $J = 4 - 3$	$\lesssim 10^{-7}$	$2.7(-14)$	$8.7(-14)$	$1.9(-13)$	(1)
[C I] $9825 + 9850$ Å	$1.7 - 5.4(-5)$	$3.6(-6)$	$5.4(-5)$	$2.3(-4)$	(2)
[O I] 63 μm	$1.1 - 3.2(-4)$	$1.5(-3)$	$2.7(-3)$	$1.7(-3)$	(3)
[O I] 146 μm	$0.4 - 1.9(-5)$	$1.3(-4)$	$1.2(-4)$	$5.1(-5)$	(3)
[C II] 158 μm	$2.7 - 6.4(-5)$	$6.3(-4)$	$2.0(-4)$	$6.7(-5)$	(3)
HeH^+ 149 μm	$\lesssim 10^{-5}$	$9.6(-7)$	$3.2(-6)$	$6.9(-6)$	(3)
HeH^+ 75 μm	$\lesssim 10^{-5}$	$9.0(-7)$	$3.2(-6)$	$1.0(-5)$	(3)
[O I] 6300 Å	$1.2(-3)$	$4.0(-6)$	$5.6(-5)$	$1.6(-3)$	(4)
[O I] 6363 Å	$4.1(-4)$	$1.3(-6)$	$1.8(-5)$	$5.1(-4)$	(4)
H_2 2.12 μm	$1.0 - 4.8(-5)$	$6.9(-8)$	$2.8(-7)$	$2.2(-7)$	(5)

Table 4.4: Observed (Gomez et al. 2012) and predicted surface brightness ratios for models with Ar/H = 5×10^{-5} and $A_V = 0.1$ (D3Z6), 0.03 (D4Z7) and 0.01 (D5Z8).

Ratio	Obs.	D3Z6	D4Z7	D5Z8
[O I] 63 μm/[O I] 146 μm	$16.4 - 38.7$	11.5	22.5	33.3
[O I] 146 μm/[C II] 158 μm	$0.13 - 0.32$	0.21	0.6	0.76
HeH^+ 149 μm/[O I] 146 μm	$\lesssim 0.1$	0.007	0.03	0.14
HeH^+ 75 μm/[O I] 63 μm	$\lesssim 0.1$	0.0006	0.001	0.006

similar to those observed.

4.4 Discussion

We find that three of our models, with an appropriate choice of cloud thickness, are capable of reproducing the observed SPIRE FTS spectral features. Table 4.6 lists some important physical properties of each model - for the cosmic ray ionization rates required, values do not significantly change with distance into the cloud, so we take the values at the outermost point to be representative of the whole cloud.

Assuming a distance to the Crab Nebula of 2 kpc (Trimble 1968), the H_2 emitting knots observed by Loh et al. (2011) have typical sizes of $\sim 10^{16}$ cm, similar in size to both

Table 4.5: Observed (Loh et al. 2012) and predicted H_2 line surface brightnesses, relative to the 2.12 μm $1-0$ S(1) line, for models with Ar/H $= 5 \times 10^{-5}$ and $A_V = 0.1$ (D3Z6), 0.03 (D4Z7) and 0.01 (D5Z8).

Ratio	Obs.	D3Z6	D4Z7	D5Z8
$1-0$ S(0)	$0.23-0.28$	0.16	0.17	0.19
$1-0$ S(2)	$0.37-0.52$	0.34	0.38	0.43
$2-1$ S(1)	$0.11-0.34$	0.01	0.05	0.30
$2-1$ S(2)	< 0.31	0.004	0.02	0.13
$2-1$ S(3)	< 0.41	0.01	0.07	0.42

Table 4.6: Density, temperature, physical size and H_2 and electron abundances for models D3Z6, D4Z7 and D5Z8, with Ar/H $= 5 \times 10^{-5}$ and $A_V = 0.1$ (D3Z6), 0.03 (D4Z7) and 0.01 (D5Z8).

Model	n_H/ cm^{-3}	T/ K	x/cm	$n(H_2)/n_H$	$n(e^-)/n_H$
D3Z6	2×10^3	2522	2.2×10^{16}	5.6×10^{-5}	0.10
D4Z7	2×10^4	2919	6.8×10^{14}	9.7×10^{-5}	0.09
D5Z8	2×10^5	3847	2.4×10^{13}	7.0×10^{-5}	0.11

our D3Z6 model and the dusty globules observed by Grenman et al. (2017). The globules have visual extinctions in the range $0.2-0.34$ mag, slightly larger than D3Z6 but of the same magnitude. Grenman et al. (2017) found that only $\sim 10\%$ of their globules were associated with an H_2-emitting knot - given that our D3Z6 model does not reproduce the observed surface brightnesses, this could explain the H_2-dark dense material in the Crab. Loh et al. (2012) used H_2 and [S II] line observations to derive the temperature and electron and H_2 densities of the gas in seven H_2-emitting knots. The typical values are $T \approx 3000$ K, $n_H \gtrsim 2 \times 10^4$ cm^{-3} and $n_e \sim 10^3$ cm^{-3}, in excellent agreement with our D4Z7 model. However, this model fails to reproduce the observed H_2 surface brightnesses, so the identification with H_2-emitting knots is somewhat suspect.

Richardson et al. (2013) modelled an H_2 knot in the Crab Nebula with a combined photoionization-PDR code, aiming to explain the observed H_2 emission. They required an additional heating source on top of the radiation field, either an increase in the cosmic ray ionization rate due to charged particles from the PWN, or an injection of mechanical energy, which they modelled as a minimum temperature of 2800 K. Their enhanced ionization rate model corresponds to $\zeta \approx 2 \times 10^6 \zeta_0$. They attribute the H_2 emission to gas with a trace molecular component, $n(H_2)/n_H \sim 5 \times 10^{-4}$, which is around a factor of 10 higher than our models. The size of the H_2 emitting region is $\sim 5 \times 10^{15}$ cm, intermediate between D3Z6 and D4Z7.

Clearly, the failure of any of our models to predict H_2 surface brightnesses of $\sim$

$10^{-5}\,\mathrm{erg\,cm^{-2}\,s^{-1}\,sr^{-1}}$ is an issue. The similarity of the model properties to those of the H_2 emitting knots suggests that the ArH^+ and OH^+ emission could originate from the same regions. Increasing the cloud thickness for D4Z7 to 0.3 mag - a similar physical size to the Richardson et al. (2013) model - we find a 2.12 μm surface brightness of $2.9 \times 10^{-6}\,\mathrm{erg\,cm^{-2}\,s^{-1}\,sr^{-1}}$, within a factor of a few of observations. However, this results in surface brightnesses for the other species in Table 4.3 far in excess of observed values.

A possible solution may be due to the angular resolutions of the different observations. The H_2 2.12 μm observations come from narrow-band imaging, with a reported plate scale of $68\,\mathrm{mas\,pixel^{-1}}$, whereas the Herschel SPIRE FTS spectra have beam size diameters of 37 and 18 arcsec, for the SLW and SSW detectors respectively. The angular sizes of the H_2 knots from Loh et al. (2011) are in the range $\sim 1 - 30\,\mathrm{arcsec^2}$, so at most one knot can cover a fractional area of ~ 0.1 of the SPIRE FTS detector, and the observed surface brightness will be reduced by a factor of ~ 10 from the intrinsic value. The PACS IFU spectra from Gomez et al. (2012) would be even more heavily affected - the detector covers $2209\,\mathrm{arcsec^2}$, so for a single knot the observed surface brightness would be around $100\times$ lower than predicted.

Table 4.7 lists the predicted surface brightnesses for models D4Z7 and D5Z8 with cloud thicknesses of 1 and 0.5 mag respectively, chosen to produce an H_2 2.12 μm surface brightness of $10^{-5}\,\mathrm{erg\,cm^{-2}\,s^{-1}\,sr^{-1}}$. The relative size of the telescope field of view to the largest H_2 knot size ($30\,\mathrm{arcsec^2}$) is also listed for each line - the OH^+ 971 GHz transition is covered by both the SLW and SSW detectors. The D3Z6 model did not reach the required 2.12 μm surface brightness even for the maximum cloud thickness. When the possible effects of beam filling are accounted for, both models are in reasonable agreement with all observations - the fine structure lines from Gomez et al. (2012) and the OH^+ 1033 GHz line are somewhat stronger than the observed values, but not by an unreasonable amount. The required extinction for the D5Z8 model is similar to that of the globules seen by Grenman et al. (2017), while the physical sizes (2×10^{16} (D4Z7) and $1 \times 10^{15}\,\mathrm{cm}$ (D5Z8)) are comparable to both the globules and the H_2 knots.

While a telescope beam is unlikely to only contain one knot, most of those listed by Loh et al. (2011) have significantly smaller sizes than the $30\,\mathrm{arcsec^2}$ we have used to determine the filling factor so would contribute less to the detected surface brightness, so it seems reasonable that all of the discussed molecular and fine-structure emission could originate from the H_2 knots. This can also account for the non-H_2 associated globules seen by

Table 4.7: Observed and predicted line surface brightnesses for models with Ar/H = 5×10^{-5} and $A_V = 1$ (D4Z7) and 0.5 (D5Z8), and beam size of the observations relative to the maximum size of H_2 knots in Loh et al. (2011) (30 arcsec^2). Surface brightnesses are in erg cm^{-2} s^{-1} sr^{-1}. References are (1) Barlow et al. (2013) (2) Gomez et al. (2012) (3) Loh et al. (2011).

Line	Obs.	D4Z7	D5Z8	Beam	Ref.
ArH^+ 617 GHz	$2.2 - 9.7(-7)$	$1.2(-5)$	$6.5(-6)$	36	(1)
ArH^+ 1234 GHz	$1.0 - 3.4(-6)$	$3.9(-5)$	$6.9(-5)$	8	(1)
OH^+ 971 GHz	$3.4 - 10.6(-7)$	$1.2(-5)$	$1.9(-5)$	36/8	(1)
OH^+ 1033 GHz	$\lesssim 10^{-7}$	$7.0(-6)$	$1.3(-5)$	8	(1)
OH^+ 909 GHz	$\lesssim 10^{-7}$	$1.9(-6)$	$3.4(-6)$	36	(1)
[C I] 492 GHz	$\lesssim 10^{-7}$	$3.7(-7)$	$1.8(-7)$	36	(1)
[C I] 809 GHz	$\lesssim 10^{-7}$	$3.4(-6)$	$1.6(-6)$	36	(1)
CO $J = 4 - 3$	$\lesssim 10^{-7}$	$2.9(-12)$	$9.7(-12)$	36	(1)
[O I] 63 μm	$1.1 - 3.2(-4)$	$6.5(-2)$	$8.0(-2)$	74	(2)
[O I] 146 μm	$0.4 - 1.9(-5)$	$4.1(-3)$	$2.6(-3)$	74	(2)
[C II] 158 μm	$2.7 - 6.4(-5)$	$6.3(-3)$	$3.3(-3)$	74	(2)
HeH^+ 149 μm	$\lesssim 10^{-5}$	$1.1(-4)$	$3.3(-4)$	74	(2)
HeH^+ 75 μm	$\lesssim 10^{-5}$	$1.1(-4)$	$5.2(-4)$	74	(2)
H_2 2.12 μm	$1.0 - 4.8(-5)$	$1.0(-5)$	$1.1(-5)$	-	(3)

Grenman et al. (2017) - lower density gas does not produce sufficient 2.12 μm emission for reasonable cloud thicknesses, while still producing ArH^+ and OH^+ lines.

This interpretation relies on the gas being subjected to cosmic ray ionization rates of $\sim 10^7 - 10^8 \zeta_0$, higher than the value found by Richardson et al. (2013) but within their derived limits. They also considered the possibility of the H_2 emission being powered by the injection of mechanical energy, by either shocks or turbulence. We follow their approach and run models at each density with a minimum temperature of 3000 K. The resulting models predict the observed H_2 2.12 μm surface brightnesses of 10^{-5} erg cm^{-2} s^{-1} sr^{-1} for cloud thicknesses ranging from 0.05 mag for $n_H = 2 \times 10^5$ cm^{-3} to 2 mag for 2×10^3 cm^{-3}. However, for all densities the results are inconsistent with the SPIRE FTS spectra - OH^+ emission is $10 - 100\times$ stronger than ArH^+, while [C I] and, for the higher density models, CO surface brightnesses are comparable or stronger than the 617 GHz line. As these transitions are measured by the same detectors, there are no beam size effects, so we conclude that shocked gas can only contribute a small fraction of the observed emission, and the majority is powered by cosmic ray heating.

Unlike Richardson et al. (2013), who self-consistently modelled both the atomic and H_2 emission, we have taken the gas-phase elemental abundances from previous photoionization modelling of optical emission lines (Owen and Barlow 2015). Given that the

agreement between our models and observations depends on the Ar/H ratio, it would be preferable to determine the elemental abundances and the density/ionization rate required to reproduce observed surface brightnesses simultaneuously. This would require integrated photoionization/PDR modelling and, given the findings of Owen and Barlow (2015), three-dimensional radiative transfer, which would be possible, if time-consuming, with TORUS-3DPDR (Bisbas et al. 2015). Our results also depend on the assumption that the cosmic-ray induced reaction rates in the ISM are also applicable to the Crab Nebula, which may have a very different spectrum of particle energies. While the particle energy spectrum in the Crab Nebula can be inferred from the synchrotron radiation (Atoyan and Aharonian 1996), translating this to reaction rates, particularly those involving secondary electrons, would require additional atomic and molecular data which is unlikely to be easily obtainable.

4.5 Conclusions

We have modelled the emission from a cloud of Crab Nebula material, subjected to the PWN synchrotron radiation and a varying flux of charged particles. The ArH^+ emission observed by Barlow et al. (2013) requires the cosmic ray ionization rate to be $\geq 10^6\times$ the standard ISM rate. The relative strengths of the ArH^+ and OH^+ emission in the Herschel SPIRE FTS spectra can be explained if the Ar/H abundance is 5×10^{-5}, at the upper end of the range of values found by Owen and Barlow (2015). When the effects of telescope beam size are accounted for, clumps of material with similar properties to the H_2 knots (Loh et al. 2011) and dusty globules (Grenman et al. 2017) observed in the Crab Nebula can account for the [C I], [O I] and [C II] fine-structure line and H_2 2.12 μm emission, as well as the SPIRE FTS observations. Artificially setting the gas temperature to 3000 K, to represent some additional heating source, also reproduces the H_2 emission, but predicts other relative line intensities inconsistent with the SPIRE FTS spectra. We conclude that the H_2 knots in the Crab Nebula are strongly irradiated by charged particles from the PWN, and account for the majority of the observed molecular emission.

Chapter 5

Description of DINAMO

In order to model the dust emission from the Cassiopeia A supernova remnant, as described in the following chapter, I have developed a new dust emission code, DINAMO (DINAMO Is Not A MOdified black-body). The code calculates the equilibrium temperature distributions and the thermal emission for a population of dust grains of arbitrary sizes and compositions, given the physical properties of the environment the grains are located in (radiation field, electron/ion density and temperature). DINAMO includes heating from both radiation and particle collisions simultaneously, and treats cooling as a state-to-state process rather than using the continuous cooling approximation (Siebenmorgen et al. 1992). The code has been benchmarked against DustEM (Compiègne et al. 2011) using the test cases from Camps et al. (2015), and found to be in excellent agreement, as shown in Figure 5.1. It is available to download from `https://github.com/fpriestley/dinamo`.

The stochastic heating of dust grains is treated following the method of Guhathakurta and Draine (1989). For each grain size, N enthalpy bins are defined between a maximum and minimum enthalpy, with the probability of a grain being found in bin i at time t given by $P_i(t)$. The probability per unit time of a grain moving from bin i to bin f is A_{fi}, with $A_{ii} = -\sum_{f \neq i} A_{fi}$, so that $\frac{d}{dt}P_f = \sum_i A_{fi}P_i$. For the steady state solution, $\sum_i A_{fi}P_i = 0$ for all i, which with the additional constraint that $\sum P_i = 1$ gives a system of linear equations which can be solved to find the 'equilibrium' temperature distribution for a particular grain size and species.

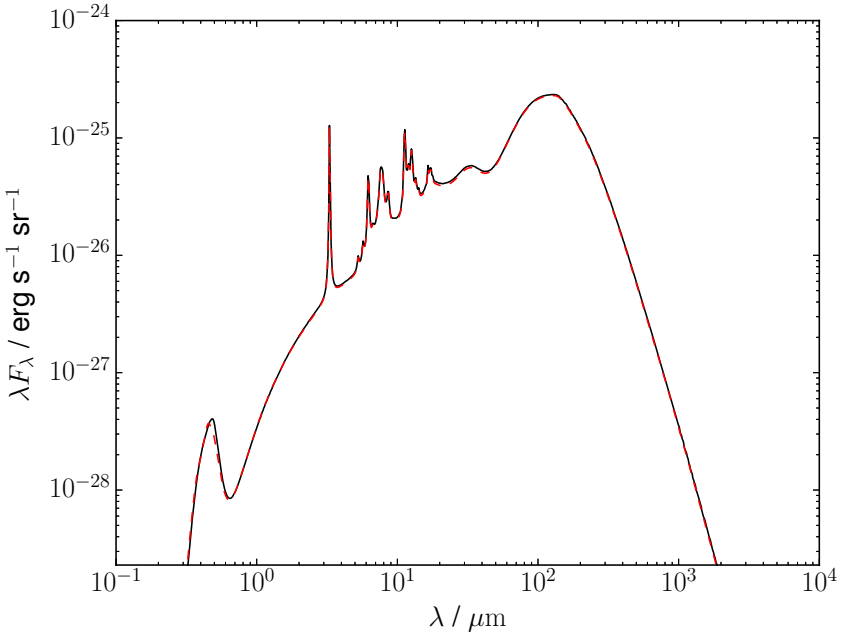

Figure 5.1: Dust emission for the Mathis et al. (1983) ISM radiation field benchmark case from Camps et al. (2015), as calculated by DINAMO (solid black line) and DustEM (dashed red line).

5.1 Radiative heating

A dust grain in enthalpy bin i, with enthalpy H_i, absorbing a photon of energy $h\nu$ will increase its enthalpy to $H_i + h\nu$, which may move it into a higher enthalpy bin. The transition rate between bins i and f due to radiative heating is given by

$$A_{fi} = 4\pi^2 a^2 Q_{\lambda_{fi}} J_{\lambda_{fi}} \frac{hc\Delta H_f}{(H_f - H_i)^3} \tag{5.1}$$

for $f > i$, where a is the grain radius, $\lambda_{fi} = \frac{hc}{H_f - H_i}$ is the wavelength of a photon with energy corresponding to the difference between enthalpy bins, $Q_{\lambda_{fi}}$ and $J_{\lambda_{fi}}$ are the absorption efficiency and radiation field strength at wavelength λ_{fi} and ΔH_f is the width of enthalpy bin f (Camps et al. 2015). Photons energetic enough to heat the grain beyond the highest enthalpy bin are included in the rate to bin N, giving an additional term

$$A'_{Ni} = 4\pi^2 a^2 \int_0^{\lambda_{\max}} \lambda Q_\lambda J_\lambda d\lambda / hc \tag{5.2}$$

where $\lambda_{\max} = \frac{hc}{H_{\max} - H_i}$ is the wavelength of the least energetic photon capable of heating a grain beyond the maximum temperature. Photons not energetic enough to heat a grain

out of the enthalpy bin contribute to a continuous heating rate

$$\frac{dH_{\rm heat}}{dt} = 4\pi^2 a^2 \int_{\lambda_0}^{\infty} Q_\lambda J_\lambda d\lambda \tag{5.3}$$

where $\lambda_0 = \frac{hc}{H_f - H_i}$. If the continuous heating rate is greater than the equivalent cooling rate then

$$A_{fi}^{\rm cont} = \frac{1}{\Delta H_i}\frac{dH_{\rm net}}{dt} \tag{5.4}$$

for $f = i+1$, where ΔH_i is the width of bin i and $H_{\rm net}$ is the net heating rate $\frac{dH_{\rm heat}}{dt} - \frac{dH_{\rm cool}}{dt}$.

5.2 Radiative cooling

Dust grains of temperature T emit radiation at wavelength λ with intensity $Q_\lambda B(\lambda, T)$ where $B(\lambda, T)$ is the Planck function, causing them to lose energy. The transition rates are similar to those for absorption of a photon, with

$$A_{fi} = 4\pi^2 a^2 Q_{\lambda_{fi}} B(\lambda, T_i) \frac{hc\Delta H_f}{(H_i - H_f)^3} \tag{5.5}$$

for $f < i$ where T_i is the temperature of a grain in enthalpy bin i, and

$$A'_{1i} = 4\pi^2 a^2 \int_0^{\lambda_{\rm min}} \lambda Q_\lambda B(\lambda, T_i) d\lambda / hc \tag{5.6}$$

where $\lambda_{\rm max} = \frac{hc}{H_i - H_{\rm min}}$. The continuous cooling rate is given by

$$\frac{dH_{\rm cool}}{dt} = 4\pi^2 a^2 \int_{\lambda_0}^{\infty} Q_\lambda B(\lambda, T_i) d\lambda \tag{5.7}$$

where $\lambda_0 = \frac{hc}{H_i - H_f}$, and for $\frac{dH_{\rm cool}}{dt} > \frac{dH_{\rm heat}}{dt}$

$$A_{fi}^{\rm cont} = -\frac{1}{\Delta H_i}\frac{dH_{\rm net}}{dt} \tag{5.8}$$

for $f = i - 1$.

5.3 Collisional heating

As with photons, a collision between a dust grain and a particle (either an electron or an atom/ion) can result in a transfer of energy to the dust grain. Unlike with photons, a colliding particle does not necessarily transfer all its energy to the grain, and the amount of heating depends on the particle energy as well as the dust properties. The transition rate between enthalpy bins due to particle heating is given by

$$A_{fi} = \pi a^2 n \int f(E) v(E) \delta(\Delta E) dE \tag{5.9}$$

where n is the number density of particles, $f(E)$ is the probability distribution of particle energies, $v(E)$ is the velocity of a particle with energy E, ΔE is the energy transferred to the dust grain and $\delta(\Delta E)$ is a function such that

$$\delta(\Delta E) = \begin{cases} 0 & |\Delta E - (H_f - H_i)| < \Delta H_f/2 \\ 1 & \text{otherwise} \end{cases} \tag{5.10}$$

where ΔH_f is the width of enthalpy bin f. The additional heating rate to enthalpies higher than H_N is given by

$$A'_{Ni} = \pi a^2 n \int f(E) v(E) \delta'(\Delta E) dE \tag{5.11}$$

where

$$\delta'(\Delta E) = \begin{cases} 0 & \Delta E < H_{\max} - H_i \\ 1 & \text{otherwise} \end{cases} \tag{5.12}$$

and the continuous heating rate is given by

$$\frac{dH_{\text{heat}}}{dt} = \pi a^2 n \int f(E) v(E) \delta''(\Delta E) \Delta E dE \tag{5.13}$$

where

$$\delta''(\Delta E) = \begin{cases} 1 & \Delta E < H_f - H_i \\ 0 & \text{otherwise} \end{cases} \tag{5.14}$$

for $f = i + 1$. For electrons, the transferred energy ΔE is determined as a function of E using the method described by Dwek and Smith (1996). For a dust grain of stopping thickness $R_0 = 4a\rho/3$ where ρ is the density, if the electron range $R_1(E) \leq R_0$ then $\Delta E = E$. For $R_1(E) > R_0$, $\Delta E = E - E'$ where $R(E') = R_1 - R_0$. A function for $R(E)$ based on fits to experimental data is given in Dwek and Smith (1996). For atoms and ions, Dwek (1987) gives the transferred energy as

$$\Delta E = \begin{cases} E & E \leq E' \\ E' & E > E' \end{cases} \tag{5.15}$$

where E' is listed for various nuclei as a function of grain radius a in Dwek (1987).

5.4 Solution algorithm

For each species and size of dust grain, the transition matrix is constructed as described above for a grid of N enthalpy bins. The grid is linearly spaced in temperature, as suggested by Siebenmorgen et al. (1992), and all grain properties are evaluated at the temperature midpoint of the bin, using the heat capacities for silicate or carbon grains from Guhathakurta and Draine (1989). The minimum temperature is set to zero, and the maximum temperature is initially set to a species-dependent sublimation temperature, beyond which grains are rapidly destroyed (Guhathakurta and Draine 1989). The equilibrium temperature probability distribution is determined by matrix inversion - a new maximum temperature is then defined as the temperature beyond which the probability falls below a user-defined threshold, by default 10^{-20}, and a new enthalpy grid and transition matrix are calculated. This process is iterated until the relative change in maximum temperature between iterations falls below another threshold (by default 0.01), ensuring that the grid samples only the relevant temperature range. When convergence is reached, the code calculates the total emission as the sum over the temperatures, weighted by the probabilities and the adopted grain size distribution, and moves on to the next grain size.

This page was intentionally left blank

Chapter 6

Dust emission from Cassiopeia A

6.1 Introduction

The detections of significant ($\gtrsim 10^8\,\mathrm{M}_\odot$) masses of dust in high-redshift quasars (Bertoldi et al. 2003; Priddey et al. 2003), and dust-enriched galaxies at redshifts $z > 7$ (Watson et al. 2015; Laporte et al. 2017), require an explanation of how sufficient quantities of dust can be formed at such early epochs. Core-collapse supernovae (SNe) have been proposed as a potential source of this dust (Dunne et al. 2003; Gall et al. 2011), as their progenitors evolve rapidly compared to the age of the universe at these redshifts ($\sim 1\,\mathrm{Gyr}$). Observations of supernova remnants (SNRs) have confirmed the presence of dust formed in the ejecta, both through infrared (IR)/sub-millimetre (submm) detection of dust emission (Barlow et al. 2010; Matsuura et al. 2011; Gomez et al. 2012; Matsuura et al. 2015) and alteration of emission line profiles due to dust extinction (Bevan and Barlow 2016; Bevan et al. 2017).

In order to explain the observed dust masses at high redshift, the average dust yield per SNe must exceed some minimum value, estimated as $\sim 1\,\mathrm{M}_\odot$ by Dwek et al. (2007) and between $0.1 - 1\,\mathrm{M}_\odot$ by Michałowski et al. (2010), although Rowlands et al. (2014) found that higher yields may be necessary if dust destruction in the interstellar medium (ISM) is taken into account. Dust masses observed in SNRs, such as the Crab Nebula ($0.1 - 0.2\,\mathrm{M}_\odot$; Gomez et al. (2012)) and SN 1987A ($0.8\,\mathrm{M}_\odot$; Matsuura et al. (2015)), approach or exceed this value, but the fraction which will survive passage through the SN

reverse shock and into the ISM is uncertain (Nozawa et al. 2007; Bianchi and Schneider 2007; Nozawa et al. 2010; Micelotta et al. 2016; Biscaro and Cherchneff 2016; Bocchio et al. 2016). In particular, large ($a \gtrsim 0.1\,\mu$m) dust grains are able to survive destruction by sputtering much more effectively than smaller grains (Silvia et al. 2010).

Cassiopeia A (Cas A), shown in Figure 6.1, is a Galactic SNR located 3.4 kpc away (Reed et al. 1995), with an age of approximately 330 yr (Fesen et al. 2006) and a radius of 1.7 pc (Reed et al. 1995). IR/submm observations have led to derived dust masses ranging from $\sim 10^{-4}\,\mathrm{M}_\odot$ of hot ($T \sim 100\,\mathrm{K}$) dust (Arendt et al. 1999; Douvion et al. 2001) to $2-4\,\mathrm{M}_\odot$ of cold dust emitting at sub-mm wavelengths (Dunne et al. 2003), although this higher mass has been attributed to foreground dust emission in the ISM (Krause et al. 2004). Analyses of integrated fluxes from *Spitzer* and *Herschel* observations (Rho et al. 2008; Barlow et al. 2010; Arendt et al. 2014) found $\sim 0.01\,\mathrm{M}_\odot$ of hot dust, with $\sim 0.1\,\mathrm{M}_\odot$ of cold, unshocked dust present in the central regions, in agreement with simulations of the dust formation and evolution in Cas A by Nozawa et al. (2010). Dunne et al. (2009) suggested the observed polarization of the submm emission could be explained by $\sim 1\,\mathrm{M}_\odot$ of cold dust, similar to the value of $1.1\,\mathrm{M}_\odot$ given by Bevan et al. (2017) as the most likely mass based on the shape of emission line profiles affected by extinction. De Looze et al. (2017) utilised spatially resolved *Herschel* and *Spitzer* observations of Cas A to fit the dust continuum emission, following the removal of line and synchrotron contamination, using a four-component model including ISM dust emission and three SNR dust temperature components. They found a large mass of unshocked cold dust in the centre of the SNR (up to $0.5\,\mathrm{M}_\odot$), significantly above previous estimates based on the IR/submm emission.

Previous modelling of the Cas A dust emission has been based on fitting the spectral energy distribution (SED) with some number of temperature components for a given dust composition (i.e. 'hot' and 'cold' dust). This assumes all dust grains radiate at the same temperature for each component, but grains of different sizes will in general have different equilibrium temperatures for the same heating source. Additionally, smaller grains can undergo large temperature fluctuations (e.g. Purcell 1976; Draine and Anderson 1985; Dwek 1986) and may not reach an equilibrium temperature at all. Temim and Dwek (2013) found that modelling the emission from a distribution of grain sizes in the Crab Nebula reduced the dust mass estimate by a factor of two compared to two-temperature fits by Gomez et al. (2012), demonstating the importance of accounting for these effects. In this chapter, we calculate the emission from a population of grains subjected to conditions

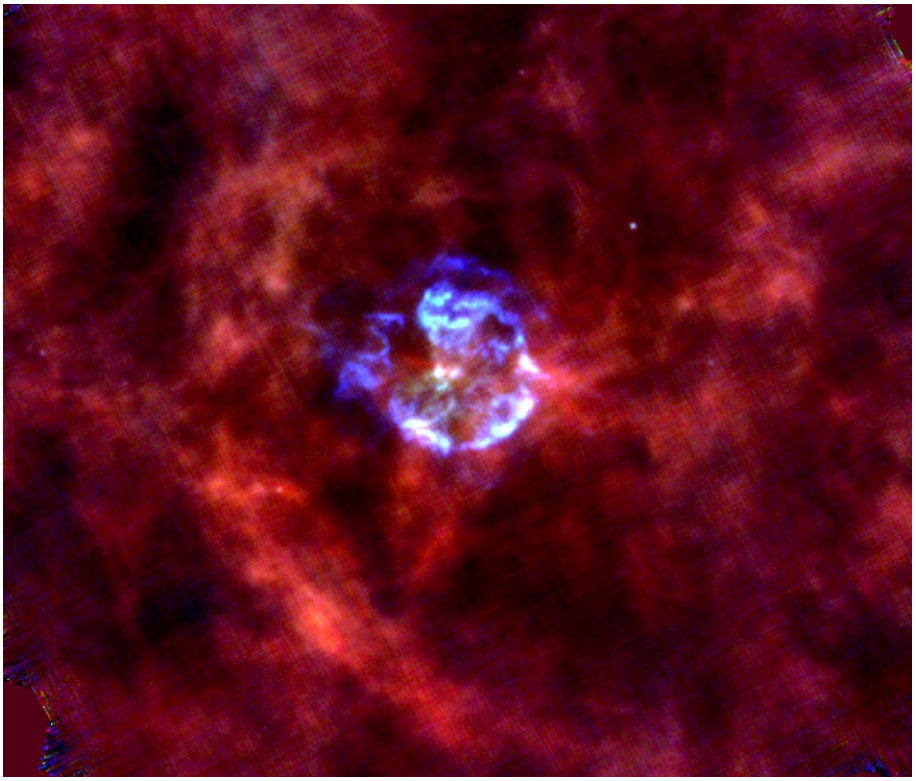

Figure 6.1: Herschel PACS far-infrared image of the Galactic supernova remnant Cassiopeia A. Blue shows supernova dust emission at a wavelength of 70 microns and red shows interstellar dust emission at a wavelength of 160 microns. The image dimensions are 22×22 arcmin. Image credit: Oliver Krause (MPIA).

appropriate for the various gas components in Cas A, and use it to constrain the mass, properties and location of the newly-formed dust.

6.2 Physical properties of the Cas A SNR

Observations of Cas A reveal a complex structure, with material covering a wide range of densities and temperatures emitting at different wavelengths. The supernova explosion has driven a forward shock into the circumstellar material, thought to be from the stellar wind of the progenitor (Hwang and Laming 2009), while the ejecta from the supernova itself crosses the reverse shock as it expands (DeLaney et al. 2004). Both shocks are visible as X-ray emitting regions, shown in Figure 6.2, with typical densities of $n \sim 1 - 10\,\mathrm{cm}^{-3}$ and temperatures $T \sim 10^7\,\mathrm{K}$ (Willingale et al. 2003; Lazendic et al. 2006; Patnaude and Fesen 2014; Wang and Li 2016). The ejecta are mostly comprised of heavy elements, principally oxygen (Chevalier and Kirshner 1979; Willingale et al. 2003). As well as the X-ray emitting gas, the shocked ejecta also consists of denser clumps or knots, emitting

in the optical and IR (Hurford and Fesen 1996; DeLaney et al. 2010; Patnaude and Fesen 2014) and associated with the dust emission (Arendt et al. 1999). Electron densities in the shocked clumps are $n_{\rm e} \sim 10^3 - 10^5\,{\rm cm}^{-3}$ (Smith et al. 2009; DeLaney et al. 2010; Lee et al. 2017), while the gas temperatures are of order $10^4\,{\rm K}$ (Arendt et al. 1999; Docenko and Sunyaev 2010). The SNR also contains ejecta which have not yet encountered the reverse shock, and are consequently much cooler. Smith et al. (2009) estimated a maximum electron density of $n_{\rm e} \lesssim 100\,{\rm cm}^{-3}$ for the unshocked ejecta based on forbidden line ratios, while observations of radio absorption by DeLaney et al. (2014) and Arias et al. (2018) give $n_{\rm e} \sim 10\,{\rm cm}^{-3}$ and $T \sim 100\,{\rm K}$. Raymond et al. (2018) inferred a preshock temperature of $\sim 100\,{\rm K}$ from [Si I] IR emission.

Krause et al. (2008) determined that the Cas A SN was of type IIb from a spectrum of its light echo, meaning that the progenitor star must have lost most of its hydrogen envelope pre-explosion. Young et al. (2006) suggested a progenitor with main-sequence mass of $15 - 25\,{\rm M}_\odot$ and a mass at explosion of $4 - 6\,{\rm M}_\odot$, based on a comparison of stellar evolution and explosion models with observed features of the SNR. Modelling of the X-ray spectra (Vink et al. 1996; Willingale et al. 2003) gives ejecta masses in the $2 - 4\,{\rm M}_\odot$ range, with the swept-up material in the forward shock contributing an additional $8 - 10\,{\rm M}_\odot$. The optical and IR-emitting knots have a total gas mass of $0.59\,{\rm M}_\odot$ (M. J. Barlow, private communication). Arias et al. (2018) estimate an unshocked ejecta gas mass of $\sim 3\,{\rm M}_\odot$. They noted that this conflicts with some models of the emission from the shocked regions, which suggest most of the ejecta has already passed the reverse shock (Chevalier and Oishi 2003; Laming and Hwang 2003), and that their result is sensitive to both the assumed gas temperature and whether the gas is clumped. However, most of the dust, whose mass was derived by De Looze et al. (2017), appears to be located inside the reverse shock. The gas temperature has since been measured to be $\sim 100\,{\rm K}$ (Raymond et al. 2018), the value used to give the $3\,{\rm M}_\odot$ mass estimate, although the (unknown) degree of clumping still allows for a potentially lower unshocked ejecta mass.

6.3 Method

Based on the above discussion, we model the SNR as consisting of four main components - the unshocked ejecta, the (reverse) shocked ejecta clumps responsible for the optical emission, the X-ray emitting diffuse shocked ejecta and the material swept up by the blast

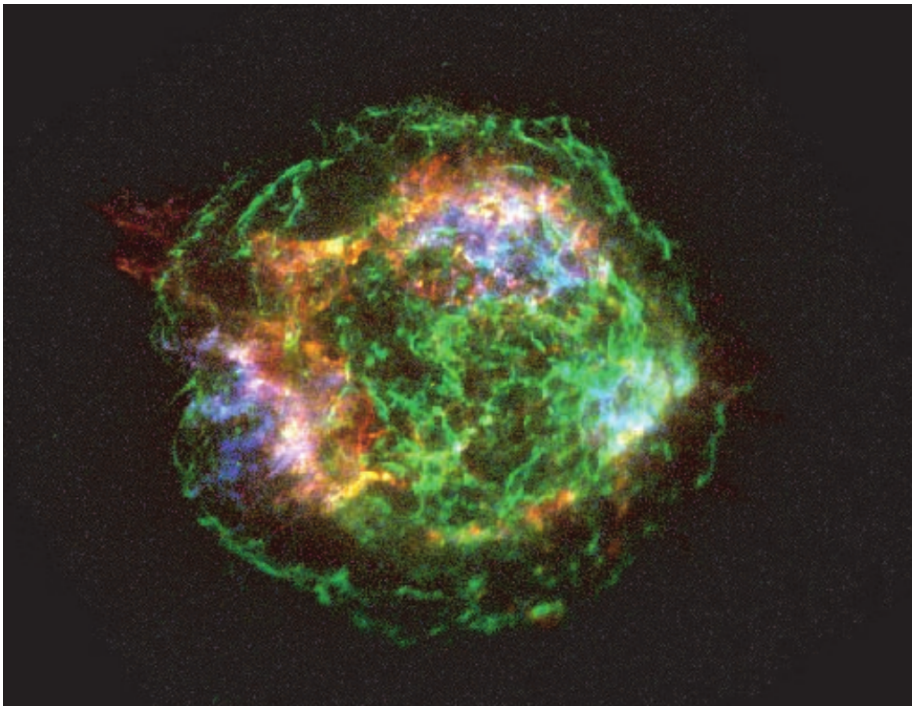

Figure 6.2: X-ray image of Cas A, with Si Hα emission in red, Fe K in blue and continuum in green, from Hwang et al. (2004). The image dimensions are 5×5 arcmin.

wave. The assumed densities and temperatures of these components are listed in Table 6.1. For the unshocked ejecta we take $n_\mathrm{e} = 100\,\mathrm{cm}^{-3}$ and $T = 100\,\mathrm{K}$, the upper limits from observations (Smith et al. 2009; Raymond et al. 2018) - we show later that lower values have no effect on the resulting emission, as the heating is dominated by the radiation field. For the shocked clumps we use $n_\mathrm{e} = 480\,\mathrm{cm}^{-3}$, used in deriving the total gas mass in this component, and $T = 10^4\,\mathrm{K}$ (Arendt et al. 1999; Docenko and Sunyaev 2010). As the values of n_e dervied from observations range from $10^2 - 10^5\,\mathrm{cm}^{-3}$, we also consider models with higher values of this parameter. For the two X-ray emitting components we use the values from Willingale et al. (2003), who determined the ion and electron densities and temperatures separately. For the other two components we assume that $T_\mathrm{i} = T_\mathrm{e}$ and $n_\mathrm{i} = n_\mathrm{e}$ - electrons are much more efficient at heating than ions for the same temperature due to their lower mass, so the exact value of n_i in these cases is unlikely to be significant. In the three ejecta components we assume the ionic species is oxygen, using the heating efficiency from Dwek (1987), while in the forward shock we use hydrogen. Willingale et al. (2003) found mean ionic masses of 15.6 and $1.33 m_\mathrm{H}$ for the reverse and forward shocks respectively, so oxygen (ejecta) and hydrogen (forward shock) are almost certainly the dominant constituents.

Table 6.1: Adopted gas masses, ion and electron number densities and temperatures, and dominant ionic species for the four gas components. References are (1) Smith et al. (2009) (2) Raymond et al. (2018) (3) Arias et al. (2018) (4) Docenko and Sunyaev (2010) (5) M. J. Barlow (private communication) (6) Willingale et al. (2003).

Component	$M_{\rm gas}/\,{\rm M}_\odot$	$n_{\rm i}/\,{\rm cm}^{-3}$	$n_{\rm e}/\,{\rm cm}^{-3}$	$T_{\rm i}/\,{\rm K}$	$T_{\rm e}/\,{\rm K}$	Ion	Ref.
Preshock	3	100	100	100	100	O	(1),(2),(3)
Clumped	0.59	480	480	10^4	10^4	O	(4),(5)
Diffuse	1.68	7.8	61	7.05×10^8	5.22×10^6	O	(6)
Blastwave	8.32	14.3	16	3.98×10^8	3.79×10^7	H	(6)

In addition to the gas, dust in Cas A is also heated by the ambient radiation field. De Looze et al. (2017) fitted the Cas A synchrotron emission with a single power law - while appropriate for the radio and IR wavelengths considered there, extrapolating to the UV and X-ray regions important for dust heating may not be valid. We find that a power law with an exponential cutoff, of the form $\nu F_\nu \propto \nu^{0.2} \exp(-(\nu/\nu_0)^{-0.4})$ with $\nu_0 = 900\,{\rm eV}$, provides a good fit to the radio and X-ray data from Wang and Li (2016), similar to theoretical predictions from Zirakashvili and Aharonian (2007). We determined the radiation field strength using a distance of 3.4 kpc from Reed et al. (1995), assuming the dust is located 1 pc from the source - the synchrotron radiation field is actually generated by the shock and so does not have a single source, but for an SNR radius of 1.7 pc (Reed et al. 1995) we consider 1 pc to be an acceptable 'average' distance, and explore the sensitivity of our results to the assumed intensity.

Given the oxygen-rich nature of the SNR, the dust in Cas A is expected to be primarily composed of silicates. Rho et al. (2008) and Arendt et al. (2014) found magnesium silicates of various compositions could reproduce a strong 21 μm feature in the *Spitzer* dust emission spectra, although Al_2O_3, carbon grains and other species were also suggested to be present. We use optical constants for magnesium and magnesium-iron silicates with varying elemental ratios (Jaeger et al. 1994; Dorschner et al. 1995; Jäger et al. 2003), which span the range $0.2 - 500\,\mu$m. As these do not extend into the shorter-wavelength regions important for dust heating, we use the optical constants for astronomical silicates from Laor and Draine (1993) for $0.001 - 0.2\,\mu$m for all silicate species, interpolating between the two data sets to avoid discontinuities, and we extrapolate the experimental data up to $1000\,\mu$m. We also investigated carbon grains, using optical constants for the ACAR and BE samples from Zubko et al. (1996), extended to $0.0003\,\mu$m with data from Uspenskii et al. (2006), as described by Owen and Barlow (2015). We assume mass densities of 2.5

Table 6.2: Dust species and their adopted densities ρ_g, sublimation temperatures $T_{\rm sub}$ and references for the optical constants. References are (1) Dorschner et al. (1995) (2) Jäger et al. (2003) (3) Laor and Draine (1993) (4) Zubko et al. (1996) (5) Uspenskii et al. (2006).

Dust species	$\rho_g/\mathrm{g\,cm^{-3}}$	$T_{\rm sub}/\mathrm{K}$	n-k
$MgSiO_3$	2.5	1500	(1),(3)
$Mg_{0.4}Fe_{0.6}SiO_3$	2.5	1500	(1),(3)
$Mg_{0.7}SiO_{2.7}$	2.5	1500	(2),(3)
$Mg_{2.4}SiO_{4.4}$	2.5	1500	(2),(3)
Am. carbon ACAR	1.6	2500	(4),(5)
Am. carbon BE	1.6	2500	(4),(5)

and $1.6\,\mathrm{g\,cm^{-3}}$ for silicate and carbon grains respectively, following De Looze et al. (2017), and sublimation temperatures of 1500 and 2500 K, although our results are not sensitive to the choice of this parameter. Dust properties used are summarised in Table 6.2.

We initially assume an MRN size distribution (Mathis et al. 1977), with $a_{\rm min} = 0.005\,\mu$m, $a_{\rm max} = 0.25\,\mu$m and a power law size distribution with $\frac{dn}{da} \propto a^{-3.5}$, and calculate the SED per grain (averaged over size and temperature distributions) for each of the four components using DINAMO (Chapter 5). As we do not consider dust self-absorption or other optically thick effects, the SEDs can be scaled to find the emission from an arbitrary number of grains, which can then be converted to a dust mass using the size distribution and grain density. Our observational data are the supernova dust fluxes reported by De Looze et al. (2017) for $G = 0.6G_0$, following the removal of line, synchrotron and ISM foreground emission, listed in Table 6.3. To fit the observed emission from Cas A, we run grids of models, with the number of dust grains in each component the four free parameters, convolve the resulting SEDs with the filter profiles for each instrument and calculate the χ^2 values for the models. Following De Looze et al. (2017), we do not include the IRAC $8\,\mu$m and WISE $12\,\mu$m points in our χ^2 calculations, as at these wavelengths the flux has significant contributions from ISM PAH features. The degree to which these features are accounted for by the THEMIS dust model is unknown, and as such including these points would potentially bias our results.

6.4 Results

Figure 6.3 shows our best-fit model SED for $MgSiO_3$ grains, with optical data from Dorschner et al. (1995). The reduced χ^2 value, excluding the $8\,\mu$m and $12\,\mu$m points, is 1.66. The model requires dust masses of 0.60, 0.065, 6×10^{-5} and $0.0018\,\mathrm{M_\odot}$ for

Table 6.3: Cas A SNR dust fluxes and uncertainties from De Looze et al. (2017), for an ISM radiation field strength $G = 0.6G_0$.

$\lambda/\,\mu$m	F_ν/Jy
8	0.2 ± 0.1
12	3.4 ± 0.3
17	63.3 ± 6.0
22	202.0 ± 19.3
24	153.4 ± 15.0
32	168.5 ± 17.3
70	149.5 ± 20.1
100	125.8 ± 19.9
160	69.9 ± 12.0
250	27.3 ± 4.8
350	10.9 ± 1.9
500	2.6 ± 0.5
850	0.4 ± 0.1

the preshock, clump, diffuse and blastwave regions respectively, for a total dust mass of $0.67\,\mathrm{M}_\odot$, comparable to the value of $0.5 \pm 0.1\,\mathrm{M}_\odot$ found by De Looze et al. (2017) for the same dust species. The De Looze et al. (2017) 'hot' dust component has a similar mass to the combined blastwave and diffuse components in our model, while their 'warm' component has $\sim 10\times$ less mass than our clumped dust. Our SED predicts more emission at 8 and 12 μm than the reported SNR fluxes from De Looze et al. (2017) - however, we note that our predicted SED in this region appears similar to the '21 μm peak' IRS spectra of Cas A from Rho et al. (2008), reproducing the broad feature at $\sim 10\,\mu$m.

Table 6.4 lists the best-fit dust masses and reduced χ^2 values for each of the dust species listed in Table 6.2. Table 6.5 lists the gas-to-dust mass ratios for each component, assuming the gas masses listed in Table 6.1. The total dust masses for the four silicate species are similar, with the exception of $Mg_{0.7}SiO_{2.7}$, which required $\sim 3\times$ as much mass. This species was also found to require a significantly larger dust mass than other silicates by De Looze et al. (2017), although their value of $21.4\,\mathrm{M}_\odot$ is much higher than ours, as they found a best-fit temperature of 21 K whereas even the largest dust grains are heated to ~ 30 K in our model, thus requiring less mass to produce the same flux. The $Mg_{0.7}SiO_{2.7}$ SED is also a noticeably worse fit to the observations than the other models. Figure 6.4 shows its best fit SED - the slope at long wavelengths is inconsistent with that observed, and the dip in flux beyond the $\sim 20\,\mu$m peak is too severe. Figure 6.5 shows the best fit SED for $Mg_{0.4}Fe_{0.6}SiO_3$, the composition which gives the lowest χ^2 value of those we consider.

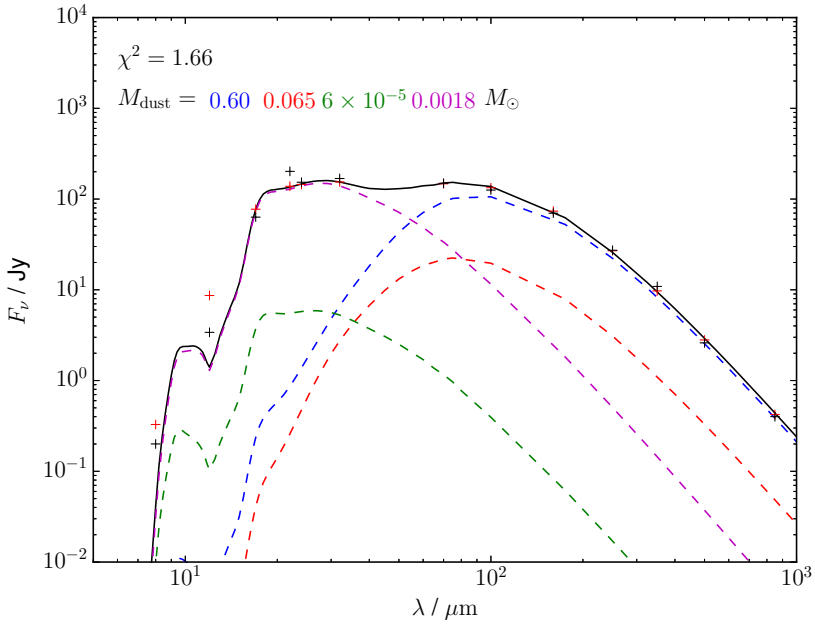

Figure 6.3: Best-fit total dust SED (black solid line) to the $G = 0.6G_0$ SNR dust fluxes from De Looze et al. (2017) (black crosses) for $MgSiO_3$ grains with an MRN size distribution, and the model fluxes (red crosses). The SEDs from each dust component as defined in Table 6.1 are shown as dashed lines (preshock: blue, clump: red, diffuse: green, blastwave: purple).

The two carbon species considered show similar behaviour, with lower dust masses than the silicates, almost all of which is contained in the clump component, rather than in the preshock component as with the silicates. Our dust masses are somewhat lower than the results for carbon grains from De Looze et al. (2017), again due to our models having higher grain temperatures than their 'cold' comopnent, which contains most of the mass. Figure 6.6 shows the best-fit SED for the ACAR grains. While the model provides an acceptable fit to the $> 20\,\mu$m data, the SED at shorter wavelengths is drastically different to the IRS spectra from Rho et al. (2008), and the predicted flux at $12\,\mu$m is higher than that observed, before the subtraction of line, synchrotron and ISM contributions. Carbon grains also fail to reproduce the $21\,\mu$m feature.

The three grain species that produce good fits to the observed fluxes predict similar dust masses for each gas component, with the majority in the preshock region and a smaller amount in the clumps. The fitted dust masses in the two X-ray emitting components are insignificant in terms of the total dust mass but are essential for reproducing the short wavelength data. The best-fit models all predict most of this high-temperature dust to be in the blast wave component. However, given the similarity of the blast wave and diffuse

Table 6.4: Best-fit model dust masses for each component, total dust masses and reduced χ^2 values for different grain species.

	$M_{\rm dust}$ / M$_\odot$					
Species	Preshock	Clump	Diffuse	Blastwave	Total	χ^2
$MgSiO_3$	0.60	0.065	6×10^{-5}	0.0018	0.67	1.66
$Mg_{0.4}Fe_{0.6}SiO_3$	0.48	0.10	1.5×10^{-4}	0.0018	0.58	0.92
$Mg_{0.7}SiO_{2.7}$	1.83	0.071	1.0×10^{-4}	0.0011	1.90	4.58
$Mg_{2.4}SiO_{4.4}$	0.56	0.11	6×10^{-5}	0.0018	0.67	1.32
Am. carbon ACAR	0.0033	0.12	6×10^{-5}	0.0019	0.13	2.39
Am. carbon BE	0.002	0.19	0.0	0.0019	0.19	2.07

Table 6.5: Best-fit model gas-to-dust mass ratios for each component for different grain species.

Species	Preshock	Clump	Diffuse	Blastwave
$MgSiO_3$	5.0	9.1	28000	4622
$Mg_{0.4}Fe_{0.6}SiO_3$	6.3	5.9	11200	4622
$Mg_{0.7}SiO_{2.7}$	1.6	8.3	16800	7564
$Mg_{2.4}SiO_{4.4}$	5.3	5.4	28000	4622
Am. carbon ACAR	909	4.9	28000	4379
Am. carbon BE	1500	3.1	-	4379

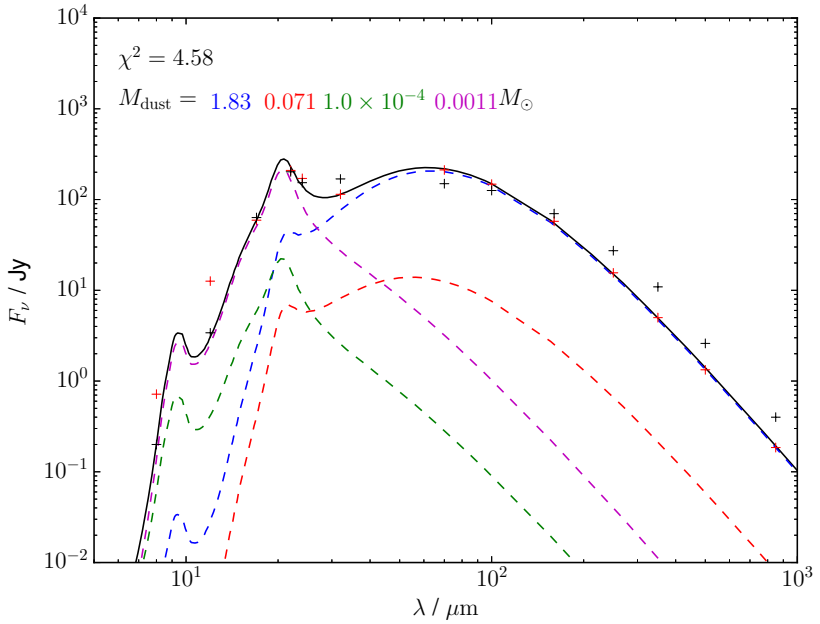

Figure 6.4: Best-fit total dust SED (black solid line) to the $G = 0.6G_0$ SNR dust fluxes from De Looze et al. (2017) (black crosses) for $Mg_{0.7}SiO_{2.7}$ grains with an MRN size distribution, and the model fluxes (red crosses). The SEDs from each dust component as defined in Table 6.1 are shown as dashed lines (preshock: blue, clump: red, diffuse: green, blastwave: purple).

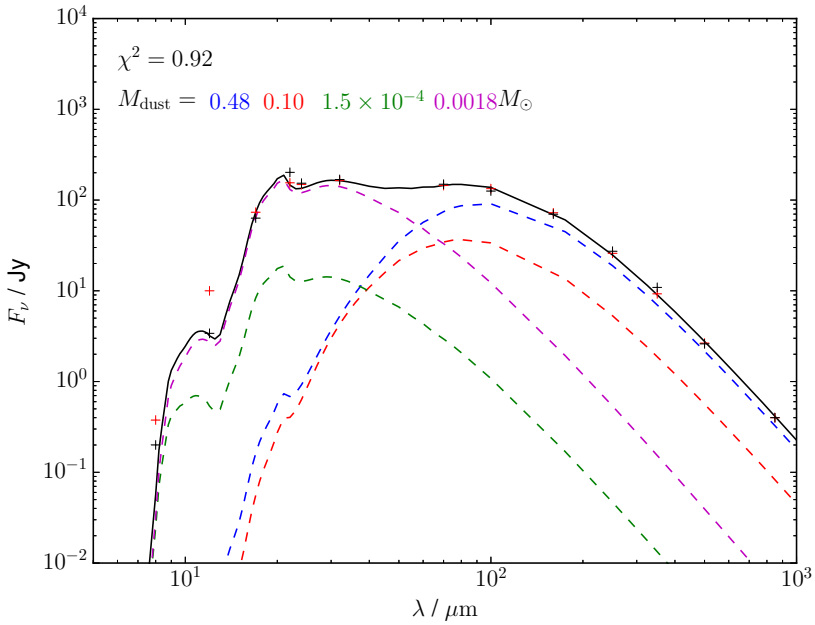

Figure 6.5: Best-fit total dust SED (black solid line) to the $G = 0.6G_0$ SNR dust fluxes from De Looze et al. (2017) (black crosses) for $Mg_{0.4}Fe_{0.6}SiO_3$ grains with an MRN size distribution, and the model fluxes (red crosses). The SEDs from each dust component as defined in Table 6.1 are shown as dashed lines (preshock: blue, clump: red, diffuse: green, blastwave: purple).

dust SEDs there is a large amount of degeneracy between them. Figure 6.7 shows an SED fit for only the three ejecta components. While the χ^2 is worse than for models with all four components, the fit is still acceptable, with the diffuse dust mass comparable to the values found for the blast wave component in Table 6.4. The total dust mass is close to the four-component fit value, although the fraction of dust in the clumps is larger. It is also clear from the figure that the preshock and clump dust SEDs are somewhat degenerate as well - however, the additional emission from the clump dust SED at $< 100\,\mu$m means that models with more dust in the unshocked ejecta provide better fits.

While the temperatures and densities of the matter in the two X-ray emitting components have been derived from observations (Willingale et al. 2003), the two cooler components, which contain most of the dust mass, have more uncertain properties. The gas temperatures are fairly well constrained, while Smith et al. (2009) found an upper limit of $n_{\rm e} \lesssim 100\,{\rm cm}^{-3}$ for the preshock ejecta, but the reported densities for the clump material range up to $10^5\,{\rm cm}^{-3}$, far higher than our model value of $480\,{\rm cm}^{-3}$. Both dust components are primarily heated by the synchrotron radiation field, which we obtained by interpolating between radio and X-ray measurements and assuming a mean distance of 1 pc from

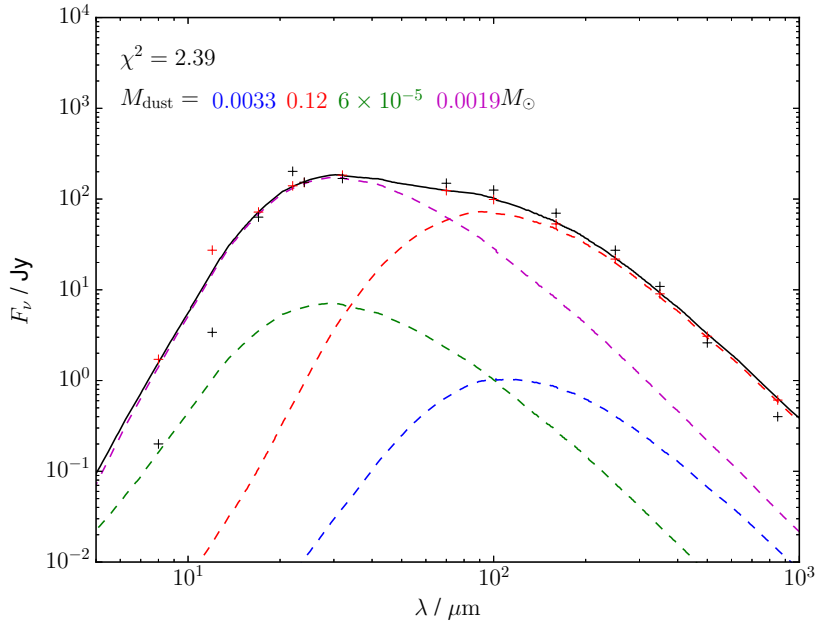

Figure 6.6: Best-fit total dust SED (black solid line) to the $G = 0.6G_0$ SNR dust fluxes from De Looze et al. (2017) (black crosses) for ACAR grains with an MRN size distribution, and the model fluxes (red crosses). The SEDs from each dust component as defined in Table 6.1 are shown as dashed lines (preshock: blue, clump: red, diffuse: green, blastwave: purple).

the synchrotron radiation source in the blastwave - the actual radiation field could differ in both strength and spectral shape. We have also assumed an MRN size distribution for all dust components, which may not be justified given the expected growth of grains in the preshock component and the processing of grains in the reverse shock.

To investigate the sensitivity of our results to the synchrotron radiation field, probably the least certain of our model inputs, we increased its strength by a factor of 10 for all components. Figure 6.8 shows the best fit SED for $MgSiO_3$ grains. The required dust masses in the preshock and clump components are reduced to $\sim 0.1\,M_\odot$, while the diffuse and blast wave components, which are heated by particle collisions, are less affected. The model is a poor fit, in particular to the long-wavelength data, where it predicts significantly less flux than observed. We find that this can be remedied by changing the size distribution in the unshocked component to grains only between radii of $0.1 - 1.0\,\mu$m. This is shown in Figure 6.9 - the dust mass is still lower than models with the original choice of radiation field, but only by about a third, and the proportion in the preshock component is even higher.

The effects of electron and ion collisional heating for the preshock dust are negligible,

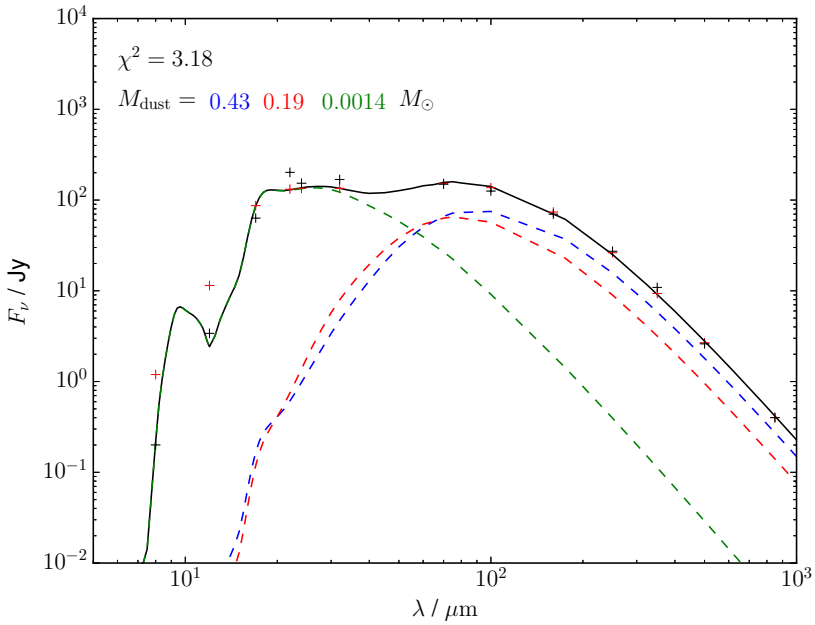

Figure 6.7: Best-fit total dust SED (black solid line) to the $G = 0.6G_0$ SNR dust fluxes from De Looze et al. (2017) (black crosses) for $MgSiO_3$ grains with an MRN size distribution, and the model fluxes (red crosses), using only the three ejecta components. The SEDs from each dust component as defined in Table 6.1 are shown as dashed lines (preshock: blue, clump: red, diffuse: green).

while for an electron density of $480\,\mathrm{cm}^{-3}$ in the clump component they contribute only a small fraction of the total heating. Increasing the density to $10^4\,\mathrm{cm}^{-3}$ reverses the situation, with electron collisions dominating the heating rate, and the predicted SED shifts towards shorter wavelengths. However, the effect on the derived dust masses is minor - the clump dust mass falls by a factor of ~ 3, and the other three components are reduced by smaller amounts, but the total dust mass is still $> 0.5\,\mathrm{M}_\odot$. Similarly, we find that varying the exponent in the grain size distribution power law between $2-4$, or the values of $a_{\rm min}$ and $a_{\rm max}$ between $0.001-1.0\,\mu$m, does not significantly affect the dust mass required for models which fit the observations well. Regardless of the choice of parameters, the observed SED requires a population of cold ($\sim 20-30\,\mathrm{K}$) dust grains to fit the long wavelength data, and hot ($\geq 100\,\mathrm{K}$) grains for the $17-32\,\mu$m fluxes. The roughly constant flux between 20 and $100\,\mu$m constrains the number of intermediate temperature grains, meaning that the long wavelength flux must be produced by cold grains, thus effectively requiring a mass of $> 0.1\,\mathrm{M}_\odot$ regardless of the assumed dust and gas properties.

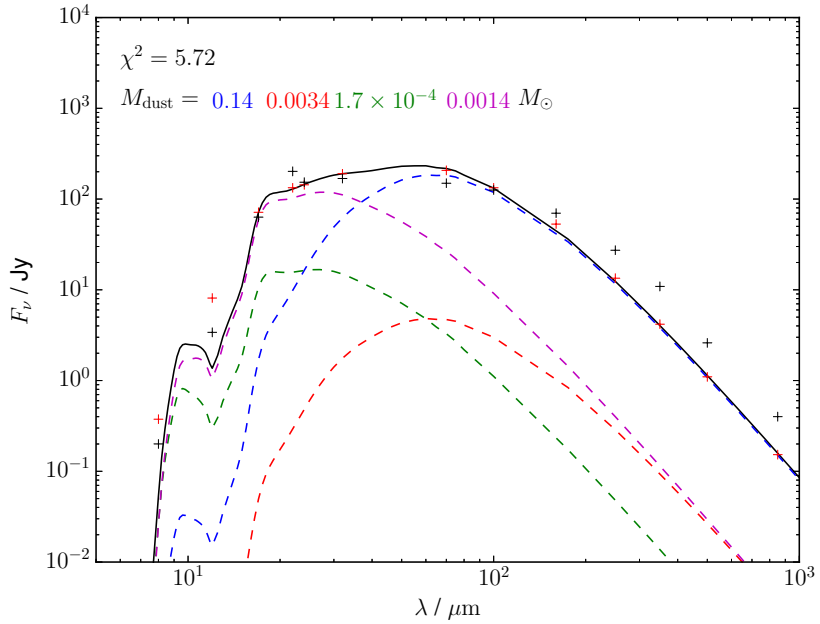

Figure 6.8: Best-fit total dust SED (black solid line) to the $G = 0.6G_0$ SNR dust fluxes from De Looze et al. (2017) (black crosses) for $MgSiO_3$ grains with an MRN size distribution, and the model fluxes (red crosses) with the radiation field strength increased by a factor of 10. The SEDs from each dust component as defined in Table 6.1 are shown as dashed lines (preshock: blue, clump: red, diffuse: green, blastwave: purple).

6.5 Discussion

6.5.1 Comparison with previous results

Our total dust masses are comparable to those found by De Looze et al. (2017) - given that we use their best-fit SNR dust fluxes as input, this is unsurprising. Although not directly equivalent, their 'cold' dust component corresponds to the flux produced by our preshock and clump components, while their 'warm' and 'hot' dust corresponds to the two X-ray emitting components. The required dust masses are greater than previous studies of the infrared emission have found for Cas A (Rho et al. 2008; Barlow et al. 2010; Arendt et al. 2014), generally $\lesssim 0.1\,M_\odot$ - as discussed by De Looze et al. (2017), this is due to the inclusion of better defined long wavelength data, allowing the cold dust contribution to be better determined. Modelling of Cas A integrated emission line profiles by Bevan et al. (2017) found a dust mass of $\sim 1\,M_\odot$, comparable to our values.

As well as the total dust mass, our preferred dust compositions are also similar to those found by De Looze et al. (2017), with various magnesium-containing silicates (with the exception of $Mg_{0.7}SiO_{2.7}$) all proving acceptable. While De Looze et al. (2017) suggested

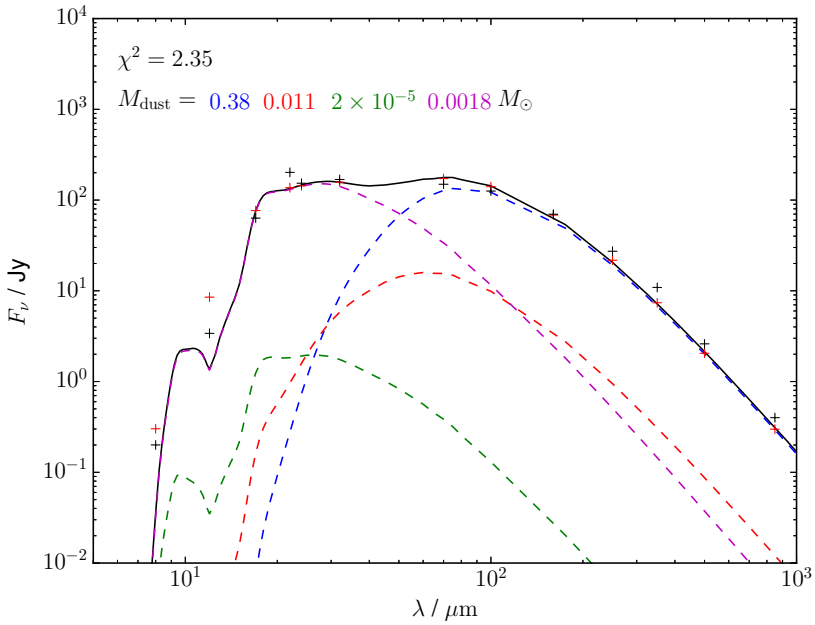

Figure 6.9: Best-fit total dust SED (black solid line) to the $G = 0.6G_0$ SNR dust fluxes from De Looze et al. (2017) (black crosses) for $MgSiO_3$ grains, and the model fluxes (red crosses) with the radiation field strength increased by a factor of 10. The preshock component MRN-like grain radius distribution is between 0.1 and 1.0 μm. The SEDs from each dust component as defined in Table 6.1 are shown as dashed lines (preshock: blue, clump: red, diffuse: green, blastwave: purple).

some carbon dust could also be present, we find that even a small ($\sim 10^{-3}\,M_\odot$) mass of carbon dust in the X-ray emitting gas predicts near-infrared fluxes in conflict with observations, although larger dust masses could be present in the cooler regions. Bevan et al. (2017) found that mixtures of carbon and silicate grains can explain line-profile asymmetries in Cas A, but increasing the proportion of silicates required increasingly large dust masses, up to unreasonably high values ($6.5\,M_\odot$ for 90% silicates). Since the unshocked ejecta would be responsible for the majority of the line asymmetry, this is not necessarily in conflict with our results, although the lack of carbon in the shocked ejecta would require explanation if it makes up a significant fraction of the unshocked ejecta. Multiple dust species have been used by Rho et al. (2008) and Arendt et al. (2014) to fit the mid-infrared spectrum, which we discuss further in the next section, but some form of magnesium silicate was required by both those studies.

Theoretical studies of the formation of dust in the specific case of Cas A have led to differing results. Nozawa et al. (2010) predicted a total dust mass of $0.167\,M_\odot$ with roughly equal quantities of carbon and magnesium silicates, and smaller contributions from other

species. Bocchio et al. (2016) predicted an even higher dust mass of $0.92\,M_\odot$, about half of which is in silicates and a smaller fraction in carbon, while Biscaro and Cherchneff (2016) predicted only $\sim 10^{-2}\,M_\odot$ with the main dust component being Al_2O_3. Of these studies only that of Bocchio et al. (2016) is consistent with our results - the others predict dust masses both significantly smaller than our required values, and of different composition. While we did not investigate Al_2O_3, De Looze et al. (2017) found that the required mass of aluminium for this composition significantly exceeded that expected from calculations of the nucleosynthetic yields by Woosley and Weaver (1995).

6.5.2 The mid-infrared spectrum

Rho et al. (2008) and Arendt et al. (2014) both used *Spitzer* IRS $5-30\,\mu$m spectra of Cas A, in addition to longer-wavelength photometric data extending to $160\,\mu$m, to investigate the dust composition in different regions of the SNR. Rho et al. (2008) categorized the spectra based on the strength of the $21\,\mu$m peak compared to the continuum, whereas Arendt et al. (2014) defined various regions of the remnant characterised by particular dominant emission features (line or continuum), and treated the dust emission from these regions as separate populations. Rho et al. (2008) found $0.02-0.05\,M_\odot$ of dust, with the dominant materials being carbon and simple iron and silicate species (e.g. FeO, SiO_2), although also requiring some form of magnesium silicate and Al_2O_3. Arendt et al. (2014) found $\sim 0.04\,M_\odot$ of dust which could mostly be fit by a combination of magnesium silicates and some additional featureless dust component (carbon, Al_2O_3 or Fe/FeS/Fe_3O_4), plus an additional featureless dust component of $\lesssim 0.1\,M_\odot$ associated with the [Si II] emission, which they could not constrain the composition of but associated with the unshocked ejecta.

Both studies found dust masses lower than our values by an order of magnitude - this is again due to the additional long wavelength fluxes used, where the majority of the dust emits. Arendt et al. (2014) did include Herschel PACS fluxes to constrain the dust masses, in particular the [Si II] component, from which they determined an upper limit of $0.1\,M_\odot$ of unshocked dust, well below our values of $\sim 0.5\,M_\odot$. However, in determining the ISM dust contribution at $160\,\mu$m they assumed a scaled version of the SPIRE $250\,\mu$m map, whereas De Looze et al. (2017) find a substantial SNR contribution to the $250\,\mu$m flux. Their SNR $160\,\mu$m flux, and the derived dust mass, are therefore lower than the values from De Looze et al. (2017) which take into account ISM and SNR dust emission

simultaneously.

Although there are variations from position to position, the main features of the mid-IR spectra are two emission peaks of varying strength at $\sim 10\,\mu$m and $21\,\mu$m, and an underlying continuum which rises to $21\,\mu$m and stays roughly constant or falls to longer wavelengths. While Rho et al. (2008) and Arendt et al. (2014) used various combinations of dust species and temperature components to fit this behaviour, our model SEDs reproduce this naturally using single silicate species - the two peaks and the rising part of the continuum are produced by grains in the high temperature X-ray emitting parts of the ejecta, while dust in the cooler regions produces an increasing fraction of the flux towards longer wavelengths, preventing the decline found with single-temperature $\sim 100\,$K SEDs. Some spectra ('featureless' in Rho et al. (2008), '[Ne II]' in Arendt et al. (2014)) required an additional dust component at $\sim 10\,$K to explain featureless emission, possibly carbon or Al_2O_3, but we find that the observations are consistent with magnesium silicate grains making up the majority of the dust present in the SNR.

Our best-fit magnesium silicate models all underpredict the flux at $21\,\mu$m, with the exception of $Mg_{0.7}SiO_{2.7}$, which otherwise provides a poor fit. The shape of our predicted SED in this region also clearly differs from many of the individual IRS spectra ('$21\,\mu$m peak dust' in Rho et al. (2008)), suggesting that some additional component may be contributing at this wavelength. Arendt et al. (2014) attribute this component to $Mg_{0.7}SiO_{2.7}$, while Rho et al. (2008) adopt a combination of FeO and SiO_2. Including an additional dust component from one of these species, assuming FeO and SiO_2 can be treated as silicates and using the diffuse X-ray emitting gas properties, we find that this $21\,\mu$m excess can be reproduced with the addition of $\sim 5 \times 10^{-4}\,M_\odot$ of dust. FeO and $Mg_{0.7}SiO_{2.7}$ both produce similar SEDs, while SiO_2 produces an additional sharp peak at $\sim 12\,\mu$m, similar to that seen in some of the IRS spectra (e.g. Figure 3 of Rho et al. (2008)) and not produced by other silicate species.

6.5.3 Gas-to-dust mass ratios

For the three dust species considered that produce acceptable fits to the observed SED ($MgSiO_3$, $Mg_{0.4}Fe_{0.6}SiO_3$ and $Mg_{2.4}SiO_{4.4}$), we find similar dust masses in each of the four components - $\sim 0.5-0.6\,M_\odot$ in the preshock ejecta, $\sim 0.1\,M_\odot$ in the clumps, and $10^{-4}/2\times 10^{-3}\,M_\odot$ in the X-ray emitting reverse shock/blast wave gas. Taking the gas masses of these components as 3.0 (Arias et al. 2018), 0.59 (M. J. Barlow, private communication),

and 1.68 and 8.32 $M_\odot$ (both from Willingale et al. (2003)) respectively, this gives gas-to-dust mass ratios of 5.0, 5.9, 16800 and 4160, compared to a typical Galactic ISM value of $\sim$ 150 Draine (2011). The gas mass of 3 $M_\odot$ obtained by Arias et al. (2018) for the preshock component was noted by those authors to be higher than expected by many models of the emission from the shocked gas for the Cas A SNR, and could be lower if the unshocked ejecta gas has a lower temperature than assumed, or has a clumpy structure. Raymond et al. (2018) found a temperature of $\sim$ 100 K for this component, the same value used to derive the 3 $M_\odot$ dust mass, but the level of clumping is still uncertain. The gas-to-dust ratio for this component is therefore an upper limit (assuming our dust mass is accurate), while for the other components the gas masses are better defined.

The ejecta gas-to-dust ratios are $\sim 20\times$ lower than in the ISM, implying that a significant fraction of the metals are condensed into dust grains (0.2, assuming all the ejecta mass is condensible material). Nozawa et al. (2010) found a condensation efficiency of 0.13 in their model of dust formation in Cas A, although they predicted a lower dust mass than our models require, and also predicted that the main dust component is carbon, which we rule out. The higher-than-ISM gas-to-dust mass ratios in the two diffuse shocked components are consistent with significant dust destruction by both the forward and reverse shocks. Even if the blastwave dust mass is attributed instead to the reverse shock (which is possible, due to the degeneracy between the two components), the gas-to-dust ratio would be 800, implying that $< 1\%$ of the original dust mass has survived. The surviving dust mass in the Cas A model of Bocchio et al. (2016) is $\sim 1\%$ of the initial mass.

Conversely, we find that the gas-to-dust ratio in the clumps is very similar to that in the the preshock ejecta, suggesting that dust within the clumps has been protected from destruction by the reverse shock. Biscaro and Cherchneff (2016) predicted a surviving dust mass fraction of $6 - 11\%$ for clumps in the Cas A SNR, while Micelotta et al. (2016) predicted a surviving fraction of 11.8% for silicate grains, lower than our implied value even for conservative estimates of the unshocked ejecta gas mass. These models include sputtering of dust grains expelled from the clumps into the inter-clump medium - the value accounting for sputtering within the clumps from Biscaro and Cherchneff (2016), before injection into the inter-clump medium, is $28 - 58\%$, which is consistent with our results if the unshocked ejecta gas mass were $\sim 2\,M_\odot$.

6.6 Conclusions

We have modelled the emission from dust grains subjected to the physical conditions present in the Cas A SNR, using the new code DINAMO, and used the SNR dust fluxes from De Looze et al. (2017) to constrain both the mass of dust present, and its distribution between various componets of the remnant. We find dust masses of $\sim 0.6 - 0.7\,\mathrm{M}_{\odot}$ depending on the silicate composition, with the majority being located in the unshocked ejecta and only a small fraction present in the hot X-ray emitting gas. The gas-to-dust ratio in the shocked clumpy ejecta is similar to that in the unshocked region, while in the diffuse components it is significantly higher. This is consistent with dust grains being efficiently sputtered at high temperatures, whereas in the ejecta clumps which have passed through the reverse shock, the dust is apparently protected from destruction. Magnesium silicate grains, with possible iron inclusions, are found to reproduce almost all of the observed Cas A dust spectrum, with a relatively minor amount of another species (FeO, SiO_2 or $Mg_{0.7}SiO_{2.7}$) required to reproduce the 21 μm emission peak. While carbon grains may be present, they cannot make up a large fraction of the total dust mass ($< 25\%$). The total dust mass in Cas A is consistent with CCSNe being significant contributors to the dust in high-redshift galaxies, particularly if much of it is present in clumps which survive the passage of the reverse shock without disruption.

This page was intentionally left blank

Chapter 7

Conclusions

In this thesis, numerical models of stellar remnants have been used to predict the values of various observational properties, primarily the emission strength of atomic and molecular lines and the dust continuum. These results have been compared to observed values, and used to constrain various physical properties of the models.

In Chapter 3, a combination of photoionization and photodissociation region codes was used to model the molecular emission from dense knots in planetary nebulae, with varying central star properties and gas densities. With the inclusion of the ionizing UV flux, usually neglected in PDR studies, the observed surface brightnesses of H_2, OH^+ and CO were well reproduced. The detection of OH^+ emission only from PNe with central star temperatures $> 100\,\mathrm{kK}$ was explained as being due to the higher ionizing flux from these stars creating larger ionized regions in the knots, where the OH^+ emission originates. Some PNe have H_2 surface brightnesses above that predicted by any of the models, suggesting an additional source of gas heating may be present. The non-detection of ArH^+ in any PN was consistent with the model predictions - however, HeH^+ line surface brightnesses were above detection thresholds, despite their non-detection. This suggests the HeH^+ reaction network may be incorrect - the models did not include photodissociation of this molecule, which would reduce the abundance and therefore the predicted emission strength. This chapter focused on the five molecules mentioned above, but observations of PNe have detected many other molecular species, which could also be used to constrain the models. The additional heating mechanism introduced to explain the highest H_2 surface brightnesses could also be

investigated further - the CO line strength is affected much more than the OH^+ emission, potentially allowing for an observational test of various scenarios, particularly with the addition of other species.

In Chapter 4, the method in Chapter 3 was applied to the Crab Nebula, a supernova remnant in which ArH^+ was detected for the first time in an astrophysical environment. The cosmic ray ionization rate, representing the flux of charged particles from the pulsar wind nebula, and the gas density were varied and the resulting line surface brightnesses compared to the Herschel SPIRE FTS observations. Cosmic ray ionization rates $\geq 10^6$ times the standard interstellar value were required to reproduce the observed line strengths and the non-detection of [C I] emission. Models consistent with the SPIRE FTS data predict [O I] and [C II] surface brightnesses in excess and H_2 emission below that of the observed values - accounting for the effects of beam size, it is possible to predict all emission lines successfully using cloud properties (visual extinction and size) similar to those of the observed dust globules in the Crab, suggesting that these are also the source of the molecular emission. Shock heating, previously suggested as the source of the H_2 emission, is ruled out due to its prediction of significant [C I] line surface brightnesses. The models suggest that the molecular-emitting gas can also contribute substantially to lines which have previously been modelled as resulting from the photoionized gas (i.e. the [C I] $9825+9850$ Å lines). Combined modelling of both components in order to disentangle their emission would allow a more accurate determination of the elemental abundances in the Crab Nebula, important for stellar nucleosynthesis models.

In Chapter 6, the dust emission from the Cassiopeia A supernova remnant was modelled assuming four main gas components in which dust is heated by both radiation and particle collisions, with the properties based on observations. The dust masses in each component were fit to match the observed SED from $17-850\,\mu$m. The required dust masses confirm previous results, with $\sim 0.6\,M_\odot$ of silicate dust primarily in the unshocked ejecta providing the best fit. Carbon grains, and silicates with low Mg ratios, were ruled out as major constituents of the dust mass. Comparison with near-infrared spectra of the remnant showed that while single silicate species could fit most features, the emission peak at 21 μm requires $\sim 10^{-4}\,M_\odot$ of some other composition in the X-ray emitting gas. FeO, SiO_2 and $Mg_{0.7}SiO_{2.7}$ could all reproduce this feature, with SiO_2 additionally contributing to peaks at shorter wavelengths seen in some of the spectra. Using estimates for the gas masses in each component, the gas-to-dust ratios were calculated, showing a high condensation

efficiency in the ejecta, significant dust destruction in the diffuse shocked components and that clumped dust is protected against destruction by the reverse shock. This analysis was carried out on the global SED for the SNR - emission maps of the remnant are also available, which would allow the location of the various components to be compared to optical and X-ray observations. The variation of the SED with location, particularly in the near-infrared, could also be used to better constrain the dust species present in the remnant, particularly in regions which do not show obvious silicate features. The method used could be applied to other supernova remnants for which sufficient data is available, for example the Crab Nebula and the remnant of SN1987A.

Appendix A

Prestellar cores

The work presented in this chapter is based on the paper Priestley et al. (2018) with S. Viti and D. A. Williams.

A.1 Introduction

Low-mass stars are formed from dense ($\gtrsim 10^4\,\mathrm{cm}^{-3}$), cold ($\sim 10\,\mathrm{K}$) regions in molecular clouds (Myers and Benson 1983; Myers 1983) - the masses of cores within molecular clouds follow a simlar distribution to the stellar initial mass function (Motte et al. 1998), and young low-mass stars are frequently found in association with dense cores (Cohen and Kuhi 1979). Observations of molecular line and dust continuum emission can be used to determine the density and velocity structure of cores, providing information on whether, and how, the core is collapsing. Relating the observed emission to the gas density requires a conversion factor, introducing systematic uncertainties to the result. Combined with observational uncertainties, the derived density structures of prestellar cores are unable to conclusively differentiate between various proposed modes of collapse, particularly as the structures predicted by hydrodynamical simulations are often qualitatively similar (e.g. Foster and Chevalier 1993; Fiedler and Mouschovias 1993; Tomisaka 1995).

The timescales of chemical reactions in prestellar cores ($t_{\mathrm{chem}}^{-1} = kn(\mathrm{Y})$ for the destruction of species X in a two-body reaction with species Y, where k is the reaction rate and $n(\mathrm{Y})$ is the number density of Y) are comparable to the timescale of gravitational collapse

($t_{ff} = \sqrt{\frac{3\pi}{32G\rho}}$ where ρ is the mass density and G the gravitational constant). As such, collapsing prestellar cores are not in chemical equilibrium, and the molecular abundances can be affected by the details of the collapse. Simulations of the chemical evolution of collapsing cores (Rawlings et al. 1992; Bergin and Langer 1997; Aikawa et al. 2001) have found that some molecules do show variations in abundance depending on the assumed hydrodynamical model, providing an alternative observational test of theoretical models of star formation. Due to the computational expense of coupling large chemical networks with hydrodynamical codes, especially with the inclusion of magnetic fields, one side of the problem is often simplified. Rawlings et al. (1992) and Aikawa et al. (2001) both used analytical expressions for the evolution of the gas density, from Shu (1977) and Larson (1969) respectively, which are not necessarily representative of realistic collapse (Hunter 1977). Aikawa et al. (2005) treated both the hydrodynamics and the chemistry self-consistently for one-dimensional collapse, while Hincelin et al. (2016) followed the chemical evolution of a full three-dimensional magnetohydrodynamical (MHD) simulation. Inclusion of non-ideal MHD effects such as ambipolar diffusion has been studied under one- (Li et al. 2002) and two-dimensional (Tassis et al. 2012) simplifications.

In this chapter we propose a different approach: we parametrize the results of hydrodynamical simulations of collapsing prestellar cores to describe how the density behaves as a function of radius and time for different models, and incorporate these parametrizations into a gas-grain time dependent chemical model. Although less accurate than a simultaneous solution of both the hydrodynamics and chemistry, this approach removes the need for simplifications in either area, while also being much less computationally expensive, and so enabling the exploration of larger regions of parameter space than has so far been feasible.

This chapter is laid out as follows: in Section A.2, we describe our parametrizations of hydrodynamical simulations, and we discuss the chemical model into which we incorporate them; in Section A.3 we present the results of our grid of models, showing how the abundances of key molecules are affected; in Section A.4 we investigate whether the inclusion of ambipolar diffusion affects star formation timescales; we briefly discuss our findings and conclude in Section A.5. In Appendix B we list the functions used in our parametrization of the numerical simulations.

A.2 Methodology

A.2.1 Parametrization of numerical simulations

Empirical models were developed to reproduce the results from four numerical simulations of collapsing prestellar cores: Aikawa et al. (2005) used a BE sphere as the initial configuration, with the density increased by a factor of either 1.1 (model BES1) or 4 (BES4) to take the core out of equilibrium and instigate collapse; Nakamura et al. (1995) studied the collapse of a magnetically supported filament when a density perturbation is applied (MS); and Fiedler and Mouschovias (1993) followed the evolution of a core as magnetic support is removed through ambipolar diffusion (AD).

Each of these studies produced the density profile (number density for BES1, BES4 and AD, mass density for MS) of the core as a function of time during the collapse. We extracted data from published plots of the density profiles at different times, as shown in Figure A.1 with data from Aikawa et al. (2005) as an example.

For each density profile, a function, depending on position in the core, reproducing its shape was found. In the two models including magnetic effects (MS and AD), density profiles were given for both the radial ($z = 0$) and z axes. Only the density profile in the radial direction was considered, as the core rapidly collapses into a thin disc so that structure along the z-axis is less significant. For the BES1, BES4 and AD models, a function of the form

$$n(r) = \frac{n_0}{1 + (\frac{r}{r_0})^a} \tag{A.1}$$

with n_0, r_0 and a free parameters determining the central density, the width of the central density peak, and the slope of the profile, provided a good fit to the simulation density profiles. Tafalla et al. (2002) used Eq. A.1 to fit the observed density profiles of prestellar cores. For the MS model, the radial profiles could not be approximated by Eq. A.1. The equilibrium density (in this case mass, rather than number, density) of the filament is given by an equation of the form

$$\rho(r) = \rho_0 \left(1 + \left(\frac{r}{r_0}\right)^2\right)^{-a} \tag{A.2}$$

which was adapted to reproduce the data by changing the outer exponent a, so that the

slope at large r is the same as in the simulated data.

The values of the free parameters were chosen to approximate the density profiles at each time point given. Figure A.1 shows the result for the Aikawa et al. (2005) data. For each parameter, the time evolution was also approximated by a similar method. For example, the central density parameter's time evolution was found to be well reproduced by

$$\log n_0(t) = A(t_0 - t)^a + B \tag{A.3}$$

for all simulations, where t_0 is the simulation's duration. a was chosen such that $\log n_0$ is approximately linear with $(t_0 - t)^a$, and the coefficients A and B can then by found by linear regression. Figure A.2 shows the variation of the central density parameter, n_0, with time for the data from Aikawa et al. (2005), along with the resulting approximation to the time dependence of this parameter. Once all the parameters have been approximated in this way, the density can be calculated as a function of time and space, shown in Figure A.3 compared with the original data. Figures A.4, A.5 and A.6 show the corresponding density profile approximations for the BES4, MS and AD collapses respectively. The equations used to approximate the time dependence of the density profiles are given in Appendix B. The maximum discrepancies between the simulations and approximated densities are 34%, 240%, 66% and 53% for the BES1, BES4, MS and AD cases respectively, while the average discrepancies are 10%, 26%, 16% and 16%. The large ($> 100\%$) errors in the BES4 approximation occur only at late times and large radii - otherwise the agreement with the data is at a similar level to the other collapses.

Our approximations give the time evolution of the density at a given radius. However, during collapse the individual parcels of gas do not remain at a constant radius, but move inwards, leading to a different density evolution than for fixed r. For the BES1 and BES4 models, we determine the new radius of a parcel at each time step by calculating the mass interior to its initial radius at $t = 0$, $M(< r_0)$, and finding the radius at the given time which encloses the same mass. The MS and AD approximations are not spherically symmetric, so this approach would require knowledge of the density at each point. Instead, we use the same methods as for the density to approximate the radial velocity profiles, and use these to calculate the new parcel radius at each timestep. The gas density versus time, for parcels of differing initial radii, in the BES1 collapse is shown in Figure A.7.

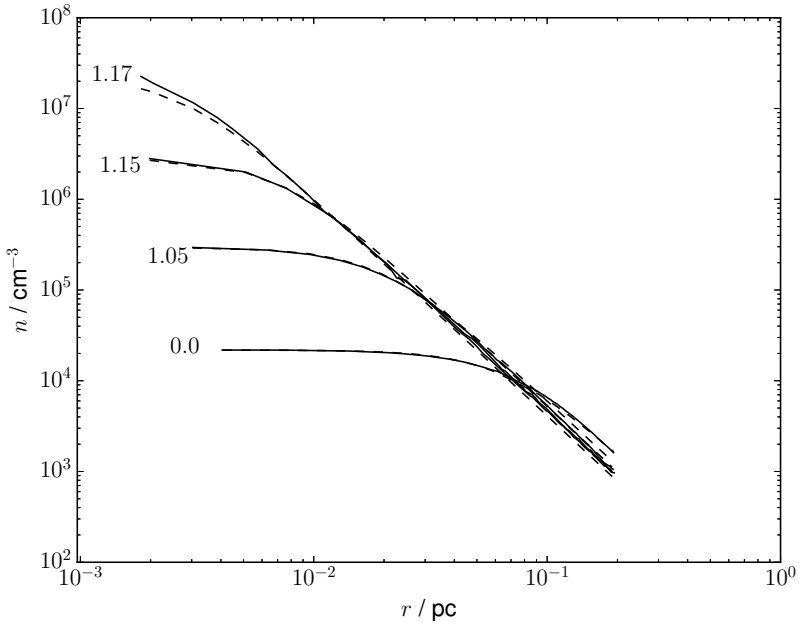

Figure A.1: Density profiles taken from Aikawa et al. (2005) (solid lines), with the approximate profiles calculated using Eq. A.1 (dashed lines). The labels indicate the time since collapse in 10^6 yr.

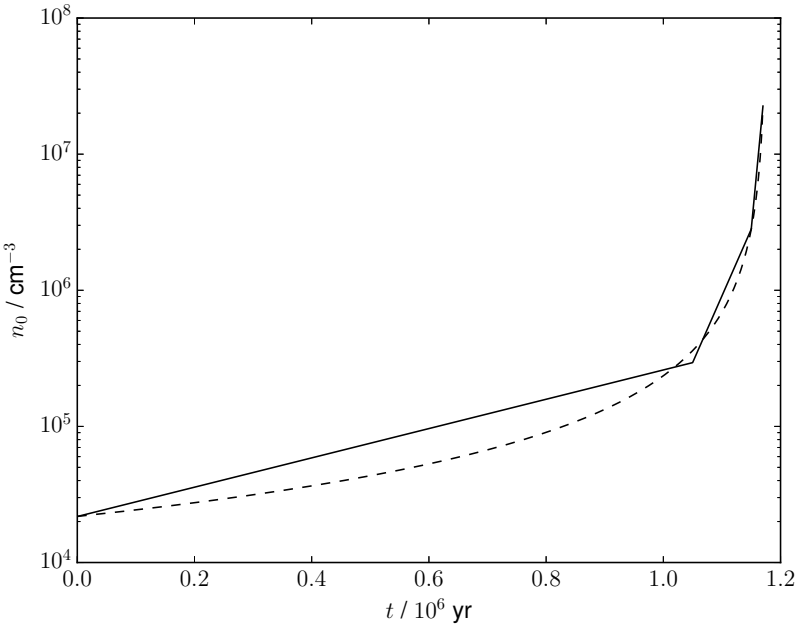

Figure A.2: Central density n_0 against t for the approximations to the Aikawa et al. (2005) data (solid), with the approximate fit to the time evolution (dashed).

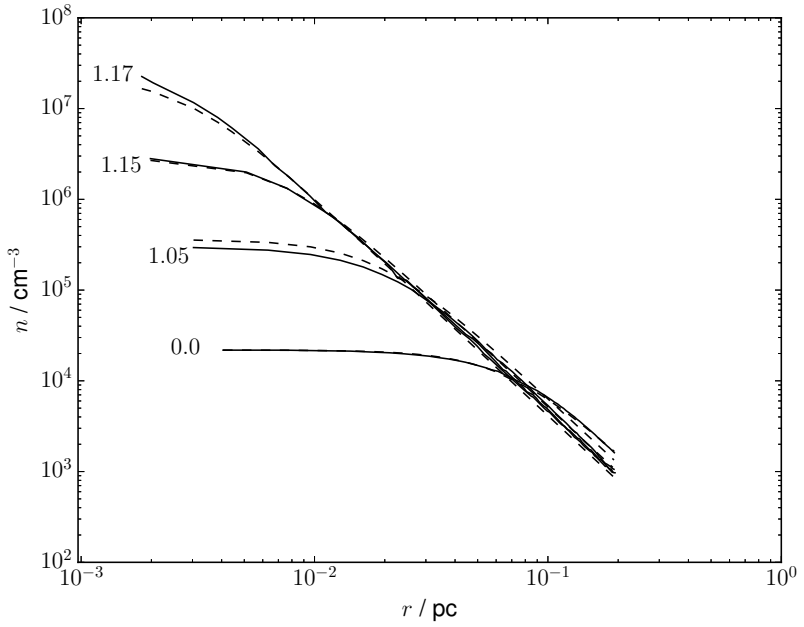

Figure A.3: As Figure A.1, but with the parameters for Eq. A.1 calculated as a function of time.

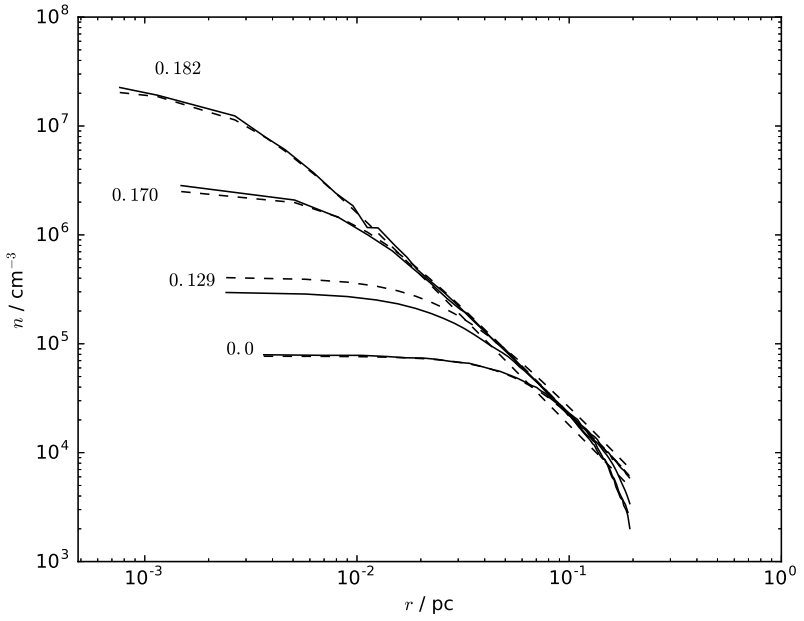

Figure A.4: As Figure A.3, for the BES4 collapse

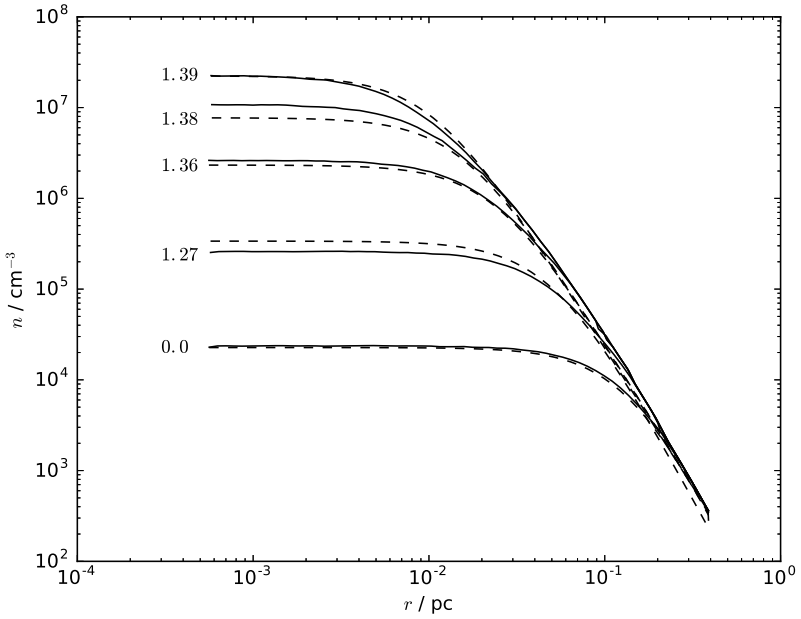

Figure A.5: As Figure A.3, for the MS collapse

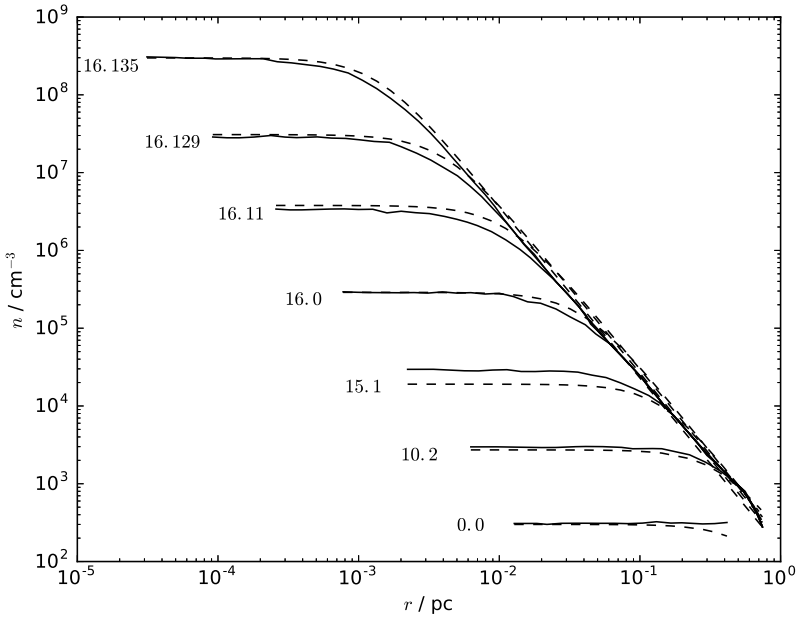

Figure A.6: As Figure A.3, for the AD collapse

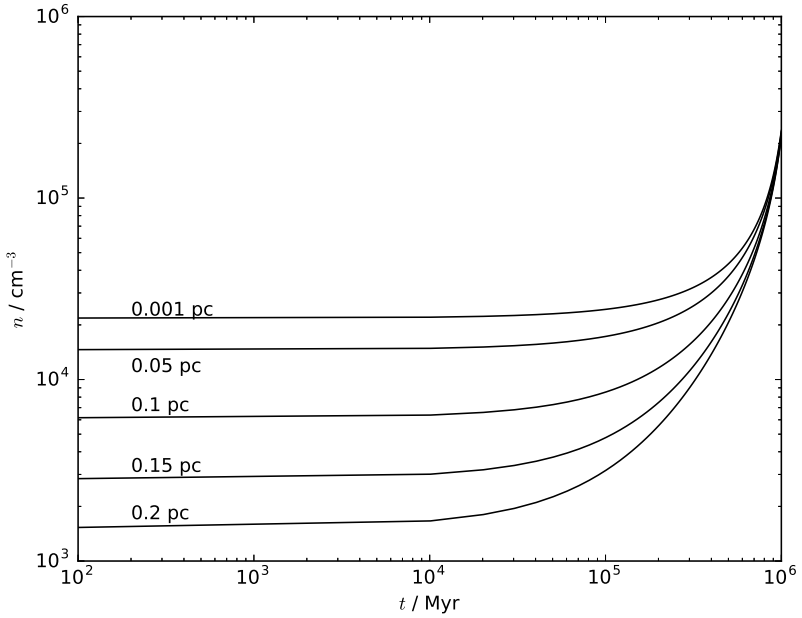

Figure A.7: Parcel density versus time for the BES1 collapse, for different initial parcel radii.

A.2.2 Chemical modelling

The four density approximations were used as input for the chemical code UCLCHEM. The code is described in Viti et al. (2004) and references therein. This code has since been made public (https://uclchem.github.io/) and is fully explained in Holdship et al. (2017). Here we briefly summarize its characteristics: UCLCHEM is a time dependent gas-grain chemical model that calculates the abundances of atoms and molecules in the gas and dust in the interstellar medium as a function of time under chemical and physical conditions set by the user. The original version of the code uses free-fall collapse to determine the density from the diffuse state to the final density of the gas where the star is born. Initial atomic elemental abundances are provided to UCLCHEM which then self-consistently calculates gas-phase chemistry, as well as sticking on to dust particles with subsequent surface processing. For the reaction network we used the UMIST 2012 network (McElroy et al. 2013), and freeze-out and grain surface reactions as described in Holdship et al. (2017). The interaction between the density approximations and UCLCHEM is shown as a flowchart in Figure A.8.

We chemically model our four parameterisations of numerical simulations: the collapse of an unstable (BES1) or highly unstable (BES4) Bonnor-Ebert sphere, collapse against

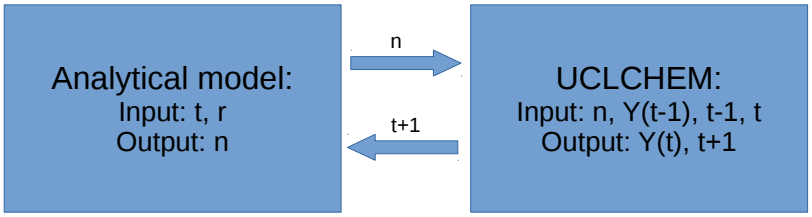

Figure A.8: Flowchart showing the interaction between the density approximations and the chemical solver in UCLCHEM. r is the initial particle radius, n is the gas density, t is the current timestep, $t-1$ and $t+1$ the preceding and following timesteps and $Y(t)$ the molecular abundances at time t.

magnetic support (MS) and collapse resulting from ambipolar diffusion (AD). A grid of models was run for each case to investigate the effects of changing other input parameters: the cosmic ray ionisation rate ζ (in units of $\zeta_0 = 1.3 \times 10^{-17}$ s^{-1}), metallicity Z, and the desorption efficiency parameters ϵ, ϕ and $Y_{\rm UV}$, corresponding to the number of molecules desorbed per H_2 molecule formed, per cosmic ray impact and per UV photon (produced by cosmic rays) absorbed respectively (Roberts et al. 2007). For our fiducial desorption efficiencies, H_2 formation is the dominant desorption mechanism, as found by Roberts et al. (2007). The values adopted for each model are given in Table A.1. We vary the cosmic ray ionization rate between the typically assumed ISM value and a value ten times higher, suggested by some studies (e.g. Neufeld and Wolfire 2017 to be a more accurate value. For the metallicity, we take minimum and maximum values spanning the range typically seen in the solar neighborhood (Hayden et al. 2015). The range of values investigated for the three desorption efficiencies are from Roberts et al. (2007). Each model was run once for each of the density approximations. We assume an external radiation field of 1 Habing, and an external extinction at the core boundary of 3 mag, the value used by Aikawa et al. (2005). The extinction from the core itself is calculated by integrating the

density profile to the boundary, (0.2 pc for the BES1 and BES4 approximations, 0.5 pc for MS and 0.75 pc for the AD case) before the onset of collapse, giving maximum extinctions (at the centremost parcel) of 6.4 (BES1), 15.2 (BES4), 7.8 (MS) and 3.3 (AD) mag. We used 13 gas parcels (14 for AD) at initial radii spaced to cover the entire range of the cores, but with an emphasis on the more rapidly evolving central regions.

The initial central number densities of the models are $n = 2.2 \times 10^4$ cm^{-3} (BES1 and MS), 8×10^4 cm^{-3} (BES4) and 300 cm^{-3} (AD). The MS equations are in terms of dimensionless variables, which can be converted into physical values by choosing the initial central density, ρ_c, and the isothermal sound speed, $c_s^2 = \frac{kT}{\mu m_H}$. The gas was assumed to be at a temperature of 10 K and composed entirely of molecular hydrogen for the purposes of calculating the mean molecular mass, giving $c_s = 203\,\mathrm{ms}^{-1}$, and we set $\rho_c = 3.67 \times 10^{-20}\,\mathrm{g\,cm}^{-3}$ to give an initial central number density equal to the BES1 model. The initial number density at each point is then given by the relevant equation for the density profile, and we allow the chemistry to evolve for 1 Myr before the onset of collapse at this density. The models were run until the central density reached 10^8 cm^{-3}. The elemental abundances relative to H for our standard model, the solar values given by Asplund et al. (2009), are listed in Table A.2 - the abundances for elements other than H and He in models with varying metallicity are multiplied by the value of Z.

Our modelling strategy relies on the ability to treat the chemistry separately from the hydrodynamics - while we account for the effect of the dynamics on the chemical evolution, we assume that the reverse can be neglected. For the BES1, BES4 and MS models, this is likely a valid assumption. The main effect of the gas composition on the hydrodynamics is in altering the cooling rate via molecular emission, and therefore the gas temperature. However, all of the hydrodynamical simulations we consider assume that the gas is isothermal, which is valid for the relevant densities (e.g. Larson 1969), and so any effect of the chemistry can be safely neglected. The AD model also assumes isothermality, but the addition of ambipolar diffusion means the dynamics depend on the degree of ionization of the gas, which determines how well-coupled it is to the magnetic field. Fiedler and Mouschovias (1993) assumed the ion density, n_i, depends on the neutral gas density as a power law with exponent 0.5, based on studies of the ionization equilibrium in static clouds (Elmegreen 1979; Nakano 1979; Falgarone and Puget 1985). As the model clouds are neither static nor in chemical equilibrium, this relation does not necessarily hold, and any difference in the ion density calculated by our chemical model should in principle

Table A.1: Model input parameters

Model	ζ/ζ_0	$Z/Z_\odot$	ϵ	ϕ	Y_{UV}
A	1	1	0.01	10^5	0.1
B1	5	1	0.01	10^5	0.1
B2	10	1	0.01	10^5	0.1
C1	1	0.3	0.01	10^5	0.1
C2	1	1.5	0.01	10^5	0.1
D1	1	1	0.1	10^5	0.1
D2	1	1	1.0	10^5	0.1
E1	1	1	0.01	10^4	0.1
E2	1	1	0.01	10^6	0.1
F1	1	1	0.01	10^5	0.001
F2	1	1	0.01	10^5	1.0

Table A.2: Elemental abundances

Element	Abundance	Element	Abundance
H	1.0	N	6.8×10^{-5}
He	0.085	S	1.3×10^{-5}
C	2.7×10^{-4}	Si	3.2×10^{-5}
O	4.9×10^{-4}	Cl	3.2×10^{-7}

affect the dynamics. As this is not possible in practice, chemical abundances for this mode of collapse should be interpreted with the caveat that they are not fully consistent with the hydrodynamics. This issue could be removed by using MHD simulations with an improved treatment of the ion density (e.g. Wurster 2016), which could be expected to agree with our chemical models. However, we do not expect the sensitivity of the dynamics to the chemistry, and vice versa, to be great enough to significantly alter our results.

A.3 Results

A.3.1 Molecular abundances across the different modes of collapse

Figure A.9 shows the density profiles of the four collapse modes at the point when the central number density, n_0, reaches $2 \times 10^5\,\mathrm{cm}^{-3}$. The BES1 and MS profiles decrease more rapidly with distance than for the BES4 and AD approximations, which have similar densities up to the end of the BES4 core at 0.2 pc. However, the time taken to reach this point is much shorter for the BES4 case ($\sim 10^5\,\mathrm{yr}$) than for AD ($\sim 10^7\,\mathrm{yr}$), so reactions which only become important at high densities have less time to affect the chemical evolution in BES4, and the molecular abundances in the two cases differ. The

BES1 and MS modes both reach $n_0 = 2\times10^5\,\mathrm{cm}^{-3}$ after $\sim 10^6\,\mathrm{yr}$, and as such the chemical evolution is similar. The densities at large ($\gtrsim 0.2\,\mathrm{pc}$) radii for BES4/AD are much higher than for BES1/MS, due to the more rapid collapse of the outer parts of the core in the BES4 case, and the magnetic support of the outer regions for AD.

Figure A.10 shows the abundances of four molecules versus radii for model A for the four density approximations, at a central density $n_0 = 2 \times 10^5\,\mathrm{cm}^{-3}$. In all cases, the CO abundance increases from a central minimum, where freeze-out has depleted most of the molecule onto grain surfaces, to a maximum value of $\sim 10^{-4}$. The BES1, BES4 and MS approximations all behave similarly in reaching the maximum, although for BES4 and MS the radius at which this occurs is larger due to the higher gas densities increasing the effect of freeze-out. The CO abundance in the AD collapse increases much more slowly, only reaching 10^{-4} at the edge of the core, whereas in the MS case the abundance begins to fall again towards the edge. This is due to the higher densities in the outer regions for the AD collapse, as magnetic support can still prevent material here from collapsing, unlike in the other three cases. The effect of the longer collapse duration is also apparent, as the AD abundances are far lower than the BES4 ones at comparable radii, despite the densities being very similar. The NH_3 abundance also increases from the centre to a maximum, before falling with radius in all models. The decline is much more gradual for the AD case than the other collapse modes, leading to an order of magnitude difference with the MS model by $r = 0.3\,\mathrm{pc}$. HCO^+ shows similar behaviour, while for HCN the AD collapse mode produces a nearly constant abundance after reaching a value of $\sim 10^{-8}$, in contrast to the others.

A.3.2 Cosmic ray ionization rate

Raising the cosmic ray ionization rate increases the abundances of molecules in the centre of the core, regardless of the collapse mode, as the rate of desorption from grain surfaces is increased. Figure A.11 shows the CO abundances for models A, B1 and B2, for the BES1 and AD density approximations, at a central density $n_0 = 2 \times 10^5\,\mathrm{cm}^{-3}$. For the BES1 collapse, the abundance at larger radii is mostly unaffected, whereas for AD the A and B2 models show noticeably different behaviour, with the CO abundance an order of magnitude lower at the edge of the core for the B2 model due to the higher cosmic ray dissociation rate. Figure A.12 shows the HCO^+ abundance for the same models. The central abundances are again enhanced for models with higher ionization rates, but

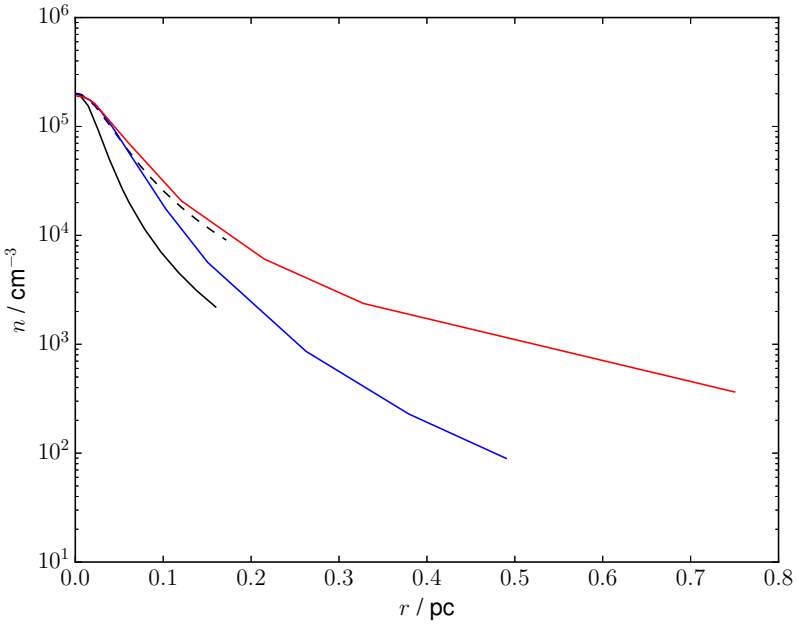

Figure A.9: Density profiles of the BES1 (solid black), BES4 (dashed black), MS (blue) and AD (red) approximations, at a central number density of $n_0 = 2 \times 10^5\,\mathrm{cm}^{-3}$.

whereas for the AD collapse mode the abundance decreases towards the edge as with CO, for BES1 the abundance is higher throughout the cloud.

A.3.3 Metallicity

Changing the metallicity of the core usually results in a corresponding change in the molecular abundances, due to the different availability of atoms to form the molecules. However, some molecules are much less affected than others. Figure A.13 shows the abundances of CO and HCN for the BES1 collapse at a central density $n_0 = 2 \times 10^5\,\mathrm{cm}^{-3}$, for models A, C1 and C2. Whereas the CO abundance scales nearly linearly with the metallicity, the HCN abundance is virtually unchanged between models. The main formation and destruction reactions for HCN both involve H^+, for which the abundance increases with decreasing metallicity (and vice versa), at least partially counteracting the effect of the changing elemental abundances on the HCN abundance.

A.3.4 Desorption efficiencies

As with the cosmic ray ionization rate, increasing the desorption efficiences increases the molecular abundances, particularly in the denser central regions where more freeze-out has taken place. Figure A.14 shows the CO abundances for models A, D1 and D2, for

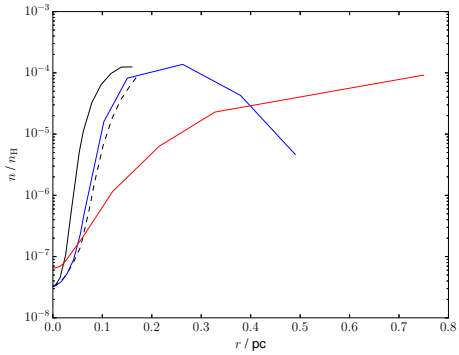

(a) CO

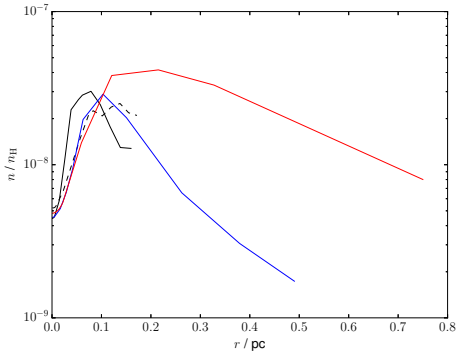

(b) NH_3

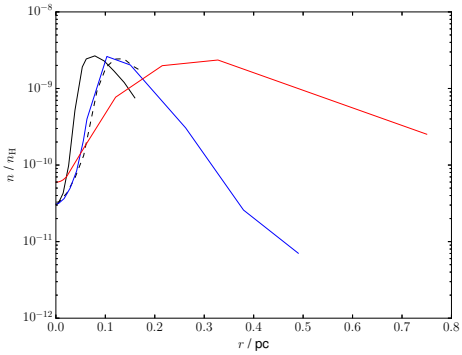

(c) HCO^+

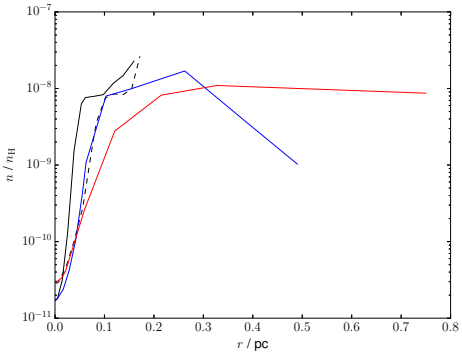

(d) HCN

Figure A.10: Abundances of CO, NH_3, HCO^+ and HCN at a central density $n_0 = 2 \times 10^5\,\mathrm{cm}^{-3}$ for model A, using the BES1 (solid black), BES4 (dashed black), MS (blue) and AD (red) density approximations.

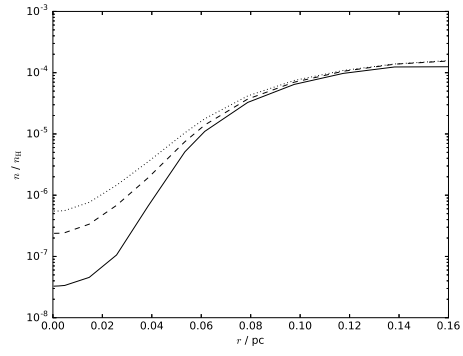

(a) BES1

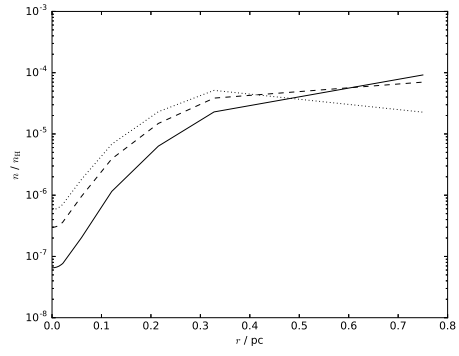

(b) AD

Figure A.11: Abundance of CO versus radius at a central density $n_0 = 2 \times 10^5\,\mathrm{cm}^{-3}$ for models A (solid line), B1 (dashed line) and B2 (dotted line), using the BES1 (left) and AD (right) density approximations.

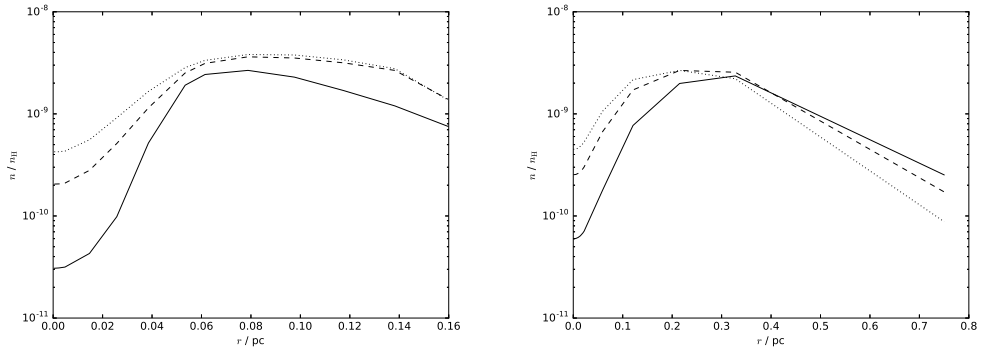

(a) BES1 (b) AD

Figure A.12: Abundance of HCO^+ versus radius at a central density $n_0 = 2 \times 10^5\,\mathrm{cm}^{-3}$ for models A (solid line), B1 (dashed line) and B2 (dotted line), using the BES1 (left) and AD (right) density approximations.

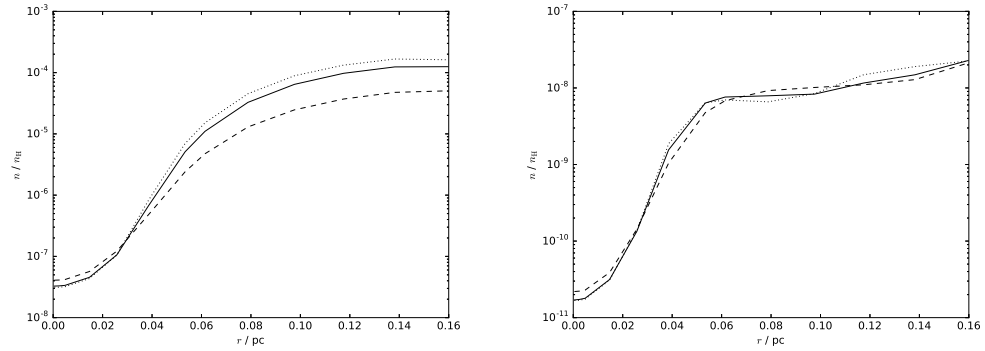

(a) CO (b) HCN

Figure A.13: Abundance of CO (left) and HCN (right) versus radius at a central density $n_0 = 2 \times 10^5\,\mathrm{cm}^{-3}$ for models A (solid line), C1 (dashed line) and C2 (dotted line), using the BES1 density approximation.

the MS and AD density approximations, where the H_2 formation desorption efficiency ϵ has been modified. While the abundances in the central regions are affected similarly for both collapse modes, at larger radii the effect is negligible for the MS collapse, whereas the CO abundance reaches 10^{-4} much more rapidly for AD - for model D2, the abundance profile looks much more similar to the other collapse modes than for model A. The BES1 and BES4 collapses behave similarly to MS for varying desorption efficiency, with very little change in the CO abundance beyond 0.1 pc. The cosmic ray heating desorption efficiency ϕ has very little effect on the abundance of any molecule, despite a factor of 100 difference between models E1 and E2. The cosmic ray induced photodesorption efficiency Y_{UV}, however, does affect molecular abundances, in particular having a significant effect on the abundance of NH_3, which is not greatly affected by variation of the other parameters

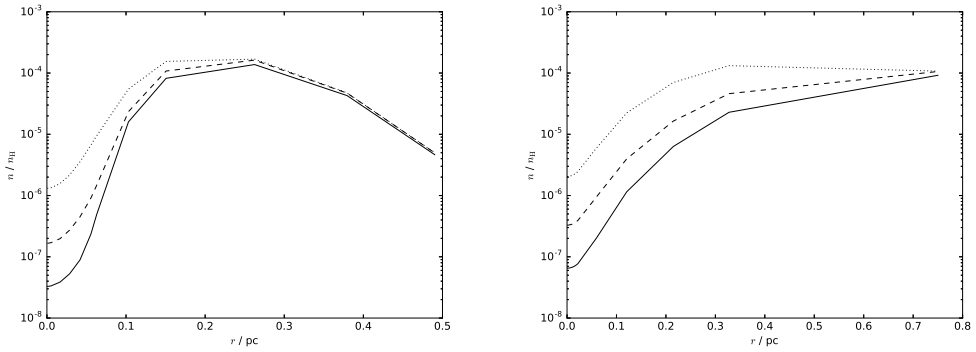

(a) MS (b) AD

Figure A.14: Abundance of CO versus radius at a central density $n_0 = 2 \times 10^5\,\mathrm{cm}^{-3}$ for models A (solid line), D1 (dashed line) and D2 (dotted line), using the MS (left) and AD (right) density approximations.

investigated.

A.4 Star formation efficiencies

Only one of our modes of collapse, AD, includes the effect of ambipolar diffusion. However, all prestellar cores are expected to be magnetised, and therefore ambipolar diffusion could be important for all collapse models. An estimate of the timescale on which ambipolar diffusion occurs is given by

$$t_{amb} = 4 \times 10^5 (x_i / 10^{-8}) yr \tag{A.4}$$

(Mouschovias 1979; Hartquist and Williams 1989). If t_{amb} is smaller than the free-fall timescale, magnetic pressure is unlikely to impede gravitational collapse, while if it is larger the impeding effects may be significant.

Banerji et al. (2009) showed that the ambipolar diffusion timescale becomes very large as the fractional ionization increases and the magnetic field is strongly coupled to the collapsing core, which, in some cases, may halt the collapse and hence the formation of the star. We calculated the ambipolar diffusion timescale at the centre of the core using Eq. A.4 at the beginning of the collapse, and at central densities of 10^6 and $10^8\,\mathrm{cm}^{-3}$, for the BES1, BES4 and MS approximations, for differing metallicities and cosmic ray ionization rates, using ionization fractions calculated in our chemical simulations. We compared these timescales with the time it takes the gas to reach the final density (10^8

Table A.3: Collapse duration and ambipolar diffusion timescales at increasing density for BES1, BES4 and MS models with varying ζ and Z.

				$t_{amb}/10^6$ yr		
Model	$Z/Z_\odot$	ζ/ζ_0	$t_{collapse}/10^6$ yr	Initial	$n_H = 10^6$ cm^{-3}	$n_H = 10^8$ cm^{-3}
BES1 A	1.0	1.0	1.173	0.80	0.09	0.08
BES1 B1	1.0	5.0	1.173	2.51	0.14	0.09
BES1 B2	1.0	10.0	1.173	4.70	0.19	0.10
BES1 C1	0.3	1.0	1.173	0.62	0.09	0.08
BES1 C2	1.5	1.0	1.173	0.95	0.09	0.07
BES4 A	1.0	1.0	0.184	0.22	0.08	0.07
BES4 B1	1.0	5.0	0.184	0.72	0.12	0.08
BES4 B2	1.0	10.0	0.184	1.35	0.18	0.09
BES4 C1	0.3	1.0	0.184	0.22	0.08	0.07
BES4 C2	1.5	1.0	0.184	0.22	0.08	0.07
MS A	1.0	1.0	1.393	0.73	0.09	0.05
MS B1	1.0	5.0	1.393	2.39	0.14	0.08
MS B2	1.0	10.0	1.393	4.49	0.19	0.09
MS C1	0.3	1.0	1.393	0.58	0.09	0.06
MS C2	1.5	1.0	1.393	0.85	0.09	0.06

cm^{-3}). Table A.3 shows the collapse duration and t_{amb} for this grid of models.

For all models considered, the value of t_{amb} at the final density, $n_H = 10^8$ cm^{-3}, is significantly lower than the collapse duration, while the initial values are comparable to or larger than the collapse time, particularly for the BES4 collapse, and for the models with increased cosmic ray ionization rates. At 10^4 cm^{-3}, the B1 and B2 models have $t_{\rm amb}$ larger than the collapse time for the BES4 case. Increasing ζ leads to larger values of t_{amb}, as the ionization, and therefore the coupling to the neutral gas, is increased. Metallicity has very little effect at higher densities, but the initial $t_{\rm amb}$ varies with the metallicity, as more readily-ionized atoms such as carbon are present. The BES1 and MS models have lower initial values of $t_{amb}/t_{\rm collapse}$ than the BES4 models, suggesting that the faster collapse should be impeded more strongly by the coupling of gas to magnetic fields. These results emphasize that ambipolar diffusion is important for diffuse material, where magnetic fields are likely to impede collapse, but once denser clumps have formed magnetic support will be removed too rapidly to affect the subsequent evolution.

A.5 Discussion & Conclusions

The typical errors on the density of our approximations, as compared to the hydrodynamical results, are of order 10%. This likely propagates into a similar level of error in

the resulting chemical abundances - given other uncertainties, for example in the reaction rates of the chemical network, this is unlikely to be the dominant source of error in our results. Another possible source of error is whether our approximate models correctly reproduce the time evolution of the density, particularly for the BES1 and BES4 cases where we only sample four timesteps. This could be avoided by post-processing the full results of a hydrodynamical simulation - however, it still seems likely that the adopted physical parameters, particularly the desorption efficiencies, are a larger source of uncertainty than our density approximations, a situation which this work has attempted to improve.

The results of our chemical modelling show that the different collapse modes and the variation of input parameters have a degenerate effect on the resulting molecular abundances. Drawing information about the dynamics of star formation from molecular abundances therefore requires a full investigation of parameter space, something which would be extremely time-consuming using combined hydrodynamical-chemical modelling. Our grid of models, although not large enough to draw robust conclusions about individual objects, does allow us to compare results with the general properties of prestellar cores, and determine whether particular collapse models or regions of parameter space are in conflict with observation.

Assuming the values from model A (see Table A.1), all density approximations predict CO abundances away from the core centre in agreement with observed values of $10^{-5} - 10^{-4}$ in starless cores (Caselli et al. (1999); Frau et al. (2012), assuming $^{18}O/^{16}O \approx 10^{-3}$ and $^{17}O/^{16}O \approx 10^{-4}$). However, the AD collapse only reaches these values at $r \gtrsim 0.3\,\mathrm{pc}$, much larger than typical core sizes ($< 0.1\,\mathrm{pc}$; Frau et al. 2012). Only models with the highest desorption efficiencies investigated for H_2 formation and cosmic-ray induced photodesorption (D2 and F2) predict CO abundances of $\sim 10^{-5}$ at a radius of 0.1 pc for an ambipolar diffusion collapse.

The BES1, BES4 and MS approximations result in similar abundance profiles for most molecules. The BES4 and MS abundances are generally more depleted in the centre than the BES1 ones, as the gas densities are higher due to either magnetic support, or higher initial densities and a more rapid collapse, causing more efficient freeze out. However, these differences are not large enough to provide a robust observational test of the mode of collapse, as the differences between them are smaller than those caused by varying the desorption efficiencies. The AD approximation produces significantly different profile shapes to the other three, due to both the longer collapse duration and the higher densities

at large radii. The slower increase with radius of the abundance of molecules such as CO, HCN and HCO^+, and the subsequent slow or negligible decline beyond the peak value, are qualitatively different to the situation with the initially unstable collapse modes, suggesting spatially resolved molecular observations could be used to discriminate between them.

All density approximations predict peak NH_3 abundances of $\sim 10^{-8}$, consistent with observed values in prestellar cores (Tafalla et al. 2002; Johnstone et al. 2010). At $n_0 = 2 \times 10^5\,\mathrm{cm}^{-3}$, N_2H^+ abundances, shown in Figure A.15, are intermediate between the values found by Frau et al. (2012) ($\sim 10^{-11}$) and Tafalla et al. (2002) and Johnstone et al. (2010) ($\sim 10^{-10}$). However, as with CO, for the AD approximation the abundances within the reported radii of the cores are much lower than the observed values. Ambipolar diffusion simulations including chemistry by Tassis et al. (2012) show similar behaviour, with the inclusion of magnetic effects leading to a more extended depleted region than in unmagnetised models, suggesting that this is a genuine feature of collapse under ambipolar diffusion, rather than being due to our approximation of the density evolution.

Lee et al. (2004) calculated the chemical evolution of a quasistatically contracting BE sphere over $10^6\,\mathrm{yr}$, finding similar abundance profiles to our BES1 approximation for CO, NH_3 and HCO^+, although for N_2H^+ we find much more depletion in the core centres, and higher HCN abundances overall. Given that our MS and BES4 approximations also give similar results to BES1, this suggests that the collapse timescale, rather than the specific details of the density evolution, are more important for the chemical evolution, at least for some observationally important molecules such as CO.

Our BES1 and BES4 approximations are based on hydrodynamical simulations presented in Aikawa et al. (2005), who modelled the chemical evolution of these models self-consistently, providing a test of the approximations' accuracy. Comparing to their results, we find good agreement (of the same order of magnitude) between the predicted peak molecular abundances of both approaches. However, the variation with radius differs - our approximations generally predict lower abundances at the core centres, especially for the BES4 collapse, where our results predict lower CO abundances to the BES1 case at the same r, whereas Aikawa et al. (2005) find the opposite. We attribute this to the differing initial conditions - Aikawa et al. (2005) assume the gas is entirely atomic prior to collapse, whereas we allow the abundances to evolve for $10^6\,\mathrm{yr}$ at the initial density before the onset of collapse, leading to significant freeze-out onto grains occurring in the denser central regions.

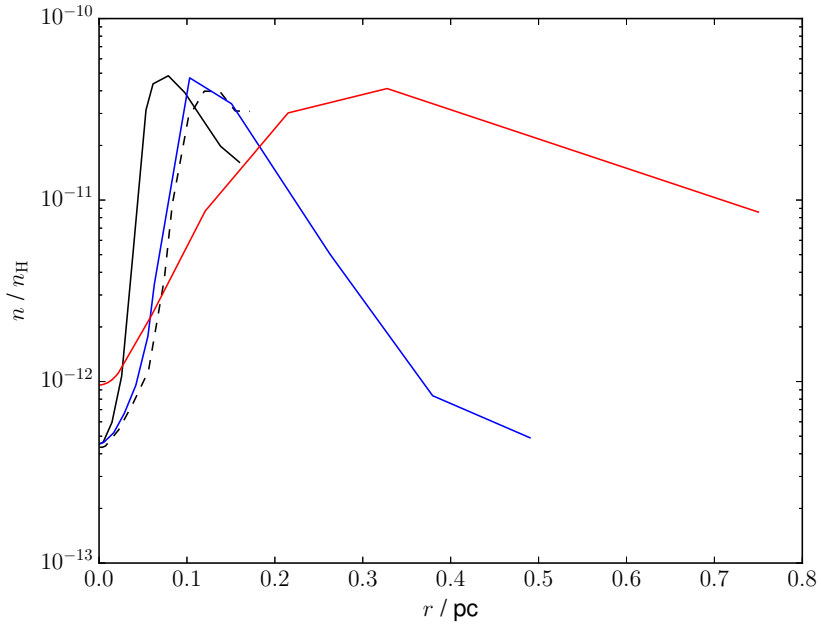

Figure A.15: N_2H^+ abundance at a central density $n_0 = 2 \times 10^5\,\mathrm{cm}^{-3}$ for model A, using the BES1 (solid black), BES4 (dashed black), MS (blue) and AD (red) density approximations.

We conclude that despite the dependence of molecular abundances on the various parameters mentioned above, molecular observations can still be useful for discriminating between different models of collapse. While models which begin from an initially gravitationally unstable state predict similar abundances and radial variations, ambipolar diffusion produces qualitatively different abundance profiles for many observationally important molecules, which appear to be in conflict with observations of prestellar cores, although varying the input parameters may be able to reduce this discrepancy. A more exhaustive investigation of parameter space, combined with observations of multiple species from the same source, could be used to draw much stronger conclusions on the nature of core collapse, as well as providing constraints on the values of the input parameters which are currently assumed ad hoc. This sort of investigation would be extremely time consuming, if not impossible, using a coupled hydrodynamical-chemical system, even without the additional complications of magnetic fields. The results we have presented here demonstrate that these large grids of models are now feasible using our method of parametrizing the dynamics, while still providing a reasonable level of accuracy compared to full simulations.

Appendix B

Approximations for the collapse of prestellar cores

B.1 Density approximations

The BES1, BES4 and AD collapse density profiles were approximated with the function

$$n(r) = \frac{n_0(t)}{1 + (\frac{r}{r_0(t)})^{a(t)}} \tag{B.1}$$

whereas the MS collapse required a different functional form,

$$\rho(r) = \rho_0(t) \left(1 + \left(\frac{r}{r_0(t)}\right)^2\right)^{-a(t)} \tag{B.2}$$

where $n_0(t)$, $\rho_0(t)$, $r_0(t)$ and $a(t)$ are functions of time since the onset of collapse given in the following subsections.

B.1.1 BES1

The time-dependent parameters are given by

$$\log_{10} n_0(t) = 61.8 \left(1.175 \times 10^6 - t\right)^{-0.01} - 49.4 \tag{B.3}$$

$$\log_{10} r_0(t) = -28.5 \left(1.175 \times 10^6 - t\right)^{-0.01} + 28.93 \tag{B.4}$$

$$a(t) = 2.4 \tag{B.5}$$

where n_0 is in cm^{-3}, r_0 is in AU and t is in years.

B.1.2 BES4

The time-dependent parameters are given by

$$\log_{10} n_0(t) = 68.4 \left(1.855 \times 10^5 - t\right)^{-0.01} - 55.7 \tag{B.6}$$

$$\log_{10} r_0(t) = -39.0 \left(1.855 \times 10^5 - t\right)^{-0.01} + 38.7 \tag{B.7}$$

$$a(t) = 1.9 + 0.5 \exp(-t/10^5) \tag{B.8}$$

where n_0 is in cm^{-3}, r_0 is in AU and t is in years.

B.1.3 MS

The time-dependent parameters are given by

$$\log_{10} \rho_0(t) = 3.54 \left(5.47 - t\right)^{-0.15} - 2.73 \tag{B.9}$$

$$\log_{10} r_0(t) = -1.34 \left(5.47 - t\right)^{-0.15} + 1.47 \tag{B.10}$$

$$a(t) = 2.0 - 0.5 \left(\frac{t}{5.47}\right)^9 \tag{B.11}$$

with the units determined by the initial central density ρ_c and the sound speed, c_s. ρ_0 is in units of ρ_c, r_0 in units of $\frac{c_s}{\sqrt{2\pi G \rho_c}}$ and t in units of $(2\pi G \rho_c)^{-0.5}$.

B.1.4 AD

The time-dependent parameters are given by

$$\log_{10} n_0(t) = \begin{cases} \log_{10}(2 + 1.7\left(\frac{t}{6} - 1\right)) + 3 & t < 6.0 \quad \text{(B.12)} \\ 5.3 \left(16.138 - t\right)^{-0.1} - 1.0 & t \geq 6.0 \quad \text{(B.13)} \end{cases}$$

$$\log_{10} r_0(t) = -2.57 \left(16.138 - t\right)^{-0.1} + 1.85 \tag{B.14}$$

$$a(t) = 2.4 - 0.2 \left(\frac{t}{16.138}\right)^{40} \tag{B.15}$$

where n_0 is in cm^{-3}, r_0 is in 0.75 pc and t is in Myr.

B.2 Velocity profiles

For the MS and AD collapses, the radial velocity profiles were also approximated in order to determine the inwards movement of the gas parcels.

B.2.1 MS

The radial velocity profile is given by

$$v_r(r) = v_{\min}(t)\left[\left(\frac{r'(t)}{r_{\min}(t)}\right)^2 - 1\right] \tag{B.16}$$

for $r < r_{\min}$ and

$$v_r(r) = v_{\min}(t)\left[\exp(-2a(t)r'(t)) - 2\exp(-a(t)r'(t))\right] \tag{B.17}$$

for $r \geq r_{\min}$, where $r'(t) = r - r_{\min}$. The time evolution is given by

$$r_{\min}(t) = \begin{cases} -1.149t + 7.2 & t < 4.95 \quad \text{(B.18)} \\ -9.2\log t + 16.25 & t < 5.33 \quad \text{(B.19)} \\ -22\log t + 37.65 & t \geq 5.33 \quad \text{(B.20)} \end{cases}$$

$$v_{\min}(t) = \begin{cases} 0.0891t & t < 4.95 \quad \text{(B.21)} \\ 5.5\log t - 8.37 & t < 5.33 \quad \text{(B.22)} \\ 18.9\log t - 30.8 & t \geq 5.33 \quad \text{(B.23)} \end{cases}$$

$$a(t) = \begin{cases} 0.0101t + 0.4 & t < 4.95 \quad \text{(B.24)} \\ 0.695\log t - 0.663 & t < 5.33 \quad \text{(B.25)} \\ 2.69\log t - 4 & t \geq 5.33 \quad \text{(B.26)} \end{cases}$$

where $v_{\min}$ is in units of c_s, $r_{\min}$ in units of $\frac{c_s}{\sqrt{2\pi G\rho_c}}$ and t in units of $(2\pi G\rho_c)^{-0.5}$.

B.2.2 AD

The radial velocity profile is given by

$$v_r(r) = \begin{cases} v_{\min}(t)\left[\left(\frac{r'(t)}{r_{\min}(t)}\right)^2 - 1\right] & r < r_{\min} \quad \text{(B.27)} \\ (v_{\min}(t) - v_{\mathrm{mid}}(t))\left(\frac{r'(t)}{0.5 - r_{\min}(t)}\right)^{0.3} - v_{\min}(t) & r < 0.5 \quad \text{(B.28)} \\ 2v_{\mathrm{mid}}(t)(r-1) & r \geq 0.5 \quad \text{(B.29)} \end{cases}$$

The time evolution is given by

$$r_{\min}(t) = \begin{cases} -0.0039t + 0.49 & t \leq 10.2 \quad \text{(B.30)} \\ -0.0306(t - 10.2) + 0.45 & t \leq 15.1 \quad \text{(B.31)} \\ -0.282(t - 15.1) + 0.3 & t > 15.1 \quad \text{(B.32)} \end{cases}$$

$$v_{\min}(t) = 3.44(16.138 - t)^{-0.35} - 0.7 \quad \text{(B.33)}$$

$$v_{\mathrm{mid}}(t) = \begin{cases} 0.143t & t \leq 10.2 \quad \text{(B.34)} \\ 0.217(t - 10.2) + 1.46 & t > 10.2 \quad \text{(B.35)} \end{cases}$$

where $r_{\min}$ is in units of 0.75 pc, $v_{\min}$ and v_{mid} are in $10^{-2}\,\mathrm{km\,s^{-1}}$ and t is in Myr.

Bibliography

A. Abdoulanziz, F. Colboc, D. A. Little, Y. Moulane, J. Z. Mezei, E. Roueff, J. Tennyson, I. F. Schneider, and V. Laporta. Theoretical study of ArH^+ dissociative recombination and electron-impact vibrational excitation. *MNRAS*, 479:2415–2420, September 2018. doi: 10.1093/mnras/sty1549.

H. Abgrall, J. Le Bourlot, G. Pineau Des Forets, E. Roueff, D. R. Flower, and L. Heck. Photodissociation of H2 and the H/H2 transition in interstellar clouds. *A&A*, 253: 525–536, January 1992.

Y. Aikawa, N. Ohashi, S.-i. Inutsuka, E. Herbst, and S. Takakuwa. Molecular Evolution in Collapsing Prestellar Cores. *ApJ*, 552:639–653, May 2001. doi: 10.1086/320551.

Y. Aikawa, E. Herbst, H. Roberts, and P. Caselli. Molecular Evolution in Collapsing Prestellar Cores. III. Contraction of a Bonnor-Ebert Sphere. *ApJ*, 620:330–346, February 2005. doi: 10.1086/427017.

S. Akras, D. R. Gonçalves, and G. Ramos-Larios. H_2 in low-ionization structures of planetary nebulae. *MNRAS*, 465:1289–1296, February 2017. doi: 10.1093/mnras/stw2736.

I. Aleman and R. Gruenwald. Molecular Hydrogen in the Ionized Region of Planetary Nebulae. *ApJ*, 607:865–872, June 2004. doi: 10.1086/383562.

I. Aleman and R. Gruenwald. H_2 infrared line emission from the ionized region of planetary nebulae. *A&A*, 528:A74, April 2011. doi: 10.1051/0004-6361/201014978.

I. Aleman, A. A. Zijlstra, M. Matsuura, R. Gruenwald, and R. K. Kimura. Modelling the warm H_2 infrared emission of the Helix nebula cometary knots. *MNRAS*, 416:790–800, September 2011. doi: 10.1111/j.1365-2966.2011.19094.x.

I. Aleman, T. Ueta, D. Ladjal, K. M. Exter, J. H. Kastner, R. Montez, A. G. G. M. Tielens, Y.-H. Chu, H. Izumiura, I. McDonald, R. Sahai, N. Siódmiak, R. Szczerba, P. A. M. van Hoof, E. Villaver, W. Vlemmings, M. Wittkowski, and A. A. Zijlstra. Herschel Planetary Nebula Survey (HerPlaNS). First detection of OH^+ in planetary nebulae. *A&A*, 566:A79, June 2014. doi: 10.1051/0004-6361/201322940.

R. G. Arendt, E. Dwek, and S. H. Moseley. Newly Synthesized Elements and Pristine Dust in the Cassiopeia A Supernova Remnant. *ApJ*, 521:234–245, August 1999. doi: 10.1086/307545.

R. G. Arendt, E. Dwek, G. Kober, J. Rho, and U. Hwang. Interstellar and Ejecta Dust in the Cas A Supernova Remnant. *ApJ*, 786:55, May 2014. doi: 10.1088/0004-637X/786/1/55.

M. Arias, J. Vink, F. de Gasperin, P. Salas, J. B. R. Oonk, R. J. van Weeren, A. S. van Amesfoort, J. Anderson, R. Beck, M. E. Bell, M. J. Bentum, P. Best, R. Blaauw, F. Breitling, J. W. Broderick, W. N. Brouw, M. Brüggen, H. R. Butcher, B. Ciardi, E. de Geus, A. Deller, P. C. G. van Dijk, S. Duscha, J. Eislöffel, M. A. Garrett, J. M. Grießmeier, A. W. Gunst, M. P. van Haarlem, G. Heald, J. Hessels, J. Hörandel, H. A. Holties, A. J. van der Horst, M. Iacobelli, E. Juette, A. Krankowski, J. van Leeuwen, G. Mann, D. McKay-Bukowski, J. P. McKean, H. Mulder, A. Nelles, E. Orru, H. Paas, M. Pandey-Pommier, V. N. Pandey, R. Pekal, R. Pizzo, A. G. Polatidis, W. Reich, H. J. A. Röttgering, H. Rothkaehl, D. J. Schwarz, O. Smirnov, M. Soida, M. Steinmetz, M. Tagger, S. Thoudam, M. C. Toribio, C. Vocks, M. H. D. van der Wiel, R. A. M. J. Wijers, O. Wucknitz, P. Zarka, and P. Zucca. Low-frequency radio absorption in Cassiopeia A. *A&A*, 612:A110, May 2018. doi: 10.1051/0004-6361/201732411.

M. Asplund, N. Grevesse, A. J. Sauval, and P. Scott. The Chemical Composition of the Sun. *Ann. Rev. Astr. Astrophys.*, 47:481–522, September 2009. doi: 10.1146/annurev.astro.46.060407.145222.

A. M. Atoyan and F. A. Aharonian. On the mechanisms of gamma radiation in the Crab Nebula. *MNRAS*, 278:525–541, January 1996. doi: 10.1093/mnras/278.2.525.

R. Bachiller, P. J. Huggins, P. Cox, and T. Forveille. The spatio-kinematic structure of the CO envelopes of evolved planetary nebulae. *A&A*, 267:177–186, January 1993.

E. L. O. Bakes and A. G. G. M. Tielens. The photoelectric heating mechanism for very small graphitic grains and polycyclic aromatic hydrocarbons. *ApJ*, 427:822–838, June 1994. doi: 10.1086/174188.

J. A. Baldwin, G. J. Ferland, P. G. Martin, M. R. Corbin, S. A. Cota, B. M. Peterson, and A. Slettebak. Physical conditions in the Orion Nebula and an assessment of its helium abundance. *ApJ*, 374:580–609, June 1991. doi: 10.1086/170146.

M. Banerji, S. Viti, D. A. Williams, and J. M. C. Rawlings. Timescales for Low-Mass Star Formation in Extragalactic Environments: Implications for the Stellar Initial Mass Function. *ApJ*, 692:283–289, February 2009. doi: 10.1088/0004-637X/692/1/283.

M. J. Barlow, O. Krause, B. M. Swinyard, B. Sibthorpe, M.-A. Besel, R. Wesson, R. J. Ivison, L. Dunne, W. K. Gear, H. L. Gomez, P. C. Hargrave, T. Henning, S. J. Leeks, T. L. Lim, G. Olofsson, and E. T. Polehampton. A Herschel PACS and SPIRE study of the dust content of the Cassiopeia A supernova remnant. *A&A*, 518:L138, July 2010. doi: 10.1051/0004-6361/201014585.

M. J. Barlow, B. M. Swinyard, P. J. Owen, J. Cernicharo, H. L. Gomez, R. J. Ivison, O. Krause, T. L. Lim, M. Matsuura, S. Miller, G. Olofsson, and E. T. Polehampton. Detection of a Noble Gas Molecular Ion, $^{36}ArH^{+}$, in the Crab Nebula. *Science*, 342: 1343–1345, December 2013. doi: 10.1126/science.1243582.

E. Bayet, D. A. Williams, T. W. Hartquist, and S. Viti. Chemistry in cosmic ray dominated regions. *MNRAS*, 414:1583–1591, June 2011. doi: 10.1111/j.1365-2966.2011.18500.x.

S. A. Becker and I. Iben, Jr. The asymptotic giant branch evolution of intermediate-mass stars as a function of mass and composition. I - Through the second dredge-up phase. *ApJ*, 232:831–853, September 1979. doi: 10.1086/157345.

T. A. Bell, S. Viti, D. A. Williams, I. A. Crawford, and R. J. Price. The chemistry of transient microstructure in the diffuse interstellar medium. *MNRAS*, 357:961–966, March 2005. doi: 10.1111/j.1365-2966.2005.08693.x.

T. A. Bell, E. Roueff, S. Viti, and D. A. Williams. Molecular line intensities as measures of cloud masses - I. Sensitivity of CO emissions to physical parameter variations. *MNRAS*, 371:1865–1872, October 2006. doi: 10.1111/j.1365-2966.2006.10817.x.

E. A. Bergin and W. D. Langer. Chemical Evolution in Preprotostellar and Protostellar Cores. *ApJ*, 486:316–328, September 1997. doi: 10.1086/304510.

E. A. Bergin and M. Tafalla. Cold Dark Clouds: The Initial Conditions for Star Formation. *Ann. Rev. Astr. Astrophys.*, 45:339–396, September 2007. doi: 10.1146/annurev.astro.45.071206.100404.

F. Bertoldi, C. L. Carilli, P. Cox, X. Fan, M. A. Strauss, A. Beelen, A. Omont, and R. Zylka. Dust emission from the most distant quasars. *A&A*, 406:L55–L58, July 2003. doi: 10.1051/0004-6361:20030710.

H. A. Bethe. Supernova mechanisms. *Reviews of Modern Physics*, 62:801–866, October 1990. doi: 10.1103/RevModPhys.62.801.

A. Bevan and M. J. Barlow. Modelling supernova line profile asymmetries to determine ejecta dust masses: SN 1987A from days 714 to 3604. *MNRAS*, 456:1269–1293, February 2016. doi: 10.1093/mnras/stv2651.

A. Bevan, M. J. Barlow, and D. Milisavljevic. Dust masses for SN 1980K, SN1993J and Cassiopeia A from red-blue emission line asymmetries. *MNRAS*, 465:4044–4056, March 2017. doi: 10.1093/mnras/stw2985.

S. Bianchi and R. Schneider. Dust formation and survival in supernova ejecta. *MNRAS*, 378:973–982, July 2007. doi: 10.1111/j.1365-2966.2007.11829.x.

T. G. Bisbas, T. J. Haworth, M. J. Barlow, S. Viti, T. J. Harries, T. Bell, and J. A. Yates. TORUS-3DPDR: a self-consistent code treating three-dimensional photoionization and photodissociation regions. *MNRAS*, 454:2828–2843, December 2015. doi: 10.1093/mnras/stv2156.

C. Biscaro and I. Cherchneff. Molecules and dust in Cassiopeia A. II. Dust sputtering and diagnosis of supernova dust survival in remnants. *A&A*, 589:A132, May 2016. doi: 10.1051/0004-6361/201527769.

M. Bocchio, A. P. Jones, L. Verstraete, E. M. Xilouris, E. R. Micelotta, and S. Bianchi. Dust heating. Photon absorption versus electron collisions. *A&A*, 556:A6, August 2013. doi: 10.1051/0004-6361/201321054.

M. Bocchio, S. Marassi, R. Schneider, S. Bianchi, M. Limongi, and A. Chieffi. Dust grains from the heart of supernovae. *A&A*, 587:A157, March 2016. doi: 10.1051/0004-6361/201527432.

W. B. Bonnor. Boyle's Law and gravitational instability. *MNRAS*, 116:351, 1956. doi: 10.1093/mnras/116.3.351.

A. I. Boothroyd, I.-J. Sackmann, and S. C. Ahern. Prevention of High-Luminosity Carbon Stars by Hot Bottom Burning. *ApJ*, 416:762, October 1993. doi: 10.1086/173275.

J. R. Burke and D. J. Hollenbach. The gas-grain interaction in the interstellar medium - Thermal accommodation and trapping. *ApJ*, 265:223–234, February 1983. doi: 10.1086/160667.

P. Camps, K. Misselt, S. Bianchi, T. Lunttila, C. Pinte, G. Natale, M. Juvela, J. Fischera, M. P. Fitzgerald, K. Gordon, M. Baes, and J. Steinacker. Benchmarking the calculation of stochastic heating and emissivity of dust grains in the context of radiative transfer simulations. *A&A*, 580:A87, August 2015. doi: 10.1051/0004-6361/201525998.

P. Caselli, C. M. Walmsley, M. Tafalla, L. Dore, and P. C. Myers. CO Depletion in the Starless Cloud Core L1544. *ApJL*, 523:L165–L169, October 1999. doi: 10.1086/312280.

S. Cazaux and A. G. G. M. Tielens. Molecular Hydrogen Formation in the Interstellar Medium. *ApJL*, 575:L29–L32, August 2002. doi: 10.1086/342607.

S. Cazaux and A. G. G. M. Tielens. H_2 Formation on Grain Surfaces. *ApJ*, 604:222–237, March 2004. doi: 10.1086/381775.

C. Cecchi-Pestellini and A. Dalgarno. Emission of HeH(+) in nebulae. *ApJ*, 413:611–618, August 1993. doi: 10.1086/173030.

D. Cesarsky, J. Lequeux, A. Abergel, M. Perault, E. Palazzi, S. Madden, and D. Tran. Infrared spectrophotometry of NGC 7023 with ISOCAM. *A&A*, 315:L305–L308, November 1996.

R. A. Chevalier and R. P. Kirshner. Abundance inhomogeneities in the Cassiopeia A supernova remnant. *ApJ*, 233:154–162, October 1979. doi: 10.1086/157377.

R. A. Chevalier and J. Oishi. Cassiopeia A and Its Clumpy Presupernova Wind. *ApJL*, 593:L23–L26, August 2003. doi: 10.1086/377572.

J. Clavel, Y. P. Viala, and N. Bel. Chemical and thermal equilibrium in dark clouds. *A&A*, 65:435–448, May 1978.

M. Cohen and L. V. Kuhi. Observational studies of star formation - Conclusions. *ApJL*, 227:L105, January 1979. doi: 10.1086/182877.

M. Cohen, W. Kunkel, B. M. Lasker, P. S. Osmer, and M. P. Fitzgerald. Studies of bipolar nebulae. IV - MZ 3 /= PK 331 - 1 deg 1/. *ApJ*, 221:151–153, April 1978. doi: 10.1086/156013.

M. Cohen, J. P. Harrington, and R. Hess. The dust content of the planetary nebula IC 3568. *ApJ*, 283:687–693, August 1984. doi: 10.1086/162355.

M. P. Collings, M. A. Anderson, R. Chen, J. W. Dever, S. Viti, D. A. Williams, and M. R. S. McCoustra. A laboratory survey of the thermal desorption of astrophysically relevant molecules. *MNRAS*, 354:1133–1140, November 2004. doi: 10.1111/j.1365-2966.2004.08272.x.

M. Compiègne, L. Verstraete, A. Jones, J.-P. Bernard, F. Boulanger, N. Flagey, J. Le Bourlot, D. Paradis, and N. Ysard. The global dust SED: tracing the nature and evolution of dust with DustEM. *A&A*, 525:A103, January 2011. doi: 10.1051/0004-6361/201015292.

R. M. Crutcher. Magnetic Fields in Molecular Clouds: Observations Confront Theory. *ApJ*, 520:706–713, August 1999. doi: 10.1086/307483.

I. Dabrowski. The Lyman and Werner bands of H2. *Canadian Journal of Physics*, 62: 1639–1664, December 1984. doi: 10.1139/p84-210.

A. Dalgarno, M. Yan, and W. Liu. Electron Energy Deposition in a Gas Mixture of Atomic and Molecular Hydrogen and Helium. *ApJSS*, 125:237–256, November 1999. doi: 10.1086/313267.

T. de Jong. Photoelectric heating of the interstellar gas. *A&A*, 55:137–145, February 1977.

T. de Jong, S. Chu, and A. Dalgarno. Carbon monoxide in collapsing interstellar clouds. *ApJ*, 199:69–78, July 1975. doi: 10.1086/153665.

I. De Looze, M. J. Barlow, B. M. Swinyard, J. Rho, H. L. Gomez, M. Matsuura, and R. Wesson. The dust mass in Cassiopeia A from a spatially resolved Herschel analysis. *MNRAS*, 465:3309–3342, March 2017. doi: 10.1093/mnras/stw2837.

T. DeLaney, L. Rudnick, R. A. Fesen, T. W. Jones, R. Petre, and J. A. Morse. Kinematics of X-Ray-Emitting Components in Cassiopeia A. *ApJ*, 613:343–348, September 2004. doi: 10.1086/422906.

T. DeLaney, L. Rudnick, M. D. Stage, J. D. Smith, K. Isensee, J. Rho, G. E. Allen, H. Gomez, T. Kozasa, W. T. Reach, J. E. Davis, and J. C. Houck. The Three-dimensional Structure of Cassiopeia A. *ApJ*, 725:2038–2058, December 2010. doi: 10.1088/0004-637X/725/2/2038.

T. DeLaney, N. E. Kassim, L. Rudnick, and R. A. Perley. The Density and Mass of Unshocked Ejecta in Cassiopeia A through Low Frequency Radio Absorption. *ApJ*, 785:7, April 2014. doi: 10.1088/0004-637X/785/1/7.

R. L. Dickman. A survey of carbon monoxide emission in dark clouds. *ApJ*, 202:50–57, November 1975. doi: 10.1086/153951.

D. Docenko and R. A. Sunyaev. Fine-structure infrared lines from the Cassiopeia A knots. *A&A*, 509:A59, January 2010. doi: 10.1051/0004-6361/200810366.

J. Dorschner, B. Begemann, T. Henning, C. Jaeger, and H. Mutschke. Steps toward interstellar silicate mineralogy. II. Study of Mg-Fe-silicate glasses of variable composition. *A&A*, 300:503, August 1995.

T. Douvion, P. O. Lagage, and E. Pantin. Cassiopeia A dust composition and heating. *A&A*, 369:589–593, April 2001. doi: 10.1051/0004-6361:20010053.

B. T. Draine. Photoelectric heating of interstellar gas. *ApJSS*, 36:595–619, April 1978. doi: 10.1086/190513.

B. T. Draine. *Physics of the Interstellar and Intergalactic Medium*. 2011.

B. T. Draine and N. Anderson. Temperature fluctuations and infrared emission from interstellar grains. *ApJ*, 292:494–499, May 1985. doi: 10.1086/163181.

B. T. Draine and A. Li. Infrared Emission from Interstellar Dust. I. Stochastic Heating of Small Grains. *ApJ*, 551:807–824, April 2001. doi: 10.1086/320227.

L. Dunne, S. Eales, R. Ivison, H. Morgan, and M. Edmunds. Type II supernovae as a significant source of interstellar dust. *Nature*, 424:285–287, July 2003. doi: 10.1038/nature01792.

L. Dunne, S. J. Maddox, R. J. Ivison, L. Rudnick, T. A. Delaney, B. C. Matthews, C. M. Crowe, H. L. Gomez, S. A. Eales, and S. Dye. Cassiopeia A: dust factory revealed via submillimetre polarimetry. *MNRAS*, 394:1307–1316, April 2009. doi: 10.1111/j.1365-2966.2009.14453.x.

E. Dwek. Temperature fluctuations and infrared emission from dust particles in a hot gas. *ApJ*, 302:363–370, March 1986. doi: 10.1086/163995.

E. Dwek. The infrared diagnostic of a dusty plasma with applications to supernova remnants. *ApJ*, 322:812–821, November 1987. doi: 10.1086/165774.

E. Dwek. The Evolution of the Elemental Abundances in the Gas and Dust Phases of the Galaxy. *ApJ*, 501:643, July 1998. doi: 10.1086/305829.

E. Dwek and R. K. Smith. Energy Deposition and Photoelectric Emission from the Interaction of 10 eV to 1 MeV Photons with Interstellar Dust Particles. *ApJ*, 459:686, March 1996. doi: 10.1086/176933.

E. Dwek, S. M. Foster, and O. Vancura. Cooling, Sputtering, and Infrared Emission from Dust Grains in Fast Nonradiative Shocks. *ApJ*, 457:244, January 1996. doi: 10.1086/176725.

E. Dwek, F. Galliano, and A. P. Jones. The Evolution of Dust in the Early Universe with Applications to the Galaxy SDSS J1148+5251. *ApJ*, 662:927–939, June 2007. doi: 10.1086/518430.

R. Ebert. Zur Instabilität kugelsymmetrischer Gasverteilungen. Mit 2 Textabbildungen. *Z. Astrophys.*, 42:263, 1957.

J. L. Edwards, E. G. Cox, and L. M. Ziurys. Millimeter Observations of CS, HCO^+, and CO toward Five Planetary Nebulae: Following Molecular Abundances with Nebular Age. *ApJ*, 791:79, August 2014. doi: 10.1088/0004-637X/791/2/79.

B. G. Elmegreen. Magnetic diffusion and ionization fractions in dense molecular clouds - The role of charged grains. *ApJ*, 232:729–739, September 1979. doi: 10.1086/157333.

B. Ercolano, M. J. Barlow, P. J. Storey, and X.-W. Liu. MOCASSIN: a fully three-dimensional Monte Carlo photoionization code. *MNRAS*, 340:1136–1152, April 2003. doi: 10.1046/j.1365-8711.2003.06371.x.

B. Ercolano, M. J. Barlow, and P. J. Storey. The dusty MOCASSIN: fully self-consistent 3D photoionization and dust radiative transfer models. *MNRAS*, 362:1038–1046, September 2005. doi: 10.1111/j.1365-2966.2005.09381.x.

B. Ercolano, P. R. Young, J. J. Drake, and J. C. Raymond. X-Ray Enabled MOCASSIN: A Three-dimensional Code for Photoionized Media. *ApJSS*, 175:534-542, April 2008. doi: 10.1086/524378.

M. Etxaluze, J. Cernicharo, J. R. Goicoechea, P. A. M. van Hoof, B. M. Swinyard, M. J. Barlow, G. C. van de Steene, M. A. T. Groenewegen, F. Kerschbaum, T. L. Lim, F. Lique, M. Matsuura, C. Pearson, E. T. Polehampton, P. Royer, and T. Ueta. Herschel spectral mapping of the Helix nebula (NGC 7293). Extended CO photodissociation and OH^+ emission. *A&A*, 566:A78, June 2014. doi: 10.1051/0004-6361/201322941.

E. Falgarone and J. L. Puget. A model of clumped molecular clouds. I - Hydrostatic structure of dense cores. *A&A*, 142:157–170, January 1985.

S. R. Federman, A. E. Glassgold, and J. Kwan. Atomic to molecular hydrogen transition in interstellar clouds. *ApJ*, 227:466–473, January 1979. doi: 10.1086/156753.

G. J. Ferland, K. T. Korista, D. A. Verner, J. W. Ferguson, J. B. Kingdon, and E. M. Verner. CLOUDY 90: Numerical Simulation of Plasmas and Their Spectra. *PASP*, 110: 761–778, July 1998. doi: 10.1086/316190.

R. A. Fesen, M. C. Hammell, J. Morse, R. A. Chevalier, K. J. Borkowski, M. A. Dopita, C. L. Gerardy, S. S. Lawrence, J. C. Raymond, and S. van den Bergh. The Expansion Asymmetry and Age of the Cassiopeia A Supernova Remnant. *ApJ*, 645:283–292, July 2006. doi: 10.1086/504254.

R. A. Fiedler and T. C. Mouschovias. Ambipolar Diffusion and Star Formation: Formation and Contraction of Axisymmetric Cloud Cores. II. Results. *ApJ*, 415:680, October 1993. doi: 10.1086/173193.

E. L. Fitzpatrick. Correcting for the Effects of Interstellar Extinction. *PASP*, 111:63–75, January 1999. doi: 10.1086/316293.

P. N. Foster and R. A. Chevalier. Gravitational Collapse of an Isothermal Sphere. *ApJ*, 416:303, October 1993. doi: 10.1086/173236.

P. Frau, J. M. Girart, M. T. Beltrán, M. Padovani, G. Busquet, O. Morata, J. M. Masqué, F. O. Alves, Á. Sánchez-Monge, G. A. P. Franco, and R. Estalella. Young Starless Cores Embedded in the Magnetically Dominated Pipe Nebula. II. Extended Data Set. *ApJ*, 759:3, November 2012. doi: 10.1088/0004-637X/759/1/3.

D. J. Frew. *Planetary Nebulae in the Solar Neighbourhood: Statistics, Distance Scale and Luminosity Function*. PhD thesis, Department of Physics, Macquarie University, NSW 2109, Australia, July 2008.

C. Gall, J. Hjorth, and A. C. Andersen. Production of dust by massive stars at high redshift. *A&ARv*, 19:43, September 2011. doi: 10.1007/s00159-011-0043-7.

R. A. Gingold and D. J. Faulkner. Thermal Pulses in Helium Shell-Burning Stars. III. *ApJ*, 188:145–148, February 1974. doi: 10.1086/152696.

P. F. Goldsmith. Molecular Depletion and Thermal Balance in Dark Cloud Cores. *ApJ*, 557:736–746, August 2001. doi: 10.1086/322255.

P. F. Goldsmith and W. D. Langer. Molecular cooling and thermal balance of dense interstellar clouds. *ApJ*, 222:881–895, June 1978. doi: 10.1086/156206.

H. L. Gomez, O. Krause, M. J. Barlow, B. M. Swinyard, P. J. Owen, C. J. R. Clark, M. Matsuura, E. L. Gomez, J. Rho, M.-A. Besel, J. Bouwman, W. K. Gear, T. Henning, R. J. Ivison, E. T. Polehampton, and B. Sibthorpe. A Cool Dust Factory in the Crab Nebula: A Herschel Study of the Filaments. *ApJ*, 760:96, November 2012. doi: 10.1088/0004-637X/760/1/96.

A. A. Goodman, P. Bastien, P. C. Myers, and F. Menard. Optical polarization maps of star-forming regions in Perseus, Taurus, and Ophiuchus. *ApJ*, 359:363–377, August 1990. doi: 10.1086/169070.

R. J. Gould and E. E. Salpeter. The Interstellar Abundance of the Hydrogen Molecule. I. Basic Processes. *ApJ*, 138:393, August 1963. doi: 10.1086/147654.

J. R. Graham, G. S. Wright, and A. J. Longmore. Infrared spectroscopy and imaging of the Crab Nebula. *ApJ*, 352:172–183, March 1990. doi: 10.1086/168525.

T. Grenman, G. F. Gahm, and E. Elfgren. Dusty globules in the Crab Nebula. *A&A*, 599: A110, March 2017. doi: 10.1051/0004-6361/201629693.

C. Gry, F. Boulanger, C. Nehmé, G. Pineau des Forêts, E. Habart, and E. Falgarone. H_2 formation and excitation in the diffuse interstellar medium. *A&A*, 391:675–680, August 2002. doi: 10.1051/0004-6361:20020691.

M. A. Guerrero and O. De Marco. Analysis of far-UV data of central stars of planetary nebulae: Occurrence and variability of stellar winds. *A&A*, 553:A126, May 2013. doi: 10.1051/0004-6361/201220623.

P. Guhathakurta and B. T. Draine. Temperature fluctuations in interstellar grains. I - Computational method and sublimation of small grains. *ApJ*, 345:230–244, October 1989. doi: 10.1086/167899.

B. Günay, T. W. Schmidt, M. G. Burton, M. Afşar, O. Krechkivska, K. Nauta, S. H. Kable, and A. Rawal. Aliphatic Hydrocarbon Content of Interstellar Dust. *MNRAS*, June 2018. doi: 10.1093/mnras/sty1582.

H. J. Habing. The interstellar radiation density between 912 A and 2400 A. *Bull. Astron. Inst. Netherlands*, 19:421, January 1968.

J. R. Hamilton, A. Faure, and J. Tennyson. Electron-impact excitation of diatomic hydride cations - I. HeH^+, CH^+, ArH^+. *MNRAS*, 455:3281–3287, January 2016. doi: 10.1093/mnras/stv2429.

J. P. Harrington, D. J. Monk, and R. E. S. Clegg. Thermal infrared emission by dust in the planetary nebula NGC 3918 - A model analysis of IRAS observations. *MNRAS*, 231:577–595, April 1988. doi: 10.1093/mnras/231.3.577.

T. W. Hartquist and D. A. Williams. On the ratio of the ambipolar diffusion and depletion time-scales and quiescent star formation. *MNRAS*, 241:417–424, December 1989. doi: 10.1093/mnras/241.3.417.

T. I. Hasegawa, E. Herbst, and C. M. Leung. Models of gas-grain chemistry in dense interstellar clouds with complex organic molecules. *ApJSS*, 82:167–195, September 1992. doi: 10.1086/191713.

M. R. Hayden, J. Bovy, J. A. Holtzman, D. L. Nidever, J. C. Bird, D. H. Weinberg, B. H. Andrews, S. R. Majewski, C. Allende Prieto, F. Anders, T. C. Beers, D. Bizyaev, C. Chiappini, K. Cunha, P. Frinchaboy, D. A. García-Herńandez, A. E.

García Pérez, L. Girardi, P. Harding, F. R. Hearty, J. A. Johnson, S. Mészáros, I. Minchev, R. O'Connell, K. Pan, A. C. Robin, R. P. Schiavon, D. P. Schneider, M. Schultheis, M. Shetrone, M. Skrutskie, M. Steinmetz, V. Smith, J. C. Wilson, O. Zamora, and G. Zasowski. Chemical Cartography with APOGEE: Metallicity Distribution Functions and the Chemical Structure of the Milky Way Disk. *ApJ*, 808:132, August 2015. doi: 10.1088/0004-637X/808/2/132.

R. B. C. Henry, K. B. Kwitter, and R. J. Dufour. Morphology and Composition of the Helix Nebula. *ApJ*, 517:782–798, June 1999. doi: 10.1086/307215.

E. Herbst and W. Klemperer. The Formation and Depletion of Molecules in Dense Interstellar Clouds. *ApJ*, 185:505–534, October 1973. doi: 10.1086/152436.

F. Herwig. Evolution of Asymptotic Giant Branch Stars. *Ann. Rev. Astr. Astrophys.*, 43: 435–479, September 2005. doi: 10.1146/annurev.astro.43.072103.150600.

J. J. Hester. The Crab Nebula: An Astrophysical Chimera. *Ann. Rev. Astr. Astrophys.*, 46:127–155, September 2008. doi: 10.1146/annurev.astro.45.051806.110608.

U. Hincelin, B. Commerçon, V. Wakelam, F. Hersant, S. Guilloteau, and E. Herbst. Chemical and Physical Characterization of Collapsing Low-mass Prestellar Dense Cores. *ApJ*, 822:12, May 2016. doi: 10.3847/0004-637X/822/1/12.

D. Hiriart. Molecular hydrogen kinematics in the ring-like planetary nebula NGC 6781. *A&A*, 434:181–187, April 2005. doi: 10.1051/0004-6361:20042010.

J. Holdship, S. Viti, I. Jiménez-Serra, A. Makrymallis, and F. Priestley. UCLCHEM: A Gas-grain Chemical Code for Clouds, Cores, and C-Shocks. *AJ*, 154:38, July 2017. doi: 10.3847/1538-3881/aa773f.

D. Hollenbach and C. F. McKee. Molecule formation and infrared emission in fast interstellar shocks. I Physical processes. *ApJSS*, 41:555–592, November 1979. doi: 10.1086/190631.

D. Hollenbach and E. E. Salpeter. Surface Recombination of Hydrogen Molecules. *ApJ*, 163:155, January 1971. doi: 10.1086/150754.

D. J. Hollenbach, T. Takahashi, and A. G. G. M. Tielens. Low-density photodissociation regions. *ApJ*, 377:192–209, August 1991. doi: 10.1086/170347.

J. L. Hora, W. B. Latter, and L. K. Deutsch. Investigating the Near-Infrared Properties of Planetary Nebulae. II. Medium-Resolution Spectra. *ApJSS*, 124:195–240, September 1999. doi: 10.1086/313256.

P. J. Huggins, R. Bachiller, P. Cox, and T. Forveille. The molecular envelopes of planetary nebulae. *A&A*, 315:284–302, November 1996.

C. Hunter. The collapse of unstable isothermal spheres. *ApJ*, 218:834–845, December 1977. doi: 10.1086/155739.

A. P. Hurford and R. A. Fesen. Reddening Measurements and Physical Conditions for Cassiopeia A from Optical and Near-Infrared Spectra. *ApJ*, 469:246, September 1996. doi: 10.1086/177775.

U. Hwang and J. M. Laming. The Circumstellar Medium of Cassiopeia a Inferred from the Outer Ejecta Knot Properties. *ApJ*, 703:883–893, September 2009. doi: 10.1088/0004-637X/703/1/883.

U. Hwang, J. M. Laming, C. Badenes, F. Berendse, J. Blondin, D. Cioffi, T. DeLaney, D. Dewey, R. Fesen, K. A. Flanagan, C. L. Fryer, P. Ghavamian, J. P. Hughes, J. A. Morse, P. P. Plucinsky, R. Petre, M. Pohl, L. Rudnick, R. Sankrit, P. O. Slane, R. K. Smith, J. Vink, and J. S. Warren. A Million Second Chandra View of Cassiopeia A. *ApJL*, 615:L117–L120, November 2004. doi: 10.1086/426186.

I. Iben, Jr. Stellar Evolution Within and off the Main Sequence. *Ann. Rev. Astr. Astrophys.*, 5:571, 1967. doi: 10.1146/annurev.aa.05.090167.003035.

I. Iben, Jr. Further adventures of a thermally pulsing star. *ApJ*, 208:165–176, August 1976. doi: 10.1086/154591.

I. Iben, Jr. and A. Renzini. Asymptotic giant branch evolution and beyond. *Ann. Rev. Astr. Astrophys.*, 21:271–342, 1983. doi: 10.1146/annurev.aa.21.090183.001415.

C. Jaeger, H. Mutschke, B. Begemann, J. Dorschner, and T. Henning. Steps toward interstellar silicate mineralogy. 1: Laboratory results of a silicate glass of mean cosmic composition. *A&A*, 292:641–655, December 1994.

C. Jäger, J. Dorschner, H. Mutschke, T. Posch, and T. Henning. Steps toward interstellar silicate mineralogy. VII. Spectral properties and crystallization behaviour of magnesium

silicates produced by the sol-gel method. *A&A*, 408:193–204, September 2003. doi: 10.1051/0004-6361:20030916.

E. B. Jenkins. A Unified Representation of Gas-Phase Element Depletions in the Interstellar Medium. *ApJ*, 700:1299–1348, August 2009. doi: 10.1088/0004-637X/700/2/1299.

D. Johnstone, E. Rosolowsky, M. Tafalla, and H. Kirk. Dense Gas Tracers in Perseus: Relating the N_2H^+, NH_3, and Dust Continuum Properties of Pre- and Protostellar Cores. *ApJ*, 711:655–670, March 2010. doi: 10.1088/0004-637X/711/2/655.

A. P. Jones, L. Fanciullo, M. Köhler, L. Verstraete, V. Guillet, M. Bocchio, and N. Ysard. The evolution of amorphous hydrocarbons in the ISM: dust modelling from a new vantage point. *A&A*, 558:A62, October 2013. doi: 10.1051/0004-6361/201321686.

M. Jura. Formation and destruction rates of interstellar H_2. *ApJ*, 191:375–379, July 1974. doi: 10.1086/152975.

I. Kamp and F. Bertoldi. CO in the circumstellar disks of Vega and beta Pictoris. *A&A*, 353:276–286, January 2000.

R. Kandori, Y. Nakajima, M. Tamura, K. Tatematsu, Y. Aikawa, T. Naoi, K. Sugitani, H. Nakaya, T. Nagayama, T. Nagata, M. Kurita, D. Kato, C. Nagashima, and S. Sato. Near-Infrared Imaging Survey of Bok Globules: Density Structure. *AJ*, 130:2166–2184, November 2005. doi: 10.1086/444619.

R. K. Kimura, R. Gruenwald, and I. Aleman. Molecular chemistry and the missing mass problem in planetary nebulae. *A&A*, 541:A112, May 2012. doi: 10.1051/0004-6361/201118429.

J. B. Kingdon and G. J. Ferland. Rate Coefficients for Charge Transfer between Hydrogen and the First 30 Elements. *ApJSS*, 106:205, September 1996. doi: 10.1086/192335.

R. L. Kingsburgh and M. J. Barlow. Elemental abundances for a sample of southern galactic planetary nebulae. *MNRAS*, 271:257–299, November 1994. doi: 10.1093/mnras/271.2.257.

O. Krause, S. M. Birkmann, G. H. Rieke, D. Lemke, U. Klaas, D. C. Hines, and K. D. Gordon. No cold dust within the supernova remnant Cassiopeia A. *Nature*, 432:596–598, December 2004. doi: 10.1038/nature03110.

O. Krause, S. M. Birkmann, T. Usuda, T. Hattori, M. Goto, G. H. Rieke, and K. A. Misselt. The Cassiopeia A Supernova Was of Type IIb. *Science*, 320:1195, May 2008. doi: 10.1126/science.1155788.

J. M. Laming and U. Hwang. On the Determination of Ejecta Structure and Explosion Asymmetry from the X-Ray Knots of Cassiopeia A. *ApJ*, 597:347–361, November 2003. doi: 10.1086/378268.

A. Laor and B. T. Draine. Spectroscopic constraints on the properties of dust in active galactic nuclei. *ApJ*, 402:441–468, January 1993. doi: 10.1086/172149.

N. Laporte, R. S. Ellis, F. Boone, F. E. Bauer, D. Quénard, G. W. Roberts-Borsani, R. Pelló, I. Pérez-Fournon, and A. Streblyanska. Dust in the Reionization Era: ALMA Observations of a z = 8.38 Gravitationally Lensed Galaxy. *ApJL*, 837:L21, March 2017. doi: 10.3847/2041-8213/aa62aa.

R. B. Larson. Numerical calculations of the dynamics of collapsing proto-star. *MNRAS*, 145:271, 1969. doi: 10.1093/mnras/145.3.271.

J. S. Lazendic, D. Dewey, N. S. Schulz, and C. R. Canizares. The Kinematic and Plasma Properties of X-Ray Knots in Cassiopeia A from the Chandra HETGS. *ApJ*, 651:250–267, November 2006. doi: 10.1086/507481.

J.-E. Lee, E. A. Bergin, and N. J. Evans, II. Evolution of Chemistry and Molecular Line Profiles during Protostellar Collapse. *ApJ*, 617:360–383, December 2004. doi: 10.1086/425153.

Y.-H. Lee, B.-C. Koo, D.-S. Moon, M. G. Burton, and J.-J. Lee. Near-Infrared Knots and Dense Fe Ejecta in the Cassiopeia A Supernova Remnant. *ApJ*, 837:118, March 2017. doi: 10.3847/1538-4357/aa60c0.

M. A. Lennon, K. L. Bell, H. B. Gilbody, J. G. Hughes, A. E. Kingston, M. J. Murray, and F. J. Smith. Recommended Data on the Electron Impact Ionization of Atoms and Ions: Fluorine to Nickel. *Journal of Physical and Chemical Reference Data*, 17:1285–1363, July 1988. doi: 10.1063/1.555809.

Z.-Y. Li, V. I. Shematovich, D. S. Wiebe, and B. M. Shustov. A Coupled Dynamical and Chemical Model of Starless Cores of Magnetized Molecular Clouds. I. Formulation and Initial Results. *ApJ*, 569:792–802, April 2002. doi: 10.1086/339353.

F. Lique, N. Bulut, and O. Roncero. Hyperfine excitation of OH^+ by H. *MNRAS*, 461: 4477–4481, October 2016. doi: 10.1093/mnras/stw1638.

K. Lodders. Solar System Abundances of the Elements. *Astrophysics and Space Science Proceedings*, 16:379, 2010. doi: 10.1007/978-3-642-10352-0_8.

E. D. Loh, J. A. Baldwin, and G. J. Ferland. A Bright Molecular Core in a Crab Nebula Filament. *ApJL*, 716:L9–L13, June 2010. doi: 10.1088/2041-8205/716/1/L9.

E. D. Loh, J. A. Baldwin, Z. K. Curtis, G. J. Ferland, C. R. O'Dell, A. C. Fabian, and P. Salomé. A Survey of Molecular Hydrogen in the Crab Nebula. *ApJSS*, 194:30, June 2011. doi: 10.1088/0067-0049/194/2/30.

E. D. Loh, J. A. Baldwin, G. J. Ferland, Z. K. Curtis, C. T. Richardson, A. C. Fabian, and P. Salomé. H_2 temperatures in the Crab Nebula. *MNRAS*, 421:789–796, March 2012. doi: 10.1111/j.1365-2966.2011.20353.x.

L. B. Lucy. Computing radiative equilibria with Monte Carlo techniques. *A&A*, 344: 282–288, April 1999.

R. Maiolino, R. Schneider, E. Oliva, S. Bianchi, A. Ferrara, F. Mannucci, M. Pedani, and M. Roca Sogorb. A supernova origin for dust in a high-redshift quasar. *Nature*, 431: 533–535, September 2004. doi: 10.1038/nature02930.

P. R. Maloney, D. J. Hollenbach, and A. G. G. M. Tielens. X-Ray–irradiated Molecular Gas. I. Physical Processes and General Results. *ApJ*, 466:561, July 1996. doi: 10.1086/177532.

R. N. Martin and A. H. Barrett. Microwave spectral lines in galactic dust globules. *ApJSS*, 36:1–51, January 1978. doi: 10.1086/190490.

J. S. Mathis, W. Rumpl, and K. H. Nordsieck. The size distribution of interstellar grains. *ApJ*, 217:425–433, October 1977. doi: 10.1086/155591.

J. S. Mathis, P. G. Mezger, and N. Panagia. Interstellar radiation field and dust temperatures in the diffuse interstellar matter and in giant molecular clouds. *A&A*, 128: 212–229, November 1983.

M. Matsuura, A. K. Speck, M. D. Smith, A. A. Zijlstra, S. Viti, K. T. E. Lowe, M. Redman, C. J. Wareing, and E. Lagadec. VLT/near-infrared integral field spectrometer observations of molecular hydrogen lines in the knots of the planetary nebula NGC 7293 (the Helix Nebula). *MNRAS*, 382:1447–1459, December 2007. doi: 10.1111/j.1365-2966.2007.12496.x.

M. Matsuura, A. K. Speck, B. M. McHunu, I. Tanaka, N. J. Wright, M. D. Smith, A. A. Zijlstra, S. Viti, and R. Wesson. A "Firework" of H_2 Knots in the Planetary Nebula NGC 7293 (The Helix Nebula). *ApJ*, 700:1067–1077, August 2009. doi: 10.1088/0004-637X/700/2/1067.

M. Matsuura, E. Dwek, M. Meixner, M. Otsuka, B. Babler, M. J. Barlow, J. Roman-Duval, C. Engelbracht, K. Sandstrom, M. Lakićević, J. T. van Loon, G. Sonneborn, G. C. Clayton, K. S. Long, P. Lundqvist, T. Nozawa, K. D. Gordon, S. Hony, P. Panuzzo, K. Okumura, K. A. Misselt, E. Montiel, and M. Sauvage. Herschel Detects a Massive Dust Reservoir in Supernova 1987A. *Science*, 333:1258, September 2011. doi: 10.1126/science.1205983.

M. Matsuura, E. Dwek, M. J. Barlow, B. Babler, M. Baes, M. Meixner, J. Cernicharo, G. C. Clayton, L. Dunne, C. Fransson, J. Fritz, W. Gear, H. L. Gomez, M. A. T. Groenewegen, R. Indebetouw, R. J. Ivison, A. Jerkstrand, V. Lebouteiller, T. L. Lim, P. Lundqvist, C. P. Pearson, J. Roman-Duval, P. Royer, L. Staveley-Smith, B. M. Swinyard, P. A. M. van Hoof, J. T. van Loon, J. Verstappen, R. Wesson, G. Zanardo, J. A. D. L. Blommaert, L. Decin, W. T. Reach, G. Sonneborn, G. C. Van de Steene, and J. A. Yates. A Stubbornly Large Mass of Cold Dust in the Ejecta of Supernova 1987A. *ApJ*, 800:50, February 2015. doi: 10.1088/0004-637X/800/1/50.

M. Matsuura, R. Indebetouw, S. Woosley, V. Bujarrabal, F. J. Abellán, R. McCray, J. Kamenetzky, C. Fransson, M. J. Barlow, H. L. Gomez, P. Cigan, I. De Looze, J. Spyromilio, L. Staveley-Smith, G. Zanardo, P. Roche, J. Larsson, S. Viti, J. T. van Loon, J. C. Wheeler, M. Baes, R. Chevalier, P. Lundqvist, J. M. Marcaide, E. Dwek, M. Meixner, C.-Y. Ng, G. Sonneborn, and J. Yates. ALMA spectral survey of Supernova 1987A - molecular inventory, chemistry, dynamics and explosive nucleosynthesis. *MNRAS*, 469:3347–3362, August 2017. doi: 10.1093/mnras/stx830.

D. McElroy, C. Walsh, A. J. Markwick, M. A. Cordiner, K. Smith, and T. J. Millar.

The UMIST database for astrochemistry 2012. *A&A*, 550:A36, February 2013. doi: 10.1051/0004-6361/201220465.

C. F. McKee and E. C. Ostriker. Theory of Star Formation. *Ann. Rev. Astr. Astrophys.*, 45:565–687, September 2007. doi: 10.1146/annurev.astro.45.051806.110602.

J. Meaburn, C. A. Clayton, M. Bryce, J. R. Walsh, A. J. Holloway, and W. Steffen. The nature of the cometary knots in the Helix planetary nebula (NGC 7293). *MNRAS*, 294: 201, February 1998. doi: 10.1046/j.1365-8711.1998.01152.x.

R. Meijerink and M. Spaans. Diagnostics of irradiated gas in galaxy nuclei. I. A far-ultraviolet and X-ray dominated region code. *A&A*, 436:397–409, June 2005. doi: 10.1051/0004-6361:20042398.

L. Mestel. On the theory of white dwarf stars. II. The accretion of insterstellar matter by white dwarfs. *MNRAS*, 112:598, 1952. doi: 10.1093/mnras/112.6.598.

L. Mestel and L. Spitzer, Jr. Star formation in magnetic dust clouds. *MNRAS*, 116:503, 1956. doi: 10.1093/mnras/116.5.503.

E. R. Micelotta, E. Dwek, and J. D. Slavin. Dust destruction by the reverse shock in the Cassiopeia A supernova remnant. *A&A*, 590:A65, May 2016. doi: 10.1051/0004-6361/201527350.

M. J. Michałowski, E. J. Murphy, J. Hjorth, D. Watson, C. Gall, and J. S. Dunlop. Dust grain growth in the interstellar medium of 5 ¡ z ¡ 6.5 quasars. *A&A*, 522:A15, November 2010. doi: 10.1051/0004-6361/201014902.

D. Middlemass. A model for the planetary nebula NGC 7027. *MNRAS*, 244:294–309, May 1990.

M. M. Miller Bertolami. New models for the evolution of post-asymptotic giant branch stars and central stars of planetary nebulae. *A&A*, 588:A25, April 2016. doi: 10.1051/0004-6361/201526577.

H. L. Morgan and M. G. Edmunds. Dust formation in early galaxies. *MNRAS*, 343: 427–442, August 2003. doi: 10.1046/j.1365-8711.2003.06681.x.

F. Motte, P. Andre, and R. Neri. The initial conditions of star formation in the rho Ophiuchi main cloud: wide-field millimeter continuum mapping. *A&A*, 336:150–172, August 1998.

T. C. Mouschovias. Ambipolar diffusion in interstellar clouds - A new solution. *ApJ*, 228: 475–481, March 1979. doi: 10.1086/156868.

S. L. Mufson, J. Lyon, and P. A. Marionni. The detection of carbon monoxide emission in planetary nebulae. *ApJL*, 201:L85–L89, October 1975. doi: 10.1086/181948.

H. S. P. Müller, S. Thorwirth, D. A. Roth, and G. Winnewisser. The Cologne Database for Molecular Spectroscopy, CDMS. *A&A*, 370:L49–L52, April 2001. doi: 10.1051/0004-6361:20010367.

H. S. P. Müller, F. Schlöder, J. Stutzki, and G. Winnewisser. The Cologne Database for Molecular Spectroscopy, CDMS: a useful tool for astronomers and spectroscopists. *Journal of Molecular Structure*, 742:215–227, May 2005. doi: 10.1016/j.molstruc.2005.01.027.

H. S. P. Müller, S. Muller, P. Schilke, E. A. Bergin, J. H. Black, M. Gerin, D. C. Lis, D. A. Neufeld, and S. Suri. Detection of extragalactic argonium, ArH^+, toward PKS 1830-211. *A&A*, 582:L4, October 2015. doi: 10.1051/0004-6361/201527254.

P. C. Myers. Dense cores in dark clouds. III - Subsonic turbulence. *ApJ*, 270:105–118, July 1983. doi: 10.1086/161101.

P. C. Myers and P. J. Benson. Dense cores in dark clouds. II - NH3 observations and star formation. *ApJ*, 266:309–320, March 1983. doi: 10.1086/160780.

F. Nakamura, T. Hanawa, and T. Nakano. Fragmentation of filamentary molecular clouds with longitudinal magnetic fields: Formation of disks and their collapse. *ApJ*, 444: 770–786, May 1995. doi: 10.1086/175650.

T. Nakano. Quasistatic Contraction of Magnetic Protostars due to Magnetic Flux Leakage - Part One - Formulation and an Example. *PASJ*, 31:697, 1979.

A. Natta and D. Hollenbach. The evolution of the neutral gas in planetary nebulae: theoretical models. *A&A*, 337:517–538, September 1998.

D. A. Neufeld and M. G. Wolfire. The Chemistry of Interstellar Argonium and Other Probes of the Molecular Fraction in Diffuse Clouds. *ApJ*, 826:183, August 2016. doi: 10.3847/0004-637X/826/2/183.

D. A. Neufeld and M. G. Wolfire. The Cosmic-Ray Ionization Rate in the Galactic Disk, as Determined from Observations of Molecular Ions. *ApJ*, 845:163, August 2017. doi: 10.3847/1538-4357/aa6d68.

D. A. Neufeld, J. R. Goicoechea, P. Sonnentrucker, J. H. Black, J. Pearson, S. Yu, T. G. Phillips, D. C. Lis, M. de Luca, E. Herbst, P. Rimmer, M. Gerin, T. A. Bell, F. Boulanger, J. Cernicharo, A. Coutens, E. Dartois, M. Kazmierczak, P. Encrenaz, E. Falgarone, T. R. Geballe, T. Giesen, B. Godard, P. F. Goldsmith, C. Gry, H. Gupta, P. Hennebelle, P. Hily-Blant, C. Joblin, R. Kołos, J. Krełowski, J. Martín-Pintado, K. M. Menten, R. Monje, B. Mookerjea, M. Perault, C. Persson, R. Plume, M. Salez, S. Schlemmer, M. Schmidt, J. Stutzki, D. Teyssier, C. Vastel, A. Cros, K. Klein, A. Lorenzani, S. Philipp, L. A. Samoska, R. Shipman, A. G. G. M. Tielens, R. Szczerba, and J. Zmuidzinas. Herschel/HIFI observations of interstellar OH^+ and H_2O^+ towards W49N: a probe of diffuse clouds with a small molecular fraction. *A&A*, 521:L10, October 2010. doi: 10.1051/0004-6361/201015077.

T. Nozawa, T. Kozasa, A. Habe, E. Dwek, H. Umeda, N. Tominaga, K. Maeda, and K. Nomoto. Evolution of Dust in Primordial Supernova Remnants: Can Dust Grains Formed in the Ejecta Survive and Be Injected into the Early Interstellar Medium? *ApJ*, 666:955–966, September 2007. doi: 10.1086/520621.

T. Nozawa, T. Kozasa, N. Tominaga, K. Maeda, H. Umeda, K. Nomoto, and O. Krause. Formation and Evolution of Dust in Type IIb Supernovae with Application to the Cassiopeia A Supernova Remnant. *ApJ*, 713:356–373, April 2010. doi: 10.1088/0004-637X/713/1/356.

C. R. O'Dell and K. D. Handron. Cometary Knots in the Helix Nebula. *AJ*, 111:1630, April 1996. doi: 10.1086/117902.

C. R. O'Dell, B. Balick, A. R. Hajian, W. J. Henney, and A. Burkert. Knots in Nearby Planetary Nebulae. *AJ*, 123:3329–3347, June 2002. doi: 10.1086/340726.

C. R. O'Dell, W. J. Henney, and G. J. Ferland. Determination of the Physical Conditions

of the Knots in the Helix Nebula from Optical and Infrared Observations. *AJ*, 133: 2343–2356, May 2007. doi: 10.1086/513011.

S. Ogino, K. Tomisaka, and F. Nakamura. Gravitational Collapse of Spherical Interstellar Clouds. *PASJ*, 51:637, October 1999. doi: 10.1093/pasj/51.5.637.

D. E. Osterbrock and G. J. Ferland. *Astrophysics of gaseous nebulae and active galactic nuclei*. University Science Books, Sausalito, CA, 2006.

M. Otsuka, T. Ueta, P. A. M. van Hoof, R. Sahai, I. Aleman, A. A. Zijlstra, Y.-H. Chu, E. Villaver, M. L. Leal-Ferreira, J. Kastner, R. Szczerba, and K. M. Exter. The Herschel Planetary Nebula Survey (HerPlaNS): A Comprehensive Dusty Photoionization Model of NGC6781. *ApJSS*, 231:22, August 2017. doi: 10.3847/1538-4365/aa8175.

P. J. Owen and M. J. Barlow. The Dust and Gas Content of the Crab Nebula. *ApJ*, 801: 141, March 2015. doi: 10.1088/0004-637X/801/2/141.

D. J. Patnaude and R. A. Fesen. A Comparison of X-Ray and Optical Emission in Cassiopeia A. *ApJ*, 789:138, July 2014. doi: 10.1088/0004-637X/789/2/138.

J. P. Phillips. The relation between Zanstra temperature and morphology in planetary nebulae. *MNRAS*, 344:501–520, September 2003. doi: 10.1046/j.1365-8711.2003.06821.x.

S. R. Pottasch, D. A. Beintema, and W. A. Feibelman. Abundances of planetary nebulae ¡ASTROBJ¿NGC 2022¡/ASTROBJ¿, ¡ASTROBJ¿NGC 6818¡/ASTROBJ¿ and IC 4191. *A&A*, 436:953–965, June 2005. doi: 10.1051/0004-6361:20042627.

S. S. Prasad and W. T. Huntress, Jr. A model for gas phase chemistry in interstellar clouds. I - The basic model, library of chemical reactions, and chemistry among C, N, and O compounds. *ApJSS*, 43:1–35, May 1980. doi: 10.1086/190665.

S. S. Prasad and S. P. Tarafdar. UV radiation field inside dense clouds - Its possible existence and chemical implications. *ApJ*, 267:603–609, April 1983. doi: 10.1086/160896.

R. S. Priddey, K. G. Isaak, R. G. McMahon, E. I. Robson, and C. P. Pearson. Quasars as probes of the submillimetre cosmos at z ¿ 5 - I. Preliminary SCUBA photometry. *MNRAS*, 344:L74–L78, October 2003. doi: 10.1046/j.1365-8711.2003.07076.x.

F. D. Priestley and M. J. Barlow. OH^+ emission from cometary knots in planetary nebulae. *MNRAS*, 478:1502–1511, August 2018. doi: 10.1093/mnras/sty1099.

F. D. Priestley, M. J. Barlow, and S. Viti. Modelling the ArH^+ emission from the Crab nebula. *MNRAS*, 472:4444–4455, December 2017. doi: 10.1093/mnras/stx2327.

F. D. Priestley, S. Viti, and D. A. Williams. An Efficient Method for Determining the Chemical Evolution of Gravitationally Collapsing Prestellar Cores. *AJ*, 156:51, August 2018. doi: 10.3847/1538-3881/aac957.

E. M. Purcell. Temperature fluctuations in very small interstellar grains. *ApJ*, 206:685–690, June 1976. doi: 10.1086/154428.

D. Quénard, I. Jiménez-Serra, S. Viti, J. Holdship, and A. Coutens. Chemical modelling of complex organic molecules with peptide-like bonds in star-forming regions. *MNRAS*, 474:2796–2812, February 2018. doi: 10.1093/mnras/stx2960.

T. Rauch. A grid of synthetic ionizing spectra for very hot compact stars from NLTE model atmospheres. *A&A*, 403:709–714, May 2003. doi: 10.1051/0004-6361:20030412.

J. M. C. Rawlings, T. W. Hartquist, K. M. Menten, and D. A. Williams. Direct diagnosis of infall in collapsing protostars. I - The theoretical identification of molecular species with broad velocity distributions. *MNRAS*, 255:471–485, April 1992. doi: 10.1093/mnras/255.3.471.

J. C. Raymond, B.-C. Koo, Y.-H. Lee, D. Milisavljevic, R. A. Fesen, and I. Chilingarian. The Temperature and Ionization of Unshocked Ejecta in Cas A. *ArXiv e-prints*, September 2018.

J. E. Reed, J. J. Hester, A. C. Fabian, and P. F. Winkler. The Three-dimensional Structure of the Cassiopeia A Supernova Remnant. I. The Spherical Shell. *ApJ*, 440:706, February 1995. doi: 10.1086/175308.

S. P. Reynolds. Supernova Remnants at High Energy. *Ann. Rev. Astr. Astrophys.*, 46: 89–126, September 2008. doi: 10.1146/annurev.astro.46.060407.145237.

J. Rho, T. Kozasa, W. T. Reach, J. D. Smith, L. Rudnick, T. DeLaney, J. A. Ennis, H. Gomez, and A. Tappe. Freshly Formed Dust in the Cassiopeia A Supernova Remnant

as Revealed by the Spitzer Space Telescope. *ApJ*, 673:271-282, January 2008. doi: 10.1086/523835.

C. T. Richardson, J. A. Baldwin, G. J. Ferland, E. D. Loh, C. A. Kuehn, A. C. Fabian, and P. Salomé. The nature of the H_2-emitting gas in the Crab nebula. *MNRAS*, 430: 1257–1279, April 2013. doi: 10.1093/mnras/sts695.

A. C. Roach and P. J. Kuntz. The potential curve of ArH^+ and the heats of the reactions $Ar^+ + H_2 \rightarrow ArH^+ + H$ and $Ar + H_2^+ \rightarrow ArH^+ + h$. *J. Chem. Soc. D*, pages 1336–1337, 1970. doi: 10.1039/C29700001336.

W. Roberge and A. Dalgarno. The formation and destruction of HeH/+/ in astrophysical plasmas. *ApJ*, 255:489–496, April 1982. doi: 10.1086/159849.

J. F. Roberts, J. M. C. Rawlings, S. Viti, and D. A. Williams. Desorption from interstellar ices. *MNRAS*, 382:733–742, December 2007. doi: 10.1111/j.1365-2966.2007.12402.x.

N. J. Rodríguez-Fernández, J. Martín-Pintado, A. Fuente, P. de Vicente, T. L. Wilson, and S. Hüttemeister. Warm H_2 in the Galactic center region. *A&A*, 365:174–185, January 2001. doi: 10.1051/0004-6361:20000020.

E. Roueff, A. B. Alekseyev, and J. Le Bourlot. Photodissociation of interstellar ArH^+. *A&A*, 566:A30, June 2014. doi: 10.1051/0004-6361/201423652.

K. Rowlands, H. L. Gomez, L. Dunne, A. Aragón-Salamanca, S. Dye, S. Maddox, E. da Cunha, and P. van der Werf. The dust budget crisis in high-redshift submillimetre galaxies. *MNRAS*, 441:1040–1058, June 2014. doi: 10.1093/mnras/stu605.

R. J. Rudy, G. S. Rossano, and R. C. Puetter. 0.95-1.3 micron spectrophotometry of two bright filaments of the crab nebula. *ApJ*, 426:646–652, May 1994. doi: 10.1086/174101.

R. P. Saxon and B. Liu. Theoretical study of OH(+) - Potential curves, transition moments, and photodissociation cross sections. *J. Chem. Phys.*, 85:2099–2104, August 1986. doi: 10.1063/1.451154.

P. Schilke, D. A. Neufeld, H. S. P. Müller, C. Comito, E. A. Bergin, D. C. Lis, M. Gerin, J. H. Black, M. Wolfire, N. Indriolo, J. C. Pearson, K. M. Menten, B. Winkel, Á. Sánchez-Monge, T. Möller, B. Godard, and E. Falgarone. Ubiquitous argonium

(ArH^+) in the diffuse interstellar medium: A molecular tracer of almost purely atomic gas. *A&A*, 566:A29, June 2014. doi: 10.1051/0004-6361/201423727.

D. R. Schmidt and L. M. Ziurys. Hidden Molecules in Planetary Nebulae: New Detections of HCN and HCO^+ from a Multi-object Survey. *ApJ*, 817:175, February 2016. doi: 10.3847/0004-637X/817/2/175.

F. Schöier, F. van der Tak, E. van Dishoeck, and J. Black. LAMDA: Leiden Atomic and Molecular Database. Astrophysics Source Code Library, October 2010.

F. H. Shu. Self-similar collapse of isothermal spheres and star formation. *ApJ*, 214: 488–497, June 1977. doi: 10.1086/155274.

J. M. Shull and M. van Steenberg. The ionization equilibrium of astrophysically abundant elements. *ApJSS*, 48:95–107, January 1982. doi: 10.1086/190769.

R. Siebenmorgen, E. Kruegel, and J. S. Mathis. Radiative transfer for transiently heated particles. *A&A*, 266:501–512, December 1992.

D. W. Silvia, B. D. Smith, and J. M. Shull. Numerical Simulations of Supernova Dust Destruction. I. Cloud-crushing and Post-processed Grain Sputtering. *ApJ*, 715:1575–1590, June 2010. doi: 10.1088/0004-637X/715/2/1575.

J. D. T. Smith, L. Rudnick, T. Delaney, J. Rho, H. Gomez, T. Kozasa, W. Reach, and K. Isensee. Spitzer Spectral Mapping of Supernova Remnant Cassiopeia a. *ApJ*, 693: 713–721, March 2009. doi: 10.1088/0004-637X/693/1/713.

N. Smith. Spatial distribution of near-infrared and optical emission properties in the bipolar nebula Menzel 3. *MNRAS*, 342:383–398, June 2003. doi: 10.1046/j.1365-8711.2003.06557.x.

T. P. Stecher and D. A. Williams. Photodestruction of Hydrogen Molecules in H I Regions. *ApJL*, 149:L29, July 1967. doi: 10.1086/180047.

T. L. Stephens and A. Dalgarno. Kinetic Energy in the Spontaneous Radiative Dissociation of Molecular Hydrogen. *ApJ*, 186:165–168, November 1973. doi: 10.1086/152484.

A. Sternberg and A. Dalgarno. The infrared response of molecular hydrogen gas to ultraviolet radiation - High-density regions. *ApJ*, 338:197–233, March 1989. doi: 10.1086/167193.

B. Strömgren. The Physical State of Interstellar Hydrogen. *ApJ*, 89:526, May 1939. doi: 10.1086/144074.

M. Tafalla, P. C. Myers, P. Caselli, C. M. Walmsley, and C. Comito. Systematic Molecular Differentiation in Starless Cores. *ApJ*, 569:815–835, April 2002. doi: 10.1086/339321.

K. Tassis, K. Willacy, H. W. Yorke, and N. J. Turner. Non-equilibrium Chemistry of Dynamically Evolving Prestellar Cores. I. Basic Magnetic and Non-magnetic Models and Parameter Studies. *ApJ*, 753:29, July 2012. doi: 10.1088/0004-637X/753/1/29.

T. Temim and E. Dwek. The Importance of Physical Models for Deriving Dust Masses and Grain Size Distributions in Supernova Ejecta. I. Radiatively Heated Dust in the Crab Nebula. *ApJ*, 774:8, September 2013. doi: 10.1088/0004-637X/774/1/8.

J. Tennyson. *Astronomical Spectroscopy: AN Introduction to the Atomic and Molecular Physics of Astronomical Spectra (2ND Edition)*. World Scientific, January 2011. doi: 10.1142/7574.

A. G. G. M. Tielens and D. Hollenbach. Photodissociation regions. I - Basic model. II - A model for the Orion photodissociation region. *ApJ*, 291:722–754, April 1985. doi: 10.1086/163111.

A. G. G. M. Tielens and D. J. Hollenbach. Photodissociation Regions and Planetary Nebulae. In R. Weinberger and A. Acker, editors, *Planetary Nebulae*, volume 155 of *IAU Symposium*, page 155, 1993.

K. Tomisaka. Collapse and fragmentation of magnetized cylindrical clouds. *ApJ*, 438: 226–243, January 1995. doi: 10.1086/175067.

K. Tomisaka, S. Ikeuchi, and T. Nakamura. Equilibria and evolutions of magnetized, rotating, isothermal clouds. II - The extreme case: Nonrotating clouds. *ApJ*, 335:239–262, December 1988. doi: 10.1086/166923.

R. R. Treffers, U. Fink, H. P. Larson, and T. N. Gautier, III. The spectrum of the planetary nebula NGC 7027 from 0.9 to 2.7 microns. *ApJ*, 209:793–799, November 1976. doi: 10.1086/154777.

V. Trimble. Motions and Structure of the Filamentary Envelope of the Crab Nebula. *AJ*, 73:535, September 1968. doi: 10.1086/110658.

R. J. Trumpler. Spectrophotometric Measures of Interstellar Light Absorption. *PASP*, 42: 267, October 1930. doi: 10.1086/124051.

T. Ueta, D. Ladjal, K. M. Exter, M. Otsuka, R. Szczerba, N. Siódmiak, I. Aleman, P. A. M. van Hoof, J. H. Kastner, R. Montez, I. McDonald, M. Wittkowski, C. Sandin, S. Ramstedt, O. De Marco, E. Villaver, Y.-H. Chu, W. Vlemmings, H. Izumiura, R. Sahai, J. A. Lopez, B. Balick, A. Zijlstra, A. G. G. M. Tielens, R. E. Rattray, E. Behar, E. G. Blackman, K. Hebden, J. L. Hora, K. Murakawa, J. Nordhaus, R. Nordon, and I. Yamamura. The Herschel Planetary Nebula Survey (HerPlaNS). I. Data overview and analysis demonstration with NGC 6781. *A&A*, 565:A36, May 2014. doi: 10.1051/0004-6361/201423395.

T. Umebayashi and T. Nakano. Recombination of Ions and Electrons on Grains and the Ionization Degree in Dense Interstellar Clouds. *PASJ*, 32:405, 1980.

Y. A. Uspenskii, J. F. Seely, B. Kjornrattanawanich, D. L. Windt, Y. A. Bugayev, V. V. Kondratenko, I. A. Artyukov, A. A. Titov, E. T. Kulatov, and A. V. Vinogradov. Determination of the optical constants of amorphous carbon in the EUV spectral region 40-450 eV. In *Society of Photo-Optical Instrumentation Engineers (SPIE) Conference Series*, volume 6317 of *Proc. SPIE*, page 631713, August 2006. doi: 10.1117/12.683878.

F. F. S. van der Tak, Z. Nagy, V. Ossenkopf, Z. Makai, J. H. Black, A. Faure, M. Gerin, and E. A. Bergin. Spatially extended OH^+ emission from the Orion Bar and Ridge. *A&A*, 560:A95, December 2013. doi: 10.1051/0004-6361/201322164.

P. P. van der Werf, K. G. Isaak, R. Meijerink, M. Spaans, A. Rykala, T. Fulton, A. F. Loenen, F. Walter, A. Weiß, L. Armus, J. Fischer, F. P. Israel, A. I. Harris, S. Veilleux, C. Henkel, G. Savini, S. Lord, H. A. Smith, E. González-Alfonso, D. Naylor, S. Aalto, V. Charmandaris, K. M. Dasyra, A. Evans, Y. Gao, T. R. Greve, R. Güsten, C. Kramer, J. Martín-Pintado, J. Mazzarella, P. P. Papadopoulos, D. B. Sanders, L. Spinoglio, G. Stacey, C. Vlahakis, M. C. Wiedner, and E. M. Xilouris. Black hole accretion and star formation as drivers of gas excitation and chemistry in Markarian 231. *A&A*, 518: L42, July 2010. doi: 10.1051/0004-6361/201014682.

E. F. van Dishoeck and J. H. Black. The photodissociation and chemistry of interstellar CO. *ApJ*, 334:771–802, November 1988. doi: 10.1086/166877.

H. van Winckel. Post-AGB Stars. *Ann. Rev. Astr. Astrophys.*, 41:391–427, 2003. doi: 10.1146/annurev.astro.41.071601.170018.

E. Vassiliadis and P. R. Wood. Post-asymptotic giant branch evolution of low- to intermediate-mass stars. *ApJSS*, 92:125–144, May 1994. doi: 10.1086/191962.

D. A. Verner and D. G. Yakovlev. Analytic FITS for partial photoionization cross sections. *A&AS*, 109:125–133, January 1995.

J. Vink, J. S. Kaastra, and J. A. M. Bleeker. A new mass estimate and puzzling abundances of SNR Cassiopeia A. *A&A*, 307:L41–L44, March 1996.

S. Viti, M. P. Collings, J. W. Dever, M. R. S. McCoustra, and D. A. Williams. Evaporation of ices near massive stars: models based on laboratory temperature programmed desorption data. *MNRAS*, 354:1141–1145, November 2004. doi: 10.1111/j.1365-2966.2004.08273.x.

W. Wang and Z. Li. Hard X-Ray Emissions from Cassiopeia A Observed by INTEGRAL. *ApJ*, 825:102, July 2016. doi: 10.3847/0004-637X/825/2/102.

D. Watson, L. Christensen, K. K. Knudsen, J. Richard, A. Gallazzi, and M. J. Michałowski. A dusty, normal galaxy in the epoch of reionization. *Nature*, 519:327–330, March 2015. doi: 10.1038/nature14164.

W. D. Watson. Heating of Interstellar H i Clouds by Ultraviolet Photoelectron Emission from Grains. *ApJ*, 176:103, August 1972. doi: 10.1086/151613.

J. C. Weingartner and B. T. Draine. Dust Grain-Size Distributions and Extinction in the Milky Way, Large Magellanic Cloud, and Small Magellanic Cloud. *ApJ*, 548:296–309, February 2001a. doi: 10.1086/318651.

J. C. Weingartner and B. T. Draine. Photoelectric Emission from Interstellar Dust: Grain Charging and Gas Heating. *ApJSS*, 134:263–281, June 2001b. doi: 10.1086/320852.

R. Wesson and X.-W. Liu. Physical conditions in the planetary nebula NGC 6543. *MNRAS*, 351:1026–1042, July 2004. doi: 10.1111/j.1365-2966.2004.07856.x.

R. Willingale, J. A. M. Bleeker, K. J. van der Heyden, and J. S. Kaastra. The mass and energy budget of Cassiopeia A. *A&A*, 398:1021–1028, February 2003. doi: 10.1051/0004-6361:20021554.

M. G. Wolfire, C. F. McKee, D. Hollenbach, and A. G. G. M. Tielens. Neutral Atomic Phases of the Interstellar Medium in the Galaxy. *ApJ*, 587:278–311, April 2003. doi: 10.1086/368016.

S. E. Woosley and T. A. Weaver. The Evolution and Explosion of Massive Stars. II. Explosive Hydrodynamics and Nucleosynthesis. *ApJSS*, 101:181, November 1995. doi: 10.1086/192237.

S. E. Woosley, A. Heger, and T. A. Weaver. The evolution and explosion of massive stars. *Reviews of Modern Physics*, 74:1015–1071, November 2002. doi: 10.1103/RevModPhys.74.1015.

J. Wurster. NICIL: A Stand Alone Library to Self-Consistently Calculate Non-Ideal Magnetohydrodynamic Coefficients in Molecular Cloud Cores. *Publ. Astron. Soc. Australia*, 33:e041, September 2016. doi: 10.1017/pasa.2016.34.

F. Wyrowski, K. M. Menten, R. Güsten, and A. Belloche. First interstellar detection of OH^+. *A&A*, 518:A26, July 2010. doi: 10.1051/0004-6361/201014364.

P. A. Young, C. L. Fryer, A. Hungerford, D. Arnett, G. Rockefeller, F. X. Timmes, B. Voit, C. Meakin, and K. A. Eriksen. Constraints on the Progenitor of Cassiopeia A. *ApJ*, 640:891–900, April 2006. doi: 10.1086/500108.

F. B. Yousif and J. B. A. Mitchell. Recombination and excitation of HeH^+. *Phys. Rev. A*, 40:4318–4321, October 1989. doi: 10.1103/PhysRevA.40.4318.

Y. Zhang and X.-W. Liu. A spectroscopic study of the bipolar planetary nebula Mz 3. *MNRAS*, 337:499–518, December 2002. doi: 10.1046/j.1365-8711.2002.05929.x.

V. N. Zirakashvili and F. Aharonian. Analytical solutions for energy spectra of electrons accelerated by nonrelativistic shock-waves in shell type supernova remnants. *A&A*, 465: 695–702, April 2007. doi: 10.1051/0004-6361:20066494.

V. Zubko, E. Dwek, and R. G. Arendt. Interstellar Dust Models Consistent with Extinction, Emission, and Abundance Constraints. *ApJSS*, 152:211–249, June 2004. doi: 10.1086/382351.

V. G. Zubko, V. Mennella, L. Colangeli, and E. Bussoletti. Optical constants of cosmic

carbon analogue grains - I. Simulation of clustering by a modified continuous distribution of ellipsoids. *MNRAS*, 282:1321–1329, October 1996. doi: 10.1093/mnras/282.4.1321.

B. Zygelman and A. Dalgarno. The radiative association of He(+) and H. *ApJ*, 365:239, December 1990. doi: 10.1086/169475.